

UNIVERSITY OF CRETE  
DEPARTMENT OF PHYSICS  
**P H D T H E S I S**  
DOCTOR OF PHILOSOPHY  
OF  
- ASTROPHYSICS -

*Defended by*  
IOANNIS LIODAKIS

**Unveiling the physics of the most  
active of galaxies: connecting  
blazar theory and observations**

COMMITTEE

---

*Prof.* Vasiliki Pavlidou - UNIVERSITY OF CRETE  
*Prof.* Iossif Papadakis - UNIVERSITY OF CRETE  
*Prof.* Andreas Zezas - UNIVERSITY OF CRETE

HERAKLION 2017

*To my family*

# Contents

<b>Abstract</b>	<b>I</b>
Περίληψη	<b>III</b>
<b>Preface &amp; Acknowledgements</b>	<b>V</b>
<b>1 Introduction</b>	<b>1</b>
1.1 Blazars . . . . .	2
1.1.1 Relativistic effects . . . . .	2
1.1.2 Morphology . . . . .	3
1.1.3 Emission mechanisms . . . . .	4
1.2 Statistical tools . . . . .	8
1.2.1 Kolmogorov-Smirnov test . . . . .	8
1.2.2 Pearson and Spearman tests . . . . .	9
1.2.3 Least-squares fit . . . . .	9
1.2.4 Maximum Likelihood estimation . . . . .	10
<b>2 New blazar physics results</b>	<b>11</b>
<b>3 Summary of Publications</b>	<b>13</b>
<b>Bibliography</b>	<b>15</b>

# Abstract

Blazars are the most extreme active galactic nuclei, with relativistic jets oriented within a small angle from our line of sight. Because of their preferential alignment, their observed properties are distorted by relativistic effects giving rise to unique phenomena such as boosted emission throughout the electromagnetic spectrum, fast variability, and apparently superluminal motions of resolved jet components. Small variations in the degree of alignment with the line of sight and/or velocity of the jet can result to a large scatter in the resulting observable quantities from otherwise similar sources, complicating our understanding of their intrinsic properties and the processes relevant to their central engines. As a result, despite decades of systematic study of their variability across the electromagnetic spectrum, little is known regarding the properties of blazars in the jet rest frame. For these reasons my thesis was focused on understanding and quantifying the relativistic effects that dominate blazar emission.

To this end, I created population models based on robust observables unaffected by variability that describe both the BL Lacs and FSRQs. Using these models I was able to advance our physical understanding of blazars in the following ways: **a)** the variability and inverse-Compton Doppler factor methods are the optimal available techniques for obtaining observational estimates of blazar Doppler factors which shows that blazars while flaring reach equipartition; **b)** a significant fraction of deboosted counter-jets will be detected by the next generation interferometers; **c)** the intrinsic distribution of the timescales of any class of events seen in blazars can be accurately recovered within flux-limited samples even if we can not resolve the relativistic effects on a blazar-by-blazar basis; I applied these findings on various types of blazars observations:

- **F-GAMMA:** Using the multi-wavelength radio light curves of the F-GAMMA program, I estimated the variability Doppler factor for 58  $\gamma$ -ray loud sources with an uncertainty of 16% on average, making them the most accurate Doppler factors available to date. With these Doppler factors I found a strong correlation between the intrinsic broad-band radio luminosity (2.6-142.33 GHz) and the black hole mass extending nine orders of magnitude to stellar mass black holes. I uncovered the first ever scaling to connect observer's and rest frames in beamed sources.
- **RoboPol:** I recovered the intrinsic timescale distribution of the longest (in time) rotations of the Electric Vector Position Angle seen in blazars. I found that that distribution is most likely a narrow Gaussian.
- **OVRO:** Modeling the flux-density distribution of sources monitored by the 40-m radio telescope at the Owens Valley Radio Observatory, I found that  $\gamma$ -ray loud sources are systematically more variable in radio than  $\gamma$ -ray quiet sources suggesting a link between radio variability and  $\gamma$ -ray loudness.
- **Reconciling Doppler factor estimates:** Using archival X-ray and VLBI radio observations I re-estimated the inverse-Compton Doppler factors for 11  $\gamma$ -ray loud sources accounting for the known sources of error in the inverse-Compton Doppler factor method. By comparing my re-estimated values with those from the literature I was able to definitively constrain the Doppler factor for five sources, namely 3C273, 3C345, 3C454.3, PKS1510-089, and PKS1633+382.



# Περίληψη

Οι φλογαστέρες (blazars) είναι από τους πιο ενεργούς γαλαξιακούς πυρήνες (AGN), με σχετικιστικούς πίδακες προσανατολισμένους στο πεδίο της όρασης μας. Εξαιτίας αυτού του προσανατολισμού όλες οι παρατηρούμενες ποσότητες στρεβλώνονται λόγω σχετικιστικών διορθώσεων δημιουργώντας μοναδικά φαινόμενα όπως ενισχυμένη εκπομπή σε όλο το ηλεκτρομαγνητικό φάσμα, γρήγορη μεταβλητότητα, και φαινομενικά υπερφωτή κίνηση του πίδακα. Μικρές διαφοροποιήσεις στην γωνία θέασης, ή/και στην ταχύτητα του πίδακα μπορεί να έχει ως αποτέλεσμα μεγάλη διαφοροποίηση στις παρατηρούμενες ποσότητες από σχετικά όμοιες πηγές. Περιπλέκοντας έτσι την κατανόηση μας για τις πραγματικές τους ιδιότητες και τις διεργασίες σχετικές με τις κεντρικές μηχανές τους. Ως αποτέλεσμα, παρά τις δεκαετίες συστηματικής έρευνας πάνω στην μεταβλητότητα τους σε όλο το ηλεκτρομαγνητικό φάσμα, γνωρίζουμε ελάχιστα για τις ιδιότητες των φλογαστέρων στο σύστημα ηρεμίας του πίδακα. Για αυτούς τους λόγους, οι διατριβή μου εστίασε στον να καταλάβουμε και να ποσοτικοποιήσουμε τα σχετικιστικά φαινόμενα που κατακυριεύουν στην εκπομπή των φλογαστέρων.

Δουλεύοντας προς αυτήν την κατεύθυνση, δημιούργησα πληθυσμιακά μοντέλα βασισμένα σε εύρωστες παρατηρούμενες ποσότητες ανεπηρέαστες από την μεταβλητότητα τα οποία περιγράφουν και τα BL Lac αντικείμενα και τους FSRQs. Χρησιμοποιώντας αυτά τα μοντέλα, κατάφερα προωθήσω την κατανόηση μας για τις φυσικές ιδιότητες των φλογαστέρων με τους εξής τρόπους: α) η μέθοδος της μεταβλητότητας και η μέθοδος του αντίστροφου σκεδασμού Compton για τον υπολογισμό του σχετικιστικού παράγοντα Doppler είναι οι καλύτερες διαθέσιμες μέθοδοι για να υπολογίσουμε παρατηρησιακά τους παράγοντες Doppler σε φλογαστέρες που δείχνει ότι κατά την διάρκεια εκλάμψεων οι φλογαστέρες φτάνουν σε κατάσταση 'equipartition'. β) Ένα σημαντικό μέρος των αντι-πιδάκων θα ανιχνευτούν από τα επομενής γενιάς συμβολόμετρα. γ) η εγγενή κατανομή χρόνων οποιοδήποτε τύπου γεγονότος παρόν σε φλογαστέρες μπορεί να ανακτηθεί με ακρίβεια σε στατιστικά δείγματα 'flux – limited' ακόμα και αν δεν έχουμε γνώση για τις σχετικιστικές διορθώσεις για κάθε πηγή. Εφάρμοσα τα ευρήματα μου σε παρατηρήσεις φλογαστέρων:

- **F – GAMMA:** Χρησιμοποιώντας τις ραδιοφωνικές χρονοσειρές πολλαπλών μηκών κύματος του προγράμματος F – GAMMA, εκτίμησα τον παράγοντα Doppler με την μέθοδο της μεταβλητότητας για 58 πηγές με ισχυρή εκπομπή στις ακτίνες γ με κατά μέσον όρο 16% αβεβαιότητα, κάνοντας τους τους πιο ακριβείς παράγοντες Doppler διαθέσιμους σήμερα. Χρησιμοποιώντας αυτούς του παράγοντες Doppler ανακάλυψα μια δυνατή συσχέτιση μεταξύ τις εγγενής βολομετρικής ραδιοφωνικής λαμπρότητας από 2.6-142.33 GHz και την μάζα της μελανής οπής που εκτείνεται εννέα τάξεις μεγέθους από αστρικής μάζας μέχρι τις πιο μαζικές μελανές οπές στο σύμπαν. Η συσχέτιση αυτή, είναι η πρώτη που ενώνει το σύστημα αναφοράς του παρατηρητή με το σύστημα ηρεμίας του πίδακα σε σχετικιστικά ενισχυόμενες πηγές.
- **RoboPol:** Ανέκτησα της εγγενή κατανομή χρόνων των μακρύτερων (σε διάρκεια) στροφών του πεδίου της πόλωσης του συμβαίνει στους φλογαστέρες. Βρήκα ότι η πιθανότερη μορφή αυτής της κατανομής είναι μια στενή κατανομή Gauss.

- OVRO: Μοντελοποιώντας την κατανομή της πυκνότητας ροής των πηγών που παρατηρούνται από το 40 μέτρων ράδιοτηλεσκόπιο του Owens Valley Radio Observatory, βρήκα ότι οι πηγές με εκπομπή ακτίνων  $\gamma$  είναι συστηματικά πιο μεταβλητές από αυτές χωρίς εκπομπή ακτίνων  $\gamma$  γεγονός που υποδηλώνει την συσχέτιση μεταξύ της μεταβλητότητας στα ραδιοκύματα και την εκπομπή ακτίνων  $\gamma$ .
- Συμφιλιώνοντας τις εκτιμήσεις παραγόντων Doppler: Χρησιμοποιώντας αρχαιακές παρατηρήσεις ακτίνων X και ραδιοφωνικής συμβολομετρίας VLBI ξανα-υπολόγισα τον παράγοντα Doppler με την μέθοδο του αντίστροφου σκεδασμού Compton για 11 πηγες με εκπομπή ακτίνων  $\gamma$  λαμβάνοντας υπόψιν όλες τις γνωστές πηγές σφαλμάτων τις μεθόδου. Συγκρίνοντας τις ξανα-υπολογισμένες τιμές με αυτές από την βιβλιογραφία κατάφερα να εκτιμήσω με σιγουριά τον σχετικιστικό παράγοντα Doppler για πέντε πηγές, και συγκεκριμένα τις 3C273, 3C345, 3C454.3, PKS1510 – 089, και PKS1633 + 382.

# Preface & Acknowledgements

This document contains the work I did during the three years as a PhD student at the University of Crete. It includes an introduction to the basic notions and tools required to familiarize the reader with the contents of this work, the important blazar physics results that resulted from this work, as well as a summary of all the attached papers. These papers have been published in the Monthly Notices of the Royal Astronomical Society and Journal of Astronomy and Astrophysics. They are publicly available online in the ArXiv database with reference numbers [ArXiv:1412.2634](#), [ArXiv:1412.2638](#), [ArXiv:1503.04780](#), [ArXiv:1511.00434](#), [ArXiv:1610.06561](#), [ArXiv:1701.01452](#), [ArXiv:1702.05493](#)

This work could not have been made possible without the guidance of Prof. Vasiliki Pavlidou (thesis advisor) who has truly shaped me into the scientist I am today. Her advice has been and continues to be invaluable to me. I also have to acknowledge the contribution of Prof. Iossif Papadakis, and Prof. Andreas Zezas (members of my PhD committee) who were always there to provide advice and help when ever I needed it. I would like to thank Prof. Dr. J. A. Zensus, Director of the VLBI group, for his hospitality at the Max-Planck institute for Radioastronomy and Prof. A. C. S. Readhead, Director of the Owens Valley Radio Observatory, for his hospitality at the Caltech Astronomy Department, where part of this work was completed.

I acknowledge support by the “Aristeia” Action of the “Operational Program Education and Lifelong Learning” and the European Commission Seventh Framework Program (FP7) through grant PCIG10-GA-2011-304001 “JetPop”, by the Erasmus programme, the FP7 Marie Curie IRSES action, the Krakow meeting (2015) and HAP-workshop (2016) organizing committees, and the Hellenic Astronomical Society.

Finally, I cannot but acknowledge my family, friends, fellow graduate students, colleagues and the staff of the Skinakas Observatory that made my stay at the University of Crete an enjoyable and rewarding experience.

Ioannis Liodakis  
Heraklion, April 2017



# Chapter 1

## Introduction

Active galactic nuclei (AGN) are objects located in the center of near and distant galaxies. They are characterized by their compact morphology and high luminosity throughout the electromagnetic spectrum from the longest wavelength radio to the most high energy  $\gamma$ -rays. The galaxies that host such objects are usually referred to as active galaxies. It is thought that AGN are a result of mass accretion onto a supermassive black hole which lies in the center of the host galaxy. What really makes AGN different from other galaxies are their unusually high luminosities, non-thermal spectrum with broad and narrow emission lines, fast variability in timescales down to hours, and in some cases highly relativistic jets showing apparent superluminal motion of resolved jet components seen through radio interferometric observations.

The first AGN to be discovered was Messier 77 by Carl Seyfert in 1943 [60]. Not long after that discovery, the first Quasars were observed in radio frequencies during the 50s. However due to their compact morphology, they were believed to be stars or star-like objects hence the name quasi-stellar objects. The true nature of these objects was revealed when Marteen Schmidt measured the redshift of 3C273 [59] and showed that it was of extragalactic origins. After their extragalactic nature was established, several mechanisms were proposed in order to account for their extreme luminosities included galaxy mergers, supernovae chain explosions, and pulsar clusters. Today, it is established that the mechanism responsible is the release of gravitation energy from the accretion of matter onto a supermassive black hole [57, 64] with mass ranging from  $10^5$  to  $10^{10}$  solar masses.

The material falling towards the black hole forms an accretion disc. The accretion disc emits a black body spectrum that extends to ultraviolet and soft X-rays. It also creates a magnetic field through the process of the “Cosmic Battery” [19] which is believed to be the main drive behind the formation of relativistic jets, either through extracting energy from the spin of the black hole [9] or through the channeling of material due to the differential rotation of the magnetic field lines anchored to the accretion disc [7].

AGN are categorized based on two criteria: (1) whether they emit a significant amount of their energy in radio wavelengths; (2) their emission lines and their intensity. If they meet the first criterion they are referred to as radio-loud, otherwise they

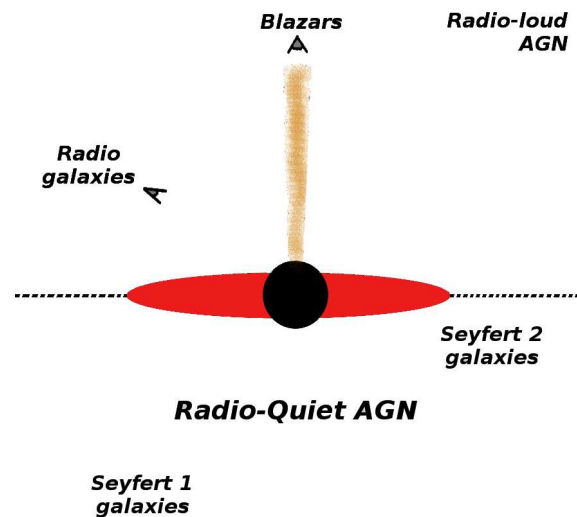


Figure 1.1: Unification of AGN.

are labeled as radio-quiet (Fig. 1.1). This characterization is relative due to the fact that it is based on the comparison of the optical-to-radio luminosity. If the radio luminosity exceeds the optical by 3-4 orders of magnitude the AGN is considered radio-loud. Radio-quiet galaxies are usually Seyfert type galaxies (AGN hosted in spiral galaxies) and Quasi Stellar Objects (QSOs, radio-quiet quasars). The radio-loudness is almost always accompanied by the presence of a jet. In this work, we will focus only on the radio-loud galaxies (radio galaxies, blazars) which are approximately 10-15% of all active galaxies.

One of the radio-loud classes are the radio galaxies. Radio galaxies are usually massive elliptical galaxies that emit strongly in radio. A typical example of a radio galaxy is Cygnus A [4, 34, 13]. It was discovered in 1946 and has a radio output at least  $10^6$  times larger than that of our own galaxy. Radio galaxies have two identical streams of hot, often relativistic, plasma emerging from the center of their galaxies called jets. These jets propagate into the intergalactic medium and can extend up to Mpc in length. At their end, there is a lobe of material, often accompanied by termination shocks called hot spots. These lobes are the source of the radio emission which is due to synchrotron radiation and hence it is highly polarized.

In 1974 B. L. Fanaroff and J. M. Riley found a clear separation of the radio galaxies into two categories according to their radio emission sites with respect to the host galaxy [26]. The first showed bright radio emission close to the host galaxy and decreasing moving further away from the central engine (FR I type galaxies) and the second showed increased brightness towards the lobes located away from the central engine (FR II type galaxies).

## 1.1 Blazars

Blazars are a unique and extremely interesting subclass of radio-loud AGN with jets pointed towards our line of sight ([6], Fig. 1.1). They are either BL Lac objects (BL Lacs) or Flat Spectrum Radio Quasars (FSRQs). BL Lacs are usually found in lower redshifts with relatively less powerful jets than the FSRQs. They are also known to show weak or even no emission lines contrary to FSRQs that show strong broad and narrow emission lines.

Current unification theories [53, 6, 58, 52] suggest that blazars are the beamed counterparts of FR type galaxies. Specifically, FR I galaxies are believed to be the parent population of BL Lacs and FR II galaxies the parent population of FSRQs. However, such an association is not straightforward due to the fact that there are still many open questions regarding the production of  $\gamma$ -rays, cosmological evolution, jet formation and even differences between the blazars classes. Attempts to answer these questions are severely hampered by our inability to quantify in a simple observational manner the velocity of the jet and its angle with our line of sight. The preferential alignment of their jets towards our line of sight, combined with their highly relativistic nature gives rise to relativistic effects that dominate their emission and distort our vision of their intrinsic properties and emission processes.

### 1.1.1 Relativistic effects

The relativistic effects that dominate blazar emission are caused due to the fact that the source of the emitted radiation is moving relativistically towards the observer. These effects can be quantified by the relativistic Doppler factor,

$$\delta = \frac{1}{\Gamma(1 - \beta \cos \theta)}, \quad (1.1)$$

where  $\beta$  is the velocity of the jet in units of speed of light,  $\theta$  is the angle to the line of sight, and  $\Gamma$  is the Lorentz factor defined as  $\Gamma = 1/\sqrt{1 - \beta^2}$ . The Doppler

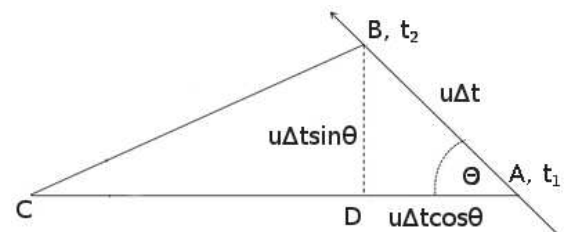


Figure 1.2: Schematic showing the geometric effect causing the apparent superluminal motion.

factor is one of the most important and hard to measure parameters in the blazar paradigm. A summary of how key parameters in blazars are affected by relativistic effects can be found in [29].

Another effect of the preferential alignment of the jet is the apparent superluminal motion [63, 41]. Observations using the Very Long Baseline Arrays (VLBI) in radio wavelengths have enough angular resolution (down to micro-arcseconds) to resolve both the radio core (see section 1.1.2) and components moving relativistically along the jet. The proper motions of such components indicated velocities larger than the speed of light. Soon after its discovery it was proposed that the apparent superluminal motion is a geometric effect due to the alignment of the jet [54]. Figure 1.2 shows a schematic of a relativistic radio component moving along the jet (A to B) with respect to the observer (C) with velocity  $u$  that forms an angle  $\theta$  to the line of sight. In the figure,  $DC = BC = L$  and  $BD = AB \sin \theta$ . Then light emitted at time  $t_1$  from point A and at time  $t_2$  from point B will arrive at the observer at point C at  $t'_1$  and  $t'_2$  respectively.

$$t'_1 = t_1 + \frac{L + v\Delta t \cos \theta}{c}. \quad (1.2)$$

and,

$$t'_2 = t_2 + \frac{L}{c}, \quad (1.3)$$

Combining Eq. 1.2 & 1.3,

$$\Delta t' = t_2 - t_1 - \frac{v\Delta t \cos \theta}{c} = \Delta t - \beta\Delta t \cos \theta \Rightarrow \Delta t' = \Delta t(1 - \beta \cos \theta). \quad (1.4)$$

Then the observed transverse velocity of the jet will be,

$$u_{obs} = \frac{L}{\Delta t'} = \frac{v\Delta t \sin \theta}{\Delta t'} = \frac{v \sin \theta}{1 - \beta \cos \theta}. \quad (1.5)$$

The apparent superluminal motion is usually expressed in units of speed of light as,

$$\beta_{obs} = \frac{u_{obs}}{c} = \frac{\beta \sin \theta}{1 - \beta \cos \theta}. \quad (1.6)$$

The apparent velocity has a different non-trivial dependence on  $\theta$  and  $\beta$  than the Doppler factor which complicates accounting for the relativistic effects. Measuring  $\beta_{obs}$  does not automatically provide information on the  $\delta$  and vice versa. However, measuring both  $\beta_{obs}$  and  $\delta$  allows one to solve for  $\theta$  and  $\beta$  and obtain the orientation of the jet and its speed.

### 1.1.2 Morphology

Blazars are characterized by their one-sided jet morphology. Although several models (e.g. [8]) suggested the existence of two identical jets emerging from the supermassive black hole, one-sidedness was initially believed to be intrinsic to the sources. As instruments improved and new VLBI techniques were developed, counter-jet features appeared in radio images. We now know that blazar jet morphology is attributed to a phenomenon called Doppler favoritism. As the radiation from the approaching jet is beamed towards us, the radiation from the receding jet is beamed away from us. The result is a contrast of 10000:1 even in a mildly relativistic case, hiding the counter-jet.

The apparent base of the radio jet is called the radio core. Some theories suggest it is the physical base of the jet, however observational evidence favor the core being a standing shock about  $10^5$  Schwarzschild radii from the supermassive black hole [43, 44]. The core dominates the radio emission in blazars and is thought to be the production site of the polarization angle rotations seen in optical as well as  $\gamma$ -rays [43, 44, 11]. Figure 1.3 shows a schematic of the most popular model for the morphology of a blazar jet [43]. The numbers on the figure indicate the different regions listed below.

1. Supermassive black hole
2. Accretion disk
3. Dusty torus
4. Broad line region
5. Narrow line region
6. Radio core
7. Radio jet components

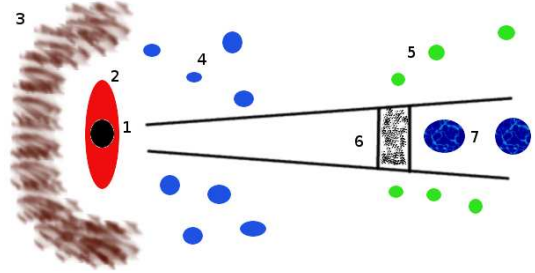


Figure 1.3: Schematic showing the most popular model of the morphology of blazar jets.

The origin of the supermassive black hole is still unknown. Models of black hole growth vary from galaxy mergers and accretion on intermediate mass black holes to collapse of massive star clusters and gas during the formation of the host galaxy. However, observations do not favor any particular model. The accretion disk is created from the gas falling in the supermassive black hole. Accretion disks can be found in a variety of objects from massive stars, protoplanetary disks and black holes of all sizes. Depending on the accretion regime, the disk can be a standard Sakura & Sunyaev thin disk (SSD, [61]) or an Advection Dominated Accretion Flow disk (ADAF, [32, 55]). ADAFs generally have lower accretion rates and lower luminosities than the SSD and their spectrum is non-thermal. The dusty torus consists of dust clouds surrounding the supermassive black hole. Although the hypothesis of a dusty torus helped explain observations of AGN and contributed to their unification, solid evidence of its existence were provided only recently [2]. The Broad Line Region (BLR) consists of clouds of emitting gas. Whether that gas is orbiting the black hole or falling towards it is still unknown. It is called the broad line region because it is responsible for the production of broad lines (typically widths  $> 1000 \text{ km s}^{-1}$ ). The most common lines produced in the BLR are MgII, CIV,  $H\beta$ . Tracking the changes of these lines with a technique called reverberation mapping is one of the most robust methods of estimating the mass of the supermassive black hole. Emission lines with widths  $< 1000 \text{ km s}^{-1}$  (typically  $200\text{-}700 \text{ km s}^{-1}$ ) are thought to originate from the Narrow Line Region (NLR). Most common NLR lines are H I, helium lines as well as the forbidden [N II] and [O III] lines.

### 1.1.3 Emission mechanisms

The broadband spectrum of blazars is characterized by two humps extending from radio to TeV energies (Fig. 1.4). The first hump extends from the long wavelength radio to soft and even hard X-rays depending on the source and it is most likely due to synchrotron radiation from relativistic electrons spiraling in the helical magnetic field of the jet. The second hump extends from X-rays to GeV and in some occasions TeV  $\gamma$ -rays with many different mechanisms proposed to explain the observed spectrum. These mechanisms range from inverse-Compton scattering of internal or external photons fields, hadronic processes, to particle cascades and synchrotron radiation from protons.

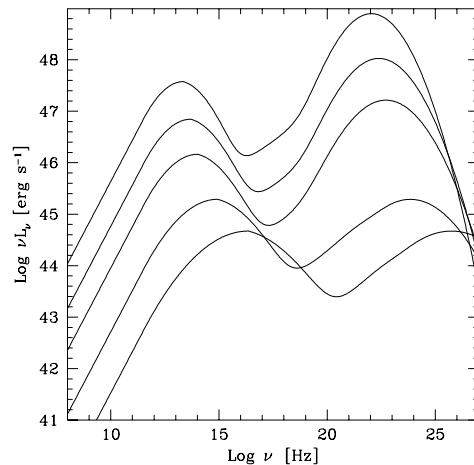


Figure 1.4: Spectral energy distribution of blazars [23].

According to the position of their synchrotron peak (of the first hump) blazars are categorized to Low Synchrotron Peak (LSP), Intermediate Synchrotron Peak (ISP), High Synchrotron Peak (HSP) [1]. FSRQs are usually LSP and ISP whereas BL Lacs are ISP and HSP. Ghisellini et al. (1998) [30] suggested an anticorrelation between the bolometric luminosity and the peak of the synchrotron emission which is due to more powerful blazars suffering more from radiative cooling than the weaker ones. Although some physical explanations have been suggested [27] including accretion disc winds [16], others suggest that the so called “blazar sequence” is too an artifact of beaming [48].

Modeling the spectral energy distribution (SED) of blazars has been an extremely important endeavor due to the wealth of information that can be obtained regarding the magnetic field strength, size of emission region, beaming, but most importantly the high-energy emission process which remain a mystery to this day. However, it has also been a cumbersome task given the many potential different emission mechanisms and physical parameters affecting the observable outcome. For this reason a large number of models have been proposed to account for all the features seen in blazar SEDs. Most commonly these models include only leptonic processes [42, 22], although several models take into account hadronic processes [15] as well as lepto-hadronic processes [18]. Usually these models are single zone models, i.e. the bulk of the emission comes from a single emission region, however there are also multi-zone models as well as models that treat SEDs in a time-dependent manner [56]. The blazar emission mechanisms and SED features can be summarized as follows.

### Synchrotron radiation

Relativistic particles accelerated by magnetic fields will emit radiation called synchrotron radiation. In the non-relativistic regime the corresponding emission mechanism is called cyclotron radiation. For a particle moving in the presence of only a magnetic field the equation of motion can be written as,

$$\frac{d}{dt}(\gamma m \vec{u}) = q \frac{\vec{u} \times \vec{B}}{c}, \quad (1.7)$$

Solving the equation results in a helical motion of the particle with gyration frequency of

$$\omega_B = \frac{qB}{\gamma mc}. \quad (1.8)$$

For uniformly distributed pitch angles of the helix the total emitted power is,

$$P_{synch} = \frac{4}{3} \sigma_T c \beta^2 \gamma^2 U_B, \quad (1.9)$$

where  $\sigma_T$  is the Thomson cross-section ( $\sigma_T = 6.63 \times 10^{-25} \text{ cm}^2$ ),  $\gamma$  is the Lorentz factor of the particle,  $\beta$  the velocity in units of speed of light, and  $U_B = B^2/8\pi$  is the energy density of the magnetic field. Due to aberration effects, as a result of the relativistic motion of the particles, the emitted radiation at angle  $\theta$  in the rest-frame will be received at angle  $\theta'$  in the lab frame. The angles are transformed using,

$$\cos\theta = \frac{\cos\theta' + \beta}{1 + \beta \cos\theta'}. \quad (1.10)$$

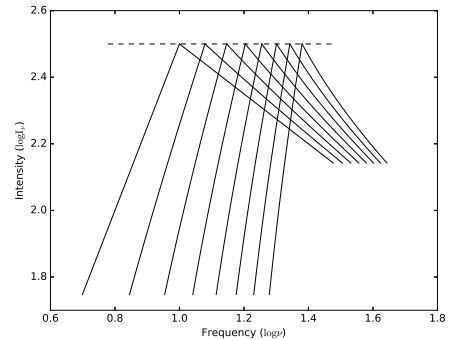


Figure 1.5: Synchrotron spectra from multiple populations with a power-law distribution of electrons. The dashed line is the resulting flat spectrum.

The result is that the isotropic radiation in the rest-frame is focused in a cone with half-opening equal to  $\theta_{op} = 1/\gamma$ . Two key characteristics of synchrotron radiation are its power-law spectrum and that it is highly polarized. For a power-law distribution of electrons the synchrotron spectrum has a characteristic shape: a rising part where  $I_\nu \propto \nu^{5/2}$  (optically thick regime), a turnover due to change in the optical depth, and a falling part where  $I_\nu \propto \nu^\alpha$  (optically thin regime, Fig. 1.5). For multiple populations of relativistic particles with power-law distribution of energies, the observed spectrum (the result of the superposition of the individual spectra) would appear to be flat (Fig. 1.5). The appearance of flat spectra in radio sources was initially considered to be some form of “cosmic conspiracy” [31] until the synchrotron nature of the radiation was established. The linear polarization of the synchrotron radiation arises from the fact that we only observe radiation coming from a particle within  $\theta_{op}$  from our line of sight. The polarization degree from a population of electrons is defined as,

$$\Pi = \frac{p+1}{p+7/3}, \quad (1.11)$$

where  $p$  is the power-law index of the electron distribution, and can reach as high as 70%. In reality non-uniform magnetic fields, depolarization from the host galaxy and other propagation effects bring the typical polarization degree to much lower values. In the radio regime polarization of blazars is of the order of a few percent, whereas in optical the typical polarization as observed by the RoboPol survey [35, 49] is about 7% with the exception of extreme flaring events that have resulted in higher, even up to 45% polarization [11, 12, 10].

In blazars, synchrotron radiation from relativistic electrons is the primary emission mechanism from the low energy radio all the way to hard X-rays. Some models have suggested that synchrotron from relativistic protons can be responsible for the production of  $\gamma$ -rays [47, 50]. However, without X-ray and  $\gamma$ -ray polarization measurements it is extremely difficult to uncover the nature of the radiating particles and confirm or reject such models.

### Inverse-Compton scattering

Inverse Compton scattering is the mechanism where energy from a moving electron is transferred to a photon through scattering. The energy of the photon in the observer’s frame before and after scattering is

$$e_i = \frac{e'_i}{\gamma(1 - \beta \cos \theta_i)}, \quad (1.12)$$

and,

$$e_f = e'_f \gamma(1 + \beta \cos \theta'_f), \quad (1.13)$$

where  $e_i$ , and  $e_f$  are the initial and final photon energy in the observer’s frame,  $\gamma$  is the Lorentz factor of the electron and  $\theta_i$  and  $\theta_f$  are the incident and scattering angles of the photon. Prime quantities are in the rest frame of the electron. The angles are transformed between frames using Eq. 1.10. The final energy of the photon in the electron rest-frame will be,

$$e'_f = \frac{e'_i}{1 + (e'_i/m_e c^2)(1 - \cos \Theta)}, \quad (1.14)$$

where  $m_e$  is the mass of the electron,  $c$  the speed of light and  $\Theta$  is defined as  $\cos \Theta = \cos \theta'_f \cos \theta'_i + \sin \theta'_i \sin \theta'_f \cos(\phi'_i - \phi'_f)$ , where  $\phi'_i$  and  $\phi'_f$  are the azimuthal angles of the incident and scattered photon in the electron rest frame. For relativistic electrons, the energy of the photons in the lab frame, in the electron rest frame before scattering, and lab frame after scattering has occurred follows approximately the ratios  $1:\gamma:\gamma^2$ .

Similar to synchrotron radiation the total emitted power can be written as,

$$P_{IC} = \frac{4}{3}\gamma^2\beta^2\sigma_T c U_{rad}, \quad (1.15)$$

where  $U_{rad}$  is the energy density of the radiating particles. The scatterings occur in the Thomson regime as long as  $h\nu \ll m_e c^2$ . For highly relativistic particles (where  $h\nu \ll m_e c^2$  is not true) scatterings occur in the Klein-Nishina regime where the cross-section is,

$$\sigma_{KN} = \sigma_T \frac{3}{4} \left[ \frac{1+x}{x^3} \left( \frac{2x(1+x)}{1+2x} - \log(1+2x) \right) + \frac{1}{2x} \log(1+2x) - \frac{1+3x}{(1+2x)^2} \right] \quad (1.16)$$

where  $x = h\nu/m_e c^2$ , and  $\nu$  is the frequency. In the Klein-Nishina regime the cross-section decreases at high energies as  $1/(h\nu)$ .

Inverse Compton scattering is thought to be the most probable mechanism for the high energy emission from X-rays to  $\gamma$ -rays. Depending on the origin of the target photon field it is distinguished in External Compton (EC) and Synchrotron Self Compton (SSC). In the SSC scenario the same electrons that produce the synchrotron photons are the ones up-scattering them to higher energies. In the EC scenario the photons can originate from either the accretion disk or the broad line region. The gas surrounding the supermassive black hole can backscatter the photons from the accretion disk back into the jet creating the target field. Due to the external origin of the photon field  $\gamma$ -rays are boosted by  $\delta^{4+\alpha}$  whereas in the SSC scenario  $\gamma$ -rays are boosted by  $\delta^{3+\alpha}$  [20]. It is also believed that the EC is more dominant in FSRQs due to the presence of strong emission lines indicating abundance of gas surrounding the supermassive black hole. SSC is believed to be dominant in BL Lacs due to the lack of strong emission lines.

### Big blue bump

The Big Blue Bump (BBB) is one of the most common features of the AGN SED. It is caused by thermal radiation from the accretion disk extending from infrared up to extreme ultra-violet and in some cases soft X-rays. In blazars the BBB is the only visible thermal component and is present only in some FSRQs. It is also responsible for the ionization of the gas in the broad line region and the appearance of emission lines. Modeling of the BBB can provide important information on the characteristics (structure, temperature etc.) of the accretion disk.

### Pair production and absorption

It is possible for  $\gamma$ -ray photons to be absorbed by lower energy photons (e.g. infrared) or even other  $\gamma$ -ray photons and create electron-positron pairs. These pairs then annihilate producing more  $\gamma$ -rays. For two photons with energies  $E_1$  and  $E_2$  colliding with angle  $\theta$  will produce particles (in the center of momentum frame) with equal velocities (in units of speed of light),

$$\beta = \sqrt{1 - \frac{2}{E_1 E_2 (1 - \cos \theta)}}. \quad (1.17)$$

The cross-section of such an interaction can be written as,

$$\sigma_{\gamma\gamma}(\beta) = \frac{3}{16}\sigma_T(1 - \beta^2) \left[ (3 - \beta^4) \left( \ln \frac{1 + \beta}{1 - \beta} \right) - 2\beta(2 - \beta^2) \right]. \quad (1.18)$$

The  $\gamma\gamma$  pair production sets a horizon after which high energy  $\gamma$ -rays cannot reach us due to the existence of the Extragalactic Background Light (EBL, i.e. ultraviolet, optical and infrared backgrounds) as well as

the cosmic microwave background. In blazars (and AGN in general) photon fields causing pair production and absorption can originate from the BLR, dusty torus and even the accretion disk.

For an external lower-energy photon field the observed energy flux will decrease exponentially,

$$S_{obs} = S_{em} \exp(-\tau_{\gamma\gamma}), \quad (1.19)$$

where  $S_{obs}$  is the observed energy flux,  $S_{em}$  is the emitted energy flux, and  $\tau_{\gamma\gamma}$  is the  $\gamma$ -ray opacity defined as,

$$\tau_{\gamma\gamma} = \int_0^l dx \int_0^{4\pi} (1 - \cos \theta) d\Omega \int_{\frac{2}{E_1(1-\cos \theta)}}^{\infty} N(E_2) \sigma_{\gamma\gamma}(E_1, E_2, \cos \theta) dE_2, \quad (1.20)$$

where  $l$  is the traveled length, and  $N(E_2)$  is the target photon field.

## Hadronic interactions

In addition to  $\gamma\gamma$  pair production high energy  $\gamma$ -rays can interact with hadrons. Since blazars, and relativistic jets in general, are prime candidates for the production and acceleration of Ultra High Energy Cosmic Rays (UHECRs), hadronic interactions might potentially have a significant contribution to the overall  $\gamma$ -ray flux. Such processes can result either to pair production (Bethe-Heitler mechanism [51]) or to the production of mesons (photomeson production [3]).

For the Bethe-Heitler mechanism, if the total energy (squared) of the particles at the center of momentum is larger than  $0.88 \text{ GeV}^2$  then the proton will interact with the photon producing a proton an electron and a positron,

$$p_i + photon = p_f + e^+ + e^-. \quad (1.21)$$

The electron-positron pair will then annihilate producing  $\gamma$ -rays. In the photomeson production mechanism a relativistic nucleus interacts with a photon (when the total energy squared of the particles in the center of mass is  $> 1.16 \text{ GeV}^2$ ) and produces mesons (mostly pions) which then decay producing  $\gamma$ -rays (in the case of  $\pi^0$ ) or muons and neutrinos (in the case of  $\pi^+$ ).

For a more detailed description of the relativistic effects and emission processes the reader should refer to [21, 14, 46] and references therein.

## 1.2 Statistical tools

### 1.2.1 Kolmogorov-Smirnov test

The Kolmogorov-Smirnov test (K-S test, [45]) is one of the most powerful non-parametric tests in order to examine whether two samples originate from the same distribution.

To apply the test, given a sample  $F$  with number of observations  $n$  and a sample  $G$  with number of observations  $m$  one constructs the cumulative distribution functions (CDF) of the two samples and estimate the maximum distance between the two CDFs.

$$D_{n,m} = \max |F - G| \quad (1.22)$$

If the two samples come from the same distribution, the value of the maximum distance will converge to

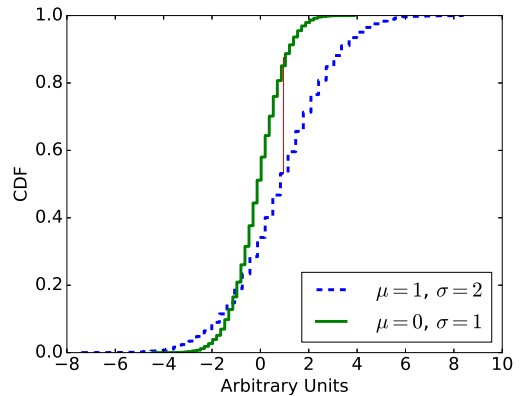


Figure 1.6: Cumulative distribution functions of two Gaussian distributions with different mean ( $\mu$ ) and standard deviation ( $\sigma$ ). The red vertical line marks the position of the maximum distance between the two CDFs.

zero with infinite number of observations. The null hypothesis (usually that the two samples are drawn from the same distribution) is then rejected at a significance level  $\alpha$  if,

$$D_{n,m} > c(\alpha) \sqrt{\frac{n+m}{nm}}, \quad (1.23)$$

where the values of  $c(\alpha)$  are calculated from the CDF of the Kolmogorov distribution [45]. Figure 1.6 shows the CDFs of two normal distributions with  $\mu = 1, \sigma = 2$  and  $\mu = 0, \sigma = 1$ . The red vertical line shows the location of the maximum distance.

## 1.2.2 Pearson and Spearman tests

The Pearson product-moment correlation test [17] is designed in order to investigate whether a correlation exists between two samples. Given two datasets  $X=\{x_1\dots x_n\}$  and  $Y=\{y_1\dots y_n\}$  both with  $n$  elements, then the Pearson correlation coefficient is,

$$r = \frac{\sum_{i=1}^n (x_i - \langle x \rangle)(y_i - \langle y \rangle)}{\sqrt{\sum_{i=1}^n (x_i - \langle x \rangle)^2} \sqrt{\sum_{i=1}^n (y_i - \langle y \rangle)^2}}, \quad (1.24)$$

where  $\langle x \rangle$ , and  $\langle y \rangle$  are the sample mean. The correlation coefficient  $r$  can take values in the  $[-1,1]$  range. For a perfect positive correlation  $r = 1$ , for a perfect negative correlation  $r = -1$  and for no correlation between the two samples  $r = 0$ . From the correlation coefficient and the degrees of freedom (number of elements minus two) we can estimate the probability of the two samples being uncorrelated. The Pearson test assumes that the samples are normally distributed and is sensitive to outliers. If the samples are not normally distributed, or there is no a priori knowledge of the distributions then a more suitable test is the Spearman rank-order correlation test.

The Spearman rank-order test [62] is a non-parametric test with a correlation coefficient defined similarly to the Pearson product-moment test,

$$r = \frac{\sum_{i=1}^n (x_i - \langle x \rangle)(y_i - \langle y \rangle)}{\sqrt{\sum_{i=1}^n (x_i - \langle x \rangle)^2} \sqrt{\sum_{i=1}^n (y_i - \langle y \rangle)^2}}. \quad (1.25)$$

The major differences between the two test are that (1) the Spearman test makes no assumption of normality; and (2) it assesses whether there is a monotonic relation between the two samples whereas the Pearson test assesses whether a linear relation exists. Hence the Spearman test is not sensitive to outliers.

## 1.2.3 Least-squares fit

The least-squares fitting method [37] is one of the most standard and robust methods of linear regression. Its purposes is to minimize the offsets between an assumed linear model given a set of parameters and the observations. It has been widely used in Astrophysics most likely due to the fact that a power-law distribution (which is one of the most commonly encountered distributions in Astrophysics) is a linear relation in logarithmic space. Given a set of observations  $X_n, Y_n$  and a model  $y = ax + b$ , then the sum of the squared offsets between model and observations is calculated setting the partial derivative equal to zero,

$$D = \sum_{i=1}^n (y_i - (ax_i + b))^2. \quad (1.26)$$

We are interested in the parameters (a,b) of the model that minimize the offset between model and observations. These parameters are estimated using,

$$\frac{\partial D}{\partial a} = 0 \quad \text{and} \quad \frac{\partial D}{\partial b} = 0. \quad (1.27)$$

The least-squares fit can be weighted using the uncertainty in the observations for both dependent and independent variables although for simplicity usually only uncertainties in the y-axis are taken into account. It is also possible to have a non-linear least squares fit. However, there is no closed-form solution for such a problem, and an estimates of the non-linear model parameters can only be obtained using numerical techniques.

#### 1.2.4 Maximum Likelihood estimation

In statistics the maximum likelihood estimation (MLE, [24, 25]) is a method of estimating the parameters of a given model that maximize the probability of making a set of observations given these parameters. It is based on the principles of Bayesian statistics assuming that all parameter values are equally probable before observations are made, i.e. a uniform prior.

Given a set of observations  $X=\{x_1\dots x_n\}$  and a model  $f(K)$  with parameters  $K=\{k_1\dots k_m\}$ , the joint probability of having an observations  $x_i$  from the model  $f(K)$  is given by,

$$f(x_1\dots x_n|K) = f(x_1|K) \times f(x_2|K) \times f(x_3|K) \times \dots f(x_n|K). \quad (1.28)$$

We can write the likelihood of the set of parameters  $K$  given the observations,

$$\mathcal{L}(K|x_1\dots x_n) = \prod_{i=1}^n f(x_i|K). \quad (1.29)$$

A more frequently used form of the likelihood is the log-likelihood,

$$\ln \mathcal{L}(K|x_1\dots x_n) = \sum_{i=1}^n \ln f(x_i|K), \quad (1.30)$$

where  $\ln$  denotes the natural logarithm. Similarly to the least-squares method, the partial derivative is used to estimate the values of the parameters that maximize the likelihood.

Once we have found the values of the parameters that maximize the likelihood, we can estimate their uncertainty using the Fisher information matrix [28], which is equal to the negative Hessian matrix.

$$H_{ij} = \frac{\partial^2 \mathcal{L}}{\partial x_i \partial x_j}, \quad (1.31)$$

where  $i, j$  are the coordinates of the matrix elements, and  $x_i, x_j$  are the different parameters. Then the variance-covariance matrix is the inverse of the information matrix. The uncertainty of each of the estimated parameters is the square root of the corresponding diagonal element of the variance-covariance matrix.

For a more thorough and detailed description of the statistical tools presented in this chapter the reader should refer to [5, 33, 36] and references therein.

## Chapter 2

# New blazar physics results

The work presented in this dissertation has advanced our physical understanding of blazars in seven major ways.

1. **BL Lacs and FSRQs are comparably relativistically beamed.** Through detailed population modeling I was able to show that the beaming characteristics of BL Lacs and FSRQs as quantified by  $\Gamma\theta$  (the product of a source's Lorentz factor  $\Gamma$  and the angle between jet and line of sight  $\theta$ ) and the timescale modulation factor ( $m = (1+z)/D$ , where  $z$  is the redshift and  $D$  the relativistic Doppler factor) are similar (Fig. 9, 14, 21 in [39]). This suggests that differences observed in the time domain of between the two classes cannot be attributed to relativistic effects, but instead are intrinsic to the sources.
2. **Magnetic field and emitting relativistic electrons are in equipartition during prominent blazar flares.** In [40] I evaluated the different methods of Doppler factor estimation and found that the variability Doppler factor method can describe both the BL Lac and FSRQ populations. Equipartition is a major assumption on which the variability Doppler factors are based. If it did not hold, this result would not have been possible as there would have been a systematic shift from the distributions derived from the population models.
3. **A significant number of de-boosted blazar counter-jets are on the edge of observability.** Using my population models I calculated the jet-to-counter-jet ratio which was then used to estimate the expected flux-density of blazar counter-jets. I found that although current instruments are not sensitive enough, future interferometric arrays will detect the majority of blazar counter-jets. Detecting these counter-jets will provide a direct observational way to independently estimate the viewing angle of the jet, as well as allow us to probe the physical conditions of the gas surrounding the supermassive black hole powering both jets.
4. **The distribution of rest-frame timescales can be recovered in flux-limited samples.** Using the results of my population models, I developed a novel mathematical formalism in order to recover the intrinsic timescale distribution of any class of events seen in blazars, even if there is no available information of the beaming characteristics on a source-by-source basis. I applied my formalism to the longest (in time) EVPA rotations seen by RoboPol. I found that a narrow Gaussian is the most likely distribution of intrinsic timescales for this type of events.
5. **Over timescales of  $\sim 10$  years, most blazars exhibit bimodal behavior in their emission.** I developed a novel maximum likelihood formalism to capture the bimodal behavior of the flux-density distribution of OVRO-monitored sources as a series of “off” and “on” states. I found that the flux-density distribution of only  $\sim 8\%$  of blazars is consistent with a single-Gaussian distribution. Using

my model I was able to show that  $\gamma$ -ray loud sources are systematically more variable than  $\gamma$ -ray quiet sources in that they have higher flaring ratio, a higher variability modulation index in their “on”-state, and a higher overall modulation index. This would suggest a link between the mechanism for the production of  $\gamma$ -ray and the mechanism responsible for blazar variability at radio frequencies.

6. **The largest contribution to the X-ray emission of most FSRQs comes through SSC.** Apart from the variability Doppler factors, I found that the Inverse-Compton Doppler factors can describe the FSRQs [40]. If SSC was not the dominant mechanism for the production of the X-ray emission in FSRQs, the comparison would have shown a systematic underestimation of their Doppler factors. Not only there is no such underestimation in FSRQs, but also an error analysis did not show any source of systematic uncertainty (see Fig. 14 in [40]) which would have been expected in the alternative case.
7. **Jets are scale invariant.** Using the multi-wavelength radio dataset of the F-GAMMA program and the most accurate Doppler factors available to date I estimated in [38], I uncovered the first ever scaling in beamed sources to connect the rest-frame broad-band radio output of the jet and the black hole mass extending from blazars to microquasars. This universal scaling constitutes an important breakthrough in blazars and so far the only way to bridge observer’s and rest-frames in beamed sources starting from first principles.

## Chapter 3

# Summary of Publications

The results of this dissertation have been published or have been submitted for publication in international peer-reviewed journals. Here, I provide a summary of each of the attached papers in the order of which they were published. The papers “*Reconciling inverse-Compton Doppler factors with variability Doppler factors in blazar jets*” and “*Scale invariant jets: from blazars to microquasars*” are submitted and are undergoing peer review at the time of writing of this dissertation.

- **Population statistics of beamed sources I: A new model for blazars.** Using simple and tested assumption regarding blazars I created population models that can describe the different blazar classes (BL Lacs and FSRQs). These models are based on robust observables (apparent velocity & redshift) unaffected by variability. I found that the mode of the  $\Gamma\theta$  distribution (which quantifies how beamed is a source) is approximately 0.5 for both classes contrary to popular belief ( $\Gamma\theta \approx 1$ ). I also found that the timescale modulation factor (i.e. how timescales are modulated from the rest-frame to the observer’s frame) follows an exponential distribution with similar means for the two classes for 1.5 Jy flux-limited samples.
- **Population statistics of beamed sources II: Evaluating Doppler factor estimates.** Using the population models I developed I tested different Doppler factor estimation methods in order to evaluate which of these methods best describes blazars. I found that the variability Doppler factor method provides good estimates for both blazar classes (with  $\sim 30\%$  error on average), while the inverse Compton Doppler factor method can describe well only the FSRQs (with  $\sim 63\%$  error on average).
- **Detecting the elusive blazar counter-jets:** I built on my population models in order to include spectral index distributions from the MOJAVE survey using a maximum likelihood approach. Using these upgraded models I predicted the jet-to-counter-jet flux-density ratio distribution and set the theoretical limits of flux sensitivity and angular resolution that current (e.g. ALMA) and future VLBI arrays (e.g. SKA) would need to achieve in order to detect the elusive blazar counter-jets. I also set the criteria that constitute a “good” candidate for detecting a counter-jet and provided potential candidates.
- **Estimating the distribution of rest-frame time-scales for blazar jets: a statistical approach.** Using that the timescale modulation factor follows an exponential distribution for both classes (derived from the population models) I created a novel mathematical formalism to recover the intrinsic probability density function of time-like events in the rest-frame of blazar jets. I benchmarked my method with respect to sample size and cadence. The benchmarking showed that for time intervals between observations of 30 days the characteristics of the intrinsic timescale distribution cannot be recovered confidently using my method. As an application, I used the longest (in time) rotations of the electric

vector position angle (EVPA) as seen by RoboPol. I found that the intrinsic distribution of EVPA rotations is narrow, most likely a normal or a uniform distribution.

- **F-GAMMA: Variability Doppler factors of blazars from multiwavelength monitoring.** The error analysis I performed on the variability Doppler factor method showed that the method suffers from systematic errors arising from the cadence of observations. With collaborators from the Max-Planck Institute for Radio Astronomy, we built on this method, by using the multiwavelength dataset of the F-GAMMA survey. We were able to estimate variability Doppler factors for 58 sources adding 20 new estimates in the literature. Our novel approach allowed us to provide *for the first time* error estimates on a blazar-by-blazar basis. We were able to estimate Doppler factors with an average of 16% error making our method the most accurate approach yet.
- **Bimodal radio variability in OVRO-40m-monitored blazars.** I created a five-dimensional likelihood code to model the flux-density ( $S$ ) distribution of the radio sources observed by the Owens valley Radio observatory's (OVRO) blazar program as a series of “off” and “on” states. I was able to recover the blazar duty cycle, and flaring ratio ( $S_{on}/S_{off}$ ), and explore the variability characteristics between different classes. This methodology allowed to verify that the  $\gamma$ -ray-detected sources are systematically more variable, and have higher outbursts than  $\gamma$ -ray-non-detected sources.
- **Reconciling inverse-Compton Doppler factors with variability Doppler factors in blazar jets.** Using contemporaneous X-ray and VLBI observations from the literature I re-estimated the inverse-Compton Doppler factor for 11 sources. Both sources and observations had to meet certain criteria, necessary for the correct application of the method. I then compared them to variability Doppler factor estimates in order to constrain the “true” Doppler factor of blazar jets and investigate potential sources of systematic and statistical error. I was able to confidently constrain the Doppler factor for five sources for which all available estimates converged to the same value.
- **Scale invariant jets: from blazars to microquasars.** Using the findings of my previous works I discovered a strong correlation between the intrinsic total radio luminosity, i.e. the total radio output of the jet, and the black hole mass. I was able to uncover the first ever scaling between blazar observables and engine physical properties and provide independent constrains on the Doppler factor and the intrinsic total power of the jet that can be used in any blazar model. Using literature values, I found that stellar mass black holes with jets (microquasars) follow the same relation, making this relation a universal scaling extending  $\sim 9$  orders of magnitude showing that jets are indeed scale invariant, as well as make predictions of the radio output of the yet undetected intermediate mass black holes.

# Bibliography

- [1] A. A. Abdo, M. Ackermann, I. Agudo, M. Ajello, H. D. Aller, M. F. Aller, E. Angelakis, A. A. Arkharov, M. Axelsson, U. Bach, and et al. The Spectral Energy Distribution of Fermi Bright Blazars. *ApJ*, 716:30–70, June 2010.
- [2] R. R. J. Antonucci and J. S. Miller. Spectropolarimetry and the nature of NGC 1068. *ApJ*, 297:621–632, October 1985.
- [3] A. Atoyan and C. D. Dermer. High-Energy Neutrinos from Photomeson Processes in Blazars. *Physical Review Letters*, 87(22):221102, November 2001.
- [4] W. Baade and R. Minkowski. Identification of the Radio Sources in Cassiopeia, Cygnus A, and Puppis A. *ApJ*, 119:206, January 1954.
- [5] P. R. Bevington. *Data reduction and error analysis for the physical sciences*. 1969.
- [6] R. D. Blandford and A. Königl. Relativistic jets as compact radio sources. *ApJ*, 232:34–48, August 1979.
- [7] R. D. Blandford and D. G. Payne. Hydromagnetic flows from accretion discs and the production of radio jets. *MNRAS*, 199:883–903, June 1982.
- [8] R. D. Blandford and M. J. Rees. A 'twin-exhaust' model for double radio sources. *MNRAS*, 169:395–415, December 1974.
- [9] R. D. Blandford and R. L. Znajek. Electromagnetic extraction of energy from Kerr black holes. *MNRAS*, 179:433–456, May 1977.
- [10] D. Blinov, V. Pavlidou, I. Papadakis, S. Kiehlmann, I. Liodakis, G. V. Panopoulou, T. J. Pearson, E. Angelakis, M. Baloković, T. Hovatta, V. Joshi, O. G. King, A. Kus, N. Kylafis, A. Mahabal, A. Marecki, I. Myserlis, E. Paleologou, I. Papamastorakis, E. Pazderski, S. Prabhudesai, A. Ramaprakash, A. C. S. Readhead, P. Reig, K. Tassis, and J. A. Zensus. RoboPol: do optical polarization rotations occur in all blazars? *MNRAS*, 462:1775–1785, October 2016.
- [11] D. Blinov, V. Pavlidou, I. Papadakis, S. Kiehlmann, G. Panopoulou, I. Liodakis, O. G. King, E. Angelakis, M. Baloković, H. Das, R. Feiler, L. Fuhrmann, T. Hovatta, P. Khodade, A. Kus, N. Kylafis, A. Mahabal, I. Myserlis, D. Modi, B. Pazderska, E. Pazderski, I. Papamastorakis, T. J. Pearson, C. Rajarshi, A. Ramaprakash, P. Reig, A. C. S. Readhead, K. Tassis, and J. A. Zensus. RoboPol: first season rotations of optical polarization plane in blazars. *MNRAS*, 453:1669–1683, October 2015.
- [12] D. Blinov, V. Pavlidou, I. E. Papadakis, T. Hovatta, T. J. Pearson, I. Liodakis, G. V. Panopoulou, E. Angelakis, M. Baloković, H. Das, P. Khodade, S. Kiehlmann, O. G. King, A. Kus, N. Kylafis, A. Mahabal,

- A. Marecki, D. Modi, I. Myserlis, E. Paleologou, I. Papamastorakis, B. Pazderska, E. Pazderski, C. Rajarshi, A. Ramaprakash, A. C. S. Readhead, P. Reig, K. Tassis, and J. A. Zensus. RoboPol: optical polarization-plane rotations and flaring activity in blazars. *MNRAS*, 457:2252–2262, April 2016.
- [13] B. Boccardi, T. P. Krichbaum, U. Bach, F. Mertens, E. Ros, W. Alef, and J. A. Zensus. The stratified two-sided jet of  $\gamma$ -ASTROBJ Cygnus A/ $\gamma$ -ASTROBJ. Acceleration and collimation. *A&A*, 585:A33, January 2016.
- [14] M. Boettcher, D. E. Harris, and H. Krawczynski. *Relativistic Jets from Active Galactic Nuclei*. January 2012.
- [15] M. Böttcher, A. Reimer, K. Sweeney, and A. Prakash. Leptonic and Hadronic Modeling of Fermi-detected Blazars. *ApJ*, 768:54, May 2013.
- [16] S. Boula, A. Mastichiadis, and D. Kazanas. Is the Blazar Sequence related to accretion disk winds? In *Active Galactic Nuclei: What's in a Name?*, page 96, August 2016.
- [17] Royal Society (Great Britain). *Notes on regression and inheritance in the case of two parents*. Number  $\tau$ . 58. Taylor & Francis, 1895.
- [18] M. Cerruti, A. Zech, C. Boisson, and S. Inoue. Lepto-hadronic modelling of blazar emission. In G. Alecian, K. Belkacem, R. Samadi, and D. Valls-Gabaud, editors, *SF2A-2011: Proceedings of the Annual meeting of the French Society of Astronomy and Astrophysics*, pages 555–558, December 2011.
- [19] I. Contopoulos and D. Kazanas. A Cosmic Battery. *ApJ*, 508:859–863, December 1998.
- [20] C. D. Dermer. On the Beaming Statistics of Gamma-Ray Sources. *ApJL*, 446:L63, June 1995.
- [21] C. D. Dermer and G. Menon. *High Energy Radiation from Black Holes: Gamma Rays, Cosmic Rays, and Neutrinos*. 2009.
- [22] C. D. Dermer and R. Schlickeiser. Model for the High-Energy Emission from Blazars. *ApJ*, 416:458, October 1993.
- [23] D. Donato, G. Ghisellini, G. Tagliaferri, and G. Fossati. Hard X-ray properties of blazars. *A&A*, 375:739–751, September 2001.
- [24] F. Y. Edgeworth. On the probable errors of frequency-constants (contd.). *Journal of the Royal Statistical Society*, 71(3):499–512, 1908.
- [25] F. Y. Edgeworth. On the probable errors of frequency-constants (contd.). *Journal of the Royal Statistical Society*, 71(4):651–678, 1908.
- [26] B. L. Fanaroff and J. M. Riley. The morphology of extragalactic radio sources of high and low luminosity. *MNRAS*, 167:31P–36P, May 1974.
- [27] J. D. Finke. A Physical Model for the Revised Blazar Sequence. *ArXiv e-prints*, January 2013.
- [28] R. A. Fisher. Probability Likelihood and Quantity of Information in the Logic of Uncertain Inference. *Proceedings of the Royal Society of London Series A*, 146:1–8, August 1934.
- [29] G. Ghisellini, editor. *Radiative Processes in High Energy Astrophysics*, volume 873 of *Lecture Notes in Physics*, Berlin Springer Verlag, 2013.

- [30] G. Ghisellini, A. Celotti, G. Fossati, L. Maraschi, and A. Comastri. A theoretical unifying scheme for gamma-ray bright blazars. *MNRAS*, 301:451–468, December 1998.
- [31] P. M. Giovanoni and D. Kazanas. Flat-spectrum radio sources - Cosmic conspiracy or relativistic neutrons? *Nature*, 345:319–322, May 1990.
- [32] S. Ichimaru. Bimodal behavior of accretion disks - Theory and application to Cygnus X-1 transitions. *ApJ*, 214:840–855, June 1977.
- [33] C. R. Jenkins J. V. Wall. *Practical Statistics for Astronomers*. Cambridge Observing Handbooks for Research Astronomers. Cambridge University Press, illustrated edition edition, 2003.
- [34] R. C. Jennison and M. K. Das Gupta. Fine Structure of the Extra-terrestrial Radio Source Cygnus I. *Nature*, 172:996–997, November 1953.
- [35] O. G. King, D. Blinov, A. N. Ramaprakash, I. Myserlis, E. Angelakis, M. Baloković, R. Feiler, L. Fuhrmann, T. Hovatta, P. Khodade, A. Kougentakis, N. Kylafis, A. Kus, D. Modi, E. Paleologou, G. Panopoulou, I. Papadakis, I. Papamastorakis, G. Paterakis, V. Pavlidou, B. Pazderska, E. Pazderski, T. J. Pearson, C. Rajarshi, A. C. S. Readhead, P. Reig, A. Steiakaki, K. Tassis, and J. A. Zensus. The RoboPol pipeline and control system. *MNRAS*, 442:1706–1717, August 2014.
- [36] Peter M. Lee. *Bayesian Statistics: An Introduction*. Wiley, 4 edition, 2012.
- [37] A.M. Legendre. *Nouvelles méthodes pour la détermination des orbites des comètes*. F. Didot, 1805.
- [38] I. Liodakis, N. Marchili, E. Angelakis, L. Fuhrmann, I. Nestoras, I. Myserlis, V. Karamanavis, T. P. Krichbaum, A. Sievers, H. Ungerechts, and J. A. Zensus. F-GAMMA: Variability Doppler factors of blazars from multiwavelength monitoring. *ArXiv e-prints*, January 2017.
- [39] I. Liodakis and V. Pavlidou. Population statistics of beamed sources - I. A new model for blazars. *MNRAS*, 451:2434–2446, August 2015.
- [40] I. Liodakis and V. Pavlidou. Population statistics of beamed sources - II. Evaluation of Doppler factor estimates. *MNRAS*, 454:1767–1777, December 2015.
- [41] M. L. Lister and D. C. Homan. MOJAVE: Monitoring of Jets in Active Galactic Nuclei with VLBA Experiments. I. First-Epoch 15 GHz Linear Polarization Images. *AJ*, 130:1389–1417, October 2005.
- [42] L. Maraschi, G. Ghisellini, and A. Celotti. A jet model for the gamma-ray emitting blazar 3C 279. *ApJL*, 397:L5–L9, September 1992.
- [43] A. P. Marscher, S. G. Jorstad, F. D. D’Arcangelo, P. S. Smith, G. G. Williams, V. M. Larionov, H. Oh, A. R. Olmstead, M. F. Aller, H. D. Aller, I. M. McHardy, A. Lähteenmäki, M. Tornikoski, E. Valtaoja, V. A. Hagen-Thorn, E. N. Kopatskaya, W. K. Gear, G. Tosti, O. Kurtanidze, M. Nikolashvili, L. Sigua, H. R. Miller, and W. T. Ryle. The inner jet of an active galactic nucleus as revealed by a radio-to- $\gamma$ -ray outburst. *Nature*, 452:966–969, April 2008.
- [44] A. P. Marscher, S. G. Jorstad, V. M. Larionov, M. F. Aller, H. D. Aller, A. Lähteenmäki, I. Agudo, P. S. Smith, M. Gurwell, V. A. Hagen-Thorn, T. S. Konstantinova, E. G. Larionova, L. V. Larionova, D. A. Melnichuk, D. A. Blinov, E. N. Kopatskaya, I. S. Troitsky, M. Tornikoski, T. Hovatta, G. D. Schmidt, F. D. D’Arcangelo, D. Bhattarai, B. Taylor, A. R. Olmstead, E. Manne-Nicholas, M. Roca-Sogorb, J. L. Gómez, I. M. McHardy, O. Kurtanidze, M. G. Nikolashvili, G. N. Kimeridze, and L. A. Sigua. Probing the Inner Jet of the Quasar PKS 1510-089 with Multi-Waveband Monitoring During Strong Gamma-Ray Activity. *ApJL*, 710:L126–L131, February 2010.

- [45] F. J. Massey. The Kolmogorov-Smirnov test for goodness of fit. *Journal of the American Statistical Association*, 46(253):68–78, 1951.
- [46] D. L. Meier. *Black Hole Astrophysics: The Engine Paradigm*. 2012.
- [47] A. Mücke and R. J. Protheroe. Modeling the April 1997 flare of Mkn 501. In B. L. Dingus, M. H. Salamon, and D. B. Kieda, editors, *American Institute of Physics Conference Series*, volume 515 of *American Institute of Physics Conference Series*, pages 149–153, June 2000.
- [48] E. Nieppola, E. Valtaoja, M. Tornikoski, T. Hovatta, and M. Kotiranta. Blazar sequence - an artefact of Doppler boosting. *A&A*, 488:867–872, September 2008.
- [49] V. Pavlidou, E. Angelakis, I. Myserlis, D. Blinov, O. G. King, I. Papadakis, K. Tassis, T. Hovatta, B. Pazderska, E. Paleologou, M. Baloković, R. Feiler, L. Fuhrmann, P. Khodade, A. Kus, N. Kylafis, D. Modi, G. Panopoulou, I. Papamastorakis, E. Pazderski, T. J. Pearson, C. Rajarshi, A. Ramaprakash, A. C. S. Readhead, P. Reig, and J. A. Zensus. The RoboPol optical polarization survey of gamma-ray-loud blazars. *MNRAS*, 442:1693–1705, August 2014.
- [50] M. Petropoulou and A. Mastichiadis. On proton synchrotron blazar models: the case of quasar 3C 279. *MNRAS*, 426:462–472, October 2012.
- [51] M. Petropoulou and A. Mastichiadis. Bethe-Heitler emission in BL Lacs: filling the gap between X-rays and  $\gamma$ -rays. *MNRAS*, 447:36–48, February 2015.
- [52] A. C. S. Readhead. On the possible non-isotropy of the radio emission from compact extragalactic objects. *PHYSSCR*, 21:662, June 1980.
- [53] A. C. S. Readhead, M. H. Cohen, T. J. Pearson, and P. N. Wilkinson. Bent beams and the overall size of extragalactic radio sources. *Nature*, 276:768–771, December 1978.
- [54] M. J. Rees. Appearance of Relativistically Expanding Radio Sources. *Nature*, 211:468–470, July 1966.
- [55] M. J. Rees, M. C. Begelman, R. D. Blandford, and E. S. Phinney. Ion-supported tori and the origin of radio jets. *Nature*, 295:17–21, January 1982.
- [56] S. Saito, Ł. Stawarz, Y. T. Tanaka, T. Takahashi, M. Sikora, and R. Moderski. Time-dependent Modeling of Gamma-Ray Flares in Blazar PKS1510–089. *ApJ*, 809:171, August 2015.
- [57] E. E. Salpeter. Accretion of Interstellar Matter by Massive Objects. *ApJ*, 140:796–800, August 1964.
- [58] P. A. G. Scheuer and A. C. S. Readhead. Superluminally expanding radio sources and the radio-quiet QSOs. *Nature*, 277:182–185, January 1979.
- [59] M. Schmidt. 3C 273 : A Star-Like Object with Large Red-Shift. *Nature*, 197:1040, March 1963.
- [60] C. K. Seyfert. Nuclear Emission in Spiral Nebulae. *ApJ*, 97:28, January 1943.
- [61] N. I. Shakura and R. A. Sunyaev. Black holes in binary systems. Observational appearance. *A&A*, 24:337–355, 1973.
- [62] C. Spearman. The proof and measurement of association between two things. *The American Journal of Psychology*, 15(1):72–101, 1904.

- [63] R. C. Vermeulen and M. H. Cohen. Superluminal Motion Statistics and Cosmology. *ApJ*, 430:467–494, 1994.
- [64] Y. B. Zel'dovich. The Fate of a Star and the Evolution of Gravitational Energy Upon Accretion. *Soviet Physics Doklady*, 9:195, September 1964.



# Population statistics of beamed sources. I

I. Liodakis<sup>1\*</sup> and V. Pavlidou<sup>1,2</sup>

<sup>1</sup>*Department of Physics and ITCP†, University of Crete, 71003, Heraklion, Greece*

<sup>2</sup>*Foundation for Research and Technology - Hellas, IESL, Voutes, 7110 Heraklion, Greece*

16 June 2015

## ABSTRACT

Observations of blazar jets are shrouded in relativistic effects, thus hindering our understanding of their intrinsic properties and dominant physical processes responsible for their generation, evolution, radiation and particle emission. In this work we focus on extracting information about timescales in the jet rest frame using a population-modeling approach. We employ Monte Carlo simulations to derive a simple population model for the intrinsic unbeamed luminosities and the Lorentz  $\Gamma$  of blazar jets that adequately describe the observed redshift and apparent superluminal speed distributions for flux-limited blazar samples. We derive separate models for BL Lacs and Flat Spectrum Radio Quasars. We then use these models to compute the predicted distribution of Doppler factors in each blazar class, and address the following questions: (a) What is the relativistically induced spread in observed timescales (e.g., event duration, time lags) in a flux-limited sample of relativistic jets? (b) Could differences between BL Lacs and FSRQs observed in the time domain be attributed to differences in beaming between the two populations? (c) Is there a statistically preferred amount of beaming in a flux-limited sample? How large are statistical deviations from that preferred value? We use our findings to propose promising approaches in phenomenological studies of timescales in blazar jets.

**Key words:** galaxies: active – galaxies: jets

## 1 INTRODUCTION

Blazars are active galactic nuclei (AGN) with jets oriented within a small angle from our line of sight (Blandford & Königl 1979). Because of their preferential alignment, their observed properties are obscured by relativistic effects such as Doppler boosting of their emission, compression of variability timescales, and apparently superluminal motions of resolved jet components. Small variations in the degree of alignment with the line of sight can result to a large scatter in the resulting observable quantities from otherwise similar sources. These effects complicate our understanding of their intrinsic properties and the processes relevant to their central engines.

Blazars are extremely variable broadband emitters. Despite decades of systematic study of their variability properties across the electromagnetic spectrum, little is known regarding the variability properties of blazars as a population *in the jet rest frame*, because of the difficulties involved in directly measuring the Doppler factor of blazar jets. One

approach that has been used to that end is to identify the shortest-duration flare that has been observed in an object, and compare it with some known rest-frame timescale one can associate with the source (for example the light-crossing time of the central black hole, see e.g. Aharonian et al. (2007); or, in radio wavelengths, the size of an emission region of known brightness temperature such as the equipartition, e.g. Readhead 1994; Lähteenmäki & Valtaoja 1999; Hovatta et al. 2009.) These approaches are valuable since they constitute our only way to assess Doppler boosting on a source-by-source basis. However, these methods have well-known drawbacks. First of all, the shortest observed timescale only gives a limit to the observed Doppler factor even if all other assumptions hold exactly, as blazar lightcurves have power-law power spectra (Abdo et al. 2010; Chatterjee et al. 2008). Second, the use of other known physical parameters of the jet, such as the black hole mass, to derive Doppler factors, prohibits any correlation studies between these parameters and Doppler factors.

Although these difficulties cannot be easily circumvented on a blazar-by-blazar basis, the connection between observed and intrinsic (jet rest frame) variability properties for blazars *as a population* can be assessed in a more straight-forward way. Assuming randomly distributed line-

\* liodakis@physics.uoc.gr

† Institute for Theoretical and Computational Physics, formerly Institute for Plasma Physics

of-sight orientations for active galactic nuclei jets, we can seek the distribution of intrinsic jet parameters (rest-frame luminosities and Lorentz factors) that best reproduce well-defined observables (such as redshifts and apparent superluminal speeds) rather than the Doppler factors themselves. Then, from these distributions, we can calculate the Doppler factor distribution for the blazar population. We can then use this distribution to deconvolve the Doppler-factor effects on the population as a whole, and gain a statistical insight on the rest-frame variability properties. In this way, we can address questions such as:

- (a) What is the relativistically induced spread in observed event timescales? Could blazar behaviors in the time domain observed to be very varied be in fact very similar in the jet rest frame?
- (b) How different is the beaming between sources in flux-limited samples? Lacking any additional information, is it useful to make statistics-based assumptions for the viewing angle of a single source?
- (c) Do BL Lacs and Flat Spectrum Radio Quasars (FSRQs) have different beaming properties? Could differences observed between them in the time domain be attributed to how relativistic effects differently affect each population?

Our primary motivations for this work are: (i) the study of blazar events of a well-defined duration, such as swings of the polarization angle seen in the optopolarimetric study of blazars (especially in light of currently ongoing large-sample, high-cadence optopolarimetric monitoring programmes such as RoboPol, Pavlidou et al. 2014); and (ii) the study of time lags between different types of events (e.g., between flares at different wavelengths, or between polarization angle swings and flares). However our results are general and can be applied to any time-domain studies of blazar jets.

This paper is organized as follows. In §2 we describe our model for the blazar population. In §3 we discuss the sample we use in order to derive model parameters. In §4 we present our optimization procedure: our model acceptability criteria, the set of observables we have required our model to reproduce, and our optimization algorithm. In §5 we present our results for our samples and in §6 and §7 we discuss the validity of our model and computations, their implementation and the conclusions derived from this work.

The cosmology we have adopted throughout this work is  $H_0 = 71 \text{ km s}^{-1} \text{ Mpc}^{-1}$ ,  $\Omega_m = 0.27$  and  $\Omega_\Lambda = 1 - \Omega_m$  (Komatsu et al. 2009). This choice was made so that our cosmological parameters agree with the MOJAVE (Monitoring Of Jets in Active galactic nuclei with VLBA Experiment, Lister & Homan 2005) analysis (Lister et al. 2009b).

## 2 MODEL

The purpose of our model is to simulate observations from a flux-limited sample of blazars. The population model will consist of a joint distribution for the intrinsic, unbeamed luminosity at a specific (radio) wavelength at different redshifts, and for the jet Lorentz factor. From these, assuming a uniform distribution of viewing angles *for the population*, we can then calculate our observables: flux density as measured by the observer, and redshifts and apparent superluminal speeds for sources above a certain flux limit.

Once we identify model parameters for which the distribution of observables are adequately reproduced for a well-defined sample, we can then calculate the distribution of hard-to-observe quantities *for the sample*, such as viewing angles and Doppler factors.

The idea of building a population model for beamed sources is not new. Models have been fitted by, e.g. Padovani & Urry (1992); Padovani (1992); Vermeulen & Cohen (1994); Lister & Marscher (1997). More recently, the observation of jet speeds by the MOJAVE program for a large, flux-limited sample of blazars, the large majority of which have measured redshifts, has provided an unprecedented set of observables against which such models can be tested and re-optimized (see, e.g., Cara & Lister 2008b).

Here, we optimize a new population model for the blazar population. The reasons why this was necessary in order to address the specific issues we are after, and the associated ways our model differs from past work using the MOJAVE dataset are summarized below.

- *We treat BL Lacs and FSRQs as distinct populations.* As the interpretation of optical wavelength data is one of our primary motivations, deriving (potentially) different models for optically distinct classes of blazars (Giommi et al. 2012) is important in order to assess any differences between these classes in the time domain.
- *We do not seek to reproduce the normalization of the luminosity function.* As our luminosity function model is that of pure luminosity evolution (up to a maximum redshift), this implies that the total number density of sources remains constant, and the total number of sources in a redshift interval is simply proportional to the volume element in that same interval. Our purpose is to determine the distribution of these sources among different (unbeamed) luminosity values rather than the total number of sources in any interval. For this reason, we have the flexibility to simply remove from our sample any sources with unknown redshift. This choice does not affect our luminosity distribution under one of the following two assumptions: if *either* the sources without a redshift measurement have the same redshift distribution as the sources with measured redshifts; *or* all of the sources without a redshift measurement reside at higher redshifts than the sources with measured redshifts, due to a bias in our ability to measure redshifts favoring nearby sources. In the latter case, we will incorrectly surmise that the luminosity distribution sharply cuts off above a redshift that is too low, but the luminosity distribution at redshifts where we can measure it will be in general correct.
- *We do not include individual blazar flux densities in the set of observables the distributions of which our model has to reproduce.* The reason is that blazars are known to show significant variability in all wavelengths and across timescales, making flux density an unreliable observable for model fitting. Instead, we only use the measured and simulated blazar flux densities to determine if a specific source would make or not the cut for inclusion in a flux-limited sample.
- *We simultaneously fit the unbeamed luminosity and bulk Lorentz factor distributions.* Since we are primarily interested in blazar timescale modulation factors in a flux-limited sample, the unbeamed luminosity function and the bulk jet Lorentz factor distribution are of equal importance in pro-

ducing the results of interest. For this reason, we want to avoid taking one of the two as input from past work and only fitting the other.

- *We focus on simplicity in both our models and our acceptability criteria.* Given that the systematic uncertainties (flux variability, redshift incompleteness, variation of component speeds within a single blazar) can be very significant, it is likely that as our understanding of blazar physics improves, our observables themselves will change, and any complex population model and/or sophisticated fit will change with them. For this reason, in this work we try to keep both the models as well as our statistical treatment as simple as possible, and our model acceptability criteria generous.

## 2.1 Unbeamed Luminosity Function

We assume that the jet Lorentz factor and the intrinsic, unbeamed monochromatic luminosity are uncorrelated. Expecting the blazar unbeamed luminosity function to evolve with redshift, we have adopted a pure luminosity evolution model, with a single power law between values  $L_{\nu, \min}$  and  $L_{\nu, \max}$  of the form

$$n(L_\nu, z) \propto \left( \frac{L_\nu}{e^{T(z)/\tau}} \right)^{-A}, \quad (1)$$

where  $n$  is the comoving number density of blazars,  $L$  is the intrinsic luminosity,  $\tau$  is the evolution parameter in units of Hubble time (Padovani & Urry 1992), and  $T(z)$  is the look-back time at a given redshift,

$$T(z) = \frac{1}{H_0} \int \frac{da}{a\sqrt{\Omega_m a^3 + \Omega_\Lambda}}, \quad (2)$$

where  $a = (1+z)^{-1}$  is the scale factor of the Universe. We take Eq. (1) to be valid up to a maximum redshift, equal to the largest measured redshift included in our sample. At higher redshifts, we assume that the normalization of the luminosity function sharply declines with redshift. We do not implement a specific functional form for this decline, simply assuming that it is steep enough so that no higher- $z$  source makes it into our flux-limited sample.

The probability density function (PDF) of the luminosity has the form

$$p(L_\nu) = C_2 \left( \frac{L_\nu}{e^{T(z)/\tau}} \right)^{-A}, \quad (3)$$

and the value of constant  $C_2$  can be obtained by the requirement that the probability density integrates to 1,

$$C_2 = \frac{(-A+1)e^{-AT(z)/\tau}}{L_{\nu, \max}^{-A+1} - L_{\nu, \min}^{-A+1}}. \quad (4)$$

The cumulative density function (CDF) of this distribution is

$$\text{CDF}(L_\nu) = \frac{L_\nu^{-A+1} - L_{\nu, \min}^{-A+1}}{L_{\nu, \max}^{-A+1} - L_{\nu, \min}^{-A+1}}. \quad (5)$$

In the pure luminosity evolution model, sources become brighter with look-back time while maintaining a constant comoving number density (Padovani & Urry 1992). Then, the number of sources  $N$  in a redshift interval from  $z$  to

$z + dz$  is proportional to the comoving volume element  $dV$  ( $N = ndV$ ), where

$$dV = \frac{c}{H_0} \frac{4\pi d_c^2 dz}{\sqrt{\Omega_m(1+z)^3 + \Omega_\Lambda}}, \quad (6)$$

and  $d_c$  is the comoving distance,

$$d_c = \frac{c}{H_0} \int_0^z \frac{dz'}{\sqrt{\Omega_m(1+z')^3 + \Omega_\Lambda}}. \quad (7)$$

## 2.2 Lorentz Factor Distribution

We assume a single power law of the Lorentz factor  $\Gamma$  of the jet is sufficient to describe any sample, as suggested by Padovani & Urry (1992) and Lister & Marscher (1997). The probability density function  $p(\Gamma)$  has the form of,

$$p(\Gamma) = C_1 \Gamma^{-\alpha}, \quad (8)$$

where  $C_1$  is a normalization constant,

$$C_1 = \frac{-\alpha + 1}{\Gamma_{max}^{-\alpha+1} - \Gamma_{min}^{-\alpha+1}}, \quad (9)$$

with  $\Gamma_{min} = 1$  and  $\Gamma_{max} \approx \beta_{app}^{max}$  (Vermeulen & Cohen 1994).

## 2.3 Viewing Angles

We assume a random viewing angle ( $\cos\theta$  uniformly distributed from 0 to 1.) Blazar jets are closely aligned with our line of sight, and we expect this to hold for the observed flux-limited sample as sources with viewing angles larger than a few degrees will not have sufficient Doppler boosting in order to pass the flux-density limit in wavelengths where blazars are the dominant AGN class.

## 2.4 Derived Quantities

Once the intrinsic unbeamed monochromatic luminosity  $L_\nu$ , the bulk Lorentz factor  $\Gamma$  of the jet, the redshift  $z$ , and the viewing angle  $\theta$  are known for a source, then we can calculate a series of derived quantities, including:

- the apparent superluminal speed of the jet,

$$\beta_{app} = \frac{\beta \sin \theta}{1 - \beta \cos \theta} \quad (10)$$

where  $\beta \lesssim 1$  is the speed of the jet in units of the speed of light, which is connected to the Lorentz factor through

$$\Gamma = \frac{1}{\sqrt{1 - \beta^2}}; \quad (11)$$

- the Doppler factor,

$$D = \frac{1}{\Gamma(1 - \beta \cos \theta)}; \quad (12)$$

- the apparent timescale  $\Delta t'$  of events that have a duration  $\Delta t$  in the jet rest frame,

$$\Delta t' = \frac{1+z}{D} \Delta t; \quad (13)$$

- and the observed monochromatic flux density,

$$S_\nu = \frac{L_\nu D^p}{4\pi d_L^2} (1+z)^{1+s}. \quad (14)$$

In Eq. (14),  $L_\nu$  is the unbeamed monochromatic luminosity,  $d_L = (1+z)d_c$  is the luminosity distance at a given redshift, and ( $s$ ) is the spectral index, with its sign defined through  $S_\nu \propto \nu^s$ . The exponent  $p$  is given by  $p = 2 - s$  for the continuous and  $p = 3 - s$  for the discrete jet cases (Ghisellini et al. 1993). Following Lister et al. 2009b we adopt the continuous jet case ( $p = 2 - s$ ). For FSRQs we take  $s = 0.37$ , (a value calculated in Lister et al. (2009b) by fitting an envelope to the  $\beta_{app}$  vs 15 GHz luminosity plot for MOJAVE sources); for BL Lacs we take  $s = 0$  (Urry & Padovani 1991; Lister & Marscher 1997; Cohen et al. 2007).

### 3 SAMPLE

Our sample consists of sources with a measured redshift from the MOJAVE survey statistically complete, flux-limited sample (Arshakian, Ros & Zensus 2006; Pushkarev et al. 2009, 2012). We have excluded objects that have shown any abnormal behavior, inward motion or poor apparent velocity measurement, as indicated by Lister et al. (2009b, 2013). We also removed objects 0805-077 and 0642+449 because they were outliers, possibly indicating unique or abnormal properties: 0805-077 exhibits a far greater apparent speed than any other object ( $\beta_{app} \approx 50$ ) and 0642+449 has an untypically high redshift ( $z = 3.396$ ).

Our final sample consists of the 74 FSRQs and 16 BL Lacs shown in table 1 and 2 respectively.

Since we will be using MOJAVE observations at 15 GHz for the component speeds, the flux densities and luminosities we use in this work will also refer to a frequency of 15 GHz. The flux limit of our adopted sample, which we will also impose on our simulated data, is 1.5 Jy.

## 4 MODEL OPTIMIZATION

### 4.1 Observables and Model Acceptability Criteria

Sources in our adopted sample have available measurements for each of the following quantities: redshift  $z$ ; mean apparent jet speed  $\langle\beta_{app}\rangle$ ; and average flux density  $\langle S_\nu\rangle$ .

In order for a model to be deemed acceptable, we require that it adequately reproduce the observed  $z$  and  $\langle\beta_{app}\rangle$  distributions, when the appropriate flux limit is applied. Formally, we require a Kolmogorov-Smirnov test to return a probability higher than 5% that the simulated and observed values of  $z$  (and, similarly, of  $\langle\beta_{app}\rangle$ ) are drawn from the same distribution.

In contrast, as discussed in §2, we do not require the model to reproduce the observed distribution of  $\langle S_\nu\rangle$ . We compare, however, the observed flux density distribution of the MOJAVE sample (Lister et al. 2009a) and the flux density distribution of the optimal model for the BL Lac objects and the FSRQs and discuss their agreement in §5.3. A detailed analysis of the effect of variability on the flux density distribution and the resulting fitted luminosity function will be the subject of a future publication.

The procedure for testing the acceptability of a specific model is the following:

- We use redshift bins of size 0.1 from  $z = 0$  to  $z = 1.4$  for the BL Lac sample and from  $z = 0$  to  $z = 2.5$  for the FSRQ sample. Since  $dN \propto dV$  for each redshift bin, we calculate the comoving volume element and the number of repetitions performed is proportional to  $dV$ . We also calculate the proper distance for each redshift and the look-back time in order to adjust the luminosity limits in each redshift bin.
- For each repetition (simulated source), we randomly choose a value for  $\cos(\theta)$ ,  $\Gamma$ , and  $L_\nu$  according to the corresponding distributions of the specific model being tested.
- From these values we calculate the velocity  $\beta$ , the apparent velocity  $\beta_{app}$ , the Doppler factor  $D$  and the flux density  $S_\nu$ .
- In order to simulate a flux-limited sample, we discard any source with  $S_\nu$  lower than 1.5 Jy.
- We construct the cumulative distribution function of the apparent velocity and redshift distributions of simulated sources, and we compare them to those obtained from the data. We use the Kolmogorov-Smirnov test (K-S test) in order to obtain the probability of the observed and the simulated data sets having been drawn from the same distribution.

### 4.2 A newly optimized model

The parameters we optimize for each population are the slope  $A$  of the luminosity function, the evolution parameter  $\tau$ , and the slope  $\alpha$  of the Lorentz factor distribution. We refer to the literature (Lister & Marscher 1997) for an estimate of the power law indices for the luminosity and Lorentz factor distributions as a starting point, and proceed to explore the parameter space setting the lower limit for the luminosity to  $10^{24} WHz^{-1}$  and the upper limit  $10^{27} WHz^{-1}$  (Arshakian, Ros & Zensus 2006). A summary of parameter values we adopt from the literature or directly from the extrema of the datasets are shown in the upper part of Table 3.

We first perform a coarse preliminary scan of the parameter space to derive initial values for the parameters to be optimized, starting from the aforementioned literature values and shifting towards higher or lower values according to the K-S test and visual inspection of the probability density and cumulative distribution functions. During that investigation we have come to the conclusion that the luminosity function of the BL Lacs does not evolve with redshift, consistent with the recent findings of Ajello et al. (2014): the pure luminosity evolution model with a finite evolution parameter was unable to adequately describe the redshift distribution of the BL Lac objects. All the corresponding K-S test of the BL Lac redshift distribution with an evolution parameter close to the literature value gave probabilities  $\leq 10^{-5}\%$  of consistency. The probability values increased while increasing the value of the evolution parameter, and reached acceptable levels, as described in §4.1, when the evolution parameter was set to infinity.

Starting from the initial values obtained in our coarse scan, we optimize the model parameters in the following way. We create a 3-dimensional cube in parameter space for the FSRQs ( $A, \tau, \alpha$ ) and a 2-dimensional plane for the BL

**Table 1.** FSRQS sample

Object Name	$\beta_{app}$	Redshift	Object Name	$\beta_{app}$	Redshift
0016+731	6.74	1.781	1219+044	2.35	0.965
0059+581	8.705	0.644	1222+216	15.882	0.432
0106+013	24.04	2.099	1226+023	9.643	0.158
0119+115	17.1	0.570	1334-127	6.99	0.539
0133+476	11.5	0.859	1417+385	15.4	1.831
0202+149	6.4	0.405	1458+718	3.907	0.904
0202+319	4.686	1.466	1502+106	10.2	1.839
0212+735	4.87	2.367	1504-166	3.413	0.876
0215+015	18.466	1.715	1510-089	16.11	0.360
0224+671	5.895	0.523	1546+027	8.5675	0.414
0234+285	12.12	1.207	1548+056	7.7	1.422
0333+321	12.2	1.259	1606+106	17.1	1.226
0336-019	13.07	0.852	1611+343	7.69	1.397
0420-014	5.6	0.914	1633+382	16.6625	1.814
0458-020	15.045	2.286	1637+574	9.07	0.751
0528+134	11.036	2.070	1638+398	8.266	1.666
0529+075	8.325	1.254	1641+399	12.4175	0.593
0529+483	17.54	1.162	1726+455	1.873	0.717
0552+398	0.363	2.363	1730-130	17.622	0.902
0605-085	16.186	0.872	1751+288	3.07	1.118
0730+504	12.75	0.720	1800+440	15.04	0.663
0736+017	9.332	0.191	1849+670	22.1	0.657
0738+313	6.986	0.631	1928+738	4.774	0.302
0748+126	14.365	0.889	1936-155	2.6	1.657
0804+499	1.83	1.436	1958-179	1.9	0.650
0827+243	17.7675	0.940	2037+511	3.3	1.686
0836+710	19.35	2.218	2121+053	10.845	1.941
0838+133	8.223	0.681	2136+141	3.7975	2.427
0906+015	19.645	1.024	2145+067	2.206	0.990
0923+392	2.44	0.695	2155-152	12.66	0.672
0945+408	13.256	1.249	2216-038	5.55	0.901
0955+476	2.48	1.882	2223-052	13.0425	1.404
1036+054	6.065	0.473	2227-088	8.1	1.560
1038+064	7.26	1.265	2243-123	3.88	0.632
1045-188	6.085	0.595	2251+158	7.27	0.859
1150+812	5.878	1.250	2331+073	3.445	0.401
1156+295	20.15	0.729	2345-167	11.21	0.576

Mean  $\beta_{app}$  from Lister et al. (2009b); redshifts from Lister et al. (2009a).

**Table 2.** BL Lac sample

Object Name	$\beta_{app}$	Redshift	Object Name	$\beta_{app}$	Redshift
0003-066	2.145	0.347	1413+135	0.755	0.247
0716+714	10.07	0.310	1538+149	4.525	0.605
0754+100	14.4	0.266	1749+096	4.013	0.322
0808+019	13.000	1.148	1803+784	2.396	0.680
0814+425	1.060	0.245	1807+698	0.056	0.051
0823+033	14.3	0.506	1823+568	7.225	0.664
0829+046	6.347	0.174	2131-021	10.318	1.285
0851+202	8.613	0.306	2200+420	5.1335	0.068

Mean  $\beta_{app}$  from Lister et al. (2009b); redshifts from Lister et al. (2009a).

Lacs ( $A, \alpha$ ). Each side of the cube is centered in the corresponding parameter value generating the smallest inconsistency between observed and simulated cumulative distribution functions, and its extent is equal to the coarse-scan step.

For each sample, we take every possible combination of parameters and choose the one that minimizes the com-

bined inconsistency between the observed and simulated cumulative distribution functions of the  $\beta_{app}$  and redshift distributions (we quantify that ‘‘combined inconsistency’’ by the product of the corresponding K-S test statistics). We then repeat the process three additional times, adjusting the boundary values to the step of the previous scan, and using smaller steps centered around the previously obtained

**Table 3.** Model Parameters. Upper part: model values adopted from the literature or directly from extrema of observable distributions (see text). Lower part: optimal parameter values; spread represents scanning step and statistical variations in simulated distributions. The second asymmetrical errors represent the range within which a parameter can produce "acceptable models"

	BL Lacs	FSRQs
$\Gamma_{min}$	1	1
$\Gamma_{max}$	16	26
$L_{min}(\text{W Hz}^{-1})$	$10^{24}$	$10^{24}$
$L_{max}(\text{W Hz}^{-1})$	$10^{27}$	$10^{27}$
$s$	0	0.37
$\alpha$	$0.738 \pm 0.002^{+0.41}_{-1.46}$	$0.57 \pm 0.001^{+0.12}_{-0.50}$
$A$	$2.251 \pm 0.02^{+0.68}_{-0.78}$	$2.6 \pm 0.01^{+0.185}_{-0.245}$
$\tau(1/H_0)$	-	$0.26 \pm 0.001^{+0.068}_{-0.003}$

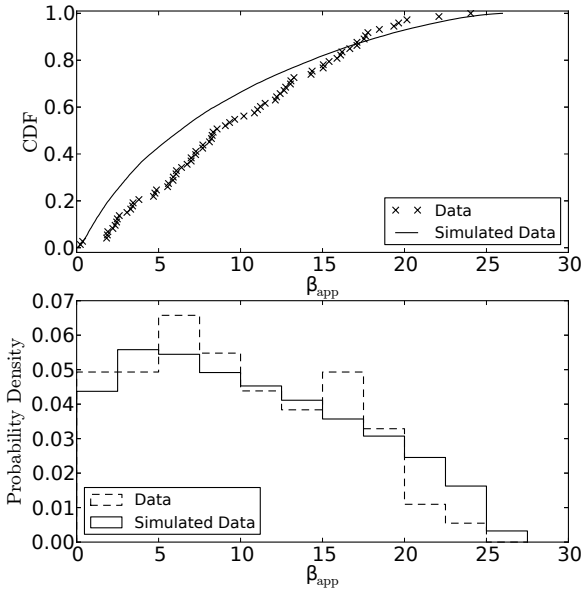


**Figure 1.** Cumulative distribution function (upper panel) and probability density function (lower panel) of simulated (with our optimal model) and observed (MOJAVE sample, see text)  $\beta_{app}$  for FSRQs.

optimal parameters, in order to converge to the best result. In order to investigate the effects of random sampling and account for statistical deviations, we repeat several times the final scan. The optimal parameters values are shown in the lower part of Table 3. Values and error bars correspond to the average and the spread (standard deviation) of the various incarnations of the final-scan optimization. They are therefore representative of the statistical spread in simulated distributions (and indicative of the step in our final scan). In contrast, the range of parameters that produce simulated distributions consistent with the observable ones is addressed later in this section. For the FSRQ optimal parameters, the K-S test p-values are 49.3% for the apparent

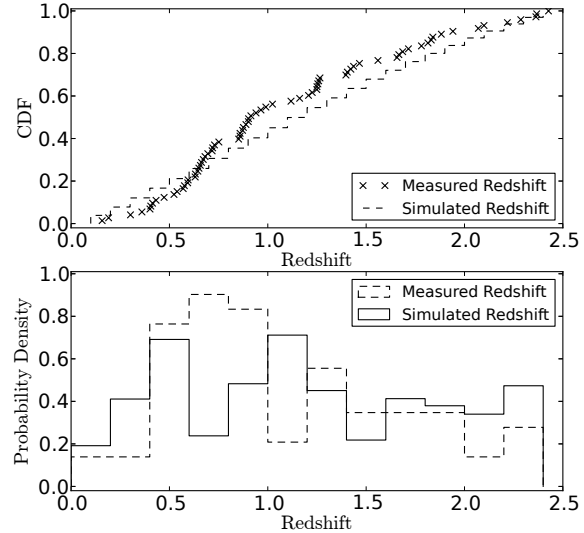


**Figure 2.** Cumulative distribution function (upper panel) and probability density function (lower panel) of simulated (with our optimal model) and observed (MOJAVE sample, see text) redshifts  $z$  for FSRQs

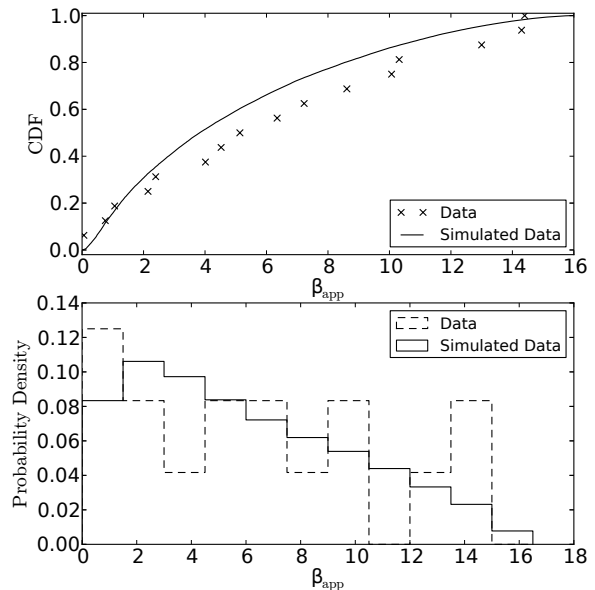


**Figure 3.** Cumulative distribution function (upper panel) and probability density function (lower panel) of simulated (with our optimal model) and observed (MOJAVE sample, see text)  $\beta_{app}$  for BL Lacs

velocity and 8.4% for the redshift distributions (see also Fig. 1,2). For the BL Lac optimal parameters, the corresponding K-S test p-values of 93.4% for the apparent velocity and 54.1% for the redshift distributions (see also Fig. 3,4).

It should be noted that the optimization procedure does not formally correspond to proper model fitting that could be achieved, for example, using a maximum-likelihood anal-

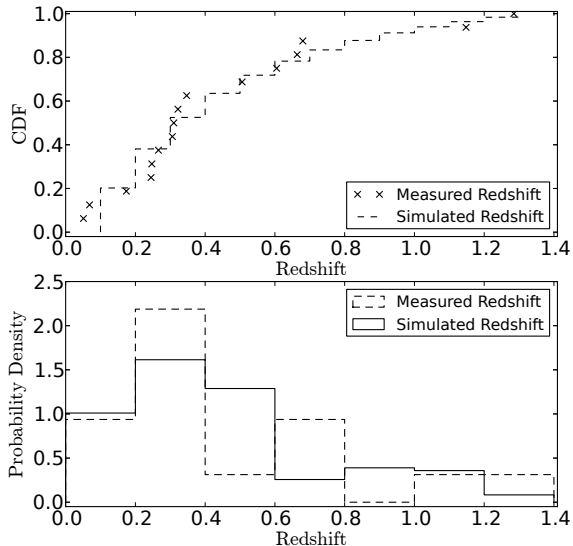


**Figure 4.** Cumulative distribution function (upper panel) and probability density function (lower panel) of simulated (with our optimal model) and observed (MOJAVE sample, see text) redshifts  $z$  for BL Lacs.

ysis, or a chi-square minimization of the simulated probability density functions on the observed ones. There are two reasons we have instead adopted the simpler procedure described here and which is based on the K-S statistic. The first one is simplicity. As discussed in §2, systematic uncertainties in the observables and their interpretation are expected to be significant, and affect the optimal model parameters much more than the details of the optimization procedure. For this reason, the investment in algorithmic complexity and computational time will likely not yield a proportional improvement in model accuracy. The second reason is that the K-S statistic provides an automatic way to assess model consistency with the data: a nominal fitting procedure will yield the model parameters *in best agreement* with the data, without any a priori guarantees that this family of model is a *good* (or even acceptable) description of that dataset. Our procedure however allows us to automatically reject poor fits up to a desired K-S p-value level and find the range of parameters (if such a range exists) for which the hypothesis that the chosen family of models produces the observed dataset cannot be rejected.

In order to determine that range that produces “acceptable models” for each parameter, we create a 2-D (for the BL Lacs), and a 3-D (for the FSRQs) parameter space centered around the best-fit values for each model. We use Monte Carlo sampling of the parameter space, to test which combination of parameters produce “acceptable” models, i.e. the K-S test yields a  $\leq 5\%$  probability of consistency between observed and simulated distributions. We repeat this process enough times in order to ensure that the parameter space is adequately sampled. The range of parameter values produced in this way represents the spread of each parameter. If the extrema of these values coincide with the extrema of the initial parameter space, we increase the range of that space and repeat the process. For the FSRQs this procedure yields

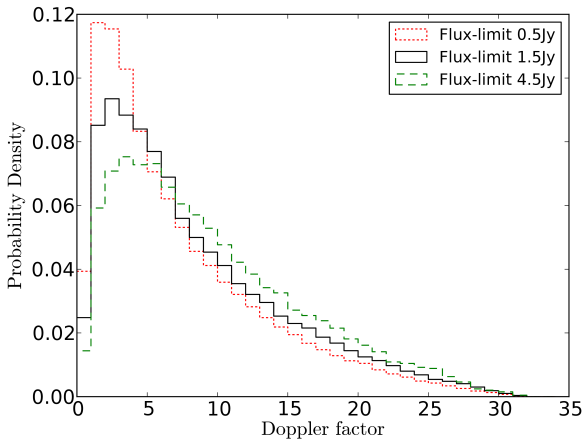


**Figure 5.** BL Lac Doppler factor distribution. Different line types corresponds to different flux limits as follows. Solid line: 1.5 Jy; dashed line: 4.5 Jy; dotted line: 0.5 Jy.

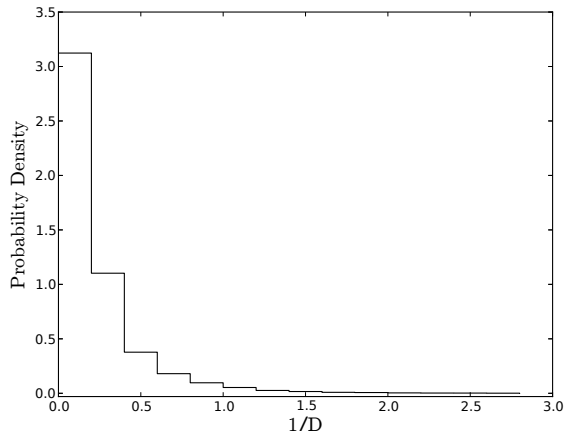


**Figure 6.** Inverse Doppler factor distribution for a flux limited ( $S_\nu \geq 1.5$  Jy) BL Lac sample.

$\alpha = 0.57^{+0.12}_{-0.50}$ ,  $A = 2.6^{+0.185}_{-0.245}$   $\tau = 0.26^{+0.068}_{-0.003}$ . For the BL Lacs the procedure yields  $\alpha = 0.738^{+0.41}_{-1.46}$ ,  $A = 2.251^{+0.68}_{-0.78}$ .

## 5 RESULTS

### 5.1 BL Lacs

Using the optimal values for the two parameters of our BL Lac population model, we explore, in this section, the distributions of the derived quantities discussed in §2. The Doppler factor distribution and inverse Doppler, which will be important in the application to the timescale analysis, are shown in Fig. 5 & 6. The distribution of the viewing angles for sources that pass the flux limit is shown in Fig. 7, and the distribution of the product ( $\Gamma\theta$ ) in Fig. 8.

We can clearly see in Fig. (7) that the sources that manage to pass the flux limit are strongly biased towards very small viewing angles, consistent with our understanding of blazars having jets closely aligned with our line of sight.

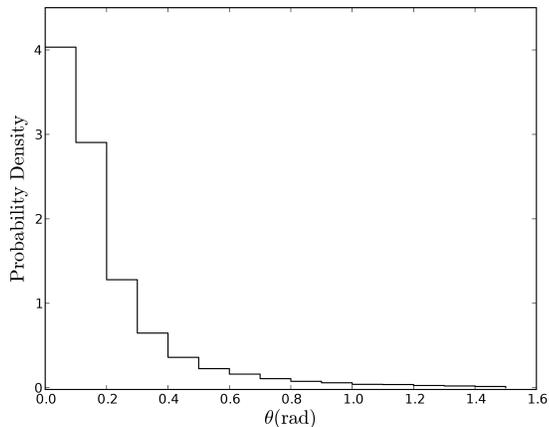


**Figure 7.** Distribution of the viewing angles  $\theta$ (rad) for a flux limited ( $S_\nu \geq 1.5$ Jy) BL Lac sample. The majority of simulated sources have small viewing angles (68.8% have  $\theta \leq 0.2$  rad =  $11.5^\circ$ ), in accordance with our understanding of blazars.

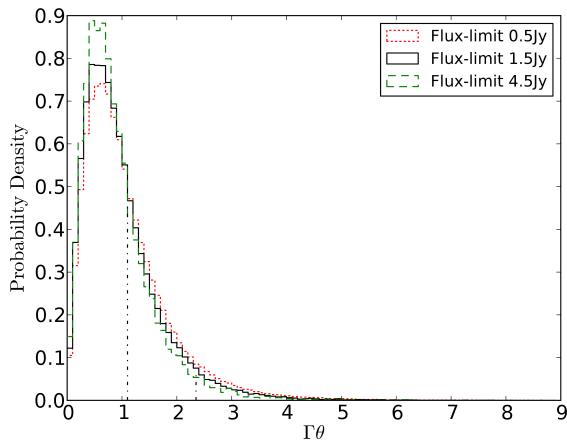


**Figure 8.** Distribution of  $\Gamma\theta$  for flux-limited BL Lac samples. Different lines correspond to different flux limits as follows. Solid line: 1.5 Jy; dashed line: 4.5 Jy; dotted line: 0.5 Jy. The vertical dashed line at 1.11 represents  $1\sigma$ , at 2.37  $2\sigma$  and the dashed line (not visible at  $\Gamma\theta = 4.8$ )  $3\sigma$  for the 1.5 Jy distribution.

Although most sources in the inverse Doppler factor distribution have  $1/D < 1$  (Fig. 5), there is a non-zero power at  $1/D > 1$ . All sources with  $1/D > 1$  are not boosted.

The optimal parameters presented in Table 3 are applicable to the entire BL Lac distribution. In contrast, the resulting derivative-quantity distributions presented in this section are specific to a sample (characterized by a certain flux limit). To demonstrate this explicitly, we plot, in Figs. 5 and 8, the resulting distributions ( $D$  and  $\Gamma\theta$ ) if we implement a different flux limit. We choose to use limits a factor of 3 higher (4.5 Jy) and lower (0.5 Jy) than the limit of the observed dataset (1.5 Jy). In both cases we see that the distributions have similar shapes, and the location of their peaks are insensitive to the flux limit; however, the power in the tails compared to the peak changes as the value of the flux limit changes. As expected, the Doppler factor dis-

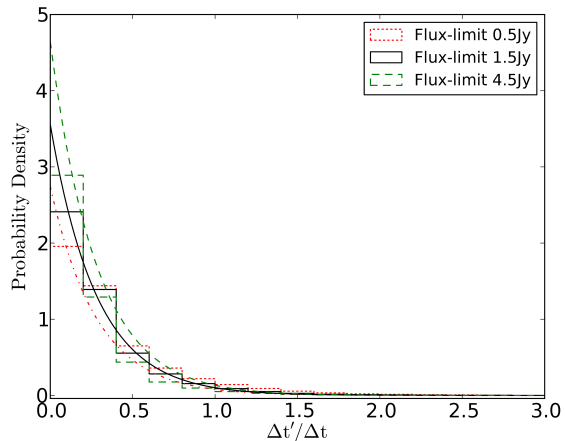


**Figure 9.** Time scale modulation factor distribution for BL Lac objects. Different line types correspond to different flux limits as follows. Solid line: 1.5 Jy; dashed line: 4.5 Jy; dotted line: 0.5 Jy. The overplotted smooth lines represent exponential distributions with the same mean as each histogram.

tribution has more power in the tails (a larger fraction of highly boosted sources) as the flux limit increases. The  $\Gamma\theta$  distribution shows an increase in the number of sources with lower values (more highly beamed sources) as the flux limit increases. We therefore emphasize that although our optimized  $\Gamma$  and  $L_\nu$  distributions describe blazars as a population, the correct flux limit must be taken into account when using them to obtain distributions of derivative quantities to compare with a specific flux-limited sample.

It is common in studies of beamed sources, when there is not enough information to estimate both  $\Gamma$  and  $\theta$  for a source, to assume an average value of  $\Gamma\theta$  (typically,  $\Gamma\theta = 1$ , e.g. Vermeulen 1995; Cohen et al. 2007). The preference for  $\Gamma\theta = 1$  stems from the fact that, if the Lorentz factor associated with the observed movement of the knots in a jet is also the Lorentz factor of the bulk flow, then the maximum apparent speed for a given  $\Gamma$  is achieved for  $\sin\theta = 1/\Gamma$ . Thus for small angles  $\theta \sim 1/\Gamma$ . Figure 8 allows us to evaluate the validity of that assumption. The most likely value of  $\Gamma\theta$  is at 0.6 (see also Jorstad et al. 2005), and this result is quite robust with respect to the sample flux limit. The mean for  $S_\nu \geq 1.5$  Jy is 0.95, close to the frequently assumed  $\Gamma\theta$  value. However, we point out that the spread of the  $\Gamma\theta$  distribution is large: 68% of all values are included between  $0 \leq \Gamma\theta \leq 1.1$ . For this reason, any assumption regarding the value of  $\Gamma\theta$ , whether that value is the mean or the mode of the simulated distributions, should be treated with caution.

The emission from a region with bulk relativistic Lorentz factor  $\Gamma$  is generally beamed within a cone of opening angle  $1/\Gamma$ . For this reason, for beamed sources we expect  $\Gamma\theta < 1$ . Due to the spread of the distribution, we conclude that most, but not all, of the sources in a flux-limited sample of relativistic jets are beamed.

Combining the Doppler factor and redshift distributions (Eq.13) we derive the timescale modulation factor distribution (Fig. 9). The distribution can be well described by an exponential distribution with mean equal to the data mean. In the case of a flux limit of 1.5 Jy, the mean timescale mod-

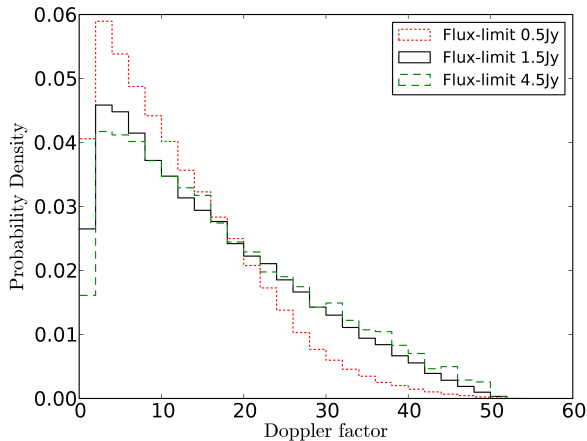


**Figure 10.** Doppler factor distribution for FSRQs. Different line types correspond to different flux limits, as follows. Solid line:1.5 Jy; dashed line: 4.5 Jy; dotted line: 0.5 Jy.

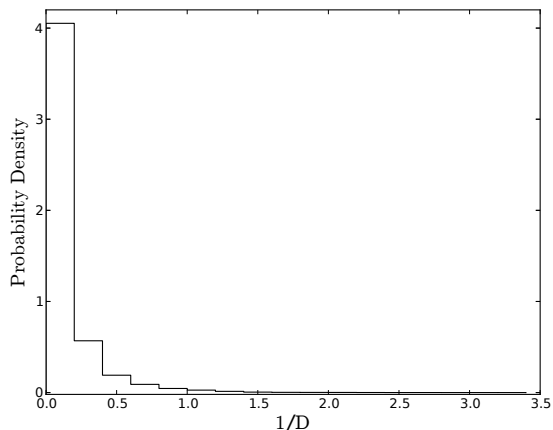


**Figure 11.** Inverse Doppler factor distribution for the FSRQs sample.

ulation factor is equal to 0.281 . However, the distribution is not a strict exponential, because the maximum Doppler factor is finite and hence the time modulation factor is never exactly equal to zero. Its smallest value in the  $S_\nu \geq 1.5Jy$  sample is  $\sim 3 \times 10^{-2}$ . In Fig. 9 we also plot the resulting distributions if we implement a different flux limit, as in Figs. 5 and 8. Higher flux limits result to a larger fraction of sources with very compressed timescales.

## 5.2 Flat spectrum Radio Quasars

In this section, we discuss the same derived distributions for FSRQs as the ones we derived for BL Lacs in §5.1. The Doppler and inverse Doppler factor distribution and the distribution of the viewing angles are shown in Figs. 10,11 and 12 respectively. The Doppler factor distributions of the BL Lac and FSRQ samples show remarkable similarities. Even though FSRQs have higher Doppler factors, both distributions peak at  $\sim 3$  and have similar shapes.

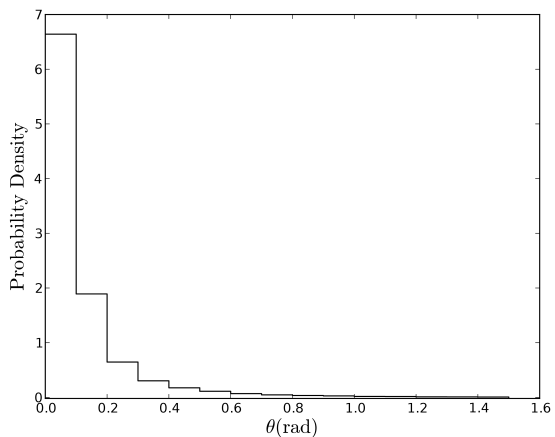


**Figure 12.** Distribution of the viewing angles  $\theta$ (rad). The majority of simulated sources have small viewing angles (85% have  $\theta \leq 0.2$  rad =  $11.5^\circ$ ), in accordance with our understanding of blazars.

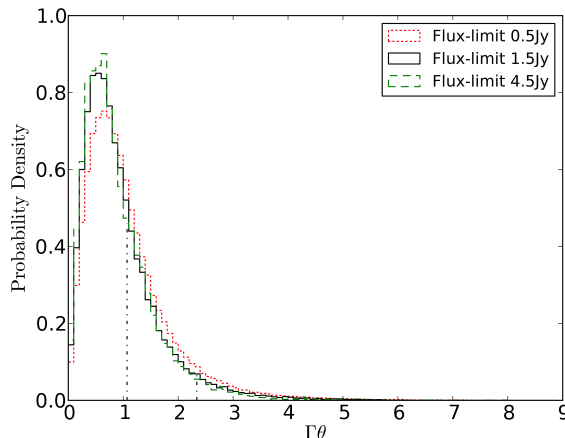


**Figure 13.** Distribution of  $\Gamma\theta$  for the FSRQ sample. The solid line represents the distribution with the flux limit we set for our model (1.5 Jy). The dashed line is the distribution for a flux limit of 4.5 Jy and the dotted line for a limit of 0.5 Jy. The vertical dashed line at 1.07 represents  $1\sigma$ , at 2.34  $2\sigma$  and the dashed line (not visible at  $\Gamma\theta = 5.0$ )  $3\sigma$  for the 1.5 Jy distribution.

The distribution of the  $(\Gamma\theta)$  is shown in Fig. 13. As in the case of BL Lacs, we find the  $\Gamma\theta$  to be peaked around 0.5, in agreement with the early analytic predictions of Vermeulen & Cohen (1994) for quasars. The consistency between the  $\Gamma\theta$  distributions in FSRQs and BL Lacs is remarkable; differences in the amount of relativistic beaming are not likely to be the culprit of any observed differences between these two classes of sources.

The same conclusion can be reached by comparing the time scale modulation factor distribution for the FSRQs, shown in Fig. 14, with that of BL Lacs. The time scale modulation factors of a 1.5Jy flux-limited FSRQ sample also follow an exponential distribution with mean=0.277. Similar to the BL Lacs, the smallest value is  $\sim 2 \times 10^{-2}$ .

As for BL Lacs, we have also produced distributions for

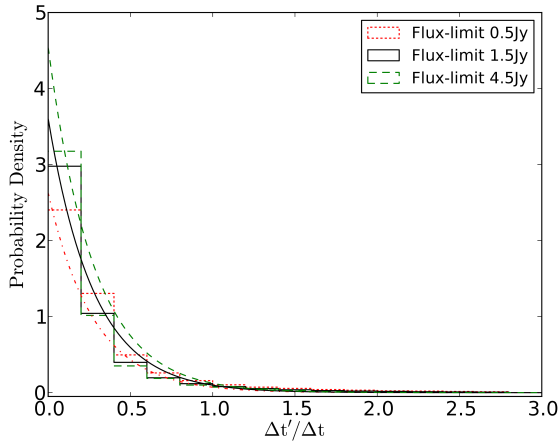


**Figure 14.** Time scale modulation factor distribution of the simulated data for the FSRQ sample. The solid line represents the distribution with the flux limit we set for our model (1.5 Jy). The dashed line is the distribution for a flux limit of 4.5 Jy and the dotted line for a limit 0.5 Jy. The overplotted lines represent exponential distributions with the same mean.

the Doppler factor,  $\Gamma\theta$  and the time scale modulation factor for samples with different flux limits. The effect of changing the flux limit is similar for the FSRQs as in the case of BL Lacs. In all three cases the distributions have similar peaks, and the Doppler factor distribution becomes shallower with higher flux limit, whereas more sources have smaller values of  $\Gamma\theta$  and  $\Delta t'/\Delta t$  for a higher flux limit.

### 5.3 Flux density and Luminosity Distributions

It was argued in §4.1 that due to the variable nature of blazars, flux density is not a good observable for model fitting. For this reason, we have not required that our acceptable models produce a flux density distribution consistent with the data. It is nevertheless interesting to compare, the flux density distributions in our simulated and observed 1.5Jy flux-limited samples. Figures 15 & 16 show the distribution of the derived flux density versus the highest flux density from observations (Lister et al. 2009a) for the BL Lac and FSRQ samples respectively. Despite our initial concerns regarding variability, simulated and observed distributions do not appear to be discrepant in either case. The Kolmogorov-Smirnov test gives a probability of  $\sim 23\%$  for the BL Lac objects and  $\sim 21\%$  for the FSRQs that the observed and simulated data are drawn from the same distribution. A possible interpretation of this result is that the probability of observing a source in a flaring state in a single-epoch survey is low. Lister (2001) has argued that even though the flux densities of beamed sources can reach high levels because of Doppler boosting, compression of flare timescales implies that these sources are most likely to be observed relatively close to their quiescent levels.

Figure 17 shows the flux density distribution of the two samples in the  $\log N - \log S_\nu$  format. The flux density distribution of the sources above the 1.5Jy flux limit follows a power law distribution with a slope of -2.2 for the BL Lacs and -2.6 for the FSRQs. For comparison, a uniformly dis-

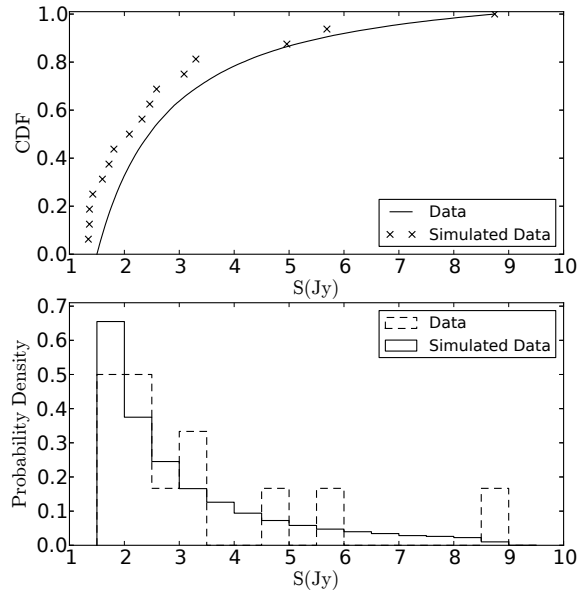


**Figure 15.** Flux density distribution of the MOJAVE sample (BL Lacs) (Lister et al. 2009a)(dashed) and the simulated flux density (solid).

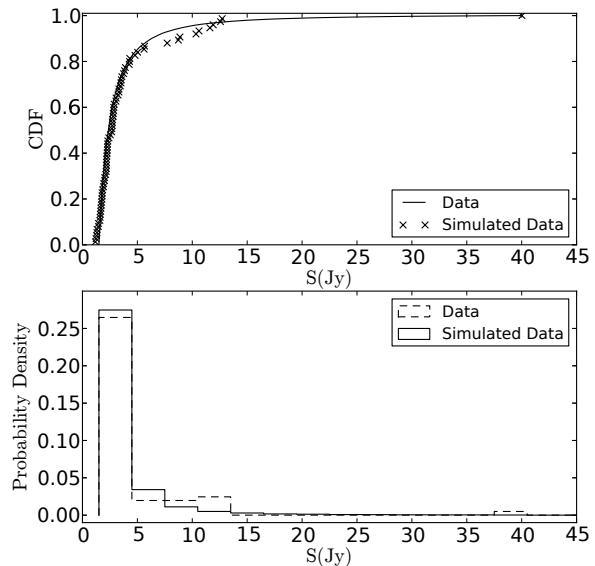


**Figure 16.** Flux density distribution of the MOJAVE sample (FSRQs) (Lister et al. 2009a)(dashed) and the simulated flux density (solid).

tributed, single-luminosity extragalactic population in a flat cosmology yields a slope of -2.5.

The  $\log N - \log L_\nu$  plots for unbeamed and beamed luminosities of the sources that pass the 1.5 Jy flux limit are shown in Figs. 18 and 19 respectively. For the unbeamed case we have also overplotted the input intrinsic luminosity functions at  $z=0$ . As expected, the intrinsic distribution of

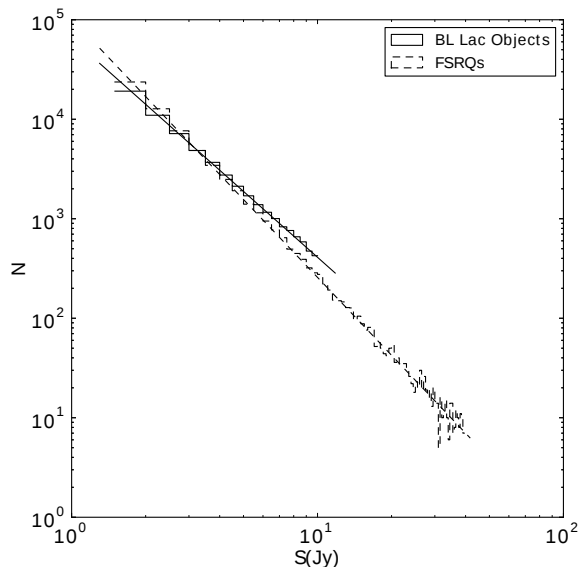


**Figure 17.**  $\log N$ - $\log S_\nu$  plot for the FSRQ (dashed) and BL Lac (solid) 1.5 Jy - limited samples. The corresponding lines represent power law distributions with slope -2.2 for the BL Lac objects and -2.6 for the FSRQs.

the luminosity is steeper than the distribution of the luminosity of the sources above the flux limit for both samples (e.g. Cara & Lister 2008a).

In the case of the beamed luminosity functions we see a clear break in the beamed  $\log N$  - $\log L_\nu$  of the FSRQ sample at  $\sim 2 \times 10^{28} \text{ W Hz}^{-1}$  and a less pronounced break in the beamed  $\log N$  - $\log L_\nu$  of the BL Lac sample.

The deviations from a single power law in the distribution of luminosities *within the sample* are not a reflection of the intrinsic luminosity function shape (which, in our case, is a single power-law by construction). Rather, they are artifacts of beaming (see also Urry & Shafer 1984; Urry & Padovani 1991) and mixing objects from different redshifts; for example, the sources above and below the break in the case of FSRQs are strongly dominated by objects at redshifts higher and lower than  $\sim 1$ , respectively. However, past studies have shown that reconstruction of the luminosity function starting from observations in a flux-limited sample can erroneously map these breaks to the intrinsic luminosity function shape (Cara & Lister 2008b,a). Our results do not show any need for a blazar luminosity function shape more complex than a single power law.

## 6 SUMMARY AND CONCLUSIONS

Using a Monte Carlo approach, we produced a new statistical model for the blazar population, parameterized by the power law indexes of the luminosity and Lorentz factor distributions, and the evolution parameter. We derive distinct distribution parameters for FSRQs and BL Lacs. Using this model we can produce distributions for the Doppler factor, viewing angle, product  $\Gamma\theta$ , and time scale modulation factor for any flux-limited sample of beamed sources.

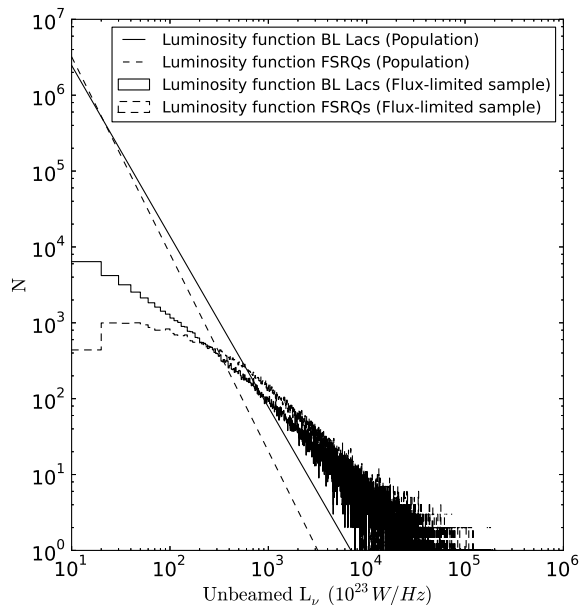


**Figure 18.** Unbeamed  $\log N$ - $\log L_\nu$  for the FSRQ (dashed) and BL Lac (solid) 1.5 Jy - limited samples. The solid and dashed lines represent the input power law distribution at  $z=0$  for the BL Lac and the FSRQ samples respectively.

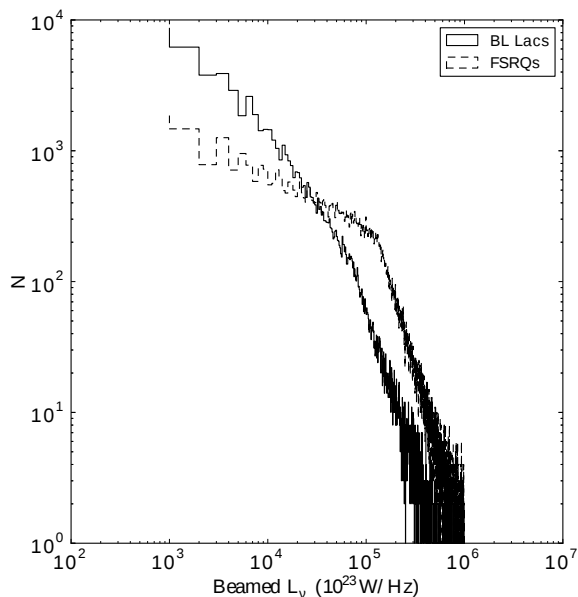


**Figure 19.** Beamed  $\log N$ - $\log L_\nu$  for the FSRQ (dashed) and BL Lac (solid) 1.5 Jy - limited samples.

We have set out with the aim to answer the following three questions regarding the blazar population.

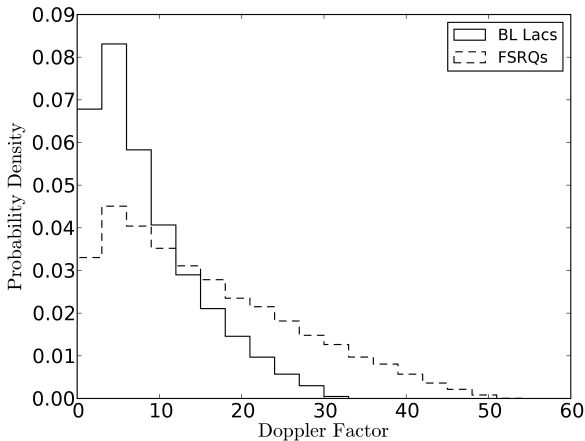


**Figure 20.** Distributions of Doppler factors for the BL Lac (solid) and the FSRQ (dashed) 1.5 Jy - limited samples

### 6.1 What is the relativistically induced spread in observed event timescales?

Because of relativistic and cosmological expansion effects, even events with identical timescales across sources would appear to have a distribution of observed timescales, as long as the members of the sample we are considering have a variety of Doppler factors (Fig. 20) and/or redshifts (Fig. 2,4). We can quantify this spread by considering the simple case where indeed we have a class of events with identical rest-frame timescales  $\tau_r = T$  across all sources, and calculating the resulting distribution of observed timescales.

Defining the timescale modulation factor  $m = \Delta t' / \Delta t$ ,  $\tau_r$  is related to the observed timescale  $\tau_o$  through  $\tau_o = m\tau_r$ . The distribution of  $\tau_r$  is a delta function,

$$p(\tau_r) = \delta(\tau_r - T). \quad (15)$$

We have shown that the distribution of  $m$  is an exponential,

$$p(m) = C \frac{1}{m_0} \exp\left[-\frac{m}{m_0}\right], m_{\min} \leq m \leq m_{\max} \quad (16)$$

where  $C$  is a normalization constant to account for the truncated range. If  $m$  and  $\tau_r$  are independent, their joint probability function is

$$p(m, \tau_r) = C \frac{1}{m_0} \exp\left[-\frac{m}{m_0}\right] \delta(\tau_r - T) \quad (17)$$

within the same limits as above. Transforming to new variables  $m, \tau_o$  and integrating over all values of  $m$  we obtain

$$p(\tau_o) \propto \exp\left[-\frac{\tau_o}{Tm_0}\right]. \quad (18)$$

Inverting this problem, we conclude that the observation of an exponential distribution of timescales associated with a class of events in a flux-limited sample of BL Lacs or of FSRQs is consistent with all timescales being identical in the rest frame of the jet. The jet rest-frame timescale of such a class of events is equal to the observed mean timescale divided by the average timescale modulation factor of the relevant sample.

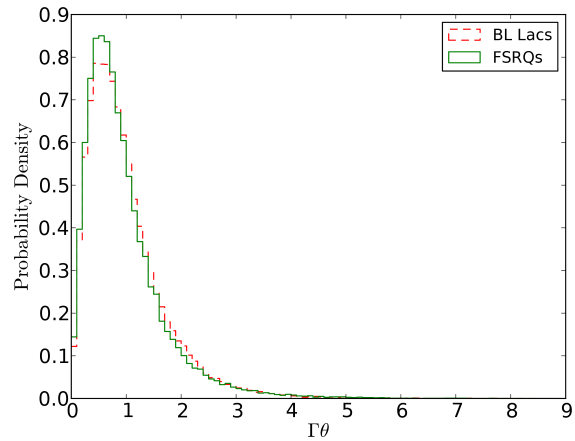


**Figure 21.** Distributions of  $\Gamma\theta$  for the BL Lac (dashed) and the FSRQ (solid) 1.5 Jy - limited samples

### 6.2 Beaming of sources in flux-limited samples.

In any flux-limited sample there is a well-defined peak in the probability distribution of  $\Gamma\theta$ , and the location of this peak is rather robust with respect to the value of the flux limit (0.6 for BL Lacs, 0.5 for FSRQs Fig. 21). The mean of this distribution is closer to 1 (0.99 for BL Lacs, 0.95 for FSRQs). As is indicated by the significant difference between mode and mean, the distribution is not only skewed but also its spread is large. Indeed, for a 1.5 Jy - limited sample, 68% of sources are contained in the interval  $0 \leq \Gamma\theta \leq 1.11$ , and 95% of sources between 0 and 2.37. The consequence is that, lacking enough information to compute both  $\Gamma$  and  $\theta$  for a source, it is precarious to make a statistical assumption for the value of  $\Gamma\theta$  in order to close the system and solve the problem. If any such assumption is made, the  $1\sigma$  uncertainty places the value of  $\Gamma\theta$  between 0 and 1.1, i.e. maximally beamed and marginally beamed.

For this reason, although the amount of beaming for a large sample of sources can be usefully constrained through models of the type discussed here, we strongly recommend against using such statistical arguments on single sources.

### 6.3 BL Lacs and FSRQs do NOT have different beaming properties.

Although BL Lacs have a steeper optimal slope in their  $\Gamma$  distribution, lower values of  $\Gamma$  (Fig. 22), and larger, on average, viewing angles (Fig. 23), than FSRQs, the distributions of the quantities characterizing beaming and timescale compression ( $\Gamma\theta$  and  $\Delta t' / \Delta t$ , respectively), are very similar. The monoparametric exponential distributions that can describe the latter have consistent mean: for the 1.5 Jy - limited sample and our optimal model, these are 0.281 for the BL Lacs and 0.277 for the FSRQs.

The consequence of this result is that any difference observed between BL Lac and FSRQ flux-limited samples (with the same flux limit) in the time domain are not due to differences in relativistic timescale compression between the two classes. Rather, they must be reflecting an intrinsic difference between these two classes of sources.

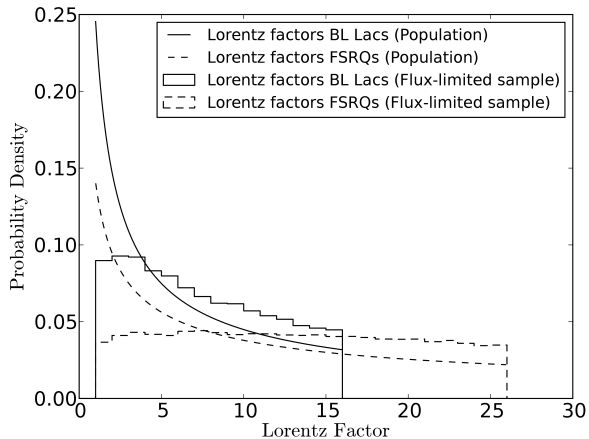


**Figure 22.** Distributions of Lorentz factors for the FSRQ (dashed) and BL Lac (solid) 1.5 Jy - limited samples. The solid and dashed lines represent the input power law distribution for the BL Lac and the FSRQ samples respectively.

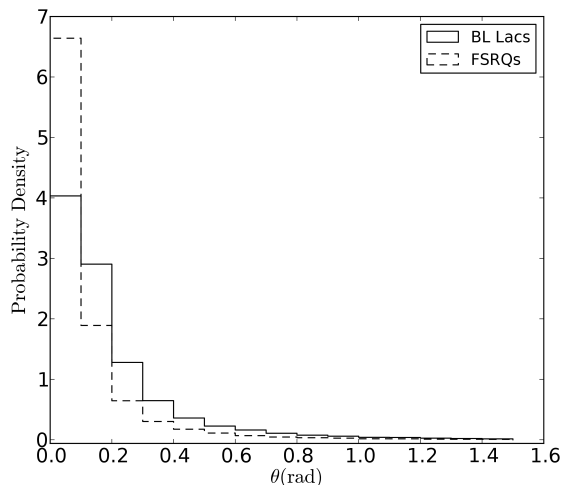


**Figure 23.** Distributions of viewing angles for the BL Lac (solid) and the FSRQ (dashed) 1.5 Jy - limited samples.

There is some uncertainty in this result stemming from uncertainty in our distribution parameters. In order to quantify this effect, we calculate the mean of  $\Delta t'/\Delta t$  in a 1.5 Jy - limited sample for different values of the input distribution parameters. As in §4.2, we have kept all but one parameters at their optimal values, and varied the remaining one to the limit (maximum and minimum) where it still produces acceptable  $z$  and  $\beta_{\text{app}}$  distributions (K-S test better than 5%). The values of the limiting parameter values are given in §4.2, and the corresponding values of the  $\Delta t'/\Delta t$  means are given in Table 4. The largest possible deviation from our optimal parameter values is produced for shallower luminosity function slopes in BL Lacs.

**Table 4.** Model Parameters

Parameters	$\langle \Delta t'/\Delta t \rangle_{\text{BL Lacs}}$	$\langle \Delta t'/\Delta t \rangle_{\text{FSRQs}}$
$\alpha_{\text{min}}$	0.167	0.208
$\alpha_{\text{max}}$	0.344	0.303
$A_{\text{min}}$	0.559	0.426
$A_{\text{max}}$	0.143	0.204
$\tau_{\text{min}}$	-	0.282
$\tau_{\text{max}}$	-	0.246
Optimal	0.281	0.277

## 7 DISCUSSION

We have made a point of optimizing different models for BL Lacs and FSRQs. An evaluation of whether this is indeed a necessary distinction can be made after the fact, by comparing the optimal models between BL Lacs and FSRQs. We find that FSRQs are:

- **Faster:** BL Lacs statistically have lower Lorentz factors than FSRQs, as their  $\Gamma$ -distribution is steeper (Fig. 22).
- **Evolving:** we have found that the luminosity distribution of FSRQs moves to higher luminosities with increasing redshift; conversely, the BL Lac redshift distribution with a luminosity function that evolves with redshift. In principle, this result could be affected by the redshift incompleteness of the BL Lac sample, which is larger than that of the FSRQ sample, if lower redshifts are preferentially easier to measure. However, there is no evidence for any evolution *among lower redshifts* (for example from  $z = 0$  to  $z = 0.4$ , where one would not expect to have our ability to measure redshifts to vary dramatically). If such a bias exists, it would have to be rather fine-tuned to exactly match the brightening of higher-redshift sources. This finding is consistent with gamma-ray studies of the BL Lac luminosity function (Ajello et al. 2014).
- **Brighter:** Even though today BL Lacs are brighter than FSRQs (Fig.19), the situation is reversed at higher redshifts, due to the evolution of FSRQs.

It is therefore particularly interesting that, despite their intrinsic differences, these two classes appear to have very consistent relativistic beaming ( $\Gamma\theta$  distribution serves as a proxy) and timescale compression distributions in flux-limited samples. Their intrinsic differences are thus expected to be imprinted in their statistical properties in the time domain measured in the observer frame.

Throughout this work we have assumed a single value for the spectral index ( $s$ ) for all sources in each sample. In reality it is different for every source and can evolve with time (Angelakis et al. 2012; Hovatta et al. 2014). However, since this simple assumption has yielded adequate results, we have not treated separately a spectral index distribution, although such an extension could be added to our model in a straight-forward fashion.

Single power law distributions for the Lorentz factors and the luminosity function are sufficient to describe both samples: the K-S test values for the FSRQs are 49.3% for the apparent velocity and 8.4% for the redshift distributions while for the BL Lacs 93.4% for the apparent velocity and 54.1% for the redshift distributions.

We have calculated, and we quote, mean values of the timescale modulation factor, for a 1.5 Jy flux-limited sample. Since we have shown that this distribution can be well-described by an exponential, the mean is the only parameter needed to completely define it. However, we emphasize that the value of the mean is a quantity dependent on the flux limit. Applications to different samples need to properly calculate the distribution appropriate to the relevant flux limit.

In addition we caution the reader that results of our models for lower flux limits involve extrapolation and should thus be treated with caution.

In this work, we have treated BL Lacs and FSRQs separately. The small number of BL Lacs make the BL Lac sample and the associated results more sensitive to contamination borderline shifting classification sources. However, it is striking that even with such a small sample, no agreement with even a mildly evolving luminosity function was possible.

The model optimized here was based on 15 GHz radio data. Any application to the statistical interpretation of data obtained in other frequencies should be done with two possible caveats in mind. First, it is not necessarily obvious that a single Lorentz factor can characterize the jet at all frequencies, or even at all locations at the same frequency (e.g., Georganopoulos & Kazanas 2004). Second, a flux-limited sample at a different frequency range (e.g., gamma-ray or optical), does not translate directly to a flux-limited sample in radio (e.g., Pavlidou et al. 2012). The scatter in the correlation between fluxes at different frequencies must therefore be accounted for.

## ACKNOWLEDGMENTS

We would like to thank Matt Lister, Talvikki Hovatta, and the anonymous referee for comments that helped improve this work.

This research was supported by the “Aristeia” Action of the “Operational Program Education and Lifelong Learning” and is co-funded by the European Social Fund (ESF) and Greek National Resources, and by the European Commission Seventh Framework Program (FP7) through grants PCIG10-GA-2011-304001 “JetPop” and PIRSES-GA-2012-31578 “EuroCal”. This research has made use of data from the MOJAVE database that is maintained by the MOJAVE team (Lister et al. 2009b)

## REFERENCES

- Abdo A. A. et al., 2010, *ApJ*, 710, 1271  
 Aharonian F. et al., 2007, *ApJ*, 664, L71  
 Ajello M. et al., 2014, *ApJ*, 780, 73  
 Angelakis E. et al., 2012, *Journal of Physics Conference Series*, 372, 012007  
 Arshakian T. G., Ros E., Zensus J. A., 2006, *A&A*, 458, 397  
 Blandford R. D., Königl A., 1979, *ApJ*, 232, 34  
 Cara M., Lister M. L., 2008a, *ApJ*, 686, 148  
 Cara M., Lister M. L., 2008b, *ApJ*, 674, 111  
 Chatterjee R. et al., 2008, *ApJ*, 689, 79  
 Cohen M. H., Lister M. L., Homan D. C., et al., 2007, *ApJ*, 658, 232  
 Georganopoulos M., Kazanas D., 2004, *NAR*, 48, 403  
 Ghisellini G., Padovani P., Celotti A., Maraschi L., 1993, *ApJ*, 407, 65  
 Giommi P., Padovani P., Polenta G., Turriziani S., D’Elia V., Piranomonte S., 2012, *MNRAS*, 420, 2899  
 Hovatta T. et al., 2014, *AJ*, 147, 143  
 Hovatta T., Valtaoja E., Tornikoski M., Lähteenmäki A., 2009, *A&A*, 494, 527  
 Jorstad S. G. et al., 2005, *AJ*, 130, 1418  
 Komatsu E. et al., 2009, *ApJS*, 180, 330  
 Lähteenmäki A., Valtaoja E., 1999, *ApJ*, 521, 493  
 Lister M. L., 2001, *ApJ*, 561, 676  
 Lister M. L., Aller H. D., Aller M. F., Cohen M. H., Homan D. C., et al., 2009a, *ApJ*, 137, 3718  
 Lister M. L. et al., 2013, *AJ*, 146, 120  
 Lister M. L. et al., 2009b, *AJ*, 138, 1874  
 Lister M. L., Homan D. C., 2005, *AJ*, 130, 1389  
 Lister M. L., Marscher A. P., 1997, *ApJ*, 476, 572  
 Padovani P., 1992, *MNRAS*, 257, 404  
 Padovani P., Urry C. M., 1992, *ApJ*, 387, 449  
 Pavlidou V. et al., 2014, *MNRAS*, 442, 1693  
 Pavlidou V. et al., 2012, *ApJ*, 751, 149  
 Pushkarev A. B., Hovatta T., Kovalev Y. Y., Lister M. L., et al., 2012, *A&A*, 545, A113  
 Pushkarev A. B., Kovalev Y. Y., Lister M. L., Savolainen T., 2009, *A&A*, 507, L33  
 Readhead A. C. S., 1994, *ApJ*, 426, 51  
 Urry C. M., Padovani P., 1991, *ApJ*, 371, 60  
 Urry C. M., Shafer R. A., 1984, *ApJ*, 280, 569  
 Vermeulen R. C., 1995, *Proceedings of the National Academy of Science*, 92, 11385  
 Vermeulen R. C., Cohen M. H., 1994, *ApJ*, 430, 467

# Population statistics of beamed sources. II: Evaluation of Doppler factor estimates.

I. Liodakis<sup>1\*</sup> and V. Pavlidou<sup>1,2</sup>

<sup>1</sup>*Department of Physics and ITCP<sup>†</sup>, University of Crete, 71003, Heraklion, Greece*

<sup>2</sup>*Foundation for Research and Technology - Hellas, IESL, Voutes, 7110 Heraklion, Greece*

21 October 2015

## ABSTRACT

In a companion paper we presented a statistical model for the blazar population, consisting of distributions for the unbeamed radio luminosity function and the Lorentz factor distribution of each of the BL Lac and Flat Spectrum Radio Quasar (FSRQ) classes. Our model has been optimized so that it reproduces the MOJAVE distributions of apparent speeds and redshifts when the appropriate flux limit is applied and a uniform distribution of jet viewing angles is assumed for the population. Here we use this model to predict the Doppler factor distribution for various flux-limited samples for which Doppler factors have been estimated in a variety of ways (equipartition, variability + equipartition, inverse Compton dominance) on a blazar-by-blazar basis. By comparing the simulated and data-estimated Doppler factor distributions in each case, we evaluate the different methods of estimating blazar Doppler factors. We find that the variability Doppler factors assuming equipartition are the ones in the best agreement with our statistical model, whereas the inverse Compton Doppler factor method is only suitable for FSRQs. In the case of variability Doppler factors, we find that while random errors are relatively low ( $\sim 30\%$ ), uncertainties are dominated by systematic effects. In the case of inverse Compton Doppler factors, random errors appear to dominate, but are significantly larger ( $\sim 60\%$ ).

**Key words:** galaxies: active – galaxies: blazars – jets – Doppler factors

## 1 INTRODUCTION

Blazar observations are shrouded in relativistic effects, due to their preferential alignment of their jets close to our line of sight (Blandford & Königl 1979). Decomposing relativistic effects from intrinsic properties would allow us to probe the processes important to jet astrophysics including the jet–black-hole connection, the structure and evolution of jet magnetic fields, the evolution of flaring events in the jet rest frame, and particle acceleration in jets.

The jet Doppler factor is a key quantity in any such effort. It is the Doppler factor that determines how much flux densities are boosted and timescales compressed in the observer frame. Additionally, the Doppler factor is a *different* function of the bulk Lorentz factor  $\Gamma$  and the viewing angle  $\theta$  than the one determining the apparent speeds of jet components. Measurement of both these quantities allows one to solve for

both  $\Gamma$  and  $\theta$ . For this reason, measurements of Doppler factors on a blazar-by-blazar basis have been actively pursued. Several methods have been proposed, including causality arguments, (Aharonian et al. 2007; Jorstad et al. 2005; Clausen-Brown et al. 2013), emission region geometry (Fan et al. 2013, 2014), assumed high-energy emission processes (Ghisellini et al. 1993), and the assumption of equipartition between jet magnetic fields and relativistic electron energy densities (Guijosa & Daly 1996; Readhead 1994; Lähteenmäki & Valtaoja 1999; Hovatta et al. 2009). However, it is not straight-forward to evaluate the accuracy of such estimates. Often these estimates represent only lower limits to the true jet Doppler factors; in other cases, different methods produce different results for the same sources. Since each method uses several different assumptions that might not hold, it is impossible to determine which method provides the most accurate estimate of the Doppler factor of a source on a blazar by blazar basis.

Here, we take a statistical approach to evaluate the accuracy of various techniques for estimating the Doppler factor of a blazar jet. In a companion paper (Liodakis & Pavlidou 2015, hereafter Paper I), we presented

\* liodakis@physics.uoc.gr

† Institute for Theoretical and Computational Physics, formerly Institute for Plasma Physics

a population model for each of the BL Lac and Flat Spectrum Radio Quasar (FSRQ) classes of blazars. The model consists of distributions for the intrinsic unbeamed 15 GHz radio luminosity and the Lorentz factor of the jets. Its parameters were optimized using well-measured observable quantities: redshift, and apparent velocity ( $\beta_{app}$ ) as measured by the MOJAVE program (Monitoring Of Jets in Active galactic nuclei with VLBA Experiments, [Lister & Homan 2005](#)). We can use this model in order to derive Doppler factor distributions for any flux-limited sample, independently of variability, flux, or equipartition brightness temperature.

Since our approach is independent of all assumptions entering methods of Doppler factor estimation in individual blazars, and is able to adequately describe blazars as a population, we are presented with a unique opportunity: we can use the derived Doppler factor distributions in order to compare them with those obtained using various single-blazar techniques, and evaluate whether each method of evaluating Doppler factors for individual sources yields consistent results, if not on a blazar-by-blazar basis, at least for the population overall. In this way, we can evaluate whether the assumptions used in each of these methods hold.

This paper is organized as follows. In §2 we describe our model and the resulting Doppler factor distributions, and in §3 the various Doppler factor estimation techniques we compare against in the following sections. In §4 we compare our statistical results with known methods of determining Doppler factors. In §5, we discuss the results of this comparison in relation to blazar physics, and we attempt to extract the level of error for Doppler factor estimates in individual blazars, for these techniques that are in overall agreement, at the population level, with our model. In addition, we test whether the derived Doppler factor distributions from our model can be themselves applied to individual sources to extract information about their Doppler factors. We summarize our conclusions in §6.

The cosmology we have adopted throughout this work is  $H_0 = 71 \text{ km s}^{-1} \text{ Mpc}^{-1}$ ,  $\Omega_m = 0.27$  and  $\Omega_\Lambda = 1 - \Omega_m$  ([Komatsu et al. 2009](#)). This choice was made so that our cosmological parameters agree with the MOJAVE analysis ([Lister et al. 2009b](#)).

## 2 DOPPLER FACTOR DISTRIBUTIONS

In this section we give a short description of our blazar population model. For a more detailed description see Paper I.

We optimized our model using data from the MOJAVE survey ([Lister et al. 2009b](#)). MOJAVE uses a statistically complete flux-limited sample ([Arshakian et al. 2006](#)). Samples determined only by strict statistical criteria are crucial for population studies such as ours. We removed outliers and any source that showed unusual behavior (jet bending, inward motions etc.) as indicated by [Lister et al. \(2009b, 2013\)](#), and separated the sample in two sub-populations: BL Lac objects, and Flat Spectrum Radio Quasars (FSRQs). A flux limit, at 1.5 Jy, serves as a constraint determining how beamed the set of the observed sources is.

We assumed single power law distributions for the

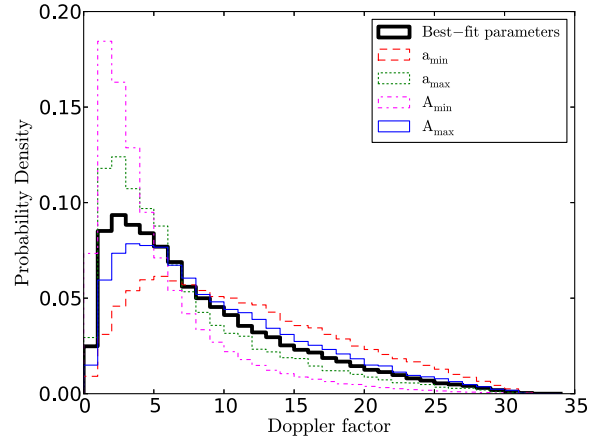


**Figure 1.** The Doppler factor distribution for the BL Lac objects with the limits of the model parameters.

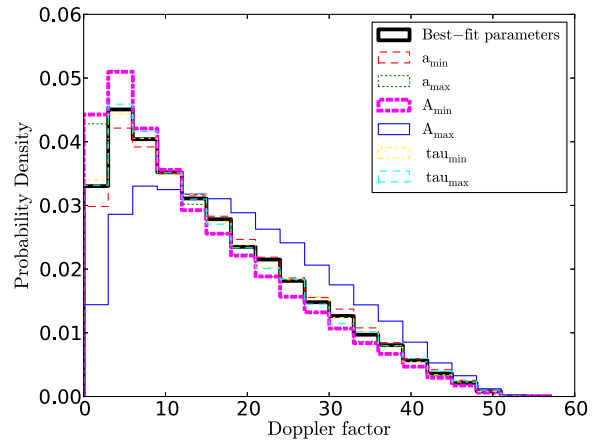


**Figure 2.** The Doppler factor distribution for the FSRQs with the limits of the model parameters.

Lorentz factor,

$$p(\Gamma) \propto \Gamma^{-\alpha}, \quad (1)$$

and the unbeamed luminosity function ([Lister & Marscher 1997](#); [Cara & Lister 2008](#); [Chatterjee et al. 2008](#); [Abdo et al. 2010a](#)), and have adopted a pure luminosity evolution model described in ([Padovani & Urry 1992](#); [Padovani 1992](#)).

$$n(L_\nu, z) \propto \left( \frac{L_\nu}{e^{T(z)/\tau}} \right)^{-A}, \quad (2)$$

where  $T(z)$  is the lookback time. We assumed random viewing angles  $\theta$  (i.e.  $\cos\theta$  uniformly distributed between 0 and 1). Thus, our model parameters are the power law indices for the Lorentz factor distribution ( $\alpha$ ) and the luminosity function ( $A$ ), and the evolution parameter ( $\tau$ ).

For every set of model parameters, we compared simulated and observed distributions for apparent speeds and redshifts of sources obeying the flux limit. We rejected any model for which the Kolmogorov-Smirnov test (K-S test) delivered a probability  $< 5\%$  of consistency between ob-

**Table 1.** Limits of the model parameters presented as deviations from the optimal value, for which the 5% K-S test requirement is still met.

	BL Lacs	FSRQs
$a_{min}$	0.738-1.46	0.57-0.50
$a_{max}$	0.738+0.41	0.57+0.12
$A_{min}$	2.251-0.78	2.6-0.245
$A_{max}$	2.251+0.68	2.6+0.185
$\tau_{min}$	-	0.26-0.003
$\tau_{max}$	-	0.26+0.068

served and simulated distributions. Our optimal model is the one which minimized the product of the K-S probability values for these two distributions. The best fit parameters for the FSRQ population are:  $\alpha = 0.57 \pm 0.001$ ;  $A = 2.6 \pm 0.01$ ;  $\tau = 0.26 \pm 0.001$ . For the BL Lac population we found:  $\alpha = 0.738 \pm 0.002$ ;  $A = 2.251 \pm 0.02$ . Note that the BL Lac parameters do not include the evolution parameter: we found that the BL Lac luminosity function is consistent with no evolution. The error represents scanning step and statistical variations in simulated distributions. We have also explored the threshold of the acceptability of our model, by keeping all the parameters but one to the best fit value, and changing the other towards higher or lower values until the K-S test threshold of 5% is violated. The limits of the parameters are shown in Table 1. For each model (determined by a set of  $A$ ,  $\alpha$ , and  $\tau$ ) and each flux limit value, we can produce distributions of derived quantities, including Doppler factors, viewing angles, and timescale modulation factors. These results are presented in detail in Paper I along with a detailed discussion on the reasoning behind our assumptions and our optimization algorithm.

In Figs. 1 and 2 we review the Doppler factor distributions produced by our model for BL Lacs and FSRQs respectively for a 1.5 Jy - limited sample. The Doppler factor is given by

$$\delta = \frac{1}{\Gamma(1 - \beta \cos \theta)}, \quad (3)$$

where  $\beta \lesssim 1$  is the speed of the jet in units of the speed of light, which is connected to the Lorentz factor through,

$$\Gamma = \frac{1}{\sqrt{1 - \beta^2}}. \quad (4)$$

The distribution obtained from our optimal model is plotted, in each case, with the thick black solid line. To give a sense of the uncertainty in these distributions due to the uncertainty in our model parameters we plot, with other line types and colors, the resulting distributions when each model parameter is at the limit that still gives apparent jet speed and redshift distributions acceptable within our 5% threshold, while all other parameters are kept at their optimal value.

### 3 SINGLE-BLAZAR DOPPLER FACTOR ESTIMATES

In this section, we review various techniques that have been used in the literature to derive Doppler factor estimates for individual blazars.

#### 3.1 Inverse Compton Doppler Factors

The inverse Compton Doppler Factor  $\delta_{IC}$  (Ghisellini et al. 1993) is derived based on the requirement that the Synchrotron self-Compton (SSC) flux density should not exceed the observed flux density at high frequencies. The SSC emission consists of photons produced by inverse-Compton up-scattering of synchrotron photons by the same relativistic electrons that produce them, and, in that sense, is a guaranteed high-energy component in any region containing magnetic fields and relativistic electrons.

Assuming a power law energy distribution for the electrons, homogeneous magnetic fields, and the observation frequency ( $\nu_m$ ) to be the self-absorption frequency of the core component dominating at that frequency, the Doppler factor would be:

$$\delta_{IC} = f(\alpha) F_m \left[ \frac{\ln(\nu_b/\nu_m)}{F_\chi \theta_d^{6+4\alpha} \nu_\chi^\alpha \nu_m^{5+3\alpha}} \right]^{1/(4+2\alpha)} (1+z), \quad (5)$$

where  $F_m$  is the synchrotron flux density at  $\nu_m$  and  $F_\chi$  the X-ray flux density both in Jy,  $\theta_d$  the angular size of the core in milli arcseconds,  $\nu_\chi$  is in keV,  $\nu_m$  is in GHz and  $\nu_b$  is the synchrotron high energy cutoff which is assumed to be  $10^{14}$  Hz. The function  $f(\alpha)$  is given by (Ghisellini 1987) to be  $f(\alpha) \simeq 0.08\alpha + 0.14$ .

Equation (5) is applicable in the case of a discrete jet ( $p = 3 + \alpha$ ). For the continuous jet case ( $p = 2 + \alpha$ ) the Doppler factor is related to the one of (Eq.5) by

$$\delta_{2+\alpha} = \delta_{3+\alpha}^{(4+2\alpha)/(3+2\alpha)}. \quad (6)$$

A more detailed description of the model can be found in Ghisellini et al. (1993); Gujosa & Daly (1996).

#### 3.2 Equipartition Doppler Factors

Equipartition Doppler factors (Readhead 1994) use the assumption of equipartition between electrons and magnetic fields in a radio emission region to calculate an intrinsic brightness temperature and, from there, a Doppler factor through comparison to an actual observed brightness temperature. Different incarnations of this method differ in the way the angular size of the emission is calculated region (direct observation through VLBI or variability timescales and causality arguments.)

##### 3.2.1 VLBI Equipartition Doppler Factors

The angular size of a uniform self-absorbed source in order to have equipartition of the radiating particles and the magnetic field, or else the equipartition angular size is (Scott & Readhead 1977),

$$\begin{aligned} \theta_{eq} &= 10^3 (2h)^{1/17} F(\alpha) [1 - (1+z)^{-1/2}]^{-1/17} \\ &\times S_p^{8/17} (1+z)^{(15-2\alpha)/34} (\nu_p \times 10^3)^{-(2\alpha+35)/34} \text{mas}, \end{aligned} \quad (7)$$

where  $h$  is the dimensionless Hubble parameter,  $S_p$  is in Jy and  $\nu_p$  in GHz. The function  $F(\alpha)$  is described in Scott & Readhead (1977).  $S_p$  and  $\nu_p$  have not been corrected for the beaming effect, thus the observed values are related to the intrinsic ones through  $S_p = \delta^{-3} S_{obs}$  and  $\nu_p = \delta^{-1} \nu_{obs}$ .

Assuming the observed angular size is  $\theta_d = \theta_{eq}$  the equipartition Doppler factor is,

$$\delta_{eq} = \left\{ \left[ 10^3 F(\alpha) \right]^{34} \left( [1 - (1+z)^{-1/2}] / 2h \right)^{-2} (1+z)^{15-2\alpha} \right. \\ \left. \times S_{obs}^{-16} \theta_d^{-34} (v_{obs} \times 10^3)^{-(2\alpha+35)} \right\}^{1/(13-2\alpha)}. \quad (8)$$

The equipartition Doppler factor can also be expressed as the ratio of the observed brightness temperature over the maximum intrinsic brightness temperature ( $T_{b,int}$ ). Since for powerful synchrotron radio sources  $T_{b,int}$  is equal to the equipartition temperature ( $T_{eq}$ ):

$$\delta_{eq} = \frac{T_{b,obs}}{T_{eq}}. \quad (9)$$

A detailed description of the method can be found in [Readhead \(1994\)](#); [Guijosa & Daly \(1996\)](#); [Britzen et al. \(2007\)](#).

### 3.2.2 Variability Doppler Factors

In this case, the time evolution of a radio flare is used to calculate the brightness temperature of the emission region. The Doppler factor is then obtained by setting that variability brightness temperature equal to the equipartition brightness temperature. Detailed descriptions of this technique [Valtaoja et al. \(1999\)](#); [Lähteenmäki et al. \(1999\)](#); [Lähteenmäki & Valtaoja \(1999\)](#); [Hovatta et al. \(2009\)](#). For their analysis, they use long flux density curves, decomposing them to exponential flares of the form,

$$\Delta S(t) = \begin{cases} \Delta S_{max} e^{(t-t_{max})/\tau}, & t < t_{max} \\ \Delta S_{max} e^{(t_{max}-t)/1.3\tau}, & t > t_{max} \end{cases} \quad (10)$$

where  $\Delta S_{max}$  is the maximum amplitude of the flare,  $t_{max}$  is the epoch of the flare maximum and  $\tau$  is the rise time of the flare defined as  $\tau = dt/d(\ln S)$  in days. The observed variability brightness temperature of the source  $T_{b,var}$  is,

$$T_{b,var} = 1.548 \text{ K} \times 10^{-32} \frac{\Delta S_{max} d_L^2}{v^2 \tau^2 (1+z)}, \quad (11)$$

where  $\Delta S_{max}$  is in Jy,  $v$  is the observed frequency in GHz, and  $d_L$  is the luminosity distance in meters. Using  $T_{b,int} = 5 \times 10^{10}$  K ([Readhead 1994](#)), they calculate the variability Doppler factor from

$$\delta_{var} = \left( \frac{T_{b,var}}{T_{b,int}} \right)^{1/3}. \quad (12)$$

### 3.3 Single-component Causality Doppler Factors

The underlying assumption of this method is that the variability timescale of a resolved jet component is determined by the light travel time across the component, rather than loss processes [Jorstad et al. \(2005, 2006\)](#). This method relies upon the observational determination of both the angular size of the component and the variability timescale, defined as:

$$\Delta t_{var} = \frac{dt}{\ln(S_{max}/S_{min})}, \quad (13)$$

where  $S_{max}$  and  $S_{min}$  are the measured maximum and minimum flux densities, respectively, and  $dt$  is the time between

$S_{max}$  and  $S_{min}$ . The Doppler factor can be calculated from:

$$\delta_{var} = \frac{sd_L}{c \Delta t_{var} (1+z)}, \quad (14)$$

where  $d_L$  is the luminosity distance, and  $s$  is the angular size of the component, equal to  $1.6a$  for a Gaussian, equal to the full width at half maximum, measured at the epoch of  $S_{max}$ . After calculating a Doppler factor for each observed component for a specific source, the weighted average of these values is assigned to a source, with the weights being inversely proportional to the uncertainty in apparent velocity of each component.

This method is resource-expensive in that it requires multi-epoch VLBI monitoring for each source. For this reason, Doppler factors at this stage have been calculated by this method, to our knowledge, only for 5 BL Lac objects and 8 FSRQs. As a result, a statistical evaluation for this method is rendered impractical due to low statistics.

### 3.4 Gamma-ray Opacity Doppler factors

The calculation of  $\gamma$ -ray opacity Doppler factors is based on the requirement that the  $\gamma$ -ray emission region must be transparent to gamma rays ([Mattox et al. 1993](#); [Fan et al. 2013, 2014](#)). The process responsible for  $\gamma$ -ray absorption is pair production due to the interaction between  $\gamma$ -ray photons and X-ray photons. They are a lower limit to the true Doppler factors. This calculation involves the assumptions that the emission region is spherical and that X-rays are produced in the same region as gamma rays. Causality arguments are used to connect variability timescales with the emission region size. The Doppler factor is then given by

$$\delta_{\gamma} \geq \left[ 1.54 \times 10^{-3} (1+z)^{4+2\alpha} \left( \frac{d_L}{\text{Mpc}} \right)^2 \right]^{1/(4+2\alpha)} \\ \times \left[ \left( \frac{\Delta T}{\text{hours}} \right)^{-1} \left( \frac{F_{keV}}{\mu\text{Jy}} \right) \left( \frac{E_{\gamma}}{\text{GeV}} \right)^{\alpha} \right]^{1/(4+2\alpha)}, \quad (15)$$

where  $\alpha$  is the X-ray spectral index,  $F_{keV}$  the flux density at 1 keV in  $\mu\text{Jy}$ ,  $E_{\gamma}$  is the energy at which the  $\gamma$ -rays are detected in GeV,  $d_L$  the luminosity distance as described in §2, and  $\Delta T$  is the time scale in hours defined as:

$$\Delta T = \frac{(1+z)R}{c\delta_{\gamma}}, \quad (16)$$

where  $R$  is the size of the emission region. A variation of this method uses UV photons as the target photon field and similar arguments to derive a Doppler factor.

In this work, we do not statistically test this technique, because the calculation of a statistical Doppler factor distribution requires a well-defined, 15 GHz radio flux-limited sample<sup>1</sup>. Because of the significant scatter in the radio/gamma-ray flux correlation ([Pavlidou et al. 2012](#)), it is not straight-forward to calculate a single radio flux limit for a gamma-ray selected sample, even if the latter is flux-limited. At the same time, the fact that gamma-ray opacity arguments can only provide lower limits to the true Doppler factor complicates the statistical comparison of these Doppler factors to other datasets

<sup>1</sup> Because for these sources the spectral index is very close to zero we have used  $F_{\nu} \approx F_{15\text{GHz}}$  for nearby frequencies.

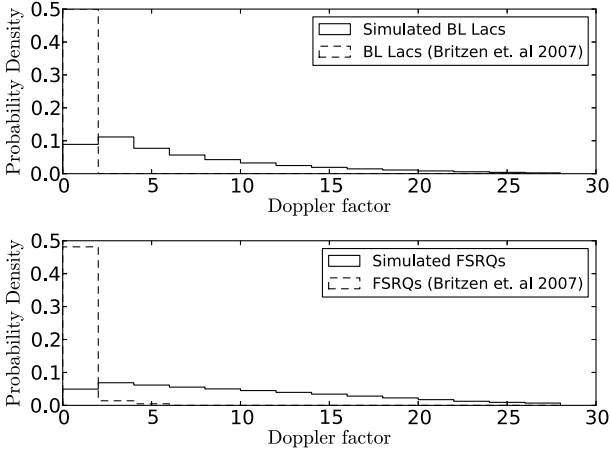


**Figure 3.** Probability density functions of statistical Doppler factors (solid line) and equipartition Doppler factors (Britzen et al. 2007) (dashed line) for the BL Lac (upper panel) and the FSRQ (lower panel) sample.

and models. However, such a comparison would in principle be very interesting, especially if it could confirm whether  $\gamma$ -ray and radio emitting regions have different outflow velocities (Georganopoulos & Kazanas 2003b,c,a; Georganopoulos 2003; Giannios et al. 2009) and hence different Doppler factors.

#### 4 COMPARISON WITH STATISTICAL DOPPLER FACTORS

In this section we compare our results on Doppler factor distributions from our blazar population models with data on Doppler factor estimates through different techniques found in the literature. Every data set we have tested was separated into two populations, one for the BL Lac objects and one for FSRQs. It was shown in Paper I that the model can adequately describe blazars as a population; however all derived distributions are sample-specific and flux-limit dependent. For this reason, if we want to compare any derived distribution with data, including the Doppler factor distributions, the flux-limit of the sample at hand must be taken into account. As a result, for each dataset and each object class, a distribution of statistical Doppler factors was derived by using our model and the flux limit of the corresponding sample of the data set we are comparing with. All the data we compare with are from flux-limited samples, either 0.35 Jy, 1 Jy or 2 Jy. Comparisons between statistical and single-blazar estimated Doppler factor distributions are made with the use of the Kolmogorov-Smirnov (K-S) test. All the values presented in this work represent the probability of the single-blazar estimates having been drawn from the corresponding statistical Doppler factor distribution. In order to accept the consistency statement we require the probability value to be higher than 5%.

We start by comparing our results with the data given in Britzen et al. (2007). They provide data for both inverse Compton ( $\delta_{IC}$ ) and equipartition ( $\delta_{eq}$ ) Doppler factors. The sample consists of 11 BL Lac objects and 108 FSRQs. The flux-limit for this sample is 0.35 Jy (Taylor et al. 1996).

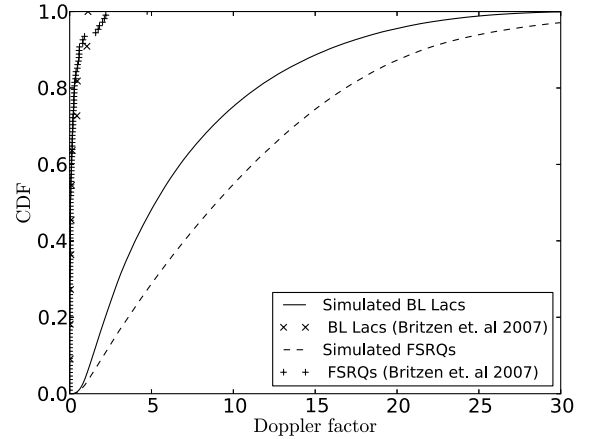


**Figure 4.** Cumulative distribution functions of statistical Doppler factors for BL Lacs (solid line) and FSRQs (dashed line), overplotted with equipartition Doppler factors (Britzen et al. 2007) (X for BL Lacs, + for FSRQs).

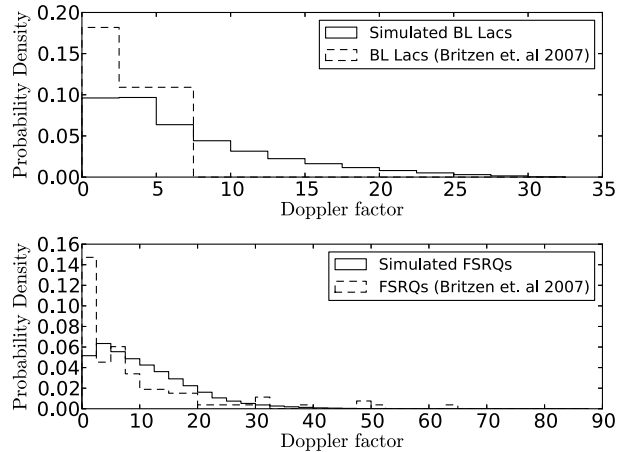


**Figure 5.** Probability density functions of statistical Doppler factors (solid line) and inverse Compton Doppler factors (Britzen et al. 2007) (dashed line) for the BL Lac (upper panel) and the FSRQ (lower panel) sample.

The data set for the  $\delta_{eq}$  features extremely low values, with the highest value for the BL Lacs  $\delta_{eq} \sim 1.11$  and for the FSRQs  $\delta_{eq} \sim 4.72$ . A K-S test confirmed that these distributions are not consistent with what is expected for these populations, with the p-value for the BL Lacs  $\sim 1.22 \times 10^{-7}\%$  and for the FSRQs  $\sim 1.16 \times 10^{-78}\%$ . For the case of the  $\delta_{IC}$  we have excluded source 1732+389 from the FSRQ sample for being an outlier ( $\delta_{IC} \approx 276$ ). The consistency between estimated and statistical Doppler factor distributions is rejected for FSRQs, with a K-S test returning a p-value of  $\sim 2.15 \times 10^{-5}\%$ . The value for the K-S test for the BL Lac sample is  $\sim 6.7\%$ . Note however that the statistics in the BL Lac sample are extremely low.

We plot the probability density function (PDF) and the cumulative distribution function (CDF) for the  $\delta_{eq}$  case, in Figs. 3 and 4 and for the  $\delta_{IC}$  case in Figs. 5 and 6.

We proceed to the data set analysed by Ghisellini et al.

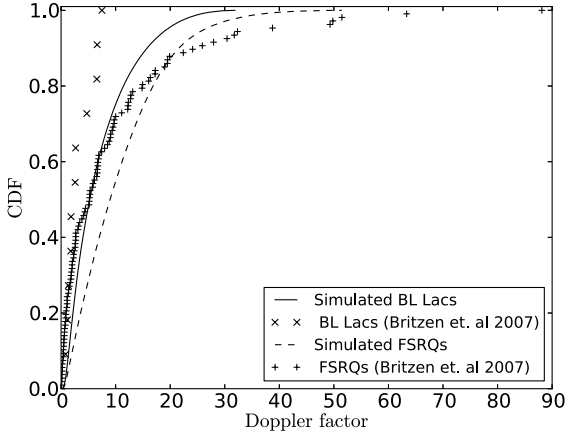


**Figure 6.** Cumulative distribution functions of statistical Doppler factors for BL Lacs (solid line) and FSRQs (dashed line), overlotted with inverse Compton Doppler factors (Britzen et al. 2007) (X for BL Lacs, + for FSRQs).

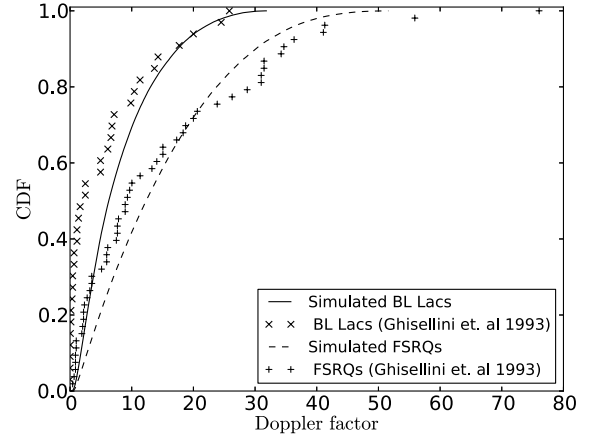


**Figure 8.** Cumulative distribution function of the statistical Doppler factors for BL Lacs (solid line) and FSRQs (dashed line), overlotted with inverse Compton Doppler factors from Ghisellini et al. (1993) (X for BL Lacs, + for FSRQs).

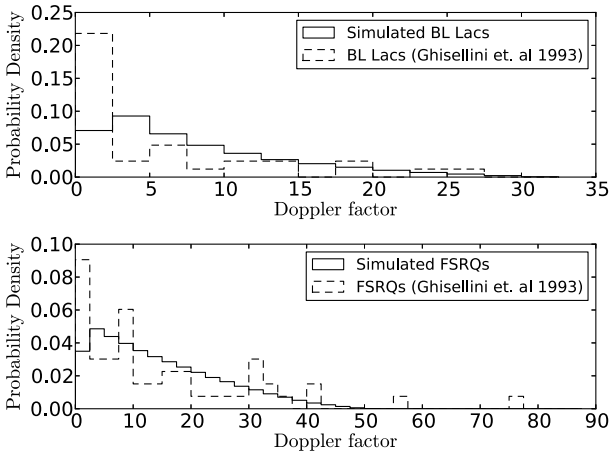


**Figure 7.** Probability density functions of statistical Doppler factors (solid line) and inverse Compton Doppler factors (Ghisellini et al. 1993) for the BL Lac (upper panel) and the FSRQ (lower panel) sample.

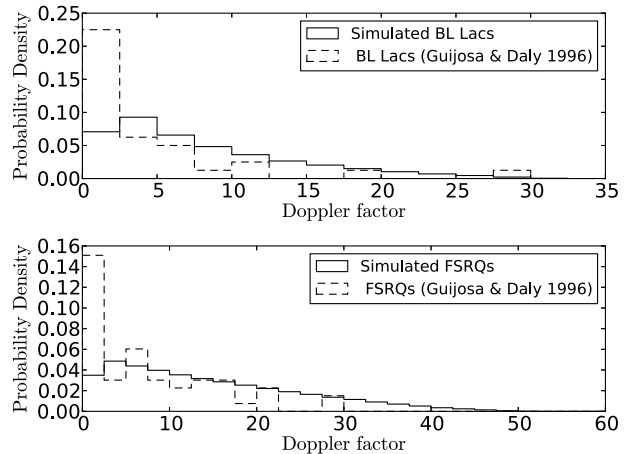


**Figure 9.** Probability density function of statistical Doppler factors (solid line) and equipartition Doppler factors from Gujosa & Daly (1996) (dashed line) for the BL Lac sample (upper panel) the FSRQ sample (lower panel).

(1993) for the inverse Compton Doppler factor. The sample consists of 33 BL Lac objects and 53 FSRQs. The flux-limit for this sample is 1 Jy (Kuehr et al. 1981). We corrected for the continuous jet case (which we also assume in our statistical model) using eq. 6. The KS-test returns a p-value of  $\sim 4 \times 10^{-3}\%$  for the BL Lacs and  $\sim 10.36\%$  for the FSRQs. We plot the PDF and CDF for the two classes in Figs. 7 and 8.

We next test equipartition Doppler factors calculated by Gujosa & Daly (1996). The sample consists of 32 BL Lac objects and 53 FSRQs. The flux-limit for this sample is 1 Jy (Ghisellini et al. 1993). The value of the KS-test for the BL Lac objects is  $\sim 1.5 \times 10^{-4}\%$  while for the FSRQs  $\sim 7.6 \times 10^{-3}\%$ . Figures 9 and 10 show the simulated and estimated probability density (fig. 9) and cumulative distribution (fig. 10) functions.

Finally, we test variability Doppler factors (using the

equipartition brightness temperature to derive a Doppler factor) using data from Hovatta et al. (2009). They use a sample consisting of 22 BL Lac objects and 60 FSRQs. The flux-limit for this sample is 2 Jy (Valtaoja et al. 1992). For the BL Lac population, the value of the K-S test is  $\sim 54\%$  while for the FSRQ  $\sim 14\%$ . The PDFs and CDFs for the comparison are shown in Figs. 11 and 12 respectively. This is the method that gives the best agreement with the statistical Doppler factors.

## 5 DISCUSSION

We have compared, in §4, results from our statistical, population model for blazars, with data provided in the literature for three distinct methods of calculating Doppler factors. The results of this comparison show that one of

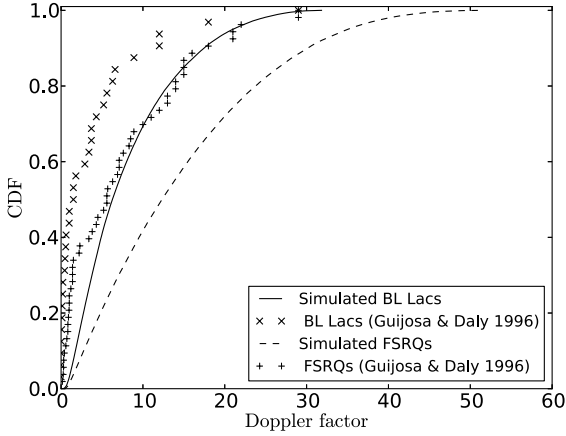


**Figure 10.** Cumulative distribution function of the statistical Doppler factors for BL Lacs (solid line) and FSRQs (dashed line) overplotted with equipartition Doppler factors from [Guijosa & Daly \(1996\)](#) (X for BL Lacs, + for FSRQs).

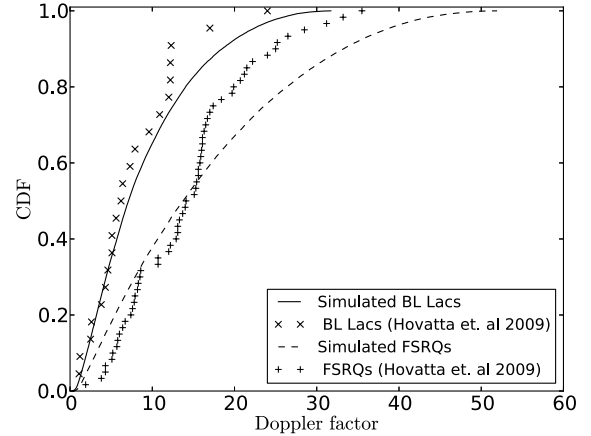


**Figure 12.** Cumulative distribution function of statistical Doppler factors for the BL Lacs (solid line) and FSRQs (dashed line) overplotted with variability Doppler factors using equipartition from [Hovatta et al. \(2009\)](#) (X for BL Lacs, + for FSRQs).

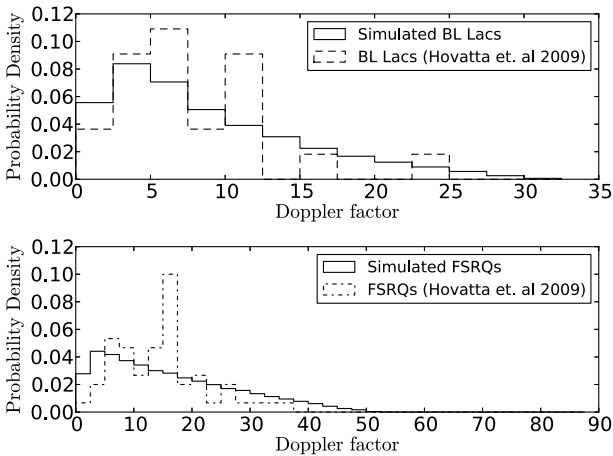


**Figure 11.** Probability density function of statistical Doppler factors (solid line) overplotted with variability Doppler factors using equipartition from [Hovatta et al. \(2009\)](#) (dashed) for the BL Lac sample (upper panel) and the FSRQ sample (lower panel).

the methods, variability Doppler factors  $\delta_{var}$ , is consistent with statistical Doppler factors (K-S test BL Lac  $\sim 54\%$ , FSRQs  $\sim 14\%$ ) whereas the other two methods seem to be drawn from completely different distributions (K-S test for both populations  $\sim \leq 10^{-3}\%$ ). This result is in agreement with [Lähteenmäki & Valtaoja \(1999\)](#) arguing that variability Doppler factors using equipartition are a better and more accurate estimate of the Doppler factors of beamed sources than equipartition Doppler factors that rely on direct measurement of the angular size of the emission region, due to a weaker dependence on the observed brightness temperature (third root compared to first power).

Of all other Doppler factor estimation techniques we tested, there were only two cases where our statistical analysis did not indicate an inconsistency between our statistical model and the data: the BL Lac sample in [Britzen et al. \(2007\)](#) and the FSRQ sample in [Ghisellini et al. \(1993\)](#).

In the first case, even though the value of the K-S test is marginally acceptable ( $\sim 6\%$ ), it is clear from the low value of the Doppler factors (maximum value  $\sim 7$ ) and from Figs. 5 and 6 that the agreement is far from good; however, the low number of sources in the BL Lac sample (11 sources) is preventing a strong conclusion either way through the K-S test.

In the second case, the test gives a probability of  $\sim 10\%$  for consistency, which is above the limit set in §4 and thus considered acceptable. It is interesting to note that the results of the comparison are very different between the two population classes (BL Lacs and FSRQs). Agreement of their results with our optimal model for the BL Lac sample is rejected at the  $\sim 4 \times 10^{-3}\%$  level. As discussed by [Britzen et al. \(2007\)](#),  $\delta_{IC}$  is equal to the real Doppler factor only if all of the observed flux in X-rays is produced through the SSC process. In any other case,  $\delta_{IC}$  represents only a lower limit. If all other assumptions entering the  $\delta_{IC}$  calculation hold, our findings would suggest that part of the X-ray flux is produced through other mechanisms for many sources in the BL Lac sample. This is consistent with our general understanding of these classes of sources: FSRQs are low synchrotron peaked (LSP) sources ([Abdo et al. 2010b](#)) so it is reasonable to expect the largest fraction of their X-ray emission to be of inverse-Compton origin; on the other hand, many BL Lacs are intermediate synchrotron peaked (ISP) and high synchrotron peaked (HSP), so part of their X-ray flux can be produced by synchrotron emission, which would result in the inverse Compton Doppler factors underestimating the true Doppler factor of their jets. Indeed, it is clear from Fig. 8 that the Doppler factors of the BL Lacs are underestimated compared to the expectations from our optimal population model.

It is troubling that the consistency of  $\delta_{IC}$  with the expectations from our population model for FSRQs is so different between the [Ghisellini et al. \(1993\)](#) sample and the [Britzen et al. \(2007\)](#) sample. While the first is acceptable, the second is rejected with a probability of  $\sim 2.15 \times 10^{-5}\%$ . Six orders of magnitude in difference might indicate poor

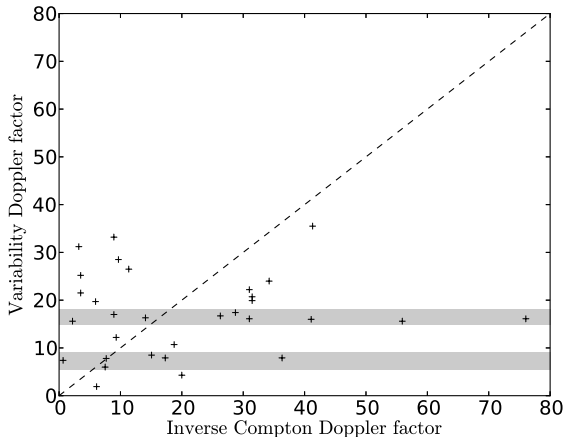


**Figure 13.** Variability Doppler factors plotted against inverse Compton Doppler factors for the FSRQs that are common between the [Hovatta et al. \(2009\)](#) and [Ghisellini et al. \(1993\)](#) samples. The gray shaded areas indicated the regions of pileups.

sample selection or/and large errors in measurements. This difference might also be due to the time difference between radio and X-ray flux measurements. The main assumption of the inverse Compton Doppler factor method is that synchrotron-emitting electrons up-scatter synchrotron photons to X-rays. The X-ray and radio flux densities must therefore be measured at the same time. Any time difference in observations might result in non-corresponding flux densities. A better evaluation of this technique could be achieved by systematically pursuing simultaneous radio and X-ray observations for a radio-selected flux-limited sample of low-synchrotron peaked sources.

For those Doppler techniques and samples that the hypothesis of being drawn from our optimal statistical model is rejected by the K-S test, we have also performed comparisons with distributions drawn from a statistical model with parameters other than the optimal, but still within the limits of acceptability discussed §2. Since in these cases there is an excess of low values for the Doppler factors, we have compared them with distributions resulting from the model using  $a_{max}$  and the model using  $A_{min}$  since these give a higher fraction of low Doppler factor values than our optimal model (see Figs. 1 and 2) for both populations. A K-S test indicated that agreement with these distributions is also rejected.

### 5.1 Error analysis

Although the variability Doppler factors using equipartition result in the best agreement with our statistical model (and, by extension, with MOJAVE results on jet speeds), the agreement is not perfect. First, there is a pileup of sources between Doppler factors of 10 and 16 in both classes of sources. In the FSRQ case, there seems to be another pileup between 5 and 8 and a deficit of low Doppler factor values (see Fig. 12). Such pileups appear to be systematics-related. For example: high Doppler factors result in very compressed timescales, and the fastest flare in a source may not be resolvable at a given cadence. Higher time resolution in the flux density curves will provide more accurate results.

Similarly, for the other case where we have a Doppler factor estimation method that is not inconsistent with our optimal model (the inverse Compton Doppler factors of [Ghisellini et al. 1993](#) for FSRQs), the agreement is also not perfect. There is a concentration of sources at low Doppler factor values compared to the expectation from our statistical model. This is expected if in the sample under study there is a considerable number of sources where the SSC emission is not the sole source of X-rays; or, if there are errors entering due to the non-simultaneity of X-ray and radio measurements.

In Fig. 13 we plot variability Doppler factors using equipartition from [Hovatta et al. \(2009\)](#) and inverse Compton Doppler factors from [Ghisellini et al. \(1993\)](#) for the 31 common FSRQ sources in their samples. We have indicated the regions of pileup of sources discussed above for the variability Doppler factor method in grey. Although a correlation can be seen for the remaining sources, the statistics are very low for a strong statement to be made. We note however that such pileups in the distribution of Doppler factors in a flux-limited sample where none are expected from a population model can be a good indicator regarding the sources for which the results of a particular technique should be used with caution.

As discussed in §2, neither the Doppler factor estimates discussed here, nor the assumptions on which they have been based have been used in any way in the optimization of the population models we used to produce simulated Doppler factor distributions. For this reason, the simulated and estimated Doppler factor distributions are statistically independent. This provides us with a unique opportunity: we can use the observed and simulated (assumed to be “intrinsic”) Doppler factor distributions to derive the (average) error on the Doppler factor estimates. This is especially important since errors on the Doppler factor estimates are difficult to calculate and are not provided in the original analyses from which the Doppler factor estimates used in this work are taken. We next provide such an error analysis for the two methods (variability and IC Doppler factors) that are consistent at the population level with our simulated distributions.

We construct the cumulative distribution function of the model Doppler factors, for each population. We set a constant fractional error  $p$  (from 0 to 1) for each Doppler factor estimate that is common for all values in each method. For the case of normal errors we draw a random value from the model Doppler factor CDF, which serves as the “true” Doppler factor of a source and the mean of the error distribution. The standard deviation, or shape parameter of each distribution is the mean multiplied by the fractional constant ( $p$ ). Then we drew a random value from that distribution. Any negative values were rejected, so, strictly, the error distribution in this case is a truncated Gaussian. By following the same procedure for different simulated sources, we created a simulated with-errors sample, which we compared with the corresponding method using the K-S test. We repeated this process with step 0.01 in  $p$  in order to assure the fractional constant’s parameter space (from 0 to 1) was adequately scanned for different distributions. The distribution which increased the agreement between the simulated with-errors and observed samples the most is the error distribution of each estimate with error the “best-fit” percentage error which is a function of  $p$ . We have also exper-

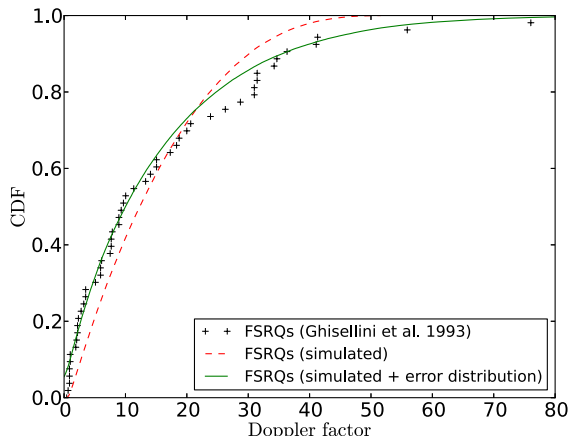


**Figure 14.** Cumulative distribution function of the simulated “errored” sample (solid green) overplotted with the initial simulated sample (dashed red) and the variability Doppler factors (Ghisellini et al. 1993) (“+”) for the FSRQs.

imented with many other error distributions (log-normal, uniform, width parameters other than  $p\delta$  etc.) and tested again whether agreement with the distribution of estimated Doppler factors improves.

In the case of the inverse Compton Doppler factor we treated only the FSRQs, since it is the only population that the method can adequately describe. We found that the error distribution that best describes the method is a normal distribution with mean  $\mu = \delta_{IC}$  and standard deviation  $\sigma = p\delta_{IC}$  with “best-fit” fractional constant  $p \approx 0.63$ , which in this case corresponds to a percentage error of  $\sim 63\%$ . The K-S test gave a probability value of 94.6% of consistency between the simulated with-errors and the observed sample. Figure 14 shows the cumulative distribution function for the simulated with-errors distribution for the FSRQ population. In §4, we found that the probability of consistency between the simulated and observed samples for the  $\delta_{IC}$  was  $\sim 10.36\%$ . Introducing the error distribution, there is a significant rise in the probability of consistency of the two samples. Since the inverse Compton Doppler factor method does not involve fitting and the calculation is performed by inputting parameter values, the error in each estimate depends only on the errors of these values. In this case, standard error propagation methods dictate that the error distribution of each estimate has a Gaussian shape, which is validated by our results. In addition, the error distribution shows that even though the error in each estimate is relatively large ( $\sim 63\%$ ) the overall error is dominated by random errors, which can be attributed to uncertainties in the measurements and/or non-simultaneity of observations. The source of errors in the inverse Compton Doppler factor method will be the subject of a future publication.

For the variability Doppler factors we were unable to find a error distribution able to adequately “fit” the data. The reason for this is that the variability Doppler factor uncertainties appear to be dominated by systematic, rather than random errors. As discussed above, there are pileups in the distribution of both the BL Lacs and FSRQs (Figs.

12, 13), for which there is no satisfactory way of treating in a statistical fashion.

It is obvious, even by eye (Fig. 12), that the BL Lac population is less affected by systematic errors. There is a small pileup at  $\delta_{var} \sim 12$ , but otherwise there seem to be no other prominent features. For this reason we used the BL Lac distribution in order to have a coarse estimate on the random errors of the variability Doppler factors. To achieve this, we constructed the cumulative distribution functions of the variability Doppler factors, and the with-errors distribution, assuming each estimate comes from a normal distribution with mean the value of that estimate ( $\mu = \delta_{var}$ ) and standard deviation the value multiplied by the fractional constant  $p$  ( $\sigma = p\delta_{var}$ ). Then, we calculated the distance between the two CDFs (i.e the K-S statistic), but this time, for the derivation of the maximum distance we excluded the three points that lay in the pileup (Fig. 12). We found that the shortest distance is achieved with  $\sim 30\%$  error in each estimate. Adding error above that increases the distance between the two CDFs. These results suggest that although the error of the variability Doppler factors is dominated by systematics, the random error in each estimate is approximately 30%. Since there is no difference between BL Lacs and FSRQs in the procedure used to estimate the variability Doppler factor, we expect the FSRQs to have the same random error as the BL Lacs, which will be  $\sim 30\%$  as well.

Comparing the two methods discussed above (variability, inverse Compton), we see that the variability Doppler factor estimates have approximately half the percentage random error of the inverse Compton Doppler factors; making them the most accurate of the two, which is consistent with the analysis in Lähteenmäki et al. (1999). Although the variability Doppler factor method is the most accurate method for describing blazars as a population, the cadence of observations warrants caution in the application of the method and the primary source of systematic errors.

## 5.2 Statistical Doppler factors

We have evaluated whether the theoretically derived Doppler factor distributions can be combined with measurements of the flux density and apparent jet speed of a source to yield an estimate of the Doppler factor in individual sources. We created two sub-samples from the common sources in the MOJAVE sample and (Hovatta et al. 2009), for which we also have flux density measurements (Lister et al. 2009a). These consist of 12 BL Lacs and 39 FSRQs respectively. For each of these sources, we generated a distribution of Doppler factors as follows: starting from our blazar population model for the relevant class of sources (BL Lacs or FSRQs), we randomly drew luminosities, Lorentz factors, and viewing angles according to their respective distributions. However, instead of keeping only sources that obeyed a specific flux limit, we only kept sources with flux density within 10% of the mean flux density of the source at hand.

We show these distributions for three of these sources in Fig. 15. These three sources have the additional property that their variability and inverse Compton Doppler factor estimates are very close to each other. The values of their variability Doppler factors are These sources are 18.4, 16.1, and 10.7, for 0106+013, 0234+285, and 1730-130 respec-

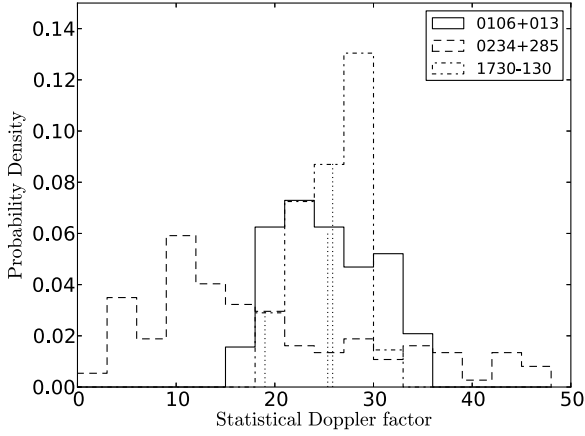


**Figure 15.** Distribution of Doppler factors for 0106+013 0234+285 and 1730-130. The vertical dotted lines represent the mean values for each of the distributions.

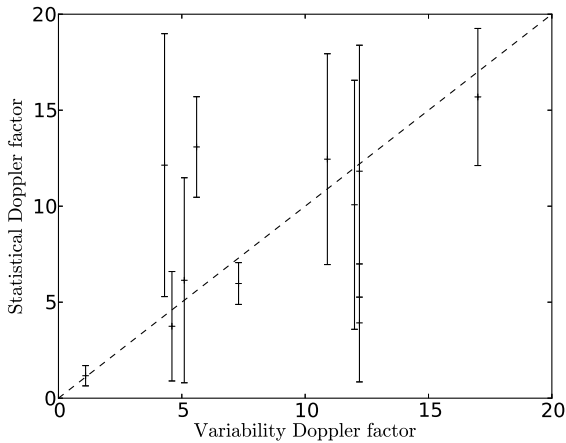


**Figure 16.** Statistical versus variability (using equipartition) Doppler factors for the BL Lac sample. The error bars represent  $1\sigma$  of the statistical Doppler factor distribution for each source.

tively. We can see that all three distributions have a very significant spread. The mean and standard deviation of these distributions are  $25.36 \pm 4.96$  for 0106+013,  $19.00 \pm 11.57$  for 0234+285, and  $25.86 \pm 2.88$  for 1730-130.

Figures 16 and 17 show the statistical Doppler factors (mean and standard deviation of the Doppler factor distribution produced for each source as described above) plotted against the variability Doppler factors for the BL Lacs and the FSRQs respectively. We can see that while there is agreement within  $2\sigma$  for most sources, the uncertainties of the statistical Doppler factors are so large that they erase any correlation between the two quantities on a source-by-source basis. We conclude that our population model is not constraining enough when applied to individual sources, and thus we strongly advise against using it to derive information about single objects.

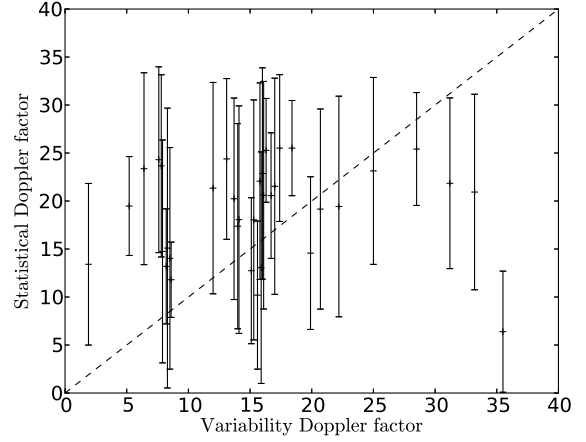


**Figure 17.** Statistical versus variability (using equipartition) Doppler factors for individual FSRQs. The error bars represent  $1\sigma$  of the statistical Doppler factor distribution for each source.

## 6 CONCLUSIONS

We have used our population models for BL Lacs and FSRQs to evaluate different techniques of calculating Doppler factors in individual sources. Our conclusions can be summarized as follows.

- Variability Doppler factors using equipartition, when calculated for a flux-limited sample, result in a distribution that is consistent for both samples (FSRQs & BL Lacs) with the distribution produced by our population model when the same flux limit is applied.

Since the only observables entering the optimization of our population model are apparent jet speeds and source redshifts, our model contains no assumption regarding variability, causality, or equipartition. The agreement between our model distributions and the distributions of variability Doppler factors points to a self-consistent picture in radio between jet speeds and Doppler factors. Additionally, this agreement can only be achieved if equipartition as discussed by [Scott & Readhead \(1977\)](#); [Readhead \(1994\)](#) indeed holds in blazars as a population.

- Inverse Compton Doppler factors are not inconsistent with the Flat Spectrum Radio Quasars as a population, while they are unable to describe BL Lacs, likely because some of the latter produce a significant fraction of their X-ray flux through synchrotron radiation. This conclusion is also in support of the self-synchrotron Compton model, a main assumption of the inverse Compton Doppler factor method, being responsible for most of the X-ray flux in a large fraction of FSRQs.

- Exploring the error distribution of the methods that can adequately describe blazars as a population, we found that: for the inverse Compton Doppler factors, the error distribution is a (truncated) normal distribution with  $\sim 63\%$  percentage error for the FSRQs. The estimates seem to be dominated by random errors. For the variability Doppler factors, estimates are dominated by systematic errors, such as pileups, due to cadence observations which sets a limit on the fastest flare the survey is able to detect. We estimated that the random error in the variability Doppler factor is  $\sim 30\%$

making the variability method the most accurate method of the two, for sources where systematics are not a concern (for example, sources where the fastest flare is well-resolved and significantly longer in timescale than the cadence) in agreement with Lähteenmäki et al. (1999).

- The main limitation of the variability Doppler factor method assuming equipartition appears to be monitoring cadence. For this reason, long-term high-cadence blazar monitoring (such as the OVRO 15GHz monitoring program, Richards et al. 2011) can be an invaluable tool in deriving accurate Doppler factor estimates (within 30% error) on a blazar-by-blazar basis.

- Population models such as the one described here are unable to yield reliable and useful estimates for Doppler factors of individual blazars, and for this reason they should not be used in this fashion.

In this work, we have used the Kolmogorov-Smirnov test to check whether the distributions of estimated Doppler factors for blazar populations are inconsistent with our simulated ones. The reader should be cautioned that while inconsistency, when established at high significance, is statistically robust, a failure of the test to establish inconsistency could mean one of two things: either (a) the two distributions are consistent, or (b) it is impossible to tell because of small sample size (as is the case, for example, for BL Lacs in the Britzen et al sample.) For this reason, the physical interpretation of our results should be done with caution. An increased number of sources with Doppler factor estimates can strengthen our conclusions and further elucidate blazar physics.

## ACKNOWLEDGMENTS

We are grateful to Talvikki Hovatta for insightful comments that improved this work. We would also like to thank Tony Readhead and Manolis Angelakis for valuable discussions.

This research was supported by the “Aristeia” Action of the “Operational Program Education and Lifelong Learning” and is co-funded by the European Social Fund (ESF) and Greek National Resources, and by the European Commission Seventh Framework Program (FP7) through grants PCIG10-GA-2011-304001 “JetPop” and PIRSES-GA-2012-31578 “EuroCal”.

## REFERENCES

- Abdo A. A., et al., 2010a, *ApJ*, **710**, 1271  
 Abdo A. A., et al., 2010b, *ApJ*, **716**, 30  
 Aharonian F., et al., 2007, *ApJ*, **664**, L71  
 Arshakian T. G., Ros E., Zensus J. A., 2006, *A&A*, **458**, 397  
 Blandford R. D., Königl A., 1979, *ApJ*, **232**, 34  
 Britzen S., Brinkmann W., Campbell R. M., Gliozzi M., Readhead A. C. S., Browne I. W. A., Wilkinson P., 2007, *A&A*, **476**, 759  
 Cara M., Lister M. L., 2008, *ApJ*, **674**, 111  
 Chatterjee R., et al., 2008, *ApJ*, **689**, 79  
 Clausen-Brown E., Savolainen T., Pushkarev A. B., Kovalev Y. Y., Zensus J. A., 2013, *A&A*, **558**, A144  
 Fan J.-H., Yang J.-H., Liu Y., Zhang J.-Y., 2013, *Research in Astronomy and Astrophysics*, **13**, 259

- Fan J.-H., Bastieri D., Yang J.-H., Liu Y., Hua T.-X., Yuan Y.-H., Wu D.-X., 2014, *Research in Astronomy and Astrophysics*, **14**, 1135  
 Georganopoulos M., 2003, *Chinese Journal of Astronomy and Astrophysics Supplement*, **3**, 404  
 Georganopoulos M., Kazanas D., 2003a, *New Astron. Rev.*, **47**, 653  
 Georganopoulos M., Kazanas D., 2003b, *ApJ*, **589**, L5  
 Georganopoulos M., Kazanas D., 2003c, *ApJ*, **594**, L27  
 Ghisellini G., 1987, *MNRAS*, **224**, 1  
 Ghisellini G., Padovani P., Celotti A., Maraschi L., 1993, *ApJ*, **407**, 65  
 Giannios D., Uzdensky D. A., Begelman M. C., 2009, *MNRAS*, **395**, L29  
 Guijosa A., Daly R. A., 1996, *ApJ*, **461**, 600  
 Hovatta T., Valtaoja E., Tornikoski M., Lähteenmäki A., 2009, *A&A*, **494**, 527  
 Jorstad S. G., et al., 2005, *AJ*, **130**, 1418  
 Jorstad S. G., et al., 2006, in Miller H. R., Marshall K., Webb J. R., Aller M. F., eds, *Astronomical Society of the Pacific Conference Series Vol. 350, Blazar Variability Workshop II: Entering the GLAST Era*. p. 149  
 Komatsu E., et al., 2009, *ApJS*, **180**, 330  
 Kuehr H., Witzel A., Pauliny-Toth I. I. K., Nauber U., 1981, *A&AS*, **45**, 367  
 Lähteenmäki A., Valtaoja E., 1999, *ApJ*, **521**, 493  
 Lähteenmäki A., Valtaoja E., Wiik K., 1999, *ApJ*, **511**, 112  
 Liodakis I., Pavlidou V., 2015, *MNRAS*, **451**, 2434  
 Lister M. L., Homan D. C., 2005, *AJ*, **130**, 1389  
 Lister M. L., Marscher A. P., 1997, *ApJ*, **476**, 572  
 Lister M. L., et al., 2009a, *AJ*, **137**, 3718  
 Lister M. L., et al., 2009b, *AJ*, **138**, 1874  
 Lister M. L., et al., 2013, *AJ*, **146**, 120  
 Mattox J. R., et al., 1993, *ApJ*, **410**, 609  
 Padovani P., 1992, *MNRAS*, **257**, 404  
 Padovani P., Urry C. M., 1992, *ApJ*, **387**, 449  
 Pavlidou V., et al., 2012, *ApJ*, **751**, 149  
 Readhead A. C. S., 1994, *ApJ*, **426**, 51  
 Richards J. L., et al., 2011, *ApJS*, **194**, 29  
 Scott M. A., Readhead A. C. S., 1977, *MNRAS*, **180**, 539  
 Taylor G. B., Vermeulen R. C., Readhead A. C. S., Pearson T. J., Henstock D. R., Wilkinson P. N., 1996, *ApJS*, **107**, 37  
 Valtaoja E., Lähteenmäki A., Terasranta H., 1992, *A&AS*, **95**, 73  
 Valtaoja E., Lähteenmäki A., Teräsraanta H., Lainela M., 1999, *ApJS*, **120**, 95

# Detecting the Elusive Blazar Counter-Jets

I. Liodakis<sup>1,2\*</sup>, V. Pavlidou<sup>1,2</sup>, and E. Angelakis<sup>3</sup>

<sup>1</sup>*Department of Physics and ITC<sup>†</sup>, University of Crete, 71003, Heraklion, Greece*

<sup>2</sup>*Foundation for Research and Technology - Hellas, IESL, Voutes, 7110 Heraklion, Greece*

<sup>3</sup>*Max-Planck-Institut für Radioastronomie, Auf dem Hügel 69, 53121 Bonn, Germany*

21 October 2016

## ABSTRACT

Detection of blazar pc scale counter-jets is difficult, but it can provide invaluable insight into the relativistic effects, radiative processes and the complex mechanisms of jet production, collimation and acceleration in blazars. We build on recent populations models (optimized using the MOJAVE apparent velocity and redshift distributions) in order to derive the distribution of jet-to-counter-jet ratios and the flux densities of the counter-jet at different frequencies, in an effort to set minimum sensitivity limits required for existing and future telescope arrays in order to detect these elusive counter-jets. We find that: for the BL Lacs 5% of their counter-jets have a flux-density higher than 100mJy, 15% are higher than 10 mJy, and 32% have higher flux-density than 1 mJy, whereas for the FSRQs 8% have a flux-density higher than 10mJy, 17% are higher than 1 mJy, and 32% are higher than 0.1 mJy (at 15 GHz). Future telescopes like the SKA and newly operating like e-MERLIN and JVLA may detect up to 99% of the BL Lac and 77% of the FSRQ counter-jets. Sources with both low apparent velocity and a low Doppler factor make prime candidates for counter-jet detection. Combining our findings with literature values we have identified five such counter-jet detection candidates. Finally, we discuss possible effects beyond relativistic deboosting that may complicate the detection of counter-jets and that need to be accounted for in the interpretation of detections.

**Key words:** galaxies: active – galaxies: jets – galaxies: blazars – galaxies: counter-jet

## 1 INTRODUCTION

Blazars, i.e Flat Spectrum Radio Quasars (FSRQs) and BL Lac objects, are active galactic nuclei (AGN) with jets oriented close to our line of sight (Readhead et al. 1978b; Blandford & Königl 1979; Scheuer & Readhead 1979; Readhead 1980a). Their broadband spectrum, from radio to  $\gamma$ -rays, is characterized by non-thermal radiation and extreme variability. The emission in the low energy regime is dominated by synchrotron radiation of relativistic electrons accelerated in the magnetic field of the jet and thus polarized, whereas the high energy regime is believed to be dominated by the inverse Compton scattering of an ambient low energy photon field. Before the relativistic nature of blazar jets was established, the one-sided morphology was thought by many to be intrinsic to the source. VLBI observations in the 1970s were critical in forming our current understanding of relativistic extragalactic jets, in-

cluding the continuity between pc-scale jets and kpc-scale jets and lobes (Readhead et al. 1978a), their relativistic nature [proposed by Rees (1966, 1967) to reconcile the synchrotron nature of radio emission from compact sources with their rapid variability, and established through the unambiguous detection of superluminal motions (Readhead et al. 1978a)], and the unification between sources viewed at large and small angles with respect to the jet (Readhead 1980b). The discovery, through spectropolarimetric observations, of the torus surrounding the central regions of radio galaxies (Antonucci & Miller 1985) completed the modern unification picture of relativistic jets associated with supermassive black holes.

Although theoretical models predict the existence of two symmetrical jets (Rees 1966; Blandford & Rees 1974; Scheuer 1974; Readhead 1980b) extending outwards from the central engine, in most cases pc-scale observations of radio jets reveal only one-sided structures (Lister et al. 2009a).

\* liodakis@physics.uoc.gr

† Institute for Theoretical and Computational Physics, formerly Institute for Plasma Physics

### 1.1 Doppler favoritism in beamed sources

Once the relativistic nature of blazar jets was established, it was generally accepted that the one-sided morphology of pc-scale jets was due to Doppler favoritism. Although, ideally, identical relativistic jets are expected to emerge symmetrically from the supermassive black hole, due to beaming and the preferred viewing angle of blazars, the jet moving towards us is boosted, whereas the counter-jet is deboosted. The emission from the jet coming towards us will be boosted by an amount equal to a power of the Doppler factor ( $D$ ) defined as:

$$D = \frac{1}{\Gamma(1 - \beta \cos \theta)}, \quad (1)$$

where  $\Gamma$  is the bulk Lorentz factor of the jet,  $\theta$  is the viewing angle, and  $\beta$  is the speed of the jet in units of speed of light. In the case of the receding jet the Doppler factor (substituting  $\beta$  with  $-\beta$ ) is:

$$D' = \frac{1}{\Gamma(1 + \beta \cos \theta)}. \quad (2)$$

For the boosted jet the monochromatic flux density is given by:

$$S_\nu = \frac{L_\nu D^p}{4\pi d_L^2} (1+z)^{1+s}, \quad (3)$$

and for the deboosted jet by:

$$S'_\nu = \frac{L_\nu D'^p}{4\pi d_L^2} (1+z)^{1+s}, \quad (4)$$

where  $s$  the spectral index defined as  $S \propto \nu^s$ ,  $L_\nu$  the monochromatic intrinsic luminosity,  $d_L$  is the luminosity distance,  $z$  the redshift, and  $p = 2 - s$  for the continuous jet case, and  $p = 3 - s$  for the discrete. Throughout this work we have adopted the continuous jet case. The ratio of the two flux densities would be:

$$j = \frac{S_\nu}{S'_\nu} = \left(\frac{D}{D'}\right)^p = \left(\frac{1 + \beta \cos \theta}{1 - \beta \cos \theta}\right)^p. \quad (5)$$

If a source is closely aligned with our line of sight ( $\theta$  is small, as is the case for blazars), then even for the mildly relativistic case the ratio will be approximately  $\sim 10^3$ . For a more typical blazar jet with Lorentz factor of  $\sim 15$ , detection of the counter-jet is indeed very hard. For this reason, although the detection of pc-scale counter-jets is a complex problem that can be affected by several factors (see section 5.2 for a detailed discussion) in the case of blazars Doppler favoritism is so strong that likely outweighs other difficulties.

In this work, we quantify, statistically, the expected distributions of  $j$  and  $S'_\nu$  produced by Doppler boosting alone, which set the *minimum* sensitivity requirements for the detection of blazar counter-jets by current and future observatories.

### 1.2 Possible applications of blazar counter-jet detection

Provided that other factors affecting the counter-jet flux density (such as free-free absorption from ionized material surrounding the black hole, see section 5.2) can be controlled, measurements of the jet-to-counter-jet ratio ( $j$ ) can be used to constrain the jet viewing angle. Blazar jets are

known to show superluminal motion (Cohen et al. 1979; Pearson et al. 1981; Vermeulen & Cohen 1994; Lister et al. 2009b, 2013). Measured velocities of the radio components in the jets vary from little over the speed of light to  $\sim 50c$  (Lister et al. 2009b, 2013). Surveys such as the MOJAVE (Monitoring of Jets in Active galactic nuclei with VLBA Experiments, Lister & Homan 2005)<sup>1</sup> and the Boston Blazar Research Group program<sup>2</sup> (Jorstad et al. 2001, 2005, 2006) have spearheaded great progress in reliably measuring apparent velocities for a large number of blazars. The apparent superluminal motion is related to the true component speed ( $\beta$ ) and the viewing angle ( $\theta$ ) by:

$$\beta_{app} = \frac{\beta \sin \theta}{1 - \beta \cos \theta}. \quad (6)$$

Combining Eq. 5, and Eq. 6 we have:

$$\theta = \arctan \left( \frac{2\beta_{app}}{j^{1/p} - 1} \right). \quad (7)$$

Detection of the counter-jet with the addition of a reliable measurement of the apparent velocity of the approaching jet may thus provide an independent estimate of the viewing angle, a key parameter in blazar modeling. Knowing the viewing angle in turn allows us to estimate the bulk Lorentz factor of the flow and the Doppler factor independently of the frequently used assumptions entering various Doppler factor estimation techniques (e.g. Variability Doppler factors Lähteenmäki & Valtaoja 1999; Hovatta et al. 2009). Such assumptions, like the equipartition of the energy density of the magnetic field and the radiation energy density, domination of synchrotron self-Compton emission at high energies, the proportionality of the synchrotron peak with luminosity etc., could be then tested in individual sources. Independent estimates of Doppler factors could also contribute to further constraining the true Doppler factor in individual sources, and aid in the identification of empirical correlations in blazar jets that have traditionally been obscured by relativistic effects and limitations in confidently estimating beaming properties (e.g., Hovatta et al. 2010; Lister et al. 2011; Blinov et al. 2016a,b; Angelakis et al. 2016).

In addition to understanding the beaming properties of blazar jets, we would be able to investigate many other important aspects of blazar and AGN physics in general. For example, since the two jets are expected to be symmetric, the supermassive black hole will lie between the radio core and counter-core (e.g. Haga et al. 2013; Baczko et al. 2016). Locating the supermassive black hole and of the broadline region with respect to the radio core would provide invaluable insight into localizing the emission regions in different wavelengths that could be complementary to other techniques (see, e.g., Fuhrmann et al. 2014, Max-Moerbeck et al. 2014, Abdo et al. 2010, Blinov et al. 2015).

### 1.3 Observational detections of pc-scale counter-jets

Counter-jets on pc-scales have been discussed in a number of one-sided jet sources, including Seyfert galaxies,

<sup>1</sup> <http://www.physics.purdue.edu/MOJAVE/>

<sup>2</sup> <http://www.bu.edu/blazars/>

radio galaxies, LINERS and blazars. These include 3C84 (Vermeulen et al. 1994), Markarian 501 (Giovannini et al. 2008), PKS1510-089 (Homan et al. 2002), M87 (Arp 1967; Sparks et al. 1992; Kovalev et al. 2007, Walker, Hardee, Davies, Ly, & Junor in prep.<sup>3</sup>). Nevertheless the vast majority of counter-jets remains undetected.

In the case of M87, an optical counter-jet was reported as early as 1967 (Arp 1967; Sparks et al. 1992). More recently, radio counter-jet features have been detected in sub-pc scales in the inner jet of M87 (Kovalev et al. 2007, Walker, Hardee, Davies, Ly, & Junor in prep.) However, the measured jet-to-counter-jet ratio (10-15) is inconsistent within the simple Doppler favoritism picture observed with the lack of evidence of fast motions within the inner 20 mas (Kovalev et al. 2007). The authors conclude that this may be due to either an intrinsic asymmetry of the jet, or the lack of distinguishable moving features within a smooth fast flowing inner jet.

A pc-scale counter-jet was detected by Vermeulen et al. (1994) in the case of 3C84. In this case the counter-jet featured an inverted spectrum, with a spectral index of 1.7, most naturally interpreted as a sign of free-free absorption by ionized, toroidal or disklike material around the black hole, which would not affect the approaching jet (see also Fujita & Nagai 2016). Free-free absorption effects have also been identified in the spectra of counter-jet features in NGC 4261, Cen A, and Cyg A by Haga et al. (2013, 2015) and Boccardi et al. (2016a). When this is the case, caution needs to be exercised when interpreting the jet-to-counter-jet ratio, as a significant function of the flux reduction may be due to absorption compounding the effect of Doppler deboosting.

The precessing jet of 4C +12.50, which is a source whose host shows signs of recent merger, is another case of detected pc-scale counter-jet. In this very well-studied source, the detection of superluminal apparent speeds, jet and counter-jet, as well as bend morphology have allowed the fitting of a detailed model describing the jet precession (Lister et al. 2003).

In the case of PKS 1510-089 a kpc-scale counter feature has been detected by O’Dea et al. (1988) although more recently Homan et al. (2002) favor a jet bend interpretation of this structure. VLBI observations of the source have been conflicting on whether there appears to be a pc-scale counter-jet towards the kpc-scale counter feature (Bondi et al. 1996; Fey & Charlot 1997; Kellermann et al. 1998; Homan et al. 2001; Jorstad et al. 2001; Wardle et al. 2005; Homan et al. 2002).

Finally, in the case of Markarian 501, Giroletti et al. (2004, 2008) used the non-detection of a counter-jet in high dynamic range observations to constrain the jet geometry.

#### 1.4 This work

In this work, we use re-optimized population models (of the same class as Liodakis & Pavlidou 2015a, hereafter Paper I) using the  $\beta_{app}$  and redshift distributions from the MOJAVE survey (Lister & Homan 2005) in order to describe statistically the underlying distribution of bulk Lorentz factors  $\Gamma$ ,

unbeamed luminosities ( $L_\nu$ ), viewing angles and redshifts for the blazar population. We then use these models to produce the distribution of the jet to counter-jet ratio, and the distribution of the counter-jet flux-density in different radio frequencies. We aim at predicting the minimum sensitivity required from future telescopes, and upgrades of the existing arrays in order to detect counter-jets from blazars.

This paper is organized as follows: In section 2 we present the modifications to the population model from Paper I; in section 3 we present the models prediction for the jet-to-counter-jet ratio and the flux density of the counter-jet in different frequencies; in section 4 we present possible counter-jet detection candidates; and in section 5 we discuss the conclusions derived from this work.

The cosmology we have adopted throughout this work is  $H_0 = 71 \text{ km s}^{-1} \text{ Mpc}^{-1}$ ,  $\Omega_m = 0.27$  and  $\Omega_\Lambda = 1 - \Omega_m$  (Komatsu et al. 2009).

## 2 POPULATION MODEL

In Paper I, separating BL Lacs and FSRQs, we created population models i.e. a bulk Lorentz factor and unbeamed luminosity distributions that can adequately reproduce the observed apparent velocity of the radio components and redshift distributions from the statistically complete, flux-limited sample of the MOJAVE survey (Lister & Homan 2005).

We determined the fraction of sources at each redshift, from  $z = 0$  to  $z = 1.4$  for the BL Lacs and from  $z = 0$  to  $z = 2.5$  for the FSRQs, assuming pure luminosity evolution. We assumed random uniformly distributed values for the viewing angle ( $\cos\theta$  distributed from 0 to 1) and power-law distributions for the Lorentz factor and the unbeamed luminosity. From these distributions we drew simulated source samples, consisting of all the sources with flux density above 1.5 Jy, which is the flux-limit of the MOJAVE survey. The number of simulated source draws was such that the final sample consisted of  $\sim 10^3$  sources. We then used the Kolmogorov-Smirnov test (K-S test) to determine the consistency of simulated and observed  $\beta_{app}$  and  $z$  distributions in order to select ranges of acceptable model parameters. The parameters we optimized are the power-law indices for the unbeamed luminosity distribution ( $A$ ) and for the Lorentz factor distribution ( $\alpha$ ), and the evolution parameter ( $\tau$ ) for the FSRQs. For the BL Lacs we only optimized for the power law indices ( $A, \alpha$ ) due to the lack of evolution in the BL Lac luminosity function (Ajello et al. 2014, Paper I). For a more detail explanation of the models, optimization techniques as well as applications see Paper I, and Liodakis & Pavlidou (2015b).

Throughout Paper I we had assumed a single spectral index for each of the BL Lac and FSRQ classes. This assumption was made for simplicity reasons, although in reality not only the spectral index is different for each source, but it is also time-variable (Angelakis et al. 2012). Since our results might be sensitive to the spectral index of each source, we need a more accurate representation than simply assuming a single spectral index for each population. For this reason, we have included a spectral index distribution for each of the blazar classes. We have incorporated a known spectral index distribution measured from observa-

<sup>3</sup> see also <http://www.aoc.nrao.edu/~cwalker/M87/>

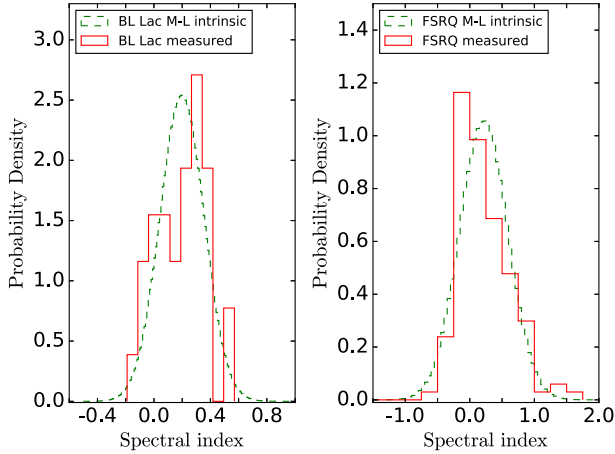


**Figure 1.** Distribution of the core spectral index. Left panel: BL Lacs; right panel: FSRQs. The red solid line is the histogram of spectral indices (Hovatta et al. 2014), whereas the green dashed line the derived distribution of the population spectral index having taken into account the error in the measurements.

tions independently (Hovatta et al. 2014, MOJAVE survey), and then re-optimized the same parameters ( $A$ ,  $\alpha$ ,  $\tau$ ) for the models as in Paper I.

## 2.1 Spectral index distribution

For our spectral index distributions we used spectral index data from the MOJAVE survey (Hovatta et al. 2014). We caution that due to the flux-density limit of the MOJAVE survey, only a small number of BL Lacs is included in the sample in comparison to FSRQs. It is possible that the BL Lac sample is a somewhat biased subsample of the class since it only includes the most luminous BL Lacs at 15 GHz. Since the radio core of the jet is dominating the emission (Lister & Homan 2005; Cooper et al. 2007), we use only the core spectral indices. Assuming that the spectral index distribution of the population is normally distributed, we estimate the mean and standard deviation of each population taking into account the errors of each measurement. In order to properly account for errors, we follow the analysis described in Venters & Pavlidou (2007). Since all the reported values have the same error, the mean of the distributions is given by:

$$s_{tr} = \frac{\sum_{j=1}^N s_j}{N}, \quad (8)$$

where  $s_{tr}$  is the true mean of the distribution, and  $s_j$  are the observed data. The standard deviation would be:

$$\sigma_{tr} = \sqrt{\frac{\sum_{j=1}^N (s_j - s_{tr})^2}{N} - \sigma_j^2}, \quad (9)$$

where  $\sigma_{tr}$  is the true standard deviation of the distribution, and  $\sigma_j$  is the reported error of each measurement. Using this method we calculated that the mean for the BL Lacs is  $s_{tr} = 0.19$  with standard deviation  $\sigma_{tr} = 0.15$  and for the FSRQs  $s_{tr} = 0.21$  with standard deviation  $\sigma_{tr} = 0.37$ . Figure 1 shows the distribution of the spectral index for the BL Lac and FSRQ populations. Simply using data from

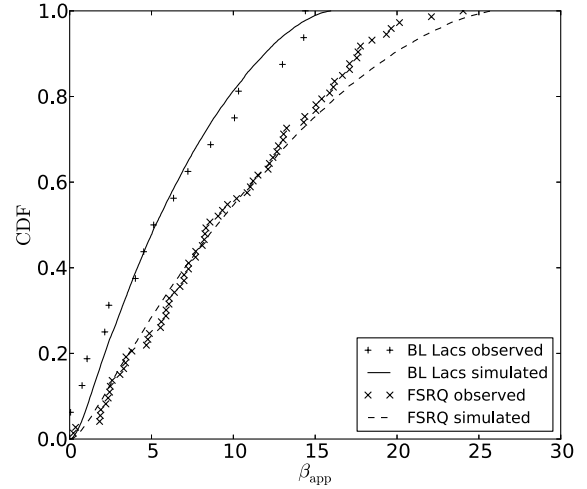


**Figure 2.** Cumulative distribution function of the apparent velocity for the BL Lacs and the FSRQs.

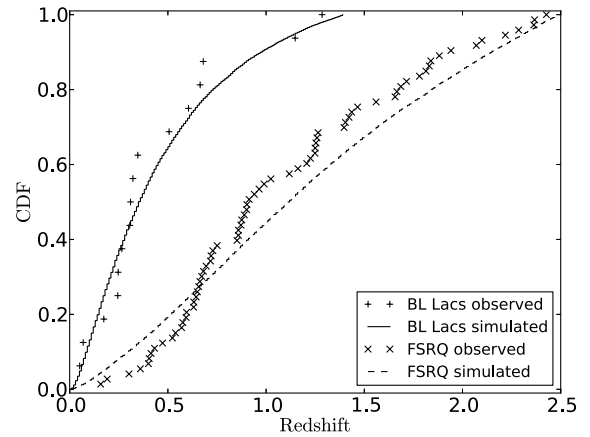


**Figure 3.** Cumulative distribution function of the redshift for the BL Lacs and the FSRQs.

the literature for this calculation without taking errors into account will overestimate the spread of the distribution.

## 2.2 A re-optimized model

In order to optimize our models, we use Monte-Carlo sampling as follows:

For each source we:

- draw a value for the viewing angle from a uniform distribution ( $\cos \theta$  uniformly distributed<sup>4</sup> between  $[0,1]$ ),
- draw a value for the bulk Lorentz factor and an unbeamed luminosity from a powerlaw distribution (Padovani & Urry 1992; Lister & Marscher 1997),

<sup>4</sup> uniformity of the cosine corresponds to the assumption of equal a priori probability to observe a given jet aligned with any line of sight, see e.g. Tassis (2007); Tassis et al. (2009)

- draw a value for the spectral index from a normal distribution with the mean and standard deviation calculated in section 2.1 for each population.

We calculate a flux-density using Eq. 3 and apply the 1.5 Jy flux-limit. When we have our final simulated sample, we construct the cumulative distribution functions for the apparent velocity and the redshift and use the Kolmogorov-Smirnov test in order to test if our model is acceptable. Following the above procedure we generate  $10^4$  samples, each time drawing a random value for the parameters uniformly. We consider a model acceptable if the joint K-S test yields a  $\geq 5\%$  probability of consistency between observed and simulated samples which is our null hypothesis.

The “best-fit” values of the model parameters as well as ranges of parameters that yield acceptable models are summarized in Table 1. We note that due to the lack of evolution in BL Lacs, the FSRQ population as a whole turns out to be considerably more luminous in our models, as is known to be the case. In addition, although all viewing angles start out equally probable, the application of a flux limit imparts a strong preference for viewing angles  $\lesssim 1/\Gamma$  (see also paper I).

For the apparent velocity the probability of consistency between observed and simulated samples using our best-fit models is 93.5% for the BL Lacs, and 81.3% for the FSRQs (Fig. 2). For the redshift, the probability values are 70.4% for the BL Lacs and 29.1% for the FSRQs (Fig. 3). Comparing this version of the model with that of Paper I, we see that the addition of the spectral index distribution resulted in small changes in the parameters and the probabilities of consistency. There is a slight flattening of the powerlaw distributions of the intrinsic luminosity for both populations, and for the Lorentz factors for the BL Lacs, whereas we see a similar steepening of the Lorentz factor distribution for the FSRQs, all within the previously reported limits of parameter values that produced acceptable models. Also the evolution parameter value for the FSRQs has a higher value, which translates into weaker evolution of the intrinsic luminosity with redshift. Moreover, the probability values of consistency between observed and simulated samples have significantly increased for all distributions except the BL Lac apparent velocity which remained at the previously high levels ( $\sim 93.5\%$ ). The probability of consistency for redshift of the BL Lacs rose from 54.1% to 70.4%. In the case of the FSRQs the probability of consistency for apparent velocities rose from 49.3% to 81.3%, and for the redshift from 8.4% to 29.1%.

An important difference between this model and other population studies of blazars is that we make no attempt to reconstruct the blazar luminosity function (we optimize a slope but not an amplitude of the luminosity distribution); this simplification allows us to forego using the flux density (beyond the application of a flux limit) as an observable, thus being much less sensitive to the effect of variability.

The sample we used for the optimization was the sample defined in Paper I. Starting from the MOJAVE sample, we had excluded all the sources with no apparent velocity and redshift measurements. The implicit assumption associated with this choice is that these sources will follow the distributions of the sources for which measurements exist. To test the validity of this assumption, we created two test-samples

(one for each population) and performed the optimization anew. In the test-samples we included all the sources with no measurements either in apparent velocity or redshift now under the assumption that sources without measurements have redshifts and apparent velocities typically higher and lower, respectively, compared to sources for which  $z$  &  $\beta_{app}$  measurements exist. If the apparent velocity was not known, we assigned that source a random value (uniformly) from 0 up to the minimum known value in the population. If the redshift was not known (occurred only in the BL Lac population), we assigned that source a random value, again uniformly, from the maximum known value in the population up to 2. Given the slope of the already known redshift distribution in our sample (Fig. 3), it is unlikely that the BL Lacs will extend to redshifts much higher than that.

In Paper I we had also excluded two sources for being outliers. One for having abnormally high mean apparent velocity ( $\beta_{app} \sim 50$ ) and one due to high redshift ( $z = 3.396$ ). In the updated online data from Lister et al. (2013) the former has now a mean apparent velocity of  $\sim 22$  which is within the limits of the original sample and it is no longer considered an outlier. Both of these sources were included in the test-samples.

We were not able to produce an acceptable model (joint K-S test  $\geq 5\%$ ) for either the BL Lac or the FSRQ populations. This fact can be interpreted in two ways: Either the models we adopt cannot adequately describe blazars, or the assumptions used to construct the test-samples were unrealistic. Given that our models are consistent with generally used assumptions regarding the blazar population, the latter possibility is preferred.

It is in principle possible that some other treatment of unknown  $z$  and  $\beta_{app}$  than the one we adopted, which however still places these quantities outside observed ranges, can produce fits. However, it is more likely that the sources without apparent velocity or redshift do not lay outside the limits of the Paper I sample but reside within. Any lack of estimates for the missing quantities is most likely due to other observational constraints such as weak emission lines in the case of  $z$ . If we consider the test-sample “fit” as indicative,  $\beta_{app}$  outside the observed range that may exist in the censored sources will drive the model towards a steeper distribution of  $\Gamma$  and a flatter distribution of luminosities.

Additionally, we performed the optimization once more for the FSRQ sample, but this time we included only the redshift outlier. The best-fit model gives a  $\sim 82\%$  probability of consistency for the apparent velocity and  $\sim 6\%$  for the redshift, producing a marginally acceptable 5% joint probability. The best-fit parameters for this model are  $\alpha = 1.57$ ,  $A = 3.41$ , and  $\tau = 0.24$ . All the parameter values are within the limits of the parameter space that produces acceptable models (section 2.2). There is a steepening of the power-law indices for the Lorentz factor distribution and luminosity function, as well as change in  $\tau$ , supporting stronger luminosity evolution. Although the probability of consistency for the apparent velocity is the same, it is not true for the redshift. There is a significant drop in the probability value, which falls even lower than the original model (Paper I).

We have limited the parameter space for the Lorentz factor power law index ( $\alpha$ ) to positive values. Negative values would imply a larger number of sources with high than with low  $\Gamma$ . Judging from the  $\beta_{app}$  distribution (Lister et al.

**Table 1.** Optimal parameter values for our population models. The asymmetrical uncertainties indicate the range within which a parameter can produce “acceptable models”. The values quoted for the spectral index are the mean and standard deviation of the population and are derived from observations independently (not through Monte-Carlo fitting), under the assumption that the spectral index is independent from other source properties.

		BL Lacs (This work)	FSRQs (This work)	BL Lacs (Paper I)	FSRQs (Paper I)
Lorentz factor	$\alpha$	$0.50^{+1.04}_{-0.5}$	$0.68^{+1.29}_{-0.68}$	$0.73^{+0.41}_{-1.46}$	$0.57^{+0.12}_{-0.50}$
Luminosity	A	$2.14^{+1.00}_{-0.76}$	$2.42^{+1.58}_{-0.52}$	$2.25^{+0.68}_{-0.78}$	$2.60^{+0.185}_{-0.245}$
	$\tau(1/H_0)$	-	$\tau = 0.29^{+0.05}_{-0.09}$	-	$0.26^{+0.068}_{-0.003}$
Spectral index	s	$0.19 \pm 0.15$	$0.21 \pm 0.37$	-	-

2009b, 2013) as well as Lorentz factor distributions from variability studies (Hovatta et al. 2009; Liidakis et al. 2016) such a scenario is unlikely. However, if we do not limit ourselves to positive values, the best-fit values do not change, but the range of parameters that produce acceptable models becomes  $\alpha$ -[1.55,1.54], A-[1.38,3.14] for the BL Lacs and  $\alpha$ -[0.14,1.97], A-[1.88,4.0],  $\tau$ -[0.19,0.34] for the FSRQs

In theory, there is the possibility of a dependence of the intrinsic luminosity to the bulk Lorentz factor which would further complicate the situation. However the ability of the model to naturally reproduce the observed 15 GHz flux-density distributions of the two populations (Paper I) gives us confidence that any effect of such a dependence would not alter our results dramatically.

### 3 DETECTABILITY OF THE COUNTER-JET

Using the optimized models obtained with the procedure described above, we will derive the ratio of the approaching and the receding jet flux densities, and the expected distribution of counter-jet flux-densities at different frequencies, assuming that the two jets are intrinsically identical. We will then attempt to establish the sensitivity required for future experiments to achieve detection of the counter-jets.

#### 3.1 Jet-to-counter-jet ratio

In order to estimate the flux-density of the counter-jet, we use the values for the velocity of jet in units of speed of light ( $\beta$ ), as well as the spectral index of each simulated source, and calculate the jet-to-counter-jet ratio using Eq.5. Figure 4 shows the distribution of the logarithm of the jet-to-counter-jet ratio ( $\log j$ ) for the BL Lac and the FSRQ population. The minimum value for the  $\log j$  is 0.03 for the BL Lacs and 0.08 for the FSRQs, whereas the maximum is  $\sim 7$  and  $\sim 10.6$  for the BL Lacs and FSRQs respectively. It is clear from Fig. 4 that the BL Lacs have smaller values of  $\log j$  than the FSRQs with a sharper distribution peaked between 4.2 and 4.9, and with a mean of  $\sim 3.9$ . The FSRQ population has a wider distribution with a peak between 5.3 and 6.4, mean at  $\sim 5.2$ , and a tail extending up to almost four orders of magnitude higher than the BL Lacs.

Figures 5 and 6 show the distribution of the jet-to-counter-jet ratio for different models for the BL Lacs and

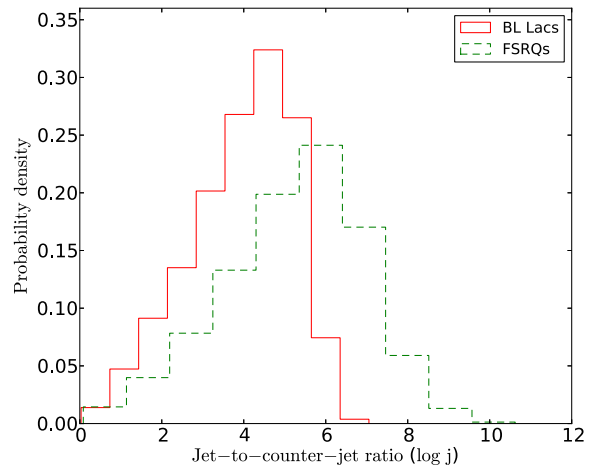


**Figure 4.** Distribution of the logarithm of the jet-to-counter-jet ratio for the BL Lacs (solid red) and the FSRQs (dashed green) for our best-fit models.

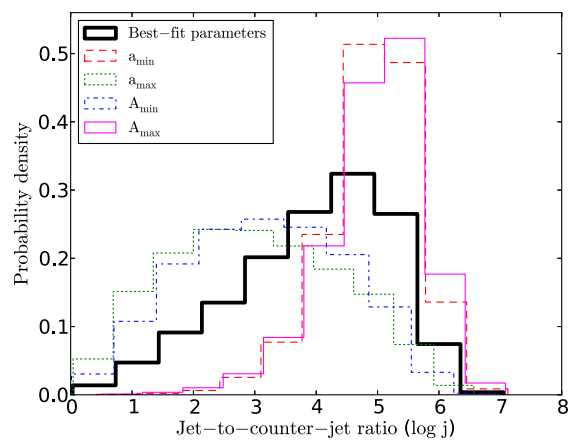


**Figure 5.** Distribution of the logarithm of the jet-to-counter-jet ratio optimal model (black solid line) and the models at the extrema of the parameter space for each parameter for the BL Lacs.

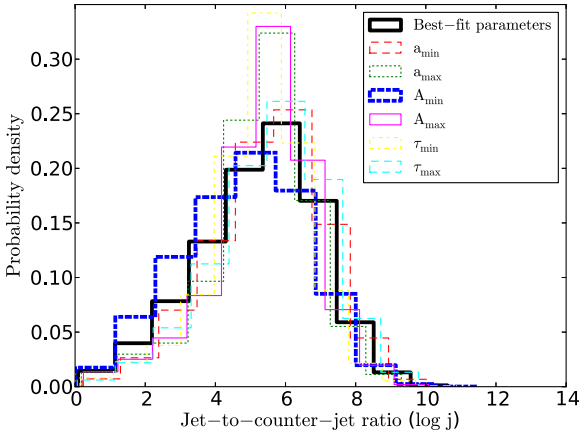


**Figure 6.** Distribution of the logarithm of the jet-to-counter-jet ratio optimal model (black solid line) and the models at the extrema of the parameter space for each parameter for the FSRQs.

FSRQs respectively. Each distribution corresponds to the resulting “acceptable” model at the extreme value of one of the parameters. Any shift in the distribution of the jet-to-counter-jet ratio will result in changes of the expected counter-jet flux density distribution and thus the number of counter-jets that could possibly be detected. In the case of the FSRQs (Fig. 6) we see little shift in the jet-to-counter-jet ratio distribution for the different models. The percentage of sources above certain flux-density values (see section 3.2) only changes by a few percent either rising or falling depending on the model. Thus our results will not be affected significantly within our parameter space. For the BL Lacs the situation is somewhat different (Fig. 5). There is a considerable shift in the distributions for the different models. Such a shift could result in changes of the fraction of detectable counter-jets up to 20-30 percentage points, depending on the parameter. The reason for this difference is that the FSRQ sample on which our model optimization is based is considerably larger than the BL Lac one, and as a result the FSRQ model parameters are better constrained.

### 3.2 Detectability limits

Our models for the blazar population do not use the flux density as an observable for the model optimization (other than as a flux limit at 15 GHz). We can however compute the predicted flux-density distributions of both jet and counter-jet at 15 GHz using our model distributions for the luminosity, Lorentz factor, redshift, and spectral index for each population, assuming random viewing angles. Figure 7 shows the 15 GHz flux density distributions for the jets of BL Lacs and FSRQs overplotted with observations. To compute the flux-density of the primary jet at frequencies other than 15 GHz, we use the spectral index for each source ( $> 10^4$  sources for each class) and equation:

$$S_n = \left( \frac{\nu_n}{\nu_m} \right)^s S_m, \quad (10)$$

where  $n$  and  $m$  indicate the frequency. Then, we use the jet-to-counter-jet ratio (Eq. 5) in order to calculate the counter-

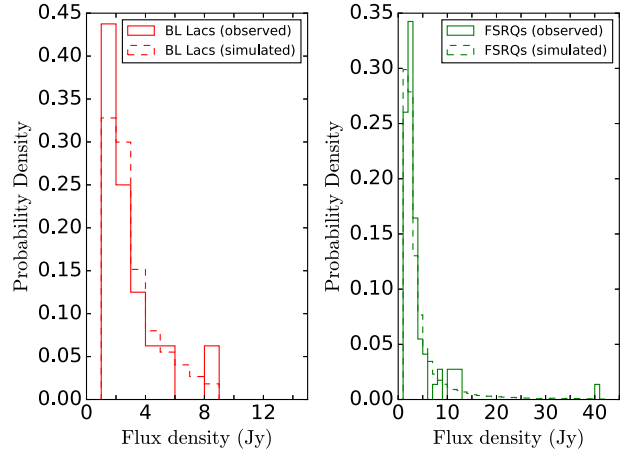


**Figure 7.** Distribution of the observed and simulated flux densities for both BL Lacs (left panel) and FSRQs (right panel). Solid red is for the observed BL Lacs, dashed red for the simulated BL Lacs, solid green is for the observed FSRQs, dashed green for the simulated FSRQs.

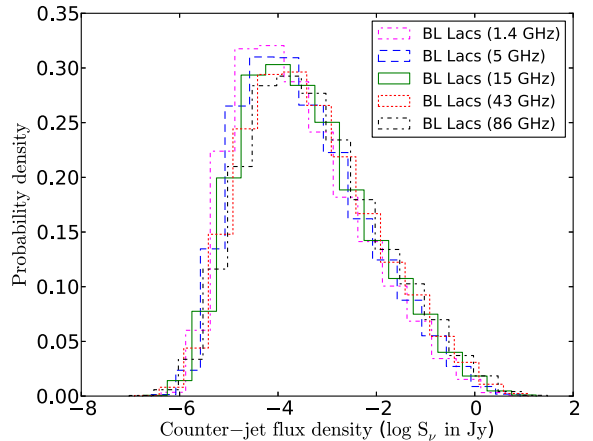


**Figure 8.** Distribution of the logarithm of the counter-jet flux density at different frequencies for the BL Lac population. Dash-dot magenta is for the 1.4 GHz, dashed blue is for the 5 GHz, solid green for the 15 GHz, dotted red for the 43 GHz, and dash-dot black for the 86 GHz.

jet flux density at different frequencies. For the present analysis, we examined four other frequencies, 1.4, 5, 43 and 86 GHz. We chose these four frequencies because they are the most widely used and/or will be used in radio interferometric experiments (e.g ALMA, SKA, VLBI) apart from 15 GHz. Figures 8 and 9 show the distribution of the counter-jet flux density for different frequencies, for the BL Lacs and FSRQs respectively. The FSRQ population has a more centrally concentrated distribution centered around lower values than that of the BL Lacs. The maximum for both populations is  $\sim 1$  Jy whereas the minimum for the BL Lacs is  $\sim 10^{-6.7}$  and for the FSRQs is  $\sim 10^{-10.2}$  Jy. The peak of the BL Lac distribution is around  $\sim 10^{-4}$  Jy whereas for the

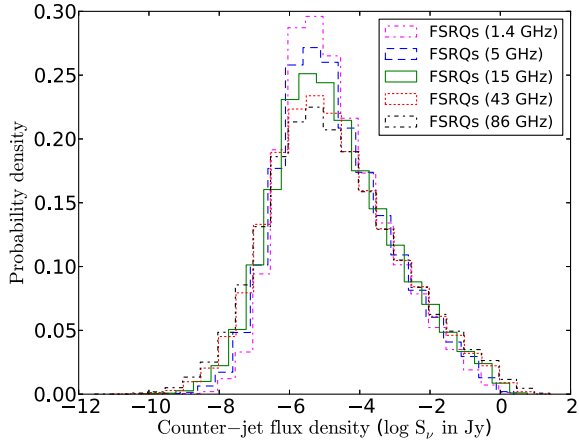


**Figure 9.** Distribution of the logarithm of the counter-jet flux density at different frequencies for the FSRQ population. Dash-dot magenta is for the 1.4 GHz, dashed blue is for the 5 GHz, solid green for the 15 GHz, dotted red for the 43 GHz, and dash-dot black for the 86 GHz.

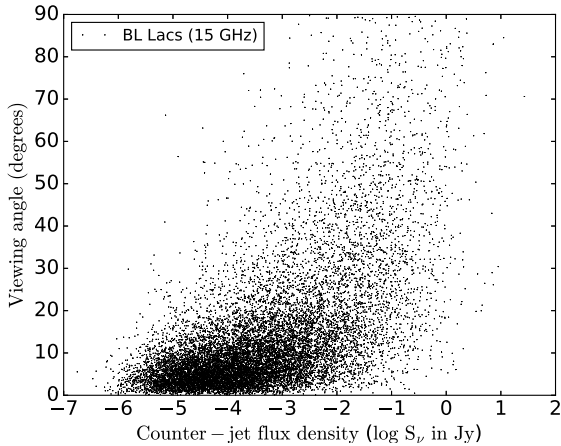


**Figure 10.** Viewing angle plotted against the counter-jet flux density at 15 GHz for the BL Lac population.

FSRQs the peak is approximately an order of magnitude lower  $\sim 10^{-5}$  Jy.

The counter-jet flux-densities can reach values as low as a few  $\mu$ Jy and even nJy. However we find that 5% of the BL Lac counter-jets have a flux-density higher than 100mJy, 15% are higher than 10 mJy, and 32% have higher flux-density than 1 mJy. For the FSRQs 8% have a flux-density higher than 10mJy, 17% are higher than 1 mJy, and 32% are higher than 0.1 mJy. Although these percentages were calculated using the 15 GHz counter-jet flux density, we find no significant change in the values quoted above for the 1.4, 5, 43, and 86 GHz flux-densities. The percentages for the 1.4 and 5 GHz flux-densities are slightly shifted to higher values whereas for the 43 and 86 GHz are shifted to lower values for the same flux-density limits set above for both populations.

In addition, we explore the connection between the

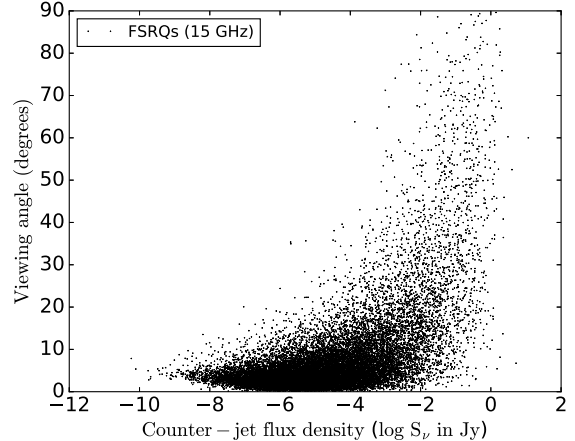


**Figure 11.** Viewing angle plotted against the counter-jet flux density at 15 GHz for the BL Lac population.

viewing angle and the predicted counter-jet flux density. Figures 10 and 11 show the viewing angle (in degrees) plotted against the counter-jet flux density (in Jy) for the BL Lacs and FSRQs respectively. The FSRQ population seem to be more concentrated on the  $\theta$ - $S_\nu$  plane than the BL Lacs. This can be attributed to the FSRQs having, on average, smaller viewing angles and faster jets. For the “typical” blazar case with viewing angle  $\leq 15^\circ$ , 68.5% of the BL Lacs and 86.2% of the FSRQs have counter-jet flux density  $\leq 1$  mJy. Although there are outliers, for the vast majority of sources in both populations there seems to be a trend where smaller viewing angle translates to fainter counter-jet.

There are also cases, especially in the BL Lac population, where sources with viewing angle larger than  $45^\circ$  have counter-jet flux densities lower than 1 mJy, suggesting that the velocity of the jet ( $\beta$ ) is high enough to conceal the receding jet even with a large viewing angle. Within the current unification scheme, BL Lac objects are the beamed counterparts of FR I galaxies, implying that the only difference between the two is the orientation of the jet to our line of sight. BL Lac objects have small viewing angles, typically  $\leq 15^\circ$ , whereas FR I galaxies have viewing angles  $\geq 30^\circ$  (Ghisellini et al. 1993). In Giommi et al. (2012) the authors find through Monte-Carlo simulation that 5% of the radio selected and 15% of the X-ray selected blazars are misclassified as radio galaxies. The BL Lac objects, in our simulated sample, with large viewing angles and one-sided jet morphology could resemble FR I galaxies. These sources, rare as they may be, could account for cases where a source is classified as a radio galaxy even though it is a blazar. Difficulties in the separation of the two classes are only in support of the unification view of FR I galaxies as the parent population of BL Lac objects.

#### 4 COUNTER JET DETECTION CANDIDATES

In order to identify the observables that could indicate a potential counter-jet detection candidate, we explored the relation between the jet-to-counter-jet ratio, the apparent velocity and the Doppler factor. Figures 12 and 13 show the

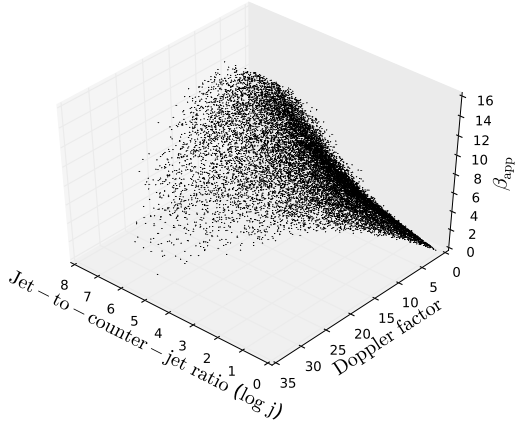


**Figure 12.** Jet-to-counter-jet ratio versus the apparent velocity and Doppler factor for the BL Lacs.

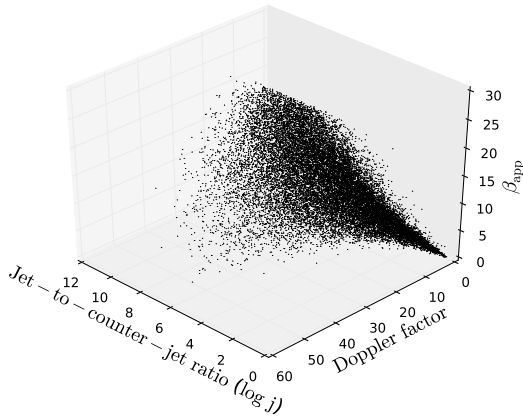


**Figure 13.** Jet-to-counter-jet ratio versus the apparent velocity and Doppler factor for the FSRQs.

3-D representation of the above observables for the BL Lacs and FSRQs respectively. Our simulations show that sources with both low apparent velocity ( $\lesssim 3$ ) and low Doppler factor ( $\lesssim 5$ ) have typically jet-to-counter-jet ratios  $\lesssim 10^4$  which makes them prime detection candidates. Although we found no trend favoring specific redshift ranges, it is obvious that sources at lower redshifts are favored in terms of spatial resolution.

For specific sources if both  $\beta_{app}$  and Doppler factor are known, then  $\Gamma$  (and therefore  $\beta$ ) and  $\theta$  can be derived. If the spectral index ( $s$ ) is also known, then the jet-to-counter-jet ratio can be calculated. Due to the MOJAVE survey (Lister & Homan 2005), accurate estimates for the apparent velocity exist for more than 100 sources. On the other hand, not all Doppler factor estimates are reliable. We have shown in Liodakis & Pavlidou (2015b) that the variability Doppler factors (Lähteenmäki & Valtaoja 1999; Hovatta et al. 2009) can adequately describe both the BL Lac and FSRQs populations. An error analysis showed that the variability esti-

mates are subject to systematic errors due to the cadence of observations. However, for low Doppler factors ( $\lesssim 5$ ) the uncertainty of the estimates is dominated by statistical uncertainties, on average 30% (Liodakis & Pavlidou 2015b). Thus we took to the literature to identify potential candidates that meet the above criteria. We found five such sources, for which we used data from Lister et al. (2013) for the apparent velocity, Hovatta et al. (2009) and Liodakis et al. (2016) for the Doppler factors, Hovatta et al. (2014) for the core spectral index, and Lister & Homan (2005); Lister et al. (2016) for the mean 15 GHz core flux density, in order to calculate the jet-to-counter-jet ratio and the expected counter-jet flux density at 15 GHz. All five sources as well as the relevant parameters are summarized in Table 2. All of the sources have, as expected,  $\log j \leq 4$  with counter-jet flux-densities from a few mJy to  $\sim 50$  mJy which is within the capabilities of current operating arrays (see section 5). Since all of the sources happen to reside at low redshift, they are, by our definition, excellent candidates for counter-jet detection. It has to be noted that attempts to detect a counter-jet have already been made for some of these sources. For example, in Mrk 421 (Lico et al. 2012) using as an upper limit the  $3\sigma$  rms noise of their images, the authors derived a  $\log j > 2.4$ . Their analysis lead to a Doppler factor of  $D = 3.2$  which is almost a factor of two larger than the value reported in Table 2. However, as we discuss in section 5.2, free-free absorption effects can significantly reduce the flux of the counter-jet which would lead to the overestimation of the Doppler factor. Another example is OW 637 (Conway et al. 1994). The authors find in their VLBI maps a diffuse “tail” seen at 1.7 GHz, and discuss the possibility of that tail being the counter-jet. If this is indeed the case, their estimate for the jet-to-counter-jet ratio is  $\log j = 1.3$ , which is consistent with the value reported in Table 2 within the error of the Doppler factor estimate.

## 5 DISCUSSION & CONCLUSIONS

Following the procedure described in Paper I we have re-optimized models for the blazar population by including a spectral index distribution. Using data from Hovatta et al. (2014) and the method in Venters & Pavlidou (2007) we calculated the mean and standard deviation for the core spectral index distribution for the BL Lacs and the FSRQs, which we included in our models, accounting for the errors in the measurements.

Including a spectral index distribution for each model led to more realistic models consistent with observations, while maintaining consistency with the previous versions of these models. Especially in the case of the FSRQs, which is the largest sample of the two populations, there was a significant increase in the probability values of consistency between observed and simulated samples. Thus, although very simple, our model appears to be able to adequately describe basic features of the blazar population, being based on samples selected with unbiased statistical criteria, and reliable observables.

With the use of our optimized models, we calculated the jet-to-counter-jet ratio (Eq. 5), and the predicted flux-density of the counter-jets in different frequencies using Eq. 10. There are no significant differences in the distributions

**Table 2.** Counter-jet detection candidates that meet the criteria set in section 4. Column (1): Name; (2): Redshift; (3): Doppler factor (Hovatta et al. 2009; Lioudakis et al. 2016); (4): mean apparent velocity (Lister et al. 2013); (5): viewing angle (degrees); (6): core spectral index (Hovatta et al. 2014); (7): logarithm of the jet-to-counter-jet ratio; (8): mean core 15 GHz flux density (in Janskys)(Lister et al. 2016); and (9): expected counter-jet 15 GHz flux density (in milli-Janskys).

Name	$z$	Doppler factor	$\beta_{app}$	$\theta(\text{deg.})$	$s$	$\log j$	$S_{15}$ (mJy)	$S_{15,counter}$ (mJy)
PKS0735+17	0.42	4.5	3.3	15.1	0.05	2.93	490	0.6
4C39.25	0.69	4.3	1.45	8.4	0.09	2.50	170	0.5
Mrk 421	0.03	1.7	0.14	8.6	0.05	0.90	288	52.2
OW 637	0.22	2.1	0.17	5.7	-0.29	1.48	1410	40.0
PKS2254+074	0.19	2.5	0.38	8.0	0.26	1.40	270	10.0

between frequencies for either population, due to the flatness of the assumed spectral index distribution for both the BL Lacs and the FSRQs. The mode of the distribution was at  $\sim 10^{-4}$  Jy for the BL Lacs and  $\sim 10^{-5}$  Jy for the FSRQs. We also found that the majority of sources' counter-jets have flux-densities  $\leq 1$  mJy for both populations. In particular 68% of the BL Lacs and 83% of FSRQs have counter-jet flux densities lower than 1 mJy. Thus a sensitivity of at least 1 mJy is required in order to have any chance of detecting a significant number of counter-jets. Previous surveys with radio interferometers have reported sensitivities from a few tens of mJy to a few mJy, with the most sensitive one being the VLA FIRST with a sensitivity of 1 mJy at 1.4 GHz (Helfand et al. 2015). Current arrays, like the Atacama Large Millimeter Array (ALMA)<sup>5</sup> have reported sensitivities of some tens to hundred  $\mu\text{Jy}$  (Brown et al. 2004; Leon et al. 2015) that will allow them to detect  $>63\%$  of BL Lac and  $>31\%$  of FSRQ counter-jets. Newly operating like e-MERLIN<sup>6</sup> and JVLA<sup>7</sup> as well as future telescopes, like the Square Kilometer Array (SKA, Taylor 2008)<sup>8</sup> are expected to reach as low as 1  $\mu\text{Jy}$ . With such high sensitivity, the aforementioned interferometers may be able to detect  $>99\%$  of the BL Lac and  $>77\%$  of the FSRQ counter-jets.

In this work, we made an attempt to set the theoretical limits required from future telescope arrays, as well as upgrades of the current running programs, in order to achieve detection of the blazar counter-jets. We found that even though previous experiments are not sensitive enough, newly operating and future telescopes like ALMA, e-MERLIN, and SKA may be able to detect the majority of the counter-jets for both the BL Lac and FSRQ populations. In reality, the problem at hand is far more complex since other factors may play a significant part. Factors such as weather conditions, atmospheric turbulence, noise, as well as instrumental effects can push these limits to even lower values.

### 5.1 Detectability and angular resolution

Besides sensitivity, the angular resolution of observations and the spatial distribution of counter-jet flux can also affect detectability. In our models, we have implicitly assumed that the compact core dominates the overall emission (Lister & Homan 2005; Cooper et al. 2007). Although

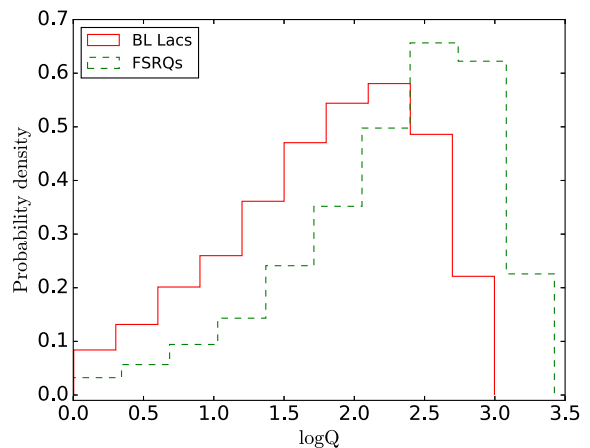


**Figure 14.** Distribution of the ratio of the apparent jet-to-counter-jet length (projected). Solid red is for BL Lacs and dashed green for the FSRQs.

our models have no knowledge of jet structure and dynamics, we can calculate the relativistic effects which will influence them. Due to relativistic effects, the counter-jet will appear shorter than the approaching jet (projected, Longair & Riley 1979). This effect as well as gravitational lensing should be taken into account when attempting to localize the supermassive black hole. The ratio ( $Q$ ) of the two lengths is given by,

$$Q = \frac{l_{jet}}{l_{counter}} = \frac{1 + \beta \cos \theta}{1 - \beta \cos \theta}. \quad (11)$$

Figure 14 shows the distribution of  $Q$  for BL Lacs and FSRQs. If we assume that the core lies at a distance of  $10^5$  Schwarzschild radii ( $R_s$ ) (Marscher et al. 2008), and we take  $10^{8.5} M_\odot$  as a typical black hole mass (Shaw et al. 2012) this translates to a distance of  $\sim 3$  pc (de-projected). Using redshift and the viewing angle, we can project the distance and calculate the expected distribution of the angular separation of core and counter-core (Fig. 15). Assuming that the average resolution of the 15 GHz MOJAVE maps is  $\sim 0.5$  mas, even with enough sensitivity only  $\sim 15\%$  of BL Lacs and  $\sim 3\%$  of FSRQs counter-jets will be detectable. Observations at higher frequencies will provide higher resolution and thus will be able to detect more counter-jets, but on the expense of sensitivity (Lister et al. 2009a). For example  $\sim 0.2$  mas resolution at 43 GHz (Jorstad et al. 2005; Boccardi et al. 2016a) increases the number of detectable

<sup>5</sup> <http://www.almaobservatory.org/>

<sup>6</sup> <http://www.e-merlin.ac.uk/>

<sup>7</sup> <https://science.nrao.edu/facilities/vla/other/publ/PrincetonFinal.pdf>

<sup>8</sup> <https://www.skatelescope.org/>

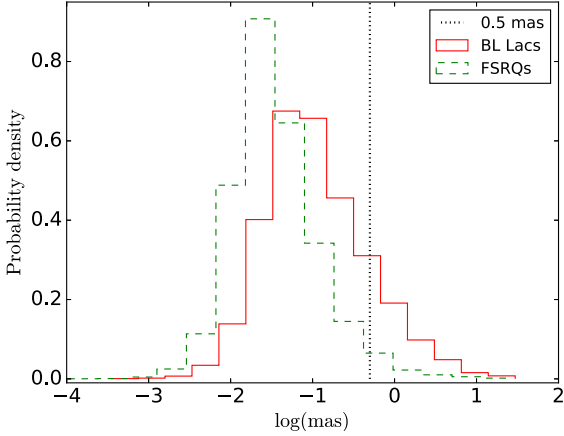


**Figure 15.** Distribution of the milli-arcsecond separation of the core and counter-core. Solid red is for BL Lacs and dashed green for the FSRQs. The black dotted line marks 0.5 mas.

counter-jets to  $\sim 30\%$  for the BL Lacs and  $\sim 8\%$  for the FSRQs. However, more recent estimates for the distance of the radio core from the supermassive black hole place it at  $< 10^3 R_s$  (Baczko et al. 2016; Boccardi et al. 2016b) for NGC1052 and CygA or even a few tens of  $R_s$  (Hada et al. 2011) for M87. If this is generally the case for the majority of sources, detection of blazar counter-cores at 15 GHz would not be feasible. It is however promising that, at least in the case of 3C 84, a counter-jet structure can be identified both in 43 GHz and 15 GHz data (see Fujita & Nagai 2016).

If in addition a significant fraction of the flux we have calculated is distributed in extended collimated emission rather than the counter-core, this will also affect detectability due to the low surface brightness of such features. If the intensity of a source follows an power-law profile ( $I_\nu \propto \Phi^{-k}$  Bicknell (1983); Zaninetti (2009), where  $\Phi$  is the synchrotron FWHM, Bridle & Perley 1984), depending on how fast the profile falls to zero will affect the percentages of counter-jet detections (given a certain sensitivity). Although the profile of the jet will be boosted, the profile of the counter-jet will be de-boosted by  $D'$  to lower values. Shallow profiles (small  $k$ ) will spatially spread the flux-density of jet and counter-jet (always under the assumption that both jets are identical) lowering the flux-density of the counter-core and increasing the sensitivity demands.

## 5.2 Other detectability issues and interpretation constraints

An additional constrain could be bends in either the approaching or receding jets that can severely hamper any attempts to detect a counter-jet, since changes in the viewing angle and the orientation of the jet will affect the beaming properties, as well as spatially conceal it from the observer (Homan et al. 2002).

Another major constrain in both the detection of a counter-jet and interpretation of the jet-to-counter-jet ratio is free-free absorption. As was shown for 3C84 in Vermeulen et al. (1994), free-free absorption by ionized,

toroidal or disklike material around the black hole may obscure the deboosted emission from the counter-jet. How much free-free absorption may reduce the counter-jet flux density depends on several factors, such as observing frequency, viewing angle and the geometry of the ionized region. A strongly inverted spectrum that cannot be explained in the context of synchrotron self-absorption (Vermeulen et al. 1994) and multi-wavelength observations (Vermeulen et al. 1994; Taylor & Vermeulen 1996) should reveal the presence of free-free absorption effects. Regarding the viewing angle, the effects might be less significant for small angles to the line of sight (as is the case for blazars) in comparison to larger viewing angles. For small column densities through the ionized material Doppler deboosting will still dominate the flux reduction.

For the case of 3C84, more recent estimates of the apparent velocity of the jet, as well as new estimates of the variability Doppler factor are now available. It is therefore interesting to revisit the expected counter-jet flux for the source before free-free absorption is accounted for, and compare it with the 1994 detection by Vermeulen et al. (1994). We use the variability Doppler factor of Hovatta et al. (2009) ( $D = 0.3$ ) and the mean apparent velocity of Lister et al. (2013) ( $\beta_{app} = 0.219$ ). From these values, the jet velocity is estimated to be  $\beta = 0.85$  and the viewing angle  $\theta = 27^\circ$ , which are consistent with the ones derived through SED fitting in Abdo et al. (2009) ( $\beta = 0.83$  and  $\theta = 25^\circ$ ). Using the core spectral index  $s = 0.48$  (Hovatta et al. 2014), the jet-to-counter-jet ratio is  $j = 20.0$ , larger than the one reported in Vermeulen et al. (1994) who observed  $j \sim 9$ . Since free-free absorption acts in the direction of reducing the counter-jet flux thus increasing the jet-to-counter-jet ratio, this result if anything indicates that the  $j = 20$  estimate, even with the latest measurements, involves significant uncertainties. Using error propagation and assuming the error of the Doppler factor to be 30% (average error derived through population modeling in Liodakis & Pavlidou 2015b) as well as all errors in the spectral index and apparent velocity, we find that  $j = 20.0 \pm 12.0$ .

This value is in agreement with the Vermeulen et al. (1994) measurement, and allows for “intrinsic” (i.e., without free-free absorption) values which are smaller than the observed one. It also allows for a scenario where Doppler deboosting is likely the dominant factor in the flux contrast between jet and counter-jet, with free-free absorption having a significant effect on the counter-jet spectrum and only a modest effect on the overall counter-jet flux compared to relativistic effects. However, if we use the  $\beta_{app} = 0.47$  estimate from Suzuki et al. (2012) we find that  $j = 5.9$ , which is consistent with the scenario discussed by Vermeulen et al. (1994) where free-free absorption has a significant contribution to the counter-jet flux reduction.

Interestingly, a counter jet component is still visible in 3C 84 in newer (2016) data from MOJAVE and the Boston University blazar monitoring program, with large counter-jet ratios in both 43 GHz and 15 GHz, supporting the scenario of free-free absorption increasing the observed value of  $j$  compared to its intrinsic (Doppler-only) one (Fujita & Nagai 2016). That work demonstrates how detailed, multi-frequency observations of counter-jets can in fact be used to probe the ambient gas density taking advantage of the presence of free-free absorption.

Similarly a comparison between the observed and predicted jet-to-counter-jet ratio can quantify the effects of free-free absorption. Multi-frequency observations and more accurate variability Doppler factor estimates (16% error on average, [Liodakis et al. 2016](#)) can in turn constrain composition, density, temperature and geometry of the ionized material causing the absorption.

Working in the opposite direction than the effects discussed above, gravitational lensing can enhance the flux from the counter-jet ([Bao & Wiita 1997](#)). A small viewing angle and high Lorentz factor can decrease the jet-to-counter-jet ratio up to two orders of magnitude ([Bao & Wiita 1997](#)). The consequence of this effect would also be the displacement of the counter-jet position, causing an apparent asymmetry of the jets in that source. This effect that needs to be taken into account, especially when trying to localize the supermassive black hole between jet and counter-jet.

In spite of these considerations, our results indicate that detecting a significant number of blazar counter jets will soon be within reach. This will provide an unprecedented and independent way of probing jet structure and dynamics, and will undoubtedly expand our understanding of the physical processes in blazars. At minimum, it will offer an independent observable that can be used to improve population models of blazars.

## ACKNOWLEDGMENTS

The authors would like to thank the anonymous referee, Tony Readhead, Tim Pearson, Craig Walker, Talvikki Hovatta, and Bia Boccardi for comments and suggestions that helped improve this work. This research was supported by the “Aristeia” Action of the “Operational Program Education and Lifelong Learning” and is co-funded by the European Social Fund (ESF) and Greek National Resources, and by the European Commission Seventh Framework Program (FP7) through grants PCIG10-GA-2011-304001 “Jet-Pop” and PIRSES-GA-2012-31578 “EuroCal”. This research has made use of data from the MOJAVE database that is maintained by the MOJAVE team ([Lister et al. 2009b](#))

## REFERENCES

- Abdo A. A., et al., 2009, *ApJ*, **699**, 31  
 Abdo A. A., et al., 2010, *Nature*, **463**, 919  
 Ajello M., et al., 2014, *ApJ*, **780**, 73  
 Angelakis E., et al., 2012, *Journal of Physics Conference Series*, **372**, 012007  
 Angelakis E., et al., 2016, *MNRAS*,  
 Antonucci R. R. J., Miller J. S., 1985, *ApJ*, **297**, 621  
 Arp H. C., 1967, *Astrophys. Lett.*, **1**, 1  
 Baczkó A.-K., et al., 2016, preprint, ([arXiv:1605.07100](#))  
 Bao G., Wiita P. J., 1997, *ApJ*, **485**, 136  
 Bicknell G. V., 1983, *Proceedings of the Astronomical Society of Australia*, **5**, 130  
 Blandford R. D., Königl A., 1979, *ApJ*, **232**, 34  
 Blandford R. D., Rees M. J., 1974, *MNRAS*, **169**, 395  
 Blinov D., et al., 2015, *MNRAS*, **453**, 1669  
 Blinov D., et al., 2016a, *MNRAS*, **457**, 2252  
 Blinov D., et al., 2016b, *MNRAS*, **462**, 1775  
 Boccardi B., Krichbaum T. P., Bach U., Mertens F., Ros E., Alef W., Zensus J. A., 2016a, *A&A*, **585**, A33  
 Boccardi B., Krichbaum T. P., Bach U., Bremer M., Zensus J. A., 2016b, *A&A*, **588**, L9  
 Bondi M., et al., 1996, *A&A*, **308**, 415  
 Bridle A. H., Perley R. A., 1984, *ARA&A*, **22**, 319  
 Brown R. L., Wild W., Cunningham C., 2004, *Advances in Space Research*, **34**, 555  
 Cohen M. H., Pearson T. J., Readhead A. C. S., Seielstad G. A., Simon R. S., Walker R. C., 1979, *ApJ*, **231**, 293  
 Conway J. E., Myers S. T., Pearson T. J., Readhead A. C. S., Unwin S. C., Xu W., 1994, *ApJ*, **425**, 568  
 Cooper N. J., Lister M. L., Kochanzyk M. D., 2007, *The Astrophysical Journal Supplement Series*, **171**, 376  
 Fey A. L., Charlot P., 1997, *ApJS*, **111**, 95  
 Fuhrmann L., et al., 2014, *MNRAS*, **441**, 1899  
 Fujita Y., Nagai H., 2016, preprint, ([arXiv:1609.04017](#))  
 Ghisellini G., Padovani P., Celotti A., Maraschi L., 1993, *ApJ*, **407**, 65  
 Giommi P., Padovani P., Polenta G., Turriziani S., D’Elia V., Piranomonte S., 2012, *MNRAS*, **420**, 2899  
 Giovannini G., Giroletti M., Taylor G. B., 2008, in Rector T. A., De Young D. S., eds, *Astronomical Society of the Pacific Conference Series Vol. 386, Extragalactic Jets: Theory and Observation from Radio to Gamma Ray*. p. 256 ([arXiv:0708.3911](#))  
 Giroletti M., Giovannini G., Taylor G. B., Falomo R., 2004, *ApJ*, **613**, 752  
 Giroletti M., Giovannini G., Cotton W. D., Taylor G. B., Pérez-Torres M. A., Chiaberge M., Edwards P. G., 2008, *A&A*, **488**, 905  
 Hada K., Doi A., Kino M., Nagai H., Hagiwara Y., Kawaguchi N., 2011, *Nature*, **477**, 185  
 Haga T., Doi A., Murata Y., Sudou H., Kameno S., Hada K., Nagai H., 2013, in *European Physical Journal Web of Conferences*. p. 08004, [doi:10.1051/epjconf/20136108004](#)  
 Haga T., Doi A., Murata Y., Sudou H., Kameno S., Hada K., 2015, *ApJ*, **807**, 15  
 Helfand D. J., White R. L., Becker R. H., 2015, *ApJ*, **801**, 26  
 Homan D. C., Ojha R., Wardle J. F. C., Roberts D. H., Aller M. F., Aller H. D., Hughes P. A., 2001, *ApJ*, **549**, 840  
 Homan D. C., Wardle J. F. C., Cheung C. C., Roberts D. H., Attridge J. M., 2002, *ApJ*, **580**, 742  
 Hovatta T., Valtaoja E., Tornikoski M., Lähteenmäki A., 2009, *A&A*, **494**, 527  
 Hovatta T., Tammi J., Tornikoski M., Valtaoja E., Torrealba J., Chavushyan V., Arshakian T. G., Cruz-Gonzales I., 2010, in Maraschi L., Ghisellini G., Della Ceca R., Tavecchio F., eds, *Astronomical Society of the Pacific Conference Series Vol. 427, Accretion and Ejection in AGN: a Global View*. p. 34  
 Hovatta T., et al., 2014, *AJ*, **147**, 143  
 Jorstad S. G., Marscher A. P., Mattox J. R., Wehrle A. E., Bloom S. D., Yurchenko A. V., 2001, *ApJS*, **134**, 181  
 Jorstad S. G., et al., 2005, *AJ*, **130**, 1418  
 Jorstad S. G., et al., 2006, in Miller H. R., Marshall K., Webb J. R., Aller M. F., eds, *Astronomical Society of the Pacific Conference Series Vol. 350, Blazar Variability Workshop II: Entering the GLAST Era*. p. 149  
 Kellermann K. I., Vermeulen R. C., Zensus J. A., Cohen M. H., 1998, *AJ*, **115**, 1295  
 Komatsu E., et al., 2009, *ApJS*, **180**, 330  
 Kovalev Y. Y., Lister M. L., Homan D. C., Kellermann K. I., 2007, *ApJ*, **668**, L27  
 Lähteenmäki A., Valtaoja E., 1999, *ApJ*, **521**, 493  
 Leon S., Cortes P. C., Guerard M., Villard E., Hidayat T., Ocana Flaquer B., Vila-Vilaro B., 2015, preprint, ([arXiv:1510.07536](#))  
 Lico R., et al., 2012, *A&A*, **545**, A117  
 Liodakis I., Pavlidou V., 2015a, *MNRAS*, **451**, 2434

- Lioudakis I., Pavlidou V., 2015b, *MNRAS*, **454**, 1767
- Lioudakis I., et al., 2016, *MNRAS* submitted
- Lister M. L., Homan D. C., 2005, *AJ*, **130**, 1389
- Lister M. L., Marscher A. P., 1997, *ApJ*, **476**, 572
- Lister M. L., Kellermann K. I., Vermeulen R. C., Cohen M. H., Zensus J. A., Ros E., 2003, *ApJ*, **584**, 135
- Lister M. L., et al., 2009a, *AJ*, **137**, 3718
- Lister M. L., et al., 2009b, *AJ*, **138**, 1874
- Lister M. L., et al., 2011, *ApJ*, **742**, 27
- Lister M. L., et al., 2013, *AJ*, **146**, 120
- Lister M. L., et al., 2016, preprint, ([arXiv:1603.03882](https://arxiv.org/abs/1603.03882))
- Longair M. S., Riley J. M., 1979, *MNRAS*, **188**, 625
- Marscher A. P., et al., 2008, *Nature*, **452**, 966
- Max-Moerbeck W., et al., 2014, *MNRAS*, **445**, 428
- O’Dea C. P., Barvainis R., Challis P. M., 1988, *AJ*, **96**, 435
- Padovani P., Urry C. M., 1992, *ApJ*, **387**, 449
- Pearson T. J., Unwin S. C., Cohen M. H., Linfield R. P., Readhead A. C. S., Seielstad G. A., Simon R. S., Walker R. C., 1981, *Nature*, **290**, 365
- Readhead A. C. S., 1980a, *Phys. Scr.*, **21**, 662
- Readhead A. C. S., 1980b, in Abell G. O., Peebles P. J. E., eds, *IAU Symposium Vol. 92, Objects of High Redshift*. pp 165–175
- Readhead A. C. S., Cohen M. H., Blandford R. D., 1978a, *Nature*, **272**, 131
- Readhead A. C. S., Cohen M. H., Pearson T. J., Wilkinson P. N., 1978b, *Nature*, **276**, 768
- Rees M. J., 1966, *Nature*, **211**, 468
- Rees M. J., 1967, *MNRAS*, **135**, 345
- Scheuer P. A. G., 1974, *MNRAS*, **166**, 513
- Scheuer P. A. G., Readhead A. C. S., 1979, *Nature*, **277**, 182
- Shaw M. S., et al., 2012, *ApJ*, **748**, 49
- Sparks W. B., Fraix-Burnet D., Macchetto F., Owen F. N., 1992, *Nature*, **355**, 804
- Suzuki K., et al., 2012, *ApJ*, **746**, 140
- Tassis K., 2007, *MNRAS*, **379**, L50
- Tassis K., Dowell C. D., Hildebrand R. H., Kirby L., Vaillancourt J. E., 2009, *MNRAS*, **399**, 1681
- Taylor A. R., 2008, in Jin W. J., Platais I., Perryman M. A. C., eds, *IAU Symposium Vol. 248, IAU Symposium*. pp 164–169, [doi:10.1017/S1743921308018954](https://doi.org/10.1017/S1743921308018954)
- Taylor G. B., Vermeulen R. C., 1996, *ApJ*, **457**, L69
- Venters T. M., Pavlidou V., 2007, *ApJ*, **666**, 128
- Vermeulen R. C., Cohen M. H., 1994, *ApJ*, **430**, 467
- Vermeulen R. C., Readhead A. C. S., Backer D. C., 1994, *ApJ*, **430**, L41
- Wardle J. F. C., Homan D. C., Cheung C. C., Roberts D. H., 2005, in Romney J., Reid M., eds, *Astronomical Society of the Pacific Conference Series Vol. 340, Future Directions in High Resolution Astronomy*. p. 67
- Zaninetti L., 2009, *Rev. Mex. Astron. Astrofis.*, **45**, 25

# Estimating the distribution of rest-frame timescales for blazar jets: a statistical approach.

I. Liodakis<sup>1,2\*</sup>, D. Blinov<sup>1,2,3</sup>, I. Papadakis<sup>1,2</sup> and V. Pavlidou<sup>1,2</sup>

<sup>1</sup>*Department of Physics and ITCP<sup>†</sup>, University of Crete, 71003, Heraklion, Greece*

<sup>2</sup>*Foundation for Research and Technology - Hellas, IESL, Voutes, 7110 Heraklion, Greece*

<sup>3</sup>*Astronomical Institute, St. Petersburg State University, Universitetsky pr. 28, Petrodvoretz, 198504 St. Petersburg, Russia*

29 November 2016

## ABSTRACT

In any flux-density limited sample of blazars, the distribution of the timescale modulation factor  $\Delta t'/\Delta t$ , which quantifies the change in observed timescales compared to the rest-frame ones due to redshift and relativistic compression follows an exponential distribution with a mean depending on the flux limit of the sample. In this work we produce the mathematical formalism that allows us to use this information in order to uncover the underlining rest-frame probability density function of measurable timescales of blazar jets. We extensively test our proposed methodology using a simulated FSRQ population with a 1.5 Jy flux-density limit in the simple case (where all blazars share the same intrinsic timescale), in order to identify limits of applicability and potential biases due to observational systematics and sample selection. We find that for monitoring with time intervals between observations longer than  $\sim 30\%$  of the intrinsic timescale under investigation the method loses its ability to produce robust results. For time intervals of  $\sim 3\%$  of the intrinsic timescale the error of the method is as low as 1% in recovering the intrinsic rest-frame timescale. We applied our method to rotations of the optical polarization angle of blazars observed by RoboPol. We found that the intrinsic timescales of the longest-duration rotation event in each blazar follows a narrow distribution, well-described by a normal distribution with mean 87 days and standard deviation 5 days. We discuss possible interpretations of this result.

**Key words:** galaxies: active – galaxies: jets – galaxies: blazars

## 1 INTRODUCTION

Blazars are among the most active of galaxies. Their jets are known to show unique properties, such as superluminal motion, boosted emission, and high variability throughout the entire electromagnetic spectrum from  $\gamma$ -rays to radio. These unique properties are attributed to the preferential alignment of their jet (Readhead et al. 1978; Blandford & Königl 1979; Scheuer & Readhead 1979; Readhead 1980). Due to beaming, small differences in the rest frame result in large scatter of observables, hampering phenomenological studies and dispersing correlations and behavior trends. This also constitutes the reason why there are still many open questions regarding blazars, despite many years of systematic study. Even today very little is known about blazar proper-

ties in their rest frame. In this work we focus on studies of blazar jets in the time domain.

Timescales in blazars are compressed due to Doppler boosting, but are also elongated due to the expansion of the Universe. This distortion is quantifiable by the timescale modulation factor  $m$ ,

$$m = \frac{\Delta t'}{\Delta t} = \frac{1+z}{D}, \quad (1)$$

where  $\Delta t'$  is the timescale in the observer's frame,  $\Delta t$  is the timescale in the rest frame of the jet,  $z$  is the redshift and  $D = \sqrt{1-\beta^2}/(1-\beta\cos\theta_j)$  is the Doppler factor, where  $\theta_j$  is the angle to the line of sight, and  $\beta$  the velocity of the jet in units of speed of light. Even though redshift is, in most cases, a well measured quantity, measuring the amount of boosting in a jet is not straight forward (Liodakis & Pavlidou 2015b). Although several methods have been proposed (e.g. Ghisellini et al. 1993; Readhead 1994; Lähteenmäki & Valtaoja 1999; Liodakis et al. 2016a), the amount of available data in the literature is limited, making a more broad statistical study of timescales unfeasible. In

\* liodakis@physics.uoc.gr

† Institute for Theoretical and Computational Physics, formerly Institute for Plasma Physics

addition, current Doppler factor estimates involve large uncertainties (Liodakis & Pavlidou 2015b), so “correcting” the measured timescales on a source-by-source basis using available Doppler factor estimates may in fact introduce even more dispersion in the distribution of observables. In order to overcome such limitations, we are proposing a methodology that can estimate the effect of boosting at a population level by using the Doppler factor distribution in flux-density limited samples predicted by blazar population models.

Information on rest-frame characteristic timescales can provide important information on blazar jets and their emission processes. For example rest-frame time delays between different frequencies are indicative of the distance between different emission regions (Fuhrmann et al. 2014; Max-Moerbeck et al. 2014). Rest-frame durations of flares can test different models of the evolution of jet disturbances (Hovatta et al. 2007, 2008, 2009). Rest-frame durations of EVPA rotations can help us distinguish between mechanisms proposed to interpret them (Blinov et al. 2015, 2016a,b).

This paper is organized as follows. In §2 we describe our model for the blazar population. In §3 we present our mathematical formalism for uncovering the probability density function of rest-frame timescales. In §4 we benchmark our method with respect to the time interval between observations and sample size. In §5 we apply our method to timescales associated with EVPA rotations as seen by the RoboPol survey as well as possible interpretations of the results, and in §6 the conclusions derived from this work.

The cosmology we have adopted throughout this work is  $H_0 = 71 \text{ km s}^{-1} \text{ Mpc}^{-1}$ ,  $\Omega_m = 0.27$  and  $\Omega_\Lambda = 1 - \Omega_m$  (Komatsu et al. 2009).

## 2 BLAZAR POPULATION MODEL

Although blazars exhibit very diverse behavior on a source-by-source basis, they can be statistically treated as a population of relativistically boosted sources with relatively simple (power-law) distributions of rest-frame properties (luminosities and Lorentz factors) viewed at random angles. Typically such population models (see e.g. Urry & Padovani 1991; Padovani & Urry 1992; Vermeulen & Cohen 1994; Lister & Marscher 1997) are developed to fit the observed luminosity and flux-density distributions.

However, because blazars are known to show high variability throughout the electromagnetic spectrum, single-epoch flux densities can be unreliable observables. For this reason, in a recent work we used observables that are not as affected by variability: the observed apparent velocity and redshift distributions of the MOJAVE<sup>1</sup> sample (Lister & Homan 2005; Lister et al. 2009, 2013). MOJAVE uses a statistically complete flux-density limited sample, selected at 15 GHz (Lister & Homan 2005), ideal for population studies of blazars. Below we present a summary of the our population models (Liodakis & Pavlidou 2015a, hereafter Paper I, Liodakis et al. 2016b, hereafter Paper II). For a more detailed description of the model, results and

applications see Paper I, Liodakis & Pavlidou (2015b), and Paper II.

We assumed single power-law distributions for the Lorentz factor and the unbeamed luminosity for the simulated parent population. We treated BL Lacs and the FSRQs as separate cases in order to assess the difference in beaming between the two classes. We adopted pure luminosity evolution (Padovani & Urry 1992), where sources become brighter with look-back time while maintaining a constant comoving volume density, making the number of sources in any redshift bin proportional to the comoving volume element in that bin ( $dN \propto dV$ ). This scaling is normalized so that the final simulated sample for the comparison with the observed distributions will consist of  $\sim 10^3$  sources. We used a Monte-Carlo approach to calculate the simulated distributions of the observables we consider: we drew values for the intrinsic luminosity  $L_\nu$  and Lorentz factor  $\Gamma$  from power-law distributions, and for the viewing angle  $\theta_j$  from a uniform distribution. We then calculated a flux density using,

$$S_\nu = \frac{L_\nu D^p}{4\pi d_L^2} (1+z)^{1+s}, \quad (2)$$

where  $D = 1/\Gamma(1-\beta\cos\theta)$ ,  $\beta = (1-\Gamma^{-2})^{1/2}$ ,  $d_L$  is the luminosity distance,  $s$  the spectral index, and  $p$  is defined as  $p = 2 - s$ ; and we finally applied the 1.5 Jy flux-density limit of the MOJAVE sample.

Following the procedure described above, we produced simulated samples for the blazar populations (Paper I), from which we extracted information regarding the Doppler factor distribution, the distribution of  $\Gamma\theta$  which quantifies how beamed is a source within a flux-density limited sample, and the distribution of the timescale modulation factor in each class.

In the original version of the model, we used a single value for the spectral index for each population. In the most recent version (Paper II) we have included a spectral index distribution in the models. The spectral index for both source classes is normally distributed with mean and standard deviation determined using the maximum likelihood analysis presented in Venters & Pavlidou (2007) and data from Hovatta et al. (2014). In Paper II, before calculating a flux density, each source is also assigned a random value for the spectral index from the distribution of the corresponding source class.

A major result of Paper I and Paper II, which is directly relevant to the work we present in this paper is that the timescale modulation factor (Eq. 1) follows an exponential distribution,

$$P(m) = C(\lambda e^{-\lambda m}), \quad (3)$$

where  $C$  is a normalization constant to account for the truncated range and  $\lambda$  is the inverse mean of the distribution, with the mean depending on the source class and the flux limit of the sample. Using the upgraded models from Paper II (which we use throughout this work), the timescale modulation factor has a similar mean (0.381 for the BL Lacs and 0.318 for the FSRQs, for 1.5 Jy flux-density limited samples) for both classes.

<sup>1</sup> Monitoring Of Jets in Active galactic nuclei with VLBA Experiments, <http://www.physics.purdue.edu/MOJAVE/>

### 3 INTRINSIC PROBABILITY DENSITY FUNCTION OF TIMESCALES

Our aim in this work is to extract information about the intrinsic (rest-frame) probability density function (pdf) of timescales for any class of events characterized by a single timescale per blazar. Examples of such classes of events include: shortest flare rise time in a blazar; the duration of the largest (in amplitude) flare ever observed in each source; the duration of the longest (in angle) rotation of the polarization angle in each blazar; and the average time delays between flares in two different frequencies in each blazar.

In order to achieve our goals, we first treat the inverse problem: given a rest-frame pdf of timescales in the blazar population for events of a particular class, what would the observed timescale pdf be, after applying the modulation induced by relativistic effects? In the following, we will use  $t_i$  to denote intrinsic (source rest-frame) timescale, and  $t_o$  to denote observed (observer-frame) timescales.

Assuming that the physical processes in the rest frame have no knowledge of redshift or Doppler factor, the intrinsic timescales of any event are independent of the timescale modulation factor  $m = (1+z)/D$ . As a result,

$$P(t_i, m) = P(t_i)P(m), \quad (4)$$

where  $P(t_i, m)$  is the probability of the intrinsic timescale,  $t_i$ , to be modified by  $m$ ;  $P(t_i)$  is the intrinsic timescale probability density; and  $P(m)$  is the timescale modulation factor probability density (Eq. 3). The observed timescales are connected to the intrinsic through  $t_o = mt_i$ . Thus Eq. 4 can be transformed as:

$$P(t_o, m) = P(t_i, m)|J(t_i, m)|, \quad (5)$$

where  $P(t_o, m)$  is the probability of observing  $t_o$  given  $m$ , and  $J(t_i, m)$  is the Jacobian of the transformation. From the relation between observed and intrinsic timescales, the Jacobian will be:

$$J(t_i, m) = \begin{bmatrix} \frac{1}{m} & 0 \\ 0 & 1 \end{bmatrix} \quad (6)$$

Thus the (absolute value of the) determinant of the Jacobian is equal to  $|J(t_i, m)| = 1/m$ , and Eq. 5 becomes  $P(t_o, m) = P(t_i)P(m)/m$ . The probability density function of the observed timescales is thus:

$$P(t_o) = \int_{m_{min}}^{m_{max}} P(t_o, m) dm = \int_{m_{min}}^{m_{max}} P(t_i) C(\lambda e^{-\lambda m}) \frac{1}{m} dm, \quad (7)$$

where  $m_{min}$ ,  $m_{max}$  are the minimum and maximum timescale modulation factors.

Since we know the functional form of  $P(m)$  from the results of Papers I and II, we can assume a family of distributions for  $P(t_i)$  and use Eq. 7 to obtain the resulting  $P(t_o)$ . The parameters of  $P(t_i)$  can then be recovered by requiring that the resulting  $P(t_o)$  fits the observed data best. In this work we provide in Appendix A some examples of this process for the most commonly used and/or encountered distributions in astrophysics in general.

### 4 METHOD BENCHMARKING

In order to benchmark the accuracy of our method under realistic observing conditions, we generate a simulated sur-

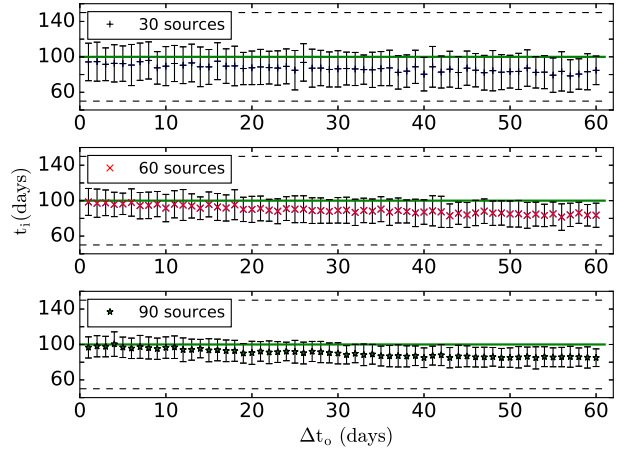


**Figure 1.** Estimated best-fit  $t_i$  versus interval between observations  $\Delta t_o$  (both in days) for samples without pileup. The error bars represent the uncertainty of the best-fit  $t_i$ . The green line at 100 days shows the value of the “true” intrinsic timescale, while the black dashed lines at 50 and 150 days show the limits of the parameter space scanned.

vey and explore the accuracy of the method with respect to the cadence of observations and sample size.

#### 4.1 Simulated sample

For our benchmarking experiments, we have chosen to use the simple case where the class of events under investigation have the same intrinsic characteristic timescale in the rest-frame of all blazars. Then the rest-frame distribution can be described by a  $\delta$ -function and the observer-frame distribution in the ideal case of perfect sampling will be an appropriately normalized exponential distribution (Eq. A6). We constructed our simulated samples by drawing a random value for the timescale modulation factor from an exponential distribution (Eq. 3), and multiplying it with the same characteristic intrinsic timescale (set to  $t_i = 100$  days to match our real-data application, see §5).

The minimum modulation factor we accept is  $10^{-2}$  following the results of Papers I and II. The mean of the timescale modulation factor distribution depends on the object class and the flux limit of the sample. For this particular experiment, we choose to use the model for the FSRQ population with an 1.5 Jy flux-density limit ( $\lambda^{-1}$  was set to 0.318). Since the mean of the BL Lac population for the 1.5 Jy flux limit is very similar with that of the FSRQs, we expect the conclusions derived for the latter to extend to the former. However, this is not necessarily true for different flux limits. We discuss the possible effects of a different flux limit to the results of our benchmarking in §6.

#### 4.2 Effects of sample size and cadence

The finite cadence of any monitoring program can affect measured timescales in three ways. First, it can introduce an artificial cut-off at the lower end of the observed timescale distribution: timescales shorter than  $\Delta t_o$  (the time interval between observations) will not be measured depending on

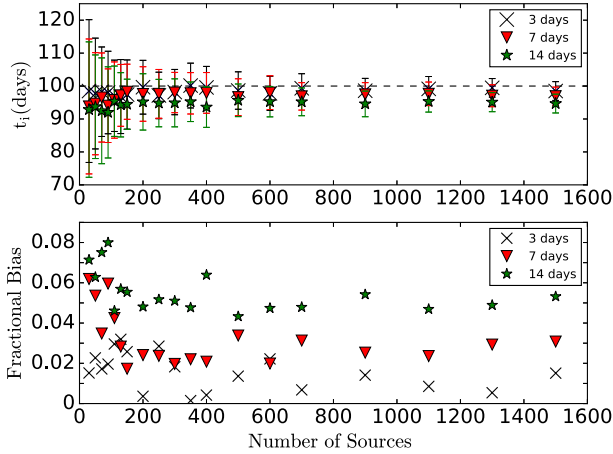


**Figure 2.** Upper panel (a): Estimated best-fit  $t_i$  versus sample size ranging from 30 to 1500 sources. The error bars represent the uncertainty of the best-fit  $t_i$ . Lower panel (b): Fractional bias between the estimated best-fit and the “true”  $t_i$  ( $|t_{i,fit} - t_i|/t_i$ ) versus sample size. Symbols as above.

$m$ . Second, it can also introduce an uncertainty in measured timescales. The measured timescale will lie between  $t_{observed}$  and  $t_{observed} + 2\Delta t_o$ . This is because in the worst case scenario, both the beginning/end of an “event” can happen exactly after/before the first/last datapoints. For this reason, once we generate our simulated observer-frame sample, we create an “observed” sample by drawing a random value from a uniform distribution with range  $[t_o - 2\Delta t_o, t_o]$ , where  $t_o$  is the actual value of the observer-frame timescale.

Third, it may introduce a “pileup” of events close to the cadence limit depending on how events faster than  $\Delta t_o$  are treated. One possibility is that every timescale smaller than  $\Delta t_o$  is rejected as not observed. In this case there is no pileup. Another possibility is that timescales smaller than  $\Delta t_o$  are set as observed, with value equal to that of  $\Delta t_o$ . Physically, the latter case corresponds to observations of events of various timescales (e.g flares in a particular frequency), of which we are interested in the smallest duration event occurring in a particular source. In this scenario faster-than-observed events may occur in a source, but the “fastest” one we record is set by the survey cadence, leading to a pileup resulting in a systematic offset in our statistical analysis. For the remainder of this section we will only consider the first possibility (no pileup). For a discussion of the possible effects of pileup, see Appendix B.

We perform our benchmarking experiments as follows:

- We generate an “observed” sample using the procedure described above for a given  $\Delta t_o$ .
- We construct the cumulative distribution function of Eq. (A6) for different assumed values of  $t_i$  and compare it with the simulated “observed” sample with the use of the Kolmogorov Smirnov test (K-S test). The K-S test provides a straightforward way of rejecting distributions that are inconsistent with our simulated dataset. We accept that for a probability value larger than  $p = 0.05$  we can not reject the null hypothesis that the two samples are drawn from the same distribution. Throughout this work, we refer to this p-value as the “probability of consistency”.

In order for our distribution to be normalized in the observer’s frame, we need to calculate the normalization constant  $C$  (see Appendix A) which depends on  $t_{o,min}$  and  $t_{o,max}$ . In practice,  $t_{o,min}$  is established by  $\Delta t_o$  and  $t_{o,max}$  by the length of the observing season. For our benchmarking experiments, we simulated an observing experiment with an observing season set to ten times the longest observed timescale in the simulated sample. The value of  $t_i$  which yielded the highest p-value of the K-S test is the value we considered the best-fit parameter value.

- We repeat the above process 100 times in order to evaluate the statistical spread of the results, for a given sample size and  $\Delta t_o$ . We quote the mean of these best-fit parameters as the most likely estimate of the rest-frame timescale and the standard deviation of the estimates in different iterations as the uncertainty of the final estimate.

Due to relativistic compression, the shortest rest-frame timescale can either be equal or longer than the shortest one observed. The longest rest-frame timescale can be up to the maximum observed divided by the smallest modulation factor ( $\sim 10^{-2}$ ). Thus in the application of the method, the expected range of the rest-frame timescale estimate should be at least from the shortest to 100 times the longest observed timescale.

For this particular exercise, since we have a priori knowledge of the  $t_i$ , the range is set from 50 to 150 days. If the best-fit  $t_i$  lies outside of that range, then the estimate will take the value of the closest boundary value. Any best-fit  $t_i$  that is either  $\leq 50$  or  $\geq 150$ , would correspond to an at least 50% error in the estimate.

We examined three sample sizes (30, 60, 90 sources) and  $\Delta t_o$  starting from 1 day, up to 60 days with a step of 1 day. We draw sources until we reach the desired sample size in the observer’s frame ignoring cases where  $t_o$  is smaller than  $\Delta t_o$ .

Figure 1 shows the estimated best-fit  $t_i$  versus  $\Delta t_o$ . The error bars are the spread of the estimated rest-frame timescale. As expected, increasing the number of sources in our samples results in a more narrow spread of estimates. There is a negative bias (systematic shift towards lower values of the estimated intrinsic characteristic timescale) with the increase of the number of days between observations. In many cases for  $\Delta t_o \geq 30$  days, the best-fit estimate is more than  $1\sigma$  away from the true value. This leads us to the conclusion that for a  $\Delta t_o$  of more than 30 days ( $\sim 1/3$  the actual timescale we are trying to measure), the method loses its ability to accurately estimate the best-fit parameter of the intrinsic probability density function.

In addition, we explore the effect of the size of the sample at a fixed interval between observations. We follow the procedure described above with  $\Delta t_o$  fixed to a predefined value, and a varying number of sources in the sample. We chose three values for  $\Delta t_o$ ; 3, 7, and 14 days, all below the 30 days limit determined above (Fig. 1). The different samples have a size starting from 30 sources up to 150 with a 20 source step, from 150 up to 400 with a 50 source step, from 400 up to 700 with a 100 source step, and from 700 up to 1500 with a 200 source step.

Figure 2a shows the estimated  $t_i$  versus the sample size with the error bars being the uncertainty of the method, while figure 2b shows the fractional bias of the estimated

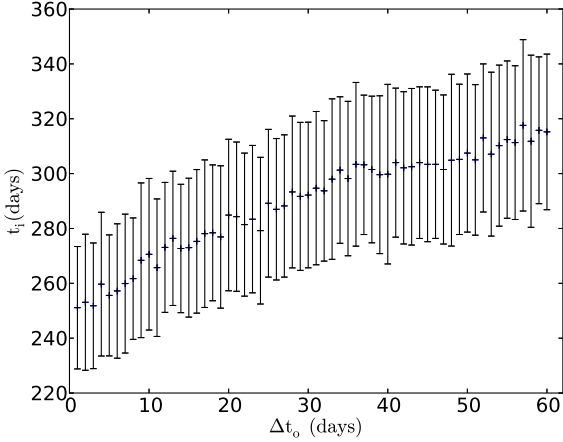


**Figure 3.** Estimated  $\delta$ -function best-fit parameter ( $t_i$ ) for an intrinsic uniform distribution versus  $\Delta t_o$ . The error bars represent the uncertainty of the best-fit  $t_i$ .

best-fit and the “true”  $t_i$  ( $|t_{i,fit} - t_i|/t_i$ ) versus sample size. It is obvious that the larger the sample the smaller the spread (Fig. 2a), and the smaller the interval between observations, the smaller the bias (Fig. 2b). There is no significant change in the fractional bias for a given  $\Delta t_o$  regardless of sample size. The method has an accuracy of  $\leq 8\%$  in the estimates (Fig. 2b) as long as  $\Delta t_o \leq 14\%$  of the intrinsic timescale value. For a large number of sources ( $\geq 200$ ) and small  $\Delta t_o$  (3 days, i.e. 3% of the timescale we are trying to determine) the bias is smaller than  $\sim 1\%$ .

### 4.3 Testing for the type of distribution

The best-fit intrinsic distribution family is not necessarily unique. Different families of distributions of intrinsic timescales can produce similar results in the observer’s frame. For example, an intrinsic sharp distribution would appear consistent with a  $\delta$ -function as well as with a narrow normal distribution. Physically this is not necessarily problematic, since all the well-fitting distributions should describe approximately the same physical reality (in our example, a “preferred” timescale in the rest-frame). A more worrisome situation would be if, because of uncertainties or systematic effects, a single dataset appeared consistent with families of distributions describing a very different physical reality. To demonstrate how this effect can cause confusion, we tested whether a finite-width intrinsic distribution can appear consistent with a  $\delta$ -function. To this end, we performed the following experiment.

We created simulated samples of  $t_o$  using an intrinsic uniform distribution from  $t_i = 50$  to  $t_i = 500$  days. The sample size was fixed to 200 sources, a size large enough to ensure accurate estimates (as seen in Fig. 2b). Using the procedure described in §4 we fitted an intrinsic  $\delta$ -function for intervals between observations ( $\Delta t_o$ ) from 1 to 60 days. We assumed no a priori knowledge of the intrinsic distribution or the range of the parameter space. Figure 3 shows the  $\delta$ -function best-fit parameter  $t_i$  versus  $\Delta t_o$ . The best-fit estimates of the characteristic timescale fall approximately at the median value of the intrinsic distribution with a system-

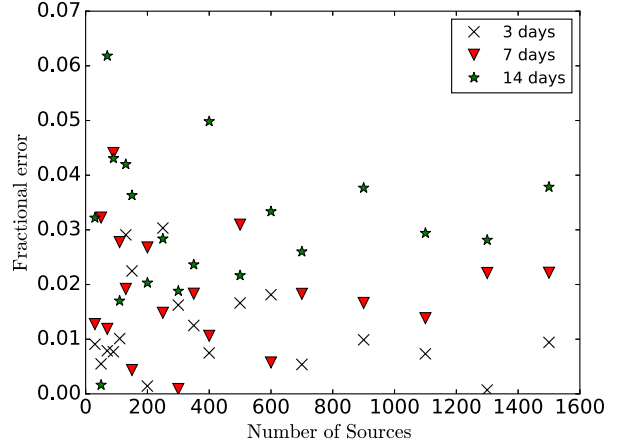


**Figure 4.** Fractional error between the maximum likelihood and K-S test fitting methods versus sample size for the 3 day, the 7 day, and the 14 day time interval between observations ( $\Delta t_o$ ).

atic shift towards higher values for increasing time intervals between observations. The K-S test yields a probability of consistency that ranges from 45% to  $\leq 65\%$ . In this case we could naively assume that all blazars have the same characteristic timescale in the jet rest frame.

However, there is a simple test for this particular case that can clarify the nature of the intrinsic distribution. If indeed the intrinsic distribution of timescales is a  $\delta$ -function, or at least a sharp distribution, then by fitting a normal distribution, we should in principle find that the best-fit distribution is very sharp. For simplicity we tested only two intervals, 7 and 30 days. The 7 day interval was chosen because it is the limit at which the method becomes very accurate ( $\leq 4\%$  error) and the 30 day interval because it is the limit after which results are unreliable (see Fig. 1).

For the 7 day interval we find that the best-fit intrinsic normal distribution would have mean  $\mu = 253.0$  and standard deviation  $\sigma = 168.0$  with a 97% probability of consistency between samples. For the 30 day interval the best-fit normal distribution has  $\mu = 168.8$  and  $\sigma = 239.0$  with a 76% probability of consistency. In both cases the resulting best-fit normal distribution is far from consistent with a  $\delta$ -function. The fact that they are significantly wider and with more than 30% higher probability of consistency is suggestive that the “true” intrinsic distribution is much wider than a  $\delta$ -function. Such simple tests can provide invaluable insights on the “true” shape of the intrinsic distribution in the application of the method.

### 4.4 K-S test versus conventional fitting methods

The K-S test provides a convenient way to automatically reject families of rest-frame distributions that are a poor fit to the data, especially in cases when there is no analytical solution. However, the K-S statistic (or the associated p-value) are not formally appropriate for fitting. To examine how much error we introduce by optimizing our parameters through K-S statistic minimization, we perform the same analysis in section 4.2 for fixed time intervals between observations, but instead of using the K-S test fitting method,

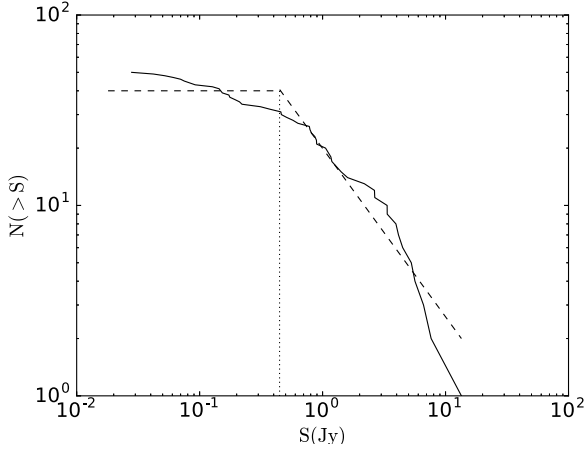


**Figure 5.** Source count distribution (number of sources  $N$  with flux density larger than  $S$ ) for the RoboPol main sample sources. The black dotted line marks the assumed radio flux-density limit.

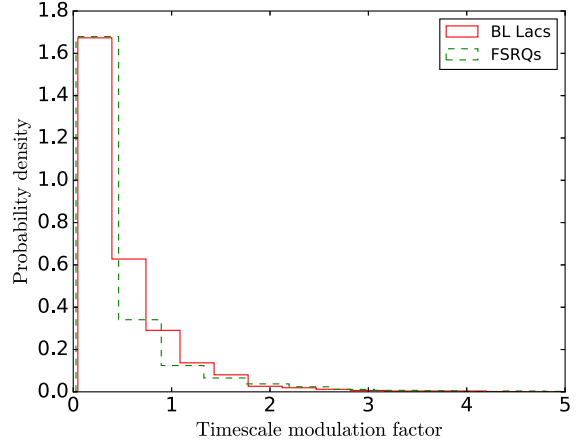


**Figure 7.** Distribution of the simulated timescale modulation factor for the RoboPol flux-density limited sample. Solid red is for the BL Lacs, and dashed green is for the FSRQs.

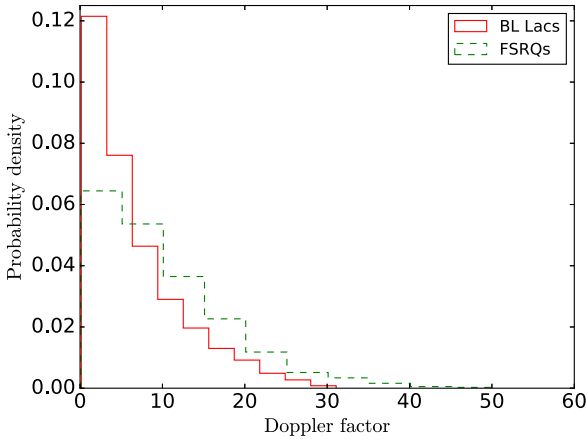


**Figure 6.** Distribution of the simulated Doppler factors for the RoboPol flux-density limited sample. Solid red is for the BL Lacs, and dashed green is for the FSRQs.

we use a maximum likelihood estimation (MLE) of parameters. Figure 4 shows the fractional error between the K-S statistic and maximum likelihood fitting methods. Even for the longest time interval (14 days) between observations, the fractional error is  $\lesssim 6\%$ . In cases with small  $\Delta t_o$  and a large number of sources, the fractional error is only  $\sim 1\%$ . We thus conclude that the K-S test method used throughout this work can adequately mimic a formally appropriate fitting method and provide robust results without the computational cost and complexity required by other methods. For a discussion of K-S versus MLE fitting in the case of population models themselves, see Paper I.

## 5 APPLICATION TO BLAZAR POLARIZATION ANGLE SWINGS

Having benchmarked our method, we present the first real-data application to timescales associated with the rota-

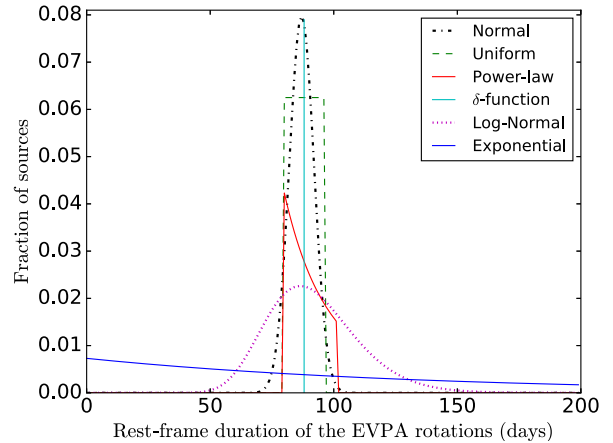


**Figure 8.** Best-fit distribution, for various distribution families, of the intrinsic timescales of the longest EVPA rotations in a radio flux-density limited subsample of RoboPol blazars.

tion of the polarization plane (Electric Vector Position Angle (EVPA) rotation), in optical, seen in blazars. The physical mechanism of these rotations is, to this day, unknown, with models ranging from random walk processes (Moore et al. 1982; Marscher 2014; Kiehlmann et al. 2016) to shocks propagating in the helical magnetic field of the jet (Marscher et al. 2008, 2010) and bends in the jet (Abdo et al. 2010). Although some rotations have been associated with  $\gamma$ -ray flares and ejections of radio components (Marscher et al. 2008, 2010) this is not always the case (Blinov et al. 2015).

In order to uncover the underline intrinsic timescale distribution of these rotations, we use data from the RoboPol survey (King et al. 2014). The RoboPol survey uses a  $\gamma$ -ray flux-limited sample, specifically designed for rigorous statistical studies (Pavlidou et al. 2014; Angelakis et al. 2016). Since our method works for radio flux-density limited samples, the first step to applying our method is to identify an appropriate subset of the RoboPol main sample that is

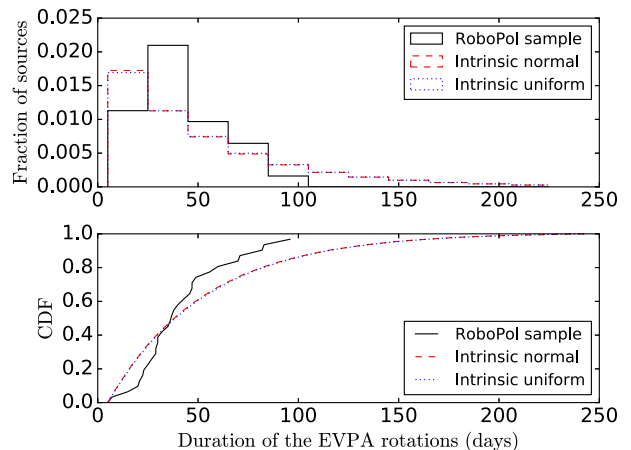
an unbiased (randomly drawn) subsample of a radio flux-density limited sample. All the RoboPol sources have been monitored by the Owens Valley Radio Observatory (OVRO) blazar program (Richards et al. 2011). We use the maximum likelihood mean flux-densities (Richards et al. 2014) to construct the source count distribution for the RoboPol main sample sources ( $N(>S)$ ) as a function of  $S$ , Fig 5) and we approximate it with a horizontal part at low flux densities  $S$  and a declining power-law at higher  $S$ . We take sources brighter than 0.446 Jy (the transition point between the two approximations, see Fig. 5) to be the desired subsample, which we consider to be approximately unbiased compared to a parent flux-density-limited sample with a limit of 0.446 Jy. We have verified that our results are not sensitive to the exact location of the flux-density limit (i.e the inclusion or the omission of one more source). The number of sources in our radio flux-density limited sample is 31.

Figure 6 shows the simulated distribution of Doppler factors and Fig. 7 the simulated distribution of the timescale modulation factor for a 0.446 Jy radio flux-density limit, as derived from the population models in Paper II. Due to the low flux-density limit, we expect that the Doppler factor values will be, on average, smaller than the ones derived from VLBI or variability studies of brighter sources (Hovatta et al. 2009; Liodakis et al. 2016a) and the ones in the higher flux-density-limit simulated samples we investigated in Papers I and II. The mean is  $\sim 6$  for the BL Lacs and  $\sim 10$  for the FSRQs. The mean of the timescale modulation factor is 0.475 for the FSRQs, and 0.49 for the BL Lacs. Since the two values are very similar, we adopted their mean (0.4825) as the common value. This way we avoid splitting the sample and reducing our statistics. We have verified that using either time scale modulation factor mean (FSRQ or BL Lac population) for the value of the whole sample does not result in any significant change on our results or our conclusions.

## 5.1 Observations

The data were collected during the 2013, 2014 and 2015 observing seasons of the RoboPol survey. The definition of the EVPA swings we adopt is similar to the definition of an EVPA rotation from Blinov et al. (2015). We define an EVPA rotation as any continuous change of EVPA with total amplitude  $\Delta\theta_{total} > 90^\circ$  comprised of at least four consecutive observations with statistically significant swings ( $\Delta\theta > \sqrt{\sigma_{\theta_{i+1}}^2 + \sigma_{\theta_i}^2}$ , where  $\sigma_\theta$  is the uncertainty in the EVPA) between them. The start and end points of a rotation are defined by a factor of 5 change of the slope of the EVPA time series,  $\Delta\theta/\Delta t$  or a change of its sign. Contrary to Blinov et al. (2015) we do not apply any limits in the number of points or the length (rotation angle  $\Delta\theta_{total}$ ) of an event. Following the definition in Blinov et al. (2015) we find 29 rotations in 14 sources, whereas with the definition adopted in this work we find 570 rotations in 31 sources making a statistical approach feasible.

Our method is applicable when each blazar is characterized by a single observed timescale. In the case of EVPA rotations, for each blazar we select the rotation (as defined above) with the longest duration (longest rotation timescale  $\Delta T_{max}$ ). The shortest time interval between observations,



**Figure 9.** Upper panel: Distribution of  $\Delta T_{max}$  in our sample. Lower panel: Cumulative distribution function of the  $\Delta T_{max}$  of the EVPA rotations.

**Table 1.** Best-fit parameters and probability of consistency (K-S test) values for each family of distributions. The uncertainties indicate the range of the parameter that can produce an acceptable fit (i.e K-S test probability  $> 5\%$ ). In the case of the log-normal distribution,  $t_i$  and  $\sigma_{t_i}$  are related to  $\mu$  and  $\sigma_{sc}$  (see A) through  $t_i = \exp(\mu + \sigma_{sc}^2/2)$  and  $\sigma_{t_i} = \sqrt{\exp(\sigma_{sc}^2 - 1)\exp(2\mu + \sigma_{sc}^2)}$

Distribution	$t_i$ (days)	$\sigma_{t_i}$ (days)	p-value (%)
Normal	$87^{+26}_{-15}$	$5^{+35}_{-4}$	31.5
$\delta$ -function	$88^{+16}_{-19}$	-	29.7
Log-Normal	$92^{+89}_{-18}$	$18^{+220}_{-17}$	25.5
Exponential	$137^{+28}_{-15}$	-	11.8

Distribution	$t_{i,min}$ (days)	$t_{i,max}$ (days)	slope	p-value (%)
Uniform	$80^{+14}_{-10}$	$96^{+33}_{-16}$	-	31
Power-law	$80^{+20}_{-20}$	$101^{+399}_{-21}$	$-4.4^{+0.8}_{-1.1}$	30

$\Delta t_o$ , is  $\sim 1$  day with an average of  $\sim 9$  days, while the events (see Fig. 9) last from 3 to 108 days.

## 5.2 Results

Following the procedure described in §4, we apply our method to the radio flux-density limited RoboPol subsample testing the six families of distributions described in Appendix A. For the intrinsic timescales, we explored a parameter space from 1 day to  $10\times$  the maximum observing season length (244 days) of the RoboPol survey. In the case of the power-law index the range of the parameter space was set to  $[-7,7]$ . The best fit parameter values for each family of distributions and the K-S test p-value for each are shown in Table 1. The uncertainties in the parameters given in Table 1 indicate the range in which for those parameters the K-S test yielded a  $> 5\%$  probability of consistency between observed and simulated samples.

All families of distributions, with the exception of the

exponential, converge to approximately the same range of intrinsic timescales (Fig. 8) with very similar K-S test probabilities. The probability of consistency is highest for the normal and uniform distributions (31.5% and 31% respectively). For these two intrinsic (rest-frame) distributions, it is clear even by inspection that the resulting observer-frame distributions are almost indistinguishable (Fig 9). We observe a lack of very short and very long duration events. Both however can be attributed to observational constraints. For example, the former could be due to the cadence being too low to observe shorter smooth variations. Indeed, there are blazars for which even the longest observed smooth variation does not last much more than the time interval between observations. The current (season 2016) RoboPol observing strategy (i.e monitoring of the most variable sources with nightly observations,  $\Delta t_o = 1$ ) will be able to resolve faster (shorter duration) events.

The latter could be due to the length of the observing seasons ( $\sim 240$  days) or due to the source not being available for observations throughout the observing season. In Appendix C, we test whether observational constraints could significantly alter our results by shortening long-duration events. We find that it is highly unlikely that the observed event timescale distribution is significantly wider than the observed, thus our results are independent of such constraints.

For the best-fit intrinsic  $t_i$  (87 days) we estimate, based on our benchmarking of §4.2, that the bias is  $\leq 8\%$  since the average  $\Delta t_o$  is only  $\sim 10\%$  of the rest-frame  $t_i$ . From Fig. 2b we can conclude that the results of our analysis are robust independent of our sample size since the average  $\Delta t_o$  is  $< 14\%$  of the  $t_i$ . Given that we are looking for the longest, rather than the shortest, event timescale in each blazar, a systematic pileup of timescales close to the average distance between observations (see Appendix B) is not expected in this particular application. It should be noted that although the narrowly peaked intrinsic distributions have a systematically higher probability of consistency than the much wider exponential distribution, the exponential remains an acceptable fit, and our sample size is not large enough to conclusively reject a significantly wider distribution of rest-frame timescales (it is clear from Table 1 that the lognormal and power-law distributions can also yield acceptable fits for a wider distribution). However, the exponential distribution is a monoparametric family, and none of the multi-parametric families prefers a shape similar to the best-fit exponential, indicating a preference of the data for the narrower distributions, according to the test we discussed in §4.3.

To check whether the “true” intrinsic distribution is an exponential, and our results arose from random sampling, we performed the following test. We created  $10^4$  simulated datasets from an intrinsic exponential distribution with the same mean as in Table 1 in a simulated observing survey with the same characteristics ( $\Delta t_o$ , observing length etc.) as RoboPol. We then used the distributions discussed above (including an exponential) with the same parameters from Table 1 to fit the simulated samples and calculate the K-S test statistic. Out of the  $10^4$  simulated samples, we calculated the percentage of trials that achieved a K-S test p-value equal or higher than the one reported in Table 1 for each family of intrinsic distributions (other than the exponential). The probability values range between  $< 10^{-4}$  and

25%. However, there was no case where at the same time an exponential distribution would yield a  $< 11.8\%$  probability while *all the other families* yield a  $> 25.5\%$ . For this reason, we formally reject the exponential distribution as an acceptable model.

### 5.3 Possible interpretations

Our findings suggest that the intrinsic timescales of the longest EVPA events in the radio flux-density limited subsample of RoboPol blazars that we have examined are confined to a relatively small range (spread of intrinsic timescales  $\sim 30$  days). It is possible that a subgroup in our sample has a small range of intrinsic timescales and is dominating over the rest of the sample.

We have tested for this scenario in the following way. We simulated a physical situation where our sample was an admixture of sources with a narrow distribution of timescales (distributed according to the best-fit uniform distribution describing the RoboPol sample) and sources with a wide distribution of timescales (uniform [50,500] days). We created a simulated sample following the procedure described in §4 and proceeded in fitting an intrinsic uniform distribution. We repeated the same procedure 31 times, and each new simulated sample had a larger (by one) number of sources that were drawn from the wider distribution. Even with a small number of sources from a wide uniform distribution ( $< 5$  sources) the method is unable to produce a distribution with such a small range. We conclude that if there were two underlying distributions of significantly different widths, the wider of the two would dominate even if it only contributed a small number of sources.

If we assume that the EVPA rotations are produced by a shock propagating downstream in a jet, we should observe a rotation when its tracing the spirals of the helix of the jet (Marscher et al. 2008, 2010). In this case our results will imply that the maximum length of the jet traveled during a rotation is similar for all blazars and is roughly between 75 and 100 light days. In this case, the sources would have a narrow distribution of intrinsic timescales but due to different Lorentz factors and viewing angles the observed distribution is much wider. This would suggest that the intrinsic size of the jets is very similar for all blazars. However, given the range of jet sizes seen in radio galaxies (i.e the unbeamed parent distribution of blazars) this is highly unlikely.

If the EVPA rotations are caused by a random walk processes, the range of intrinsic timescales found in this work would represent a typical timescale of the smooth variation of turbulent plasma cells. To test if random walk processes can produce such a small range of timescales we perform the following experiment. We use the random walk model described in Blinov et al. (2015) to create a simulated EVPA curve comparable to the EVPA curve of each source. We create a simulated distribution of the longest EVPA rotations and we repeat the process to recover the intrinsic timescale distribution as described above. The simulated sample created via the random walk process has a 56% probability of consistency with the observed according to the K-S test. We found that the best-fit distribution is a normal distribution with mean 69 days and standard deviation 5 days with a 82% probability of consistency followed by a uniform with  $t_{i,min} = 66$  and  $t_{i,max} = 73$  and 81.5% probability

of consistency. The results are very similar, showing that the random walk process can indeed reproduce such a small range and cannot be ruled out as a potential mechanism. It is interesting that the probability of consistency is more than twice as much as the one of the observed data. This could be coincidental, due to the random processes responsible for the simulated distribution, or could indicate the existence of two EVPA rotation mechanisms. It is argued in [Blinov et al. \(2015\)](#) and [Kiehlmann et al. \(2016\)](#) that not all rotations can be explained by a random walk or a deterministic event. Therefore it is not unlikely that rotations created by random walks dominate our observed sample, yet there are still deterministic events present creating the large difference between K-S test p-values of random walk simulated and observed samples.

The assumption implied in treating the RoboPol data is that the beaming between the optical and radio regions is the same. If this is not the case, then the timescale modulation factor distribution would change, altering our results. The fact that the intrinsic distribution is narrow suggests that the difference in beaming is likely to be systematic, with all sources having either higher or lower Doppler factors. Otherwise the induced spread would create the appearance of a much wider distribution. If this is indeed the case, the width of the best-fit distributions will not change, but the distribution will be shifted to higher or lower values. Finally, we caution that, although disfavoured by the data, distributions allowing for a much wider range of rest-frame timescales are not formally rejected by our relatively small source sample (Table 1).

## 6 SUMMARY AND CONCLUSIONS

In Papers I and II, we found that the distributions of observer-frame timescales of the blazar populations are modulated by an exponential distribution compared to their rest-frame counterparts. This exponential has a mean depending on source class and the flux-density limit of the sample.

In this work, assuming that the intrinsic timescales of blazars are independent of redshift and Doppler boosting, we have developed a novel method of uncovering the underlying rest-frame probability density function of timescales of blazar jets using the observer-frame probability density.

We caution that the independence of rest-frame timescales from redshift and Doppler boosting is not obvious. There may be a dependence on either redshift or Doppler boosting, or both. However such a dependence can best be addressed in a model-dependent fashion (i.e. by testing an explicit model proposing such a relationship). Our formalism can be extended in a straightforward fashion to test such models.

In addition we have benchmarked our method in a realistic observing scenario using the timescale modulation factor distribution for the FSRQ population with a flux-density limit of 1.5 Jy and we assessed the impact of various systematic effects.

We found that when the interval  $\Delta t_o$  between observations is longer than 30% of the timescale we try to measure, there is a systematic negative bias in the estimates that can lead to best-fit parameters deviating more than  $1\sigma$  from the

characteristic timescale. Low cadence of observations can thus prevent our method from producing robust results.

Exploring the method's sensitivity to sample size we found that all estimates for sample sizes  $\geq 30$  sources have an accuracy of  $\leq 8\%$  if  $\Delta t_o$  is sufficiently low. Monitoring programs with small  $\Delta t_o$  and large number of sources such as the Owens Valley Radio Observatory (OVRO)<sup>2</sup> blazar monitoring program ([Richards et al. 2011](#)) would make an ideal candidate for the application of our method.

In practice, observational constraints of specific experiments may induce additional effects other than the ones discussed in our general benchmarking. For this reason, we encourage the users of our method to conduct additional program-specific simulations that can uncover such effects, as we have also done in Appendix C to address the specific effect of interrupted seasonal observations on EVPA rotation lengths.

The family of distributions that best fits a particular observer-frame dataset does not need to be unique. Different families can provide similarly fitting results. A test that can help determine whether the deduced rest-frame distribution is an acceptable description of the physical reality of the source population is to compare the best fits from different families of distributions. All distributions with the same number of parameters should converge to a similar answer (for example, regarding distribution width) for the obtained fit to be considered reliable. Distributions with more parameters should converge to the simpler distribution shapes, if the simpler distributions are acceptable descriptions of reality, otherwise the simpler distributions should be rejected.

The results of the analysis presented in this work during the benchmarking of our method are representative for a simulated 1.5 Jy flux-density limited FSRQ sample. For the same flux-density limit the mean of the timescale modulation factor distribution for the BL Lac population is fairly similar. Thus we would not expect any significant differences with the conclusions derived for the FSRQ sample. However, for a sample with a different flux-density limit the overall amount of beaming will be in principle different for different classes. The flux-density limit will affect the regimes of robustness of our method.

Samples with flux-density limit lower than 1.5 Jy will have a larger mean of the timescale modulation factor distribution, whereas a higher flux-density limit will result in a smaller mean. In the first case (lower flux-density limit) there will be a shift towards higher values of the observed timescales which in turn will push the limit ( $\Delta t_o = 30$  days) for the method to produce robust results to higher values. The opposite effect will be true for the higher flux-density limit. Shorter observed timescales will bring that limit to smaller  $\Delta t_o$  values.

We have applied our method to the maximum duration of optical EVPA rotations observed in each blazar in a radio flux-density limited sample observed by RoboPol. We have found that the best-fit intrinsic distribution is a normal distribution with mean 87 days and standard deviation 5 days with a 31.5% probability of consistency between observed and simulated samples. An intrinsic uniform distribution with  $t_{i,min} = 80$  and  $t_{i,max} = 96$  has a 31% probability of

<sup>2</sup> <http://www.astro.caltech.edu/ovroblazars>

consistency making it an equally preferred candidate since the two simulated observer-frame distributions are indistinguishable (Fig. 9). We have examined several interpretations of our results. If a significant fraction of our events are the result of a random-walk process, a result similar to the one of this work would be obtained. However, without better statistics we cannot exclude other interpretations.

In the case of timescale distributions in different wavelengths (e.g optical,  $\gamma$ -rays), whether the same boosting (Doppler factor) applies is still an open question. Deceleration in the jet from the  $\gamma$ -ray to the radio emission region (Georganopoulos & Kazanas 2003a,b, 2004; Giannios et al. 2009) may result in the underestimation of the intrinsic timescales. If such a deceleration does not exist or its effect is not significant, timescales derived from the Fermi Gamma-Ray Space observatory all sky survey (Acero et al. 2015) will also constitute an ideal dataset for the application of our method due to the high cadence of observations and sample size, although one should keep in mind that a flux-density limited sample in  $\gamma$ -rays does not translate directly into a flux-density limited sample in radio (Pavlidou et al. 2012), which is the basis of our population models.

On the other hand, applications of our method to timescales extracted by radio monitoring of flux-density limited samples do not suffer from either of these potential problems, and thus constitute prime candidates where our method could be applied with maximum confidence, provided that the cadence of the monitoring is sufficiently high.

## ACKNOWLEDGMENTS

The authors would like to thank Talvikki Hovatta, Dimitrios Giannios and Sebastian Kiehlmann for comments that helped improve this work. This research was supported by the “Aristeia” Action of the “Operational Program Education and Lifelong Learning” and is co-funded by the European Social Fund (ESF) and Greek National Resources, and by the European Commission Seventh Framework Program (FP7) through grants PCIG10-GA-2011-304001 “Jet-Pop” and PIRSES-GA-2012-31578 “EuroCal”.

## REFERENCES

- Abdo A. A., et al., 2010, *Nature*, **463**, 919  
 Acero F., et al., 2015, *ApJS*, **218**, 23  
 Angelakis E., et al., 2016, *MNRAS*, **463**, 3365  
 Blandford R. D., Königl A., 1979, *ApJ*, **232**, 34  
 Blinov D., et al., 2015, *MNRAS*, **453**, 1669  
 Blinov D., et al., 2016a, *MNRAS*, **457**, 2252  
 Blinov D., et al., 2016b, *MNRAS*, **462**, 1775  
 Fuhrmann L., et al., 2014, *MNRAS*, **441**, 1899  
 Georganopoulos M., Kazanas D., 2003a, *ApJ*, **589**, L5  
 Georganopoulos M., Kazanas D., 2003b, *ApJ*, **594**, L27  
 Georganopoulos M., Kazanas D., 2004, *New Astron. Rev.*, **48**, 403  
 Ghisellini G., Padovani P., Celotti A., Maraschi L., 1993, *ApJ*, **407**, 65  
 Giannios D., Uzdensky D. A., Begelman M. C., 2009, *MNRAS*, **395**, L29  
 Hovatta T., Tornikoski M., Lainela M., Lehto H. J., Valtaoja E., Tornainen I., Aller M. F., Aller H. D., 2007, *A&A*, **469**, 899

- Hovatta T., Nieppola E., Tornikoski M., Valtaoja E., Aller M. F., Aller H. D., 2008, *A&A*, **485**, 51  
 Hovatta T., Valtaoja E., Tornikoski M., Lähteenmäki A., 2009, *A&A*, **494**, 527  
 Hovatta T., et al., 2014, *AJ*, **147**, 143  
 Kiehlmann S., et al., 2016, *A&A*, **590**, A10  
 King O. G., Blinov D., Ramaprakash A. N., Myserlis I., et al., 2014, *MNRAS*, **432**, 87  
 Komatsu E., et al., 2009, *ApJS*, **180**, 330  
 Lähteenmäki A., Valtaoja E., 1999, *ApJ*, **521**, 493  
 Liodakis I., Pavlidou V., 2015a, *Paper I*, *MNRAS*, **451**, 2434  
 Liodakis I., Pavlidou V., 2015b, *MNRAS*, **454**, 1767  
 Liodakis I., Pavlidou V., Angelakis E., 2016b, preprint, ([arXiv:1610.06561](https://arxiv.org/abs/1610.06561))  
 Liodakis I., et al., 2016a, *MNRAS* submitted  
 Lister M. L., Homan D. C., 2005, *AJ*, **130**, 1389  
 Lister M. L., Marscher A. P., 1997, *ApJ*, **476**, 572  
 Lister M. L., et al., 2009, *AJ*, **137**, 3718  
 Lister M. L., et al., 2013, *AJ*, **146**, 120  
 Marscher A. P., 2014, *ApJ*, **780**, 87  
 Marscher A. P., et al., 2008, *Nature*, **452**, 966  
 Marscher A. P., et al., 2010, *ApJ*, **710**, L126  
 Max-Moerbeck W., et al., 2014, *MNRAS*, **445**, 428  
 Moore R. L., et al., 1982, *ApJ*, **260**, 415  
 Padovani P., Urry C. M., 1992, *ApJ*, **387**, 449  
 Pavlidou V., et al., 2012, *ApJ*, **751**, 149  
 Pavlidou V., et al., 2014, *MNRAS*, **442**, 1693  
 Readhead A. C. S., 1980, *Phys. Scr.*, **21**, 662  
 Readhead A. C. S., 1994, *ApJ*, **426**, 51  
 Readhead A. C. S., Cohen M. H., Pearson T. J., Wilkinson P. N., 1978, *Nature*, **276**, 768  
 Richards J. L., et al., 2011, *ApJS*, **194**, 29  
 Richards J. L., Hovatta T., Max-Moerbeck W., Pavlidou V., Pearson T. J., Readhead A. C. S., 2014, *MNRAS*, **438**, 3058  
 Scheuer P. A. G., Readhead A. C. S., 1979, *Nature*, **277**, 182  
 Urry C. M., Padovani P., 1991, *ApJ*, **371**, 60  
 Venters T. M., Pavlidou V., 2007, *ApJ*, **666**, 128  
 Vermeulen R. C., Cohen M. H., 1994, *ApJ*, **430**, 467

## APPENDIX A: OBSERVED PROBABILITY DENSITY FUNCTIONS

### A1 Intrinsic Delta Function Distribution

If the intrinsic timescale distribution is a Delta function (all events share the same duration in the rest frame in all blazars) in the form of  $\delta(t_i - \frac{t_o}{m})$ , where  $t_i$  is the characteristic timescale of the  $\delta$ -function, Eq. 7 becomes:

$$P(t_o) = \int_{m_{min}}^{m_{max}} \delta(t_i - \frac{t_o}{m}) C(\lambda e^{-\lambda m}) \frac{1}{m} dm. \quad (A1)$$

In order to solve the integral we have to transform  $\delta(t_i - \frac{t_o}{m})$  to  $\delta(m - \frac{t_o}{t_i})$  taking into account that, in general,

$$\delta(g(x)) = \frac{\delta(x - x_0)}{|g'(x)|_{x_0}}. \quad (A2)$$

In our case  $g(m) = t_i - \frac{t_o}{m}$  and  $\delta(m - x_0) = \delta(m - \frac{t_o}{t_i})$ . From Eq. A2 we have:

$$\delta(t_i - \frac{t_o}{m}) = \frac{t_o}{t_i^2} \delta(m - \frac{t_o}{t_i}) \quad (A3)$$

The probability density function of the observed timescales will be:

$$\begin{aligned} P(t_o) &= \int_{m_{\min}}^{m_{\max}} \frac{t_o}{t_i^2} \delta(m - \frac{t_o}{t_i}) C (\lambda e^{-\lambda m}) \frac{1}{m} dm \\ &= \frac{C \lambda}{t_i} e^{-\lambda(t_o/t_i)}. \end{aligned} \quad (\text{A4})$$

The value of C can be calculated as a function of  $t_i$  and  $t_{o,\min}$ ,  $t_{o,\max}$  (the bounds of the observed timescales) by requiring  $P(t_o)$  to be normalized:

$$C = \frac{1}{t_i [e^{-\lambda t_{o,\min}/t_i} - e^{-\lambda t_{o,\max}/t_i}]}. \quad (\text{A5})$$

Thus the probability density function will be:

$$P(t_o) = \frac{\lambda e^{-\lambda(t_o/t_i)}}{t_i [e^{-\lambda t_{o,\min}/t_i} - e^{-\lambda t_{o,\max}/t_i}]}. \quad (\text{A6})$$

Equation A6 can be fitted to the observed data, in order to optimize the characteristic timescale  $t_i$  of the intrinsic  $\delta$ -function

## A2 Intrinsic Uniform Distribution

If all timescales in blazar jets in the rest-frame are equally probable, we can assume an intrinsic uniform distribution in the form of:

$$P(t_i) = \begin{cases} \frac{1}{t_{i,\max} - t_{i,\min}}, & t_{i,\min} \leq t_i \leq t_{i,\max} \\ 0, & t_i \leq t_{i,\min} \text{ or } t_i \geq t_{i,\max} \end{cases} \quad (\text{A7})$$

Using the Heaviside step function defined as:

$$H(x) = \begin{cases} 0, & x < 0 \\ 1, & x > 0 \end{cases} \quad (\text{A8})$$

we can re-write Eq. A7:

$$\begin{aligned} P(t_i) &= \frac{1}{t_{i,\max} - t_{i,\min}} H(t_i - t_{i,\min}) H(t_{i,\max} - t_i) \\ &= \frac{1}{t_{i,\max} - t_{i,\min}} H\left(\frac{t_o}{m} - t_{i,\min}\right) H\left(t_{i,\max} - \frac{t_o}{m}\right). \end{aligned} \quad (\text{A9})$$

Then Eq. 7 becomes:

$$\begin{aligned} P(t_o) &= \frac{C \lambda}{t_{i,\max} - t_{i,\min}} \int_{m_{\min}}^{m_{\max}} \frac{1}{m} e^{-\lambda m} \\ &\quad \times H\left(\frac{t_o}{m} - t_{i,\min}\right) H\left(t_{i,\max} - \frac{t_o}{m}\right) dm. \end{aligned} \quad (\text{A10})$$

Due to the properties of the Heaviside step function (Eq. A8) the observed probability density will be non-zero for  $\frac{t_o}{m} - t_{i,\min} > 0 \Rightarrow m < \frac{t_o}{t_{i,\min}}$  and  $t_{i,\max} - \frac{t_o}{m} > 0 \Rightarrow m > \frac{t_o}{t_{i,\max}}$ . For the bounds of the integral there are four cases, two for the upper and two for the lower bound. For the upper bound either  $m_{\max} > \frac{t_o}{t_{i,\min}}$  and the bound is  $\frac{t_o}{t_{i,\min}}$ , or  $m_{\max} < \frac{t_o}{t_{i,\min}}$  and the bound is  $m_{\max}$ . For the lower bound either  $m_{\min} > \frac{t_o}{t_{i,\max}}$  and the lower bound is  $m_{\min}$ , or  $m_{\min} < \frac{t_o}{t_{i,\max}}$  and the lower bound is  $\frac{t_o}{t_{i,\max}}$ :

If  $m_{\max} < \frac{t_o}{t_{i,\min}}$  then:

$$P(t_o) = \begin{cases} \frac{C \lambda}{t_{i,\max} - t_{i,\min}} \int_{m_{\min}}^{m_{\max}} \frac{1}{m} e^{-\lambda m} dm, & t_o \leq t_{i,\max} m_{\min} \\ \frac{C \lambda}{t_{i,\max} - t_{i,\min}} \int_{t_o/t_{i,\max}}^{m_{\max}} \frac{1}{m} e^{-\lambda m} dm, & t_o \geq t_{i,\max} m_{\min} \end{cases} \quad (\text{A11})$$

If  $m_{\max} > \frac{t_o}{t_{i,\min}}$  then:

$$P(t_o) = \begin{cases} \frac{C \lambda}{t_{i,\max} - t_{i,\min}} \int_{m_{\min}}^{t_o/t_{i,\min}} \frac{1}{m} e^{-\lambda m} dm, & t_o \leq t_{i,\max} m_{\min} \\ \frac{C \lambda}{t_{i,\max} - t_{i,\min}} \int_{t_o/t_{i,\max}}^{t_o/t_{i,\min}} \frac{1}{m} e^{-\lambda m} dm, & t_o \geq t_{i,\max} m_{\min} \end{cases} \quad (\text{A12})$$

Fitting Eq. A11 and A12 to the observed data, we can optimize for  $t_{i,\min}$  and  $t_{i,\max}$  that enter Eq. A9.

## A3 Intrinsic Power Law Distribution

We now assume that the intrinsic timescales in all blazars follow a power law distribution with slope k in the form of:

$$P(t_i) = C_1 t_i^k H(t_i - t_{i,\min}) H(t_{i,\max} - t_i). \quad (\text{A13})$$

$H(t_i - t_{i,\min})$  and  $H(t_{i,\max} - t_i)$  are Heaviside step functions (Eq. A8) in order to account for the truncated range of the intrinsic timescales. Equation 7 becomes:

$$P(t_o) = \int_{m_{\min}}^{m_{\max}} C_1 \left(\frac{t_o}{m}\right)^k H\left(\frac{t_o}{m} - t_{i,\min}\right) H\left(t_{i,\max} - \frac{t_o}{m}\right) C (\lambda e^{-\lambda m}) \frac{1}{m} dm \quad (\text{A14})$$

Setting  $C_2 = C_1 C$ , and following the procedure described in §A2:

If  $m_{\max} < \frac{t_o}{t_{i,\min}}$  then:

$$P(t_o) = \begin{cases} C_2 \lambda t_o^k \int_{m_{\min}}^{m_{\max}} \frac{1}{m^{k+1}} e^{-\lambda m}, & t_o \leq t_{i,\max} m_{\min} \\ C_2 \lambda t_o^k \int_{t_o/t_{i,\max}}^{m_{\max}} \frac{1}{m^{k+1}} e^{-\lambda m}, & t_o \geq t_{i,\max} m_{\min} \end{cases} \quad (\text{A15})$$

If  $m_{\max} > \frac{t_o}{t_{i,\min}}$  then:

$$P(t_o) = \begin{cases} C_2 \lambda t_o^k \int_{m_{\min}}^{t_o/t_{i,\min}} \frac{1}{m^{k+1}} e^{-\lambda m}, & t_o \leq t_{i,\max} m_{\min} \\ C_2 \lambda t_o^k \int_{t_o/t_{i,\max}}^{t_o/t_{i,\min}} \frac{1}{m^{k+1}} e^{-\lambda m}, & t_o \geq t_{i,\max} m_{\min} \end{cases} \quad (\text{A16})$$

We can thus fit a function of the form given in equations A15 and A16 to the observed data to obtain the optimal  $k$ ,  $t_{i,\min}$ , and  $t_{i,\max}$  that enter Eq. A13.

## A4 Intrinsic Exponential Distribution

Assuming that the intrinsic timescales in blazar jets follow an exponential distribution in the form of:

$$P(t_i) = C_3 \nu e^{-\nu t_i}, \quad (\text{A17})$$

where  $C_3$  is the normalization constant, and  $\nu$  is the inverse mean of the distribution, equation 7 becomes:

$$P(t_o) = C C_3 \nu \lambda \int_{m_{\min}}^{m_{\max}} \frac{1}{m} \exp[-(\lambda m + \nu t_o/m)] dm \quad (\text{A18})$$

Fitting Eq. A18 to the observed data we can optimize  $\nu$  that enters Eq. A17.

## A5 Intrinsic Normal and Log-Normal Distributions

Assuming that the intrinsic timescales in all blazars are normally distributed with mean  $\mu$ , and standard deviation  $\sigma$  in the form of:

$$P(t_i) = \frac{1}{\sigma \sqrt{2\pi}} \exp\left[-\frac{(t_i - \mu)^2}{2\sigma^2}\right], \quad (\text{A19})$$

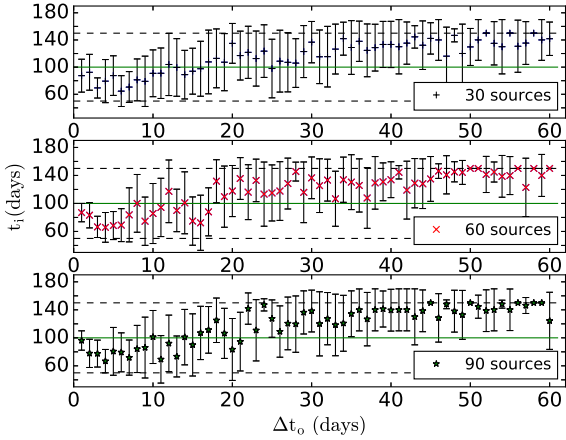


**Figure B1.** Estimated best-fit  $t_i$  versus interval of observations (both in days) for samples with pileup. The black “+” is for the 30 source sample, red “x” for the 60 source sample and the green “\*” for the 90 source sample. The error bars represent the uncertainty of the best-fit  $t_i$ . The green line at 100 days shows the position of the “true” intrinsic timescale, while the black dashed lines at 50 and 150 days show the limits of the parameter space.

equation 7 becomes:

$$\begin{aligned}
 P(t_o) &= C\lambda \int_{m_{\min}}^{m_{\max}} \frac{1}{\sigma\sqrt{2\pi}} \exp\left[-\frac{\left(\frac{t_o}{m} - \mu\right)^2}{2\sigma^2} - \lambda m\right] \frac{1}{m} dm \\
 &= \frac{C\lambda}{\sigma\sqrt{2\pi}} \int_{m_{\min}}^{m_{\max}} \exp\left[-\frac{\left(\frac{t_o}{m}\right)^2 + \mu^2 - 2\mu\frac{t_o}{m}}{2\sigma^2} - \lambda m\right] \\
 &\quad \times \frac{1}{m} dm. \tag{A20}
 \end{aligned}$$

If the logarithm of the intrinsic timescales is normally distributed with mean  $\tilde{\mu}$  and scale  $\sigma_{sc}$  then:

$$P(t_i) = \frac{1}{t_i\sigma_{sc}\sqrt{2\pi}} \exp\left[-\frac{(\ln t_i - \tilde{\mu})^2}{2\sigma_{sc}^2}\right], \tag{A21}$$

The probability density function of observed timescales will be:

$$\begin{aligned}
 P(t_o) &= \frac{C\lambda \exp\left[-\frac{(\ln t_o - \tilde{\mu})^2}{2\sigma_{sc}^2}\right]}{t_o\sigma_{sc}\sqrt{2\pi}} \\
 &\quad \times \int_{m_{\min}}^{m_{\max}} \exp\left[-\frac{(\ln m)^2 + 2\ln m(\tilde{\mu} + \ln t_o) - \lambda m}{2\sigma_{sc}^2}\right] dm. \tag{A22}
 \end{aligned}$$

By fitting equations A20 and A22 to the observed data we can optimize for the mean ( $\mu$ ) and standard deviation ( $\sigma$ ) entering Eq. A19 and the mean ( $\tilde{\mu}$ ) and scale ( $\sigma_{sc}$ ) entering Eq. A21.

The derivation of an analytical solution was only possible for the case of the  $\delta$ -function. The rest of the cases have to be solved either numerically or with the use of Monte-Carlo sampling.

## APPENDIX B: ASSESSING FINITE-SAMPLING SYSTEMATIC EFFECTS

As discussed in §4.2, the finite sampling of a light curve could lead to a systematic offset in the observed timescale distribu-

tion, especially in cases where we are interested in the fastest event observed in a source (e.g. flares). The time duration of events shorter than the time interval between observations will be observed with duration equal to that time interval, thus creating pileups. For this reason, knowledge of the survey  $\Delta t_o$  is important in understanding such observational bias. A simple comparison between  $\Delta t_o$  and the minimum observed timescale can provide insight on the existence (or not) of pileups in the data. The situation becomes even more complicated in highly variable sources where it is possible to observe multiple overlapping flares within a short period of time. The blending of the flares will lead to overestimating their duration according to the survey  $\Delta t_o$ . In this case, a more sophisticated approach is required, one that will take into account such overlap, mitigating the effects of finite sampling (Liodakis et al. 2016a).

Here we focus only on the simple case where the fastest events observed are those with duration equal to the survey  $\Delta t_o$ . To examine the effects and systematic shifts induced by the sampling of our survey in this case, we repeat the procedure described in §4.2. This time, when creating the “simulated-observed” sample, timescales shorter than the time interval of observations are not discarded, but instead are set equal to that time interval. It is clear from Fig. B1 that event pileup results in a significantly larger scatter in the estimated best-fit  $t_i$  with a negative bias for small values of  $\Delta t_o$  and a positive bias for larger values. There are also cases (samples produced with large  $\Delta t_o$ ) where the estimated best-fit parameter is  $t_i \approx 150$  (Fig. B1), which is the upper end of the parameter space. This means that these estimates have a  $\geq 50\%$  error. This effect is to be expected, since we are contaminating our simulated samples with longer timescales according to the chosen  $\Delta t_o$ . Moreover, the majority of cases have their  $1\sigma$  error reaching that level regardless of  $\Delta t_o$ . We conclude that the presence of pileup prevents the method from providing an accurate estimate and will lead to the overestimation of the intrinsic timescales.

Since many events in the time domain of blazar jets are connected to the size of the emission region through causality arguments, such an overestimation would also lead to the overestimation of that region’s size and induce scatter or create artificial correlations between events in the time domain and physical properties of blazar jets. Thus datasets should be treated with great caution with respect to the  $\Delta t_o$  of the survey in the application of the method.

## APPENDIX C: ASSESSING THE EFFECTS OF LIMITED OBSERVING SEASON LENGTH

Our simulations show a surplus of long EVPA rotations (Fig. 9). As discussed in §5 this is due to observational constraints related to the amount of time a source is available, with respect to the total RoboPol observing season length. Although the RoboPol sample was selected so that the sources would be available for the majority of the Skinakas observatory’s observing period, it is not always the case. A limit on the observing season length sets an upper limit on the longest rotation the survey is able to detect, which in the best case scenario is the length of that observing season. Moreover, the time gap between observing seasons can affect the observed duration of any time-like event including

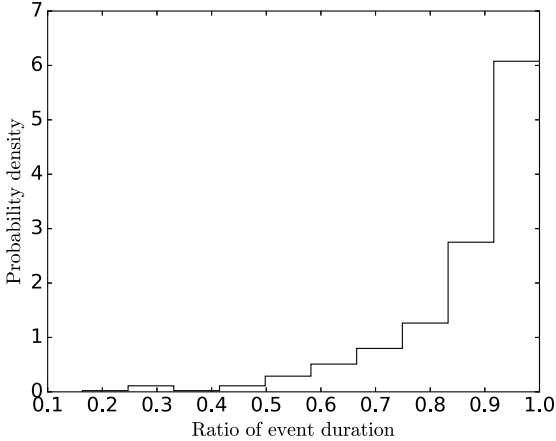


**Figure C1.** Distribution of the ratio of durations ( $T_i/T_{i+1}$ ) for all the EVPA events in each source observed with the definition adopted in this work for the RoboPol flux-limited subsample.

an EVPA rotation. It is often unknown whether a rotation has begun prior to the beginning of the observing season, or if it continues after its end. Thus the observed time duration of an event can be significantly shorter than the “true” duration.

Figure 9 (upper panel) shows the observed distribution of EVPA rotations. There is a peak at  $\sim 40$  days after which the distribution rapidly declines for longer events. Here we examine the possibility that the “true” observed distribution extends to 250 days (approximately the length of the RoboPol observing season) or longer, but the limited availability of the sources prevents us from observing longer rotations than the ones in Fig. 9.

For every source, we sort the observed events by increasing duration, calculate the ratios  $T_i/T_{i+1}$ , and construct the distribution of ratios (Fig. C1) for the whole sample. This ratio is indicative of the spread of the observed durations between one event and the following longer/shorter event. Since each event in a given source is modulated by the same modulator factor, the ratio is independent of any relativistic effects, which allows us to combine all the ratios for individual sources in one distribution.

Using the above distribution, and assuming that the “true” duration of events is uniformly distributed from 3 (the shortest observed duration) to 250 days, we use random sampling to create a simulated dataset of the longest events that would have been observed given all the observational constraints (observing gap, limited availability, random event starting time with respect to beginning and end of the observing season) of the RoboPol survey. We then compare the distribution of simulated durations to the observed (Fig. 9) using the K-S test. We repeat the process  $10^6$  times and calculate the number of trials for which the K-S test could not reject the null hypothesis that the samples are drawn from the same distribution (i.e. the probability value was  $>5\%$ ). We find that  $\sim 0.5\%$  of the trials resulted in a distribution consistent with the observed. If we extend the “true” duration of the events to 500 days, the number of trials drops to  $< 10^{-6}$ . Thus it is unlikely that the “true” observer’s frame duration of EVPA events is much longer,

yet due to observational constraints we are not able to observe them. However, the fact that our method predicts the existence of events longer than what is observed in the data suggests that, although not very significant, there is a bias towards shorter in time events due to the availability of a source. Our findings stress the importance of long term uninterrupted observations in uncovering the true nature of EVPA rotations.

# F-GAMMA: Variability Doppler factors of blazars from multiwavelength monitoring

I. Liodakis<sup>1,2\*</sup>, N. Marchili<sup>4</sup>, E. Angelakis<sup>3</sup>, L. Fuhrmann<sup>3,6</sup>, I. Nestoras<sup>3</sup>, I. Myserlis<sup>3</sup>, V. Karamanavis<sup>3</sup>, T. P. Krichbaum<sup>3</sup>, A. Sievers<sup>5</sup>, H. Ungerechts<sup>5</sup>, J. A. Zensus<sup>3</sup>

<sup>1</sup>*Department of Physics and ITCP†, University of Crete, 71003, Heraklion, Greece*

<sup>2</sup>*Foundation for Research and Technology - Hellas, IESL, Voutes, 7110 Heraklion, Greece*

<sup>3</sup>*Max-Planck-Institut für Radioastronomie, Auf dem Hügel 69, 53121 Bonn, Germany*

<sup>4</sup>*IAPS-INAF, Via Fosso del Cavaliere 100, 00133, Roma, Italy*

<sup>5</sup>*Instituto de Radio Astronomía Milimétrica, Avenida Divina Pastora 7, Local 20, 18012 Granada, Spain*

<sup>6</sup>*ZESS - Center for Sensorsystems, University of Siegen, Paul-Bonatz-Str. 9-11, 57076 Siegen, Germany*

9 January 2017

## ABSTRACT

Recent population studies have shown that the variability Doppler factors can adequately describe blazars as a population. We use the flux density variations found within the extensive radio multi-wavelength datasets of the F-GAMMA program, a total of 10 frequencies from 2.64 up to 142.33 GHz, in order to estimate the variability Doppler factors for 58  $\gamma$ -ray bright sources, for 20 of which no variability Doppler factor has been estimated before. We employ specifically designed algorithms in order to obtain a model for each flare at each frequency. We then identify each event and track its evolution through all the available frequencies for each source. This approach allows us to distinguish significant events producing flares from stochastic variability in blazar jets. It also allows us to effectively constrain the variability brightness temperature and hence the variability Doppler factor as well as provide error estimates. Our method can produce the most accurate (16% error on average) estimates in the literature to date.

**Key words:** galaxies: active – galaxies: jets – BL Lacertae objects: general – processes: relativistic

## 1 INTRODUCTION

Blazars, the sub-class of active galactic nuclei (AGN) with their jet axis pointing towards us, includes the Flat Spectrum Radio Quasars (FSRQs) and BL Lac objects that dominate the  $\gamma$ -ray extragalactic sky. Blazars are characterized by extremely broad-band emission (from long cm radio wavelengths to TeV energies), intense variability at all wavelengths, relativistic boosting of the emitted luminosity and often significantly apparent superluminal motion. Most of these exotic phenomena are attributed to the combination of the relativistic speeds and the alignment of the jet to our line of sight (Blandford & Königl 1979), which obscure our view of their intrinsic properties. The observed properties of blazar jets are modulated by the Doppler factor defined as  $\delta = [\Gamma(1 - \beta \cos \theta)]^{-1}$ , where  $\Gamma = (\sqrt{1 - \beta^2})^{-1}$  is the

Lorentz factor,  $\beta$  the velocity of the jet in units of speed of light, and  $\theta$  the jet viewing angle.

Being one of the most important parameters in the blazar paradigm many methods have been proposed for estimating  $\delta$ . Such methods are the equipartition Doppler factors (Readhead 1994; Guijosa & Daly 1996), the variability Doppler factors (Valtaoja et al. 1999; Lähteenmäki & Valtaoja 1999), the single component causality Doppler factors (Jorstad et al. 2005, 2006), as well as the inverse Compton Doppler factors (Ghisellini et al. 1993), and the  $\gamma$ -ray opacity Doppler factors (Mattox et al. 1993; Dondi & Ghisellini 1995). The equipartition and variability Doppler factors are based on the assumption of equipartition between the energy density of the magnetic field and the radiating particles (Readhead 1994). The former uses the brightness temperature measured from VLBI observations while the latter the variability brightness temperature from flux density variations. The single component causality Doppler factor method uses the observed angular size and variability timescale to calculate the Doppler

\* liodakis@physics.uoc.gr

† Institute for Theoretical and Computational Physics, formerly Institute for Plasma Physics

factor for each individual component. The Doppler factor of a source is then calculated as the weighted mean of the Doppler factors of all the components, with weights inversely proportional to the uncertainty in the apparent velocity of each component. The inverse Compton Doppler factors use the framework of the Synchrotron Self-Compton (SSC) model in order to estimate the expected X-ray flux density given the angular size and flux density of the core from VLBI observations. The Doppler factor is obtained by comparing the observed and the theoretically expected X-ray flux density. The  $\gamma$ -ray opacity Doppler factors use pair production absorption effects resulting from the interaction of  $\gamma$ - and X-rays. Assuming that the emission region has a spherical geometry, that X-rays and  $\gamma$ -rays are co-spatial and that the region is transparent to  $\gamma$ -rays, a lower limit of the Doppler factor can be obtained by relating the variability timescale to the size of the emission region.

Each one of the above methods is using different assumptions, that might not hold. Thus a direct comparison of the results from different methods is unable to provide the answer to which method can best describe blazars. Recent population models (Liidakis & Pavlidou 2015a) have shown that the variability Doppler factor method (Valtaoja et al. 1999; Lähteenmäki et al. 1999; Lähteenmäki & Valtaoja 1999; Hovatta et al. 2009) can adequately describe both the FSRQ and BL Lac populations (Liidakis & Pavlidou 2015b), although application on a source-by-source basis has to be performed with caution. Moreover, an error analysis has shown that although it is the most accurate (30% on average error on each estimate), it suffers from systematics introduced due to the cadence of observations. Since the method involves fitting with exponentials the flux density radio light curves (in order to calculate the variability timescale, flare amplitude, and then the variability brightness temperature), flares faster than the cadence of observations will be unresolved, setting an upper limit to the fastest observed timescale and thus the Doppler factor. We can overcome such limitation in two ways. Either by using data from surveys with high cadence observations such as the Owens Valley Radio Observatory (OVRO)<sup>1</sup> blazar program (Richards et al. 2011) or, as in our case, by modeling the flares.

In this work we use the extensive 8-year-long multi-wavelength radio light curves from the F-GAMMA program<sup>2</sup> (Fuhrmann et al. 2007; Angelakis et al. 2010, 2012; Fuhrmann et al. 2016). The F-GAMMA program monitored a sample of powerful and variable sources detected by the Fermi gamma-ray space telescope<sup>3</sup> (Acero et al. 2015) at ten frequencies from 2.64 up to 142.33 GHz with an approximately monthly cadence (sparse datasets at 228.9 and 345 GHz are also available). Our goals were to distinguish significant events occurring in blazar jets from stochastic variations, and effectively constrain the variability parameters of each source in order to estimate their variability Doppler factor. The method we use to estimate the variability Doppler factors is described in detail in Angelakis et al. (2015). For

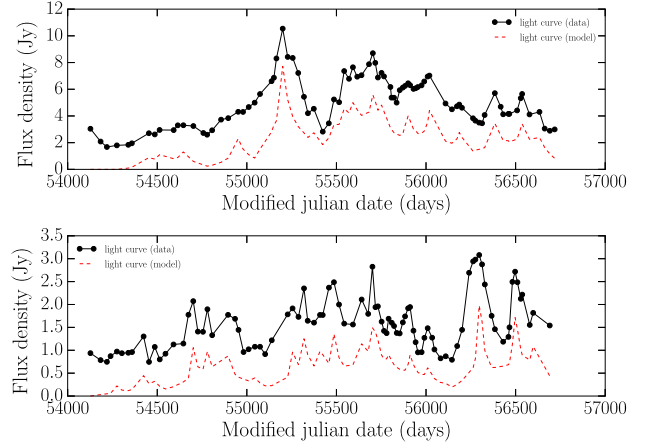


**Figure 1.** Observed (solid black) and simulated (dashed red) light curves for OJ287 (15 GHz, upper panel) and J0721+7120 (10.45 GHz, lower panel) after the flare modeling procedure has been completed.

the purposes of the current work, an error estimation step has been added in our analysis pipeline.

The paper is organized as follows. In Section 2 we give a short description of the methods used. In section 3 we present our estimates for the variability Doppler factors, Lorentz factors, and viewing angles of the sources in our sample, in Section 4 a comparison with estimates from the literature which we use as a proxy to validate our estimates, and in Section 5 we summarize our results.

The cosmological parameters we adopt in this work are  $H_0 = 71 \text{ km s}^{-1} \text{ Mpc}^{-1}$ ,  $\Omega_m = 0.27$  and  $\Omega_\Lambda = 1 - \Omega_m$  (Komatsu et al. 2009).

## 2 METHODS

The calculation of the variability brightness temperatures and Doppler factors of our sources depends on the estimation of their variability characteristics, i.e. the amplitude and time scales of the corresponding flares. The variability characteristics of multiple flares have been evaluated for 58 sources of the F-GAMMA sample using the flare decomposition method of Angelakis et al. (2015). With the addition of an error analysis step, the method consists now of four steps:

(i) **Flare modelling.** This step of the method aims at identifying one basic flare pattern common among all events. The operation is executed separately for source and frequency. At first, all the flares in the light curve need to be localised by the identification of local maxima. Because flares appear at different times and with different amplitudes, the detected events are shifted in time and scaled in flux density so that eventually they are all superimposed on the most prominent event. A lower envelope is then fitted to the pattern that has resulted from this stacking. It is this envelope that we consider as the template flare itself for further analysis.

(ii) **Correlation.** This operation aims at finding the optimum time delays between events at different frequencies.

<sup>1</sup> <http://www.astro.caltech.edu/ovroblazars/>

<sup>2</sup> <http://www3.mpifr-bonn.mpg.de/div/vlbi/fgamma/fgamma.html>

<sup>3</sup> <http://fermi.gsfc.nasa.gov/>

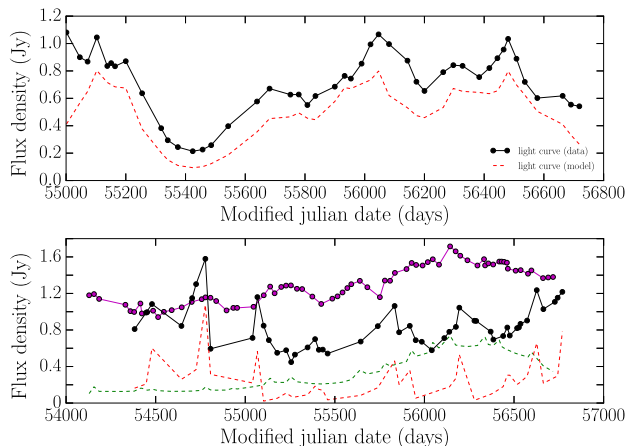


**Figure 2.** Observed (solid black) and simulated (dashed red) light curves for J0050-0929 (8.35 GHz, upper panel) and J0241-0815 (142.33 GHz solid black and dashed red, 10.45 GHz solid magenta and dashed green) after the flare modeling procedure has been completed.

Instead of using a standard cross-correlation function (e.g. Edelson& Krolik 1988; Lehar et al. 1992), which would treat one pair of light curves each time, we simultaneously include them all. A cumulative correlation degree is calculated by multiplying the cross-correlation coefficients of all light curve pairs after applying to them different time shifts. The set of time shifts that returns the highest degree of cumulative correlation defines the optimum average time delays among frequencies. Clearly, the more the available frequencies, the more accurate the estimate of the time shifts is.

(iii) **Flare Characterisation.** Using the temporal information from the previous step (Correlation), this step is meant to identify and characterise the flares that are visible at multiple frequencies, using the model from the first step (Flare modelling). The identification of flares at multiple frequencies ensures that only significant events are taken into account. Since the frequency availability is not constant the number of required frequencies for an event is not strict and it is decided empirically. From the flare decomposition, we can calculate variability timescale and amplitude of each flare, which can be used for the computation of the variability brightness temperature at each frequency (Eq. 1).

(iv) **Error analysis.** This operation is meant to provide an estimate of the uncertainty in the flares characteristics. Both amplitude and timescales are affected by some degree of uncertainty. This uncertainty can be assessed by changing the basic shape of the flare models (both their duration and amplitude) and then repeating the flare characterisation using the modified flare models. To each model we associate a goodness of fit, provided by the standard deviation of residuals. All models for which this value exceeds by more than 10% the goodness of fit of the best model are disregarded. The range of flare time scales and amplitudes for acceptable models set our uncertainty and what we quote as the error of our estimates.

Figures 1 and 2 shows some examples of simulated light curves (having subtracted the baseline) created after the

modeling procedure has been completed. OJ287 (Fig. 1, upper panel) and 0716+714 (Fig. 1, lower panel) are among the fastest sources in our sample; it appears that our method can trace their flux-density variations well. Similarly efficient is the analysis of J0050-0929 (Fig. 2, upper panel), which shows slow variability. Less clear is however the case of J0241-0815 (Fig. 2, lower panel): although we can trace the variability at individual frequencies well, the significant differences in the variability characteristics at different frequencies makes it hard to efficiently trace the evolution of single flares.

The analyzed sources have been classified according to the quality of their analysis results into three categories: very confident, confident, and less confident. The first category includes sources whose variability characteristics, along with the sampling rate, allow to clearly identify and trace the evolution of flares across all available frequencies. The second category includes sources for which some difficulties have been encountered in modeling the light curves; these difficulties (e.g. a gap in the data, high noise in a minority of frequencies) are expected to have mild effects on the estimation of the variability characteristics. Results for sources of the third category should be regarded as least reliable, because of poor sampling, noisy data, or few available frequencies.

Multi-wavelength modeling of flares provides several advantages over a simple fit. Examining the light curves in different frequencies provides valuable information regarding the evolution of the flares, the type of variability in the source (fast or slow), and the quality of each dataset. This information is taken into account during flare modeling.

In addition, the simultaneous use of all light curves allows us to mitigate the issues related to both the cadence of observations and the superposition of multiple flares. This is obtained by exploiting the general decrease of timescales with frequency. Sources with very fast variability can be best modeled at low frequencies, allowing us to trace back the probable location of flares at high frequency, even below the cadence of observations. On the contrary, flares in slowly varying sources can be best recognized at the highest frequencies; knowing their spectral evolution, we can roughly estimate the contribution of each flare to the variability observed at low frequencies, where, due to the long timescales, single flares cannot easily be isolated. Examples of the multi-wavelength light curves can be found in Angelakis et al. (2010, 2012); Fuhrmann et al. (2016) and in the F-GAMMA website<sup>4</sup>.

Given the above considerations, our flare characterization is limited by the cadence of observations at the lowest frequencies. The F-GAMMA sources have a sampling of  $\sim 30$  days and in some cases (sources known to show significant variability e.g. PKS 0716+714)  $\sim 14$  days. Given the typical blazar variability timescales in radio, multi-wavelength information, and the method's ability to mitigate effects of observing cadence, it is rather unlikely any significant event during the F-GAMMA monitoring period has not been accounted for. However, if there are sources in our sample that show variability at timescales significantly shorter than  $\sim 14$  days, our results should be treated with caution.

<sup>4</sup> <http://www3.mpifr-bonn.mpg.de/div/vlbi/fgamma/fgamma.html>

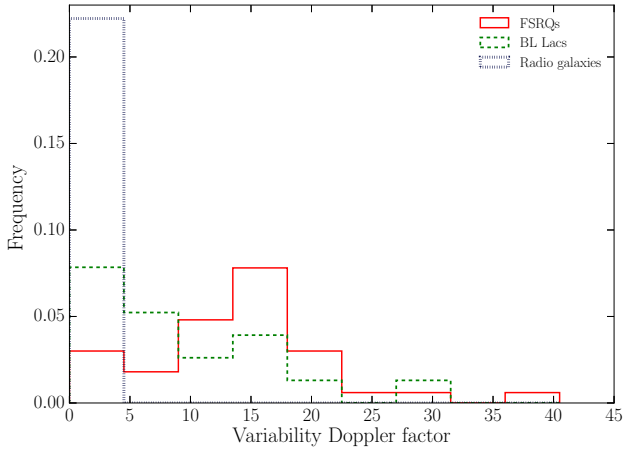


**Figure 3.** Distribution of the variability Doppler factor for the F-GAMMA sources. Solid red is for the FSRQs, dashed green for the BL Lacs, and dotted blue for the radio galaxies in our sample.

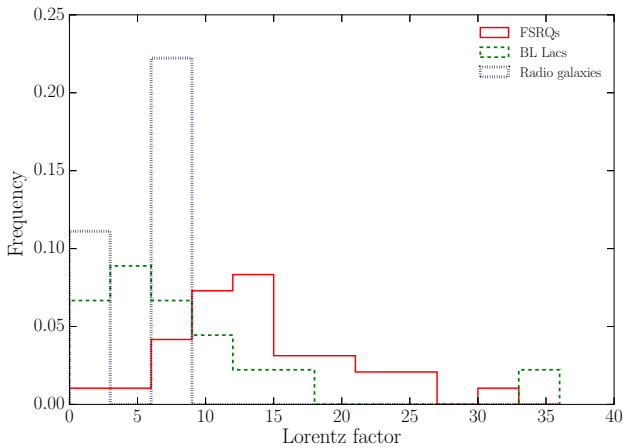


**Figure 4.** Distribution of the Lorentz factor for the F-GAMMA sources. Solid red is for the FSRQs, dashed green for the BL Lacs, and dotted blue for the radio galaxies in our sample.

### 3 VARIABILITY DOPPLER FACTORS

Once the flares have been identified and modeled, their variability characteristics can be estimated. Their amplitude coincides with the flux density at the peak. The timescales of a flare are the time spans between the beginning of the flare and its peak, and between its peak and its end. We define the beginning of a flare as the time at which its flux density exceeds a threshold of 0.25 times the average uncertainty in the flux density measurements. The end of a flare is defined similarly, as the time when the flux density drops below that threshold. This definition helps dealing with flares that extend to very long timescales without carrying any significant contribution to the total flux density.

Through the variability characteristics of flares, the associated variability brightness temperatures can be calculated using the following formula (Eq. 1).

$$T_{\text{var}} = 1.47 \cdot 10^{13} \frac{D_L^2 \Delta S_{\text{ob}}(\nu)}{\nu^2 t_{\text{var}}^2 (1+z)^4}, \quad (1)$$

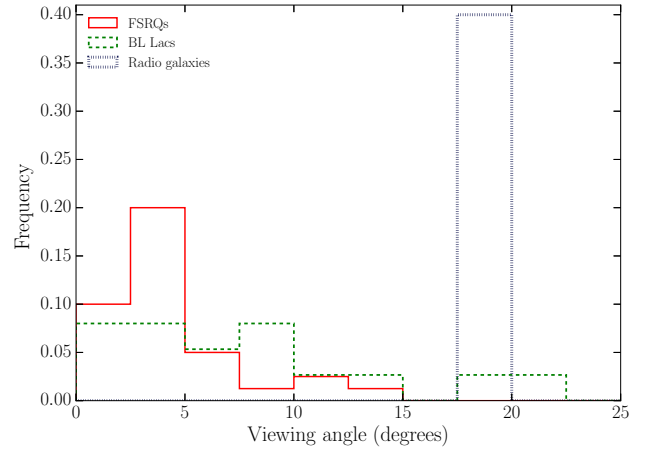


**Figure 5.** Distribution of the viewing angle for the F-GAMMA sources. Solid red is for the FSRQs, dashed green for the BL Lacs, and dotted blue for the radio galaxies in our sample.

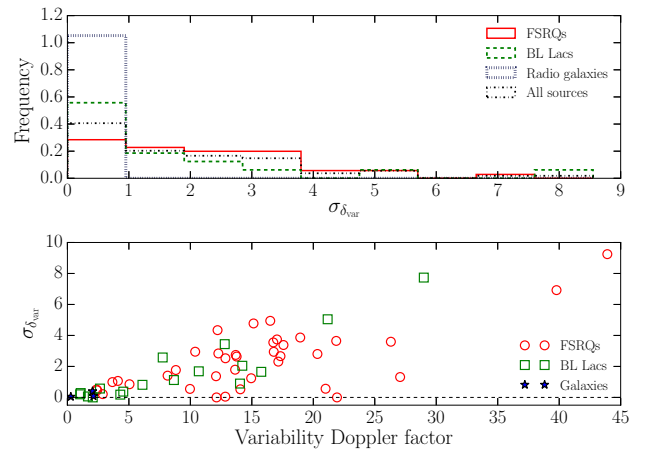


**Figure 6.** Upper panel: Distribution of the error estimates of the variability Doppler factor for the F-GAMMA sources. Solid red is for the FSRQs, dashed green for the BL Lacs, and dotted blue for the radio galaxies, while black dash-dot for the whole sample. Lower panel: Variability Doppler factor versus the error of each estimate. Red circle is for the FSRQs, green square for the BL Lacs, and blue star for the radio galaxies.

where  $T_{\text{var}}$  is the variability brightness temperature in Kelvin,  $D_L$  is the luminosity distance in Mpc,  $S_{\text{ob}}(\nu)$  the flux density in Jy,  $t_{\text{var}}$  the variability timescale in days,  $z$  is the redshift, and  $\nu$  the observing frequency in GHz. The numerical factor is related to units and the geometry of the emitting region. Assuming that while flaring, sources reach equipartition (Readhead 1994), the intrinsic brightness temperature will be equal to the equipartition brightness temperature  $T_{\text{eq}} = 5 \times 10^{10} K$  (Readhead 1994; Lähteenmäki et al. 1999). By comparing the observed and intrinsic brightness temperature we estimate the variability Doppler factor as follows:

$$\delta_{\text{var}} = (1+z) \sqrt[3]{\frac{T_{\text{var}}}{T_{\text{eq}}}}. \quad (2)$$

For the full derivation of Eq. 2 see appendix A. The high-

**Table 1.** Variability Doppler factors, Lorentz factors and viewing angles for the F-GAMMA sample. Column (1) is the F-GAMMA identification, (2) alternative source name, (3) class (B is for BL Lacs, Q for FSRQs, and G for radio galaxies), (4) redshift, (5) variability Doppler factor, (6) error of the variability Doppler factor (7) Lorentz factor, (8) viewing angle, (9) mean apparent velocity, (10) number of flares characterized, (11) number of frequencies used for the calculation, (12) frequency that gave the highest estimate of the variability Doppler factor and (13) confidence on the Doppler factor (0 is for estimates for which we are less confident in our analysis, 1 estimates for which we are confident, and 2 estimates we are very confident in our analysis).

F-GAMMA (ID)	Alt. name	Class	z	$\delta_{var}$	$\sigma_{\delta_{var}}$	$\Gamma$	$\theta$ (deg.)	$\beta_{app}$	No flares	No freq.	$\nu$ (GHz)	Conf.
J0050-0929	0048-097	B	0.634	12.8	3.4	-	-	-	7	9	2.64	2
J0102+5824	0059+5808	Q	0.644	21.9	3.6	12.0	1.5	6.89	8	9	2.64	2
J0136+4751	0133+476	Q	0.859	13.7	2.7	9.5	3.7	8.43	4	7	8.35	2
J0217+0144	PKS0215+015	Q	1.715	27.1	1.3	19.1	1.9	17.30	7	9	2.64	2
J0222+4302	B0219+428	B	0.444	4.3	0.2	-	-	-	3	9	2.64	1
J0237+2848	0234+285	Q	1.206	12.2	4.3	14.9	4.6	14.65	4	9	2.64	2
J0238+1636	0235+164	B	0.940	29.0	7.7	14.6	0.3	2.00	7	9	2.64	2
J0241-0815	0238-084	G	0.005	0.3	0.0	2.0	26.9	0.22	6	8	8.35	0
J0336+3218	PKS0333+321	Q	1.259	2.9	0.2	21.4	10.0	10.66	4	2	86.00	0
J0339-0146	0336-019	Q	0.850	16.7	3.5	12.2	3.2	11.34	5	9	4.85	0
J0359+5057	0355+50	Q	1.520	26.3	3.6	13.2	0.2	1.39	4	10	2.64	1
J0418+3801	B20415+37	G	0.049	2.0	0.4	7.0	20.0	4.85	6	9	2.64	2
J0423-0120	0420-014	Q	0.916	43.9	9.2	22.2	0.3	4.44	8	9	2.64	1
J0433+0521	0430+052	G	0.033	2.1	0.1	6.8	19.9	4.81	4	9	4.85	1
J0530+1331	0528+134	Q	2.070	12.9	2.5	10.8	4.4	10.50	5	7	8.35	2
J0654+4514	S40650+453	Q	0.928	13.8	2.6	-	-	-	6	9	14.6	2
J0719+3307	TXS0716+332	Q	0.779	14.1	0.5	-	-	-	5	7	2.64	0
J0721+7120	0716+714	B	0.328	14.0	0.9	10.8	3.9	10.22	14	10	2.64	2
J0730-1141	PKS0727-115	Q	1.591	39.8	6.9	-	-	-	7	9	2.64	2
J0738+1742	0735+178	B	0.424	4.5	0.4	3.6	12.2	3.30	3	9	4.85	1
J0808-0751	0805-077	Q	1.837	14.9	1.2	24.3	3.5	22.42	4	9	8.35	2
J0818+4222	0814+425	B	0.530	7.8	2.6	4.1	3.2	1.72	5	9	23.05	1
J0824+5552	S40820+560	Q	1.417	2.4	0.5	-	-	-	4	2	86.00	0
J0841+7053	0836+710	Q	2.218	12.1	0.0	19.0	4.4	17.69	1	9	2.64	0
J0854+2006	0851+202	B	0.306	8.7	1.1	7.6	6.6	7.49	10	10	4.85	2
J0920+4441	S40917+449	Q	2.190	5.0	0.9	2.8	6.2	1.45	1	8	4.85	0
J0958+6533	0954+658	B	0.367	10.7	1.7	7.9	5.0	7.31	9	9	2.64	2
J1104+3812	PKS1101+384	B	0.030	1.7	0.1	1.1	8.6	0.14	6	9	2.64	2
J1130-1449	1127-145	Q	1.184	21.9	0.0	13.0	1.9	9.46	4	8	4.85	1
J1159+2914	PKS1156+295	Q	0.725	12.8	0.0	16.6	4.3	16.13	6	9	2.64	2
J1217+3007	PKS1215+303	B	0.130	1.1	0.3	1.0	20.7	0.03	3	8	86.00	0
J1221+2813	QSOB1219+285	B	0.102	2.6	0.6	4.6	19.8	4.08	5	8	2.64	1
J1229+0203	1226+023	Q	0.158	3.7	1.0	12.0	11.3	8.58	6	8	8.35	1
J1256-0547	1253-055	Q	0.536	16.8	2.9	12.3	3.2	11.42	9	9	23.05	1
J1310+3220	1308+326	B	0.997	15.8	1.7	17.1	3.6	16.99	6	9	2.64	1
J1332-0509	PKS1329-049	Q	2.150	18.9	3.9	11.1	2.1	7.70	6	8	4.85	1
J1504+1029	1502+106	Q	1.839	17.3	2.7	11.4	2.8	9.63	5	10	4.85	2
J1512-0905	1510-089	Q	0.360	12.3	2.8	19.0	4.4	17.76	10	9	2.64	2
J1613+3412	1611+343	Q	1.400	2.4	0.5	31.5	9.2	11.93	3	2	86.00	0
J1635+3808	1633+382	Q	1.814	20.3	2.8	14.9	2.6	13.78	8	10	8.35	2
J1642+3948	1641+399	Q	0.593	10.4	2.9	11.3	5.5	11.22	6	9	2.64	2
J1653+3945	1652+398	B	0.033	2.1	0.0	1.3	8.2	0.24	5	9	2.64	0
J1733-1304	PKS1730-130	Q	0.902	17.6	3.4	15.3	3.2	15.09	7	10	42.00	0
J1751+0939	1749+096	B	0.322	14.2	2.0	7.8	2.3	4.36	9	9	2.64	2
J1800+7828	1803+784	B	0.680	21.2	5.0	10.8	0.6	2.53	8	9	2.64	2
J1824+5651	1823+568	B	0.664	1.0	0.2	34.8	13.4	8.36	5	1	86.00	0
J1848+3219	TXS1846+322	Q	0.798	12.1	1.4	7.0	3.2	4.69	7	9	2.64	2
J1849+6705	S41849+670	Q	0.657	8.1	1.4	17.0	6.0	14.48	6	9	4.85	1
J2025-0735	PKS2022-077	Q	1.388	16.5	4.9	24.6	3.3	23.20	7	9	2.64	2
J2143+1743	PKS2141+175	Q	0.213	8.8	1.8	4.7	3.0	2.15	8	9	2.64	2
J2147+0929	2144+092	Q	1.113	13.6	1.8	-	-	-	5	9	2.64	2
J2202+4216	2200+420	B	0.069	6.1	0.8	5.6	9.4	5.49	12	9	2.64	2
J2203+1725	PKS2201+171	Q	1.076	10.0	0.5	8.4	5.7	8.17	4	9	8.35	0
J2203+3145	2201+315	Q	0.295	4.1	1.1	6.3	13.2	5.79	8	5	23.05	0
J2229-0832	2227-088	Q	1.560	21.0	0.6	10.6	0.5	1.92	5	9	4.85	1
J2232+1143	2230+114	Q	1.037	15.1	4.8	8.1	1.9	4.00	8	9	4.85	1
J2253+1608	2251+158	Q	0.859	17.0	3.7	10.4	2.6	7.90	7	10	42.00	2
J2327+0940	PKS2325+093	Q	1.841	17.2	2.3	-	-	-	6	9	4.85	2

est variability brightness temperature observed in a source provides the highest constrain to the variability Doppler factor. The highest estimate for the variability Doppler factor found in each source is the estimate we quote in Table 1.

We calculate the Lorentz factor ( $\Gamma_{var}$ ) and viewing angle ( $\theta_{var}$ ) using Eq. 3, 4 and the apparent velocity ( $\beta_{app}$ ). In order to estimate the mean  $\beta_{app}$ , we use data from the MOJAVE survey (Lister & Homan 2005), for all our sources with available estimates in the literature (Lister et al. 2009, 2013).

$$\Gamma_{var} = \frac{\beta_{app}^2 + \delta_{var}^2 + 1}{2\delta_{var}}, \quad (3)$$

$$\theta_{var} = \arctan \frac{2\beta_{app}}{\beta_{app}^2 + \delta_{var}^2 - 1}. \quad (4)$$

All the estimates for the Doppler factors as well as Lorentz factors and viewing angles are summarized in Table 1. It is obvious that the more flares and frequencies used for the characterization of the light curves, the better we can constrain the variability brightness temperature, and the more confident we are about the results of our analysis. The number on the last column of Table 1 (column 13) denotes our confidence on the estimate. 0 is for the cases that we are less confident in the results of our analysis, 1 is for the cases we are confident, and 2 is for the cases we are very confident. The confidence in the estimate of the Doppler factor depends on the abundance of data points available for each source. Sparse data, large observational gaps or fewer available frequencies could severely hamper tracking the evolution and characterization of the flares which is the basis of our methodology. Such problems in the analysis could lead to the underestimation of the variability brightness temperature. An additional cause for our lack in confidence would be a general lack of flares in a source. For a discussion and notes on the analysis of individual sources see Marchili et al. (in prep.). A more conservative approach to the equipartition brightness temperature would be to use the inverse Compton catastrophe limit  $T_{IC} = 10^{12}K$  (Kellermann & Pauliny-Toth 1969). This would bring our estimates lower by a factor of  $\sim 2.7$ . We chose to use the equipartition limit since the variability Doppler factors using equipartition (Hovatta et al. 2009) best describe the blazar populations (Liidakis & Pavlidou 2015b).

Figure 3 shows the distribution of the variability Doppler factors, Fig. 4 the distribution of Lorentz factors, and Fig. 5 the distribution of viewing angles for the F-GAMMA sources, where solid red is for the FSRQs, dashed green for the BL Lacs and dotted blue for the radio galaxies. FSRQs and BL Lacs (except two BL Lacs) have viewing angles lower than 15 degrees, consistent with the current view of blazars (Ghisellini et al. 1993; Urry & Padovani 1995). The values for the mean and std of the populations are summarized in Table 2.

The FSRQs appear to have higher Doppler factors than the BL Lacs, and both higher than the radio galaxies as expected. The same is the case for the Lorentz factors and the opposite for the viewing angles. The highest Lorentz factor is attributed to the BL Lac object J1824+5651; this estimate, however, falls within the category of the “less confident” results. The high Lorentz factor that we found for this source may be caused by an underestimation of the Doppler factor

**Table 2.** Mean and standard deviation (std) of the Doppler factors, Lorentz factors and viewing angles for the three populations in our sample.

	FSRQ	BL Lacs	Radio galaxies
$\delta_{var}$			
mean	15.21	9.2	1.4
std	8.7	7.6	0.8
$\Gamma_{var}$			
mean	13.9	9.2	5.2
std	6.1	8.8	2.2
$\theta_{var}$ (degrees)			
mean	4.2	7.8	22.2
std	2.9	6.1	3.3

( $\delta_{var} = 1$ ). A higher Doppler factor estimate (even  $\delta_{var} = 2$ ) would bring the value of the Lorentz factor lower than that of the fastest FSRQs with estimates labeled “confident” and “very confident” (J0423–0120  $\Gamma_{var} = 22.2$  and J2025–0735  $\Gamma_{var} = 24.6$  respectively).

The mean value for the Doppler factor for the “confident” and “very confident” estimates ( $\sim 14$ ) is very similar to the overall mean ( $\sim 12$ ). Thus we can conclude that the reliability of the estimates (in these two categories) does not strongly influence the results of our analysis. However for the “less confident” estimates, the mean is  $\sim 6$  while the mean of the apparent velocity (7.6) is similar to the sample mean (8.3) as is the case for the “confident” and “very confident” categories. The resulting  $\Gamma_{var}$  and  $\theta_{var}$  for the “less confident” estimates are larger than that of the sample. There are two possible explanations for this discrepancy. Either there are indeed unaccounted for peculiarities of the analysis which lead to underestimating the Doppler factor for these sources or the majority of the sources labeled “less confident” are slowly variable. In the latter case, their Doppler factors will be low, causing an increase of the value of the Lorentz factor. In that case, the source composition of the category is biasing the results. In either case, estimates labeled as “less confident” should be treated with caution.

In order to assess the significance in possible differences between FSRQs and BL Lacs in our sample, we use the Wilcoxon rank-sum test which gives the probability of two samples to have been drawn from the same distribution (the alternative hypothesis is that values from one sample are more likely to be larger than the other). The probability of the two samples being drawn from the same distribution is 1.1% for the variability Doppler factors, 0.3% for the Lorentz factors, and 4.9% for the viewing angles. Although we cannot reach solid conclusions for the populations, this would imply that FSRQs have on average higher Doppler factors, Lorentz factors, and smaller viewing angles than the BL Lacs (Jorstad et al. 2005; Hovatta et al. 2009; Lister et al. 2013; Liidakis & Pavlidou 2015a).

Figure 6 shows the distribution of the errors in our estimates (upper panel) and the error of each estimate against the value of the Doppler factor (lower panel). The mean of the error distribution for the whole sample is 2.07 with a standard deviation of 1.99. The highest percentage error in our estimates is 35.5%, which is comparable to the most accurate estimates available in the literature ( $\sim 30\%$  error

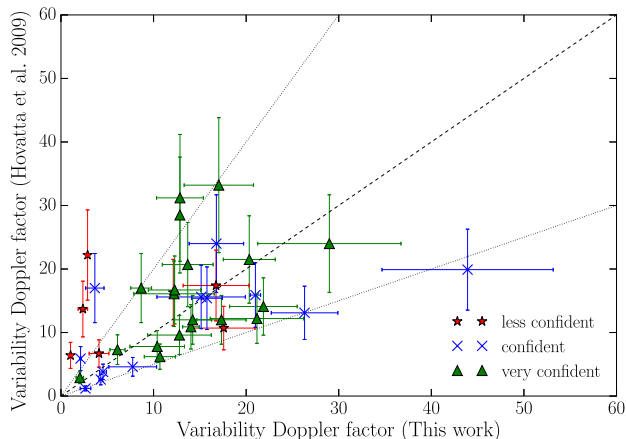


**Figure 7.** Variability Doppler factors (this work) versus the variability Doppler factors from Hovatta et al. (2009). The green triangle is for sources for which we are very confident of our analysis, blue x for the sources we are confident, and red star for the sources we are less confident (see Table 1). The dashed line denotes the  $y = x$  line, whereas the dotted lines mark the factor of two envelope. The error of the  $y$ -axis is the 30% average error derived through population modeling.

on average) as derived from population models. Overall our method has a 16% error on average, making our method the most accurate approach to date.

#### 4 COMPARISON WITH OTHER METHODS

The F-GAMMA sample is not flux-limited or complete, and hence our results (drawn from it) cannot be statistically tested against blazar population models. We can, however, use as a proxy estimates that have been shown to be consistent with the population. We chose to compare our Doppler factors with Hovatta et al. (2009) for two reasons: (a) it is the most recent study on the variability Doppler factors using a different approach for estimating the variability brightness temperature; (b) estimates from Hovatta et al. (2009) have been tested against population models (Liodakis & Pavlidou 2015b) and it was shown that they can adequately describe both the FSRQ and BL Lac populations.

Figure 7 shows the comparison between the variability Doppler factors derived in this work, and the variability Doppler factors from Hovatta et al. (2009). The two samples have 38 sources in common. In Hovatta et al. (2009) the authors comment on how difficult is to determine the exact error of the  $\delta_{var}$ . They provide an upper limit to the error of their estimates by calculating the standard deviation of the different  $\delta_{var}$  for individual well-defined flares in each source. They find a median standard deviation of  $\sim 27\%$ . However, populations models find that the on-average error of their estimates is  $\sim 30\%$ . The error of the  $y$ -axis is the  $\sim 30\%$  average error derived from population modeling (Liodakis & Pavlidou 2015b).

Although there are some discrepancies, the majority of the estimates are within the factor of two envelope and most are within errors. The two-sample Kolmogorov-Smirnov test

(K-S test) yielded a 69.25% probability of consistency between the estimates of the two methods (the null hypothesis is that the two samples are drawn from the same population). Testing for their correlation, the Spearman rank-order correlation yielded a correlation coefficient  $r=0.5$  (-1 negative correlation, 0 no correlation, 1 positive correlation) with a  $\sim 0.1\%$  probability of the two samples being uncorrelated. Excluding the estimates for which we are less confident in our analysis, the K-S test yielded a 94.4% probability of consistency, and the Spearman rank-order a  $r=0.57$  with a  $\sim 0.08\%$  probability of uncorrelated samples. Thus we can conclude that the estimates of the two methods are drawn from the same population.

Our method tends to yield higher estimates of the Doppler factors than those of Hovatta et al. (2009), although this is not confirmed by the Wilcoxon rank-sum test (41.18%). This trend is more prominent at high values of the Doppler factor, which is to be expected since in our approach the effects of cadence of observations are mitigated. On the other hand there are sources for which our estimates are lower. Although some of these estimates fall under our “less confident” category, there are sources for which we are confident in our results. A possible explanation of this discrepancy would be the uncertainty in the estimates in Hovatta et al. (2009). For example, an inadequate fit or fitting what would appear as a flaring event but is instead stochastic variability, could lead to underestimating the timescale and consequently overestimating the Doppler factor. A more probable scenario, given the span (roughly  $\sim 35$  years) of the Metsähovi monitoring program, would be the occurrence of a major flare in each of these sources outside the F-GAMMA monitoring period. This could lead to higher brightness temperatures and hence higher Doppler factors for these sources. The origin of this discrepancy needs to be investigated on the basis of a source-by-source analysis, which is currently in progress. In any case, inconsistencies only concern 9 sources. Their impact on the results of this study is therefore very low.

#### 5 SUMMARY

We used specially designed algorithms in order to identify, track and characterize flares throughout a large number of radio frequencies from 2.64 up to 142.33 GHz with data from the F-GAMMA blazar monitoring program (Fuhrmann et al. 2007; Angelakis et al. 2010, 2012; Fuhrmann et al. 2016). Using the variability brightness temperature obtained with this approach (Angelakis et al. 2015) we were able to calculate the variability Doppler factor (Eq. 2) for 58 sources, for 20 of which no variability Doppler factor had been estimated before, and provide error estimates on a source-by-source basis. Combined with apparent velocities from the MOJAVE survey (Lister & Homan 2005) we calculated the Lorentz factor and viewing angles for 50 sources. All values, as well as additional information on the sources, are listed in Table 1. Our results can be summarized as follows.

- There are differences in the Doppler factor estimates between the BL Lacs and FSRQs. FSRQs appear to have significantly larger Doppler factors and Lorentz factors and

smaller viewing angles consistent with our current understanding of blazars. (Jorstad et al. 2005; Hovatta et al. 2009; Lister et al. 2013; Liidakis & Pavlidou 2015a).

- Both FSRQ and BL Lac populations have higher Doppler and Lorentz factors than the radio galaxies. The viewing angles are typically  $< 15$  degrees for all blazars but one BL Lac object, whereas radio galaxies have viewing angles  $\geq 20$  degrees consistent with our current view on the unification of radio galaxies (Ghisellini et al. 1993; Urry & Padovani 1995).

- The mean error of our estimates is 2.07. Our highest percentage error (35.5%) is comparable to the most accurate estimates available in the literature (30% on average, Hovatta et al. 2009), whereas our on average error is 16%. Thus, our method is the most accurate for estimating the Doppler factor of blazar jets to date, with the unique ability to provide error estimates on a source-by-source basis.

- We compared the Doppler factors derived from this work to estimates from the literature (Hovatta et al. 2009) that have been shown to adequately describe the blazar populations (Liidakis & Pavlidou 2015b). There are very few discrepancies which can be attributed either to uncertainties in the analysis of the literature values or in the analysis presented here. Nevertheless, the two samples are consistent within the errors, as is validated confidently by the Kolmogorov-Smirnov and the Spearman rank-order correlation tests.

The multi-wavelength variability Doppler factors presented here were found to be consistent with the estimates in (Hovatta et al. 2009) that can adequately describe the FSRQ and BL Lac populations (Liidakis & Pavlidou 2015b). Hence, we can conclude that they are not only the most accurate estimates yet, but can also describe blazars as a population, validating our results and stressing the importance and wealth of information that can be obtained from multi-wavelength monitoring programs such as the F-GAMMA.

## ACKNOWLEDGMENTS

The authors would like to thank Talvikki Hovatta, Shoko Koyama, and the anonymous referee for comments and suggestions that helped improve this work. This research was supported by the “Aristeia” Action of the “Operational Program Education and Lifelong Learning” and is co-funded by the European Social Fund (ESF) and Greek National Resources, and by the European Commission Seventh Framework Program (FP7) through grants PCIG10-GA-2011-304001 “JetPop” and PIRSES-GA-2012-31578 “EuroCal”. This research has made use of data from the MOJAVE database that is maintained by the MOJAVE team (Lister et al. 2009). Our study is based on observations carried out with the 100 m telescope of the MPIFR (Max-Planck-Institut für Radioastronomie) and the IRAM 30 m telescope. IRAM is supported by INSU/CNRS (France), MPG (Germany) and IGN (Spain). I. N., I.M. and V.K. were supported for this research through a stipend from the International Max Planck Research School (IMPRS) for Astronomy and Astrophysics at the Universities of Bonn and Cologne.

## APPENDIX A: VARIABILITY DOPPLER FACTOR DERIVATION

We use the expression for the variability brightness temperature (Eq. A1) from Blandford & Königl (1979), and Eq. A2 and A3 in order to obtain the correct expression for the variability Doppler factor.

$$T_{\text{var}} = \frac{D_L^2 \Delta S_{\text{ob}}(\nu)}{2\nu^2 t_{\text{var}}^2 k(1+z)^4}, \quad (\text{A1})$$

$$I(\nu) = \frac{2k\nu^2 T_{\text{var}}}{c^2} = \frac{\Delta S(\nu)}{\theta^2}, \quad (\text{A2})$$

$$\frac{I'(\nu)}{\nu'^3} = \frac{I(\nu)}{\nu^3}, \quad (\text{A3})$$

where  $T_{\text{var}}$  is the variability brightness temperature,  $D_L$  the luminosity distance,  $\nu$  is the frequency,  $t_{\text{var}}$  the variability timescale,  $z$  the redshift,  $I(\nu)$  the intensity,  $k$  Boltzman’s constant,  $c$  the speed of light,  $\Delta S(\nu)$  the flux density, and  $\theta$  the angular size of the source. Primed symbols denote rest-frame quantities. Combining equations A1 and A2:

$$T_{\text{var}} = \frac{D_L^2 I(\nu) \theta^2}{2\nu^2 t_{\text{var}}^2 k(1+z)^4}. \quad (\text{A4})$$

The observed transverse size is:

$$R = \frac{\delta_{\text{var}} c t_{\text{var}}}{1+z} = D_A \theta \Rightarrow \theta = \frac{\delta_{\text{var}} c t_{\text{var}}}{D_A (1+z)}, \quad (\text{A5})$$

where  $D_A$  is the angular diameter distance to the source and  $\delta_{\text{var}}$  the Doppler factor. From Eq. A3 we have that  $I(\nu) = \delta_{\text{var}}^3 I'(\nu)$ . If we take cosmological expansion into account  $I(\nu) = \delta_{\text{var}}^3 I'(\nu)(1+z)^{-3}$  (because  $\nu' = (1+z)\nu$ ). Putting everything in equation A4 then:

$$T_{\text{var}} = \frac{D_L^2 I(\nu)}{2\nu^2 t_{\text{var}}^2 k(1+z)^4} \left( \frac{\delta_{\text{var}} c t_{\text{var}}}{D_A (1+z)} \right)^2. \quad (\text{A6})$$

The angular diameter distance is defined as  $D_A = \frac{D}{1+z}$  and the luminosity distance as  $D_L = D(1+z) \Rightarrow D^2 = \frac{D_L^2}{(1+z)^2}$ . The variability brightness temperature becomes,

$$\begin{aligned} T_{\text{var}} &= \frac{c^2}{2k} \frac{D^2 I(\nu)}{\nu^2 t_{\text{var}}^2 (1+z)^2} \frac{\delta_{\text{var}}^2 c^2 t_{\text{var}}^2}{D^2} \\ &= \frac{c^2}{2k} \frac{I(\nu)}{\nu^2 (1+z)^2} \delta_{\text{var}}^2 c^2 \\ &= \frac{c^2}{2k} \frac{I'(\nu) \delta_{\text{var}}^3 \delta_{\text{var}}^2}{\nu'^2 \delta_{\text{var}}^2 (1+z)^3 (1+z)^2 (1+z)^{-2}} \\ &= \frac{c^2 I'(\nu)}{2k \nu'^2} \frac{\delta_{\text{var}}^3}{(1+z)^3} = \frac{\delta_{\text{var}}^3}{(1+z)^3} T'_{\text{var}} \end{aligned} \quad (\text{A7})$$

Assuming that while flaring the source reaches equipartition between the energy density of the magnetic field and that of the radiating particles (Readhead 1994) we can substitute the intrinsic brightness temperature with the equipartition brightness temperature ( $T_{\text{eq}} = 5 \times 10^{10} \text{ K}$ ),

$$T_{\text{var}} = \frac{\delta_{\text{var}}^3}{(1+z)^3} T_{\text{eq}} \quad (\text{A8})$$

The variability Doppler factor will be:

$$\delta_{\text{var}} = (1+z) \sqrt[3]{\frac{T_{\text{var}}}{T_{\text{eq}}}} \quad (\text{A9})$$

## REFERENCES

- Acero F., et al., 2015, *ApJS*, **218**, 23
- Angelakis E., Fuhrmann L., Nestoras I., Zensus J. A., Marchili N., Pavlidou V., Krichbaum T. P., 2010, preprint, ([arXiv:1006.5610](#))
- Angelakis E., et al., 2012, *Journal of Physics Conference Series*, **372**, 012007
- Angelakis E., et al., 2015, *A&A*, **575**, A55
- Blandford R. D., Königl A., 1979, *ApJ*, **232**, 34
- Dondi L., Ghisellini G., 1995, *MNRAS*, **273**, 583
- Fuhrmann L., Zensus J. A., Krichbaum T. P., Angelakis E., Readhead A. C. S., 2007, in Ritz S., Michelson P., Meegan C. A., eds, American Institute of Physics Conference Series Vol. 921, The First GLAST Symposium. pp 249–251 ([arXiv:0704.3944](#)), doi:10.1063/1.2757314
- Fuhrmann L., et al., 2016, preprint, ([arXiv:1608.02580](#))
- Ghisellini G., Padovani P., Celotti A., Maraschi L., 1993, *ApJ*, **407**, 65
- Guijosa A., Daly R. A., 1996, *ApJ*, **461**, 600
- Hovatta T., Valtaoja E., Tornikoski M., Lähteenmäki A., 2009, *A&A*, **494**, 527
- Jorstad S. G., et al., 2005, *AJ*, **130**, 1418
- Jorstad S. G., et al., 2006, in Miller H. R., Marshall K., Webb J. R., Aller M. F., eds, Astronomical Society of the Pacific Conference Series Vol. 350, Blazar Variability Workshop II: Entering the GLAST Era. p. 149
- Kellermann K. I., Pauliny-Toth I. I. K., 1969, *ApJ*, **155**, L71
- Komatsu E., et al., 2009, *ApJS*, **180**, 330
- Lähteenmäki A., Valtaoja E., 1999, *ApJ*, **521**, 493
- Lähteenmäki A., Valtaoja E., Wiik K., 1999, *ApJ*, **511**, 112
- Liodakis I., Pavlidou V., 2015a, *MNRAS*, **451**, 2434
- Liodakis I., Pavlidou V., 2015b, *MNRAS*, **454**, 1767
- Lister M. L., Homan D. C., 2005, *AJ*, **130**, 1389
- Lister M. L., et al., 2009, *AJ*, **138**, 1874
- Lister M. L., et al., 2013, *AJ*, **146**, 120
- Mattox J. R., et al., 1993, *ApJ*, **410**, 609
- Readhead A. C. S., 1994, *ApJ*, **426**, 51
- Richards J. L., et al., 2011, *ApJS*, **194**, 29
- Urry C. M., Padovani P., 1995, *PASP*, **107**, 803
- Valtaoja E., Lähteenmäki A., Teräsranata H., Lainela M., 1999, *ApJS*, **120**, 95

# Bimodal radio variability in OVRO-40m-monitored blazars

I. Liodakis<sup>1,2\*</sup>, V. Pavlidou<sup>1,2</sup>, T. Hovatta<sup>3,4,5</sup>, W. Max-Moerbeck<sup>6</sup>, T. J. Pearson<sup>7</sup>,  
J. L. Richards<sup>7</sup>, and A. C. S. Readhead<sup>7</sup>

<sup>1</sup>*Department of Physics and ITCP†, University of Crete, 71003, Heraklion, Greece*

<sup>2</sup>*Foundation for Research and Technology - Hellas, IESL, Voutes, 7110 Heraklion, Greece*

<sup>3</sup>*Aalto University Metsähovi Radio Observatory, Metsähovintie 114, 02540 Kylmälä, Finland*

<sup>4</sup>*Aalto University Department of Radio Science and Engineering, P.O. BOX 13000, FI-00076 AALTO, Finland*

<sup>5</sup>*Tuorla Observatory, Department of Physics and Astronomy, University of Turku, Finland*

<sup>6</sup>*Max-Planck-Institut für Radioastronomie, Auf dem Hügel 69, 53121 Bonn, Germany*

<sup>7</sup>*Cahill Center for Astronomy and Astrophysics, California Institute of Technology, 1200 E California Blvd, Pasadena, CA 91125, USA*

28 February 2017

## ABSTRACT

Blazars are known to show periods of quiescence followed by outbursts visible throughout the electromagnetic spectrum. We present a novel maximum likelihood approach to capture this bimodal behavior by examining blazar radio variability in the flux-density domain. We separate quiescent and flaring components of a source’s light curve by modeling its flux-density distribution as a series of “off” and “on” states. Our modeling allows us to extract information regarding the flaring ratio, duty cycle, and the modulation index in the “off”-state, in the “on”-state, as well as throughout the monitoring period of each blazar. We apply our method to a flux-density-limited subsample from the Owens Valley Radio observatory’s 15 GHz blazar monitoring program, and explore differences in the variability characteristics between BL Lacs and FSRQs as well as between  $\gamma$ -ray detected and non-detected sources. We find that: (1) BL Lacs are more variable and have relatively larger outbursts than the FSRQs; (2) unclassified blazar candidates in our sample show similar variability characteristics as the FSRQs; and (3)  $\gamma$ -ray detected differ from the  $\gamma$ -ray non-detected sources in all their variability properties, suggesting a link between the production of  $\gamma$ -rays and the mechanism responsible for the radio variability. Finally, we fit distributions for blazar flaring ratios, duty cycles, and on- and off- modulation indices that can be used in population studies of variability-dependent blazar properties.

**Key words:** galaxies: active – galaxies: jets – processes: relativistic – methods: statistical

## 1 INTRODUCTION

BL Lac objects (BL Lacs) and Flat Spectrum Radio Quasars (FSRQs) constitute a sub-class of active galactic nuclei (AGN) called blazars. Blazars are known for their powerful and highly relativistic jets, which are pointed close to our line of sight (Readhead et al. 1978; Blandford & Königl 1979; Scheuer & Readhead 1979; Readhead 1980). Due to the alignment of the jet, their emission, from radio to the highest energy  $\gamma$ -rays, is dominated by relativistic effects such as boosting of the observed flux and compression of timescales. They show a compact one-sided core-dominated

jet morphology, as well as apparent superluminal motion of the radio jet components propagating downstream of the core as seen through VLBI observations (Readhead et al. 1978; Scheuer & Readhead 1979; Readhead 1980). Such radio components have shown superluminal motions of up to about 50c (Lister et al. 2009, 2013), while they have also been associated with numerous other phenomena such as the production of  $\gamma$ -rays and rotations of the optical polarization plane (Marscher et al. 2008, 2010).

Variability in the radio regime was one of the first identified characteristics of blazars (Dent 1965). Although there are cases of quasi-periodicity (Carrasco et al. 1985; Valtaoja et al. 1985; King et al. 2013), generally the variability is erratic. However, it cannot be fully explained by a stochastic process, due to the appearance of outbursts, often in several frequency bands simultaneously (Aller et al.

\* liodakis@physics.uoc.gr

† Institute for Theoretical and Computational Physics, formerly Institute for Plasma Physics

1999; Hovatta et al. 2008; Max-Moerbeck et al. 2014; Fuhrmann et al. 2014; Blinov et al. 2015; Angelakis et al. 2016; Hovatta et al. 2016), followed by periods of relatively low activity. It has been suggested that such outbursts can be characterized by an exponential rise and decay with the ratio of the respective timescales to be approximately 1.3 (Valtaoja et al. 1999; Lähteenmäki et al. 1999; Lähteenmäki & Valtaoja 1999; Hovatta et al. 2009). The timescale and flux-density amplitude of an outburst can vary from days to months and from comparable, to orders of magnitude higher than the quiescent one (Aller et al. 1999). Thus the radio flux-density curve of a blazar can generally be described by a quiescent level (the minimum radio output of the source), and a series of consecutive aperiodic outbursts on top of that minimum output.

Modeling the variability of blazars has been the subject of several studies. Valtaoja et al. (1988) attempted to separate the quiescent from the flaring flux through multi-wavelength flux-density curves (several frequencies from 4.8-90 GHz). The authors examined the spectrum of each source at periods of minimum flux between outbursts (what they considered as the “constant” flux of the jet), and subtracted it from the source spectrum during an outburst in order to obtain the “variable” flux. Lister (2001) chose to model the blazar flux-density curves (4.8 and 5 GHz) with a shot-noise process (Lister 2001, and references therein). Using Poisson statistics [and the exponential profile for the flares described in Valtaoja et al. (1999); Lähteenmäki et al. (1999); Lähteenmäki & Valtaoja (1999)] the authors investigated the variability duty cycles and sample selection biases due to variability in blazars.

The interest in the subject is well-motivated: understanding the general variability properties of blazars in different frequencies can provide important information on their emission mechanisms as well as the location of the emission region. Although rest-frame time delays between frequencies are necessary to constrain the location of emission regions on a source-by-source basis (Fuhrmann et al. 2014; Max-Moerbeck et al. 2014), differences in the variability properties at different frequency bands could be indicative of the spatial connection of their respective emission regions on a population level.

The OVRO 40m monitoring program (Richards et al. 2011, 2014) provides a unique opportunity for studies of blazar radio variability, thanks to its unprecedented sample size and cadence (about 1800 sources observed twice weekly on average over 8 years). OVRO data from 2 years of monitoring were used in Richards et al. (2011) to examine blazar variability and amplitudes using a likelihood approach. Modeling each source’s flux-density distribution by a single Gaussian distribution, the “intrinsic” mean flux-density and modulation indices (what one would have observed in the limit of infinite accuracy and sampling) were estimated. The authors used these results to uncover a statistically significant discrepancy between the radio variability (as quantified by the intrinsic modulation index) of  $\gamma$ -ray loud and  $\gamma$ -ray quiet sources that were otherwise similar. For this reason, the radio intrinsic modulation index has since been used to select  $\gamma$ -ray quiet sources that are as similar in their radio properties as possible to  $\gamma$ -ray loud blazars, for monitoring in other frequencies (e.g. Pavlidou et al. 2014; Angelakis et al. 2016).

The likelihood formalism used by Richards et al. (2011) provides a robust way to account for observational uncertainties and finite cadence as well as calculate uncertainties for the estimated quantities, but at the expense of model-independence. In this case, model-dependence enters through the assumption that a single-Gaussian is a good description of the distribution of flux-densities. If that assumption is not valid for some sources, this can affect the results in two ways. First, any estimated quantities that are sensitive to the assumed underlying family of flux-density distributions may exhibit systematic offsets. Most importantly, these offsets could *not* be accounted for by the calculated uncertainties, which are statistical and based on the assumption that the underlying distribution model holds (see e.g., Mouschovias & Tassis 2010). Second, important information regarding the detailed behavior of the source (such as bimodality in the flux-density distribution) is lost through the simplified treatment.

As discussed in Richards et al. (2011), some of the OVRO 40m-monitored blazars show a flux-density distribution that can be well described by a single Gaussian, while others show a bimodal distribution. To remedy the first of the two problems described above (i.e. cases where a single Gaussian model is not a good description of the flux-density distribution) Richards et al. (2011) used, and reported, only quantities that their method estimates robustly. Such quantities are the mean flux and the modulation index, in contrast, for example with the most likely flux of a source. A typical example of such a source is BL Lac, the flux distribution of which (using the full 8 years OVRO dataset) is shown in Fig. 1. The maximum-likelihood single Gaussian for this data set is overplotted with the dashed line. As BL Lac is very bright, and the observational uncertainties are very small compared to the typical flux ( $< 2\%$ ), we do not expect the uncertainties to widen the flux distribution significantly, or, conversely, the maximum-likelihood distribution to be appreciably narrower than the data. Indeed, this is the case in Fig. 1. The source exhibits bimodality. For this reason, the maximum-likelihood single Gaussian is *not* a good description of the underlying flux-density distribution. As a result, while the single-Gaussian mean and spread are clearly reasonable representations of the corresponding parameters of the data distribution, the most-likely flux is missed by the single Gaussian, and information such as the flaring ratio (ratio of the mean “on”-state flux-density to “off”-state flux density  $R = S_{\text{on}}/S_{\text{off}}$ ) is lost. On the other hand, a model that can account for the bimodality of the sources can recover this important information. Such a model is particularly important given the large size, good sampling, low noise and statistical completeness of the dataset at hand.

In this work, we extend the formalism of Richards et al. (2011) in order to model the observed blazar variability as an alternation between a low-flux state and a high-flux state with the possibility of different degrees of variations about the mean flux of each state. The physical interpretation of such a model is that blazars spend a fraction of their time in a state characterized by relatively low or no activity, and the remaining time in a state of increased variability and outbursts. This way we attempt to separate the quiescent and flaring components of the flux-density distribution of each source, and examine the general variability characteristics, as well as differences between different blazar subclasses.

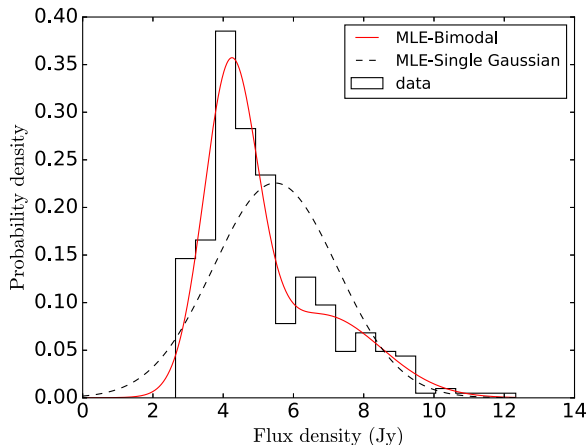


**Figure 1.** Distribution of the 15 GHz flux-density of BL Lac. The red line represents the maximum likelihood fit of the bimodal model whereas the dashed black is the fit for the single Gaussian model (Richards et al. 2011).

The paper is organized as follows. In section 2 we present the maximum likelihood formalism we developed in order to model the blazar flux-density distributions. In section 3 we present the sample used in this work. In section 4 we compare the results from our model with that of a single Gaussian distribution and test the bimodality of the flux-density distributions of the sources in our sample. In section 5 we derive best-fit distributions of all quantities characterizing bimodal variability for the blazar population and we compare the variability characteristics of different blazar subsamples. Finally in section 6 we summarize and discuss our findings and conclusions.

The cosmological parameters we adopt in this work are  $H_0 = 71 \text{ km s}^{-1} \text{ Mpc}^{-1}$ ,  $\Omega_m = 0.27$  and  $\Omega_\Lambda = 1 - \Omega_m$  (Komatsu et al. 2009).

## 2 MAXIMUM LIKELIHOOD ANALYSIS

At any time of observation the flux-density ( $S$ ) emitted by a source, given the observational uncertainty (which we assume to be Gaussian), can be described as

$$P(S|S_{\text{obs}}, \sigma_{\text{obs}}) = \frac{1}{\sigma_{\text{obs}} \sqrt{2\pi}} \exp \left[ -\frac{(S - S_{\text{obs}})^2}{2\sigma_{\text{obs}}^2} \right], \quad (1)$$

where  $S_{\text{obs}}$  is the observed flux-density, and  $\sigma_{\text{obs}}$  is the error on the measurement. We model the flux-density distribution of blazars as a sequence of two states dubbed “off” and “on”. Each state can be assumed to follow a Gaussian distribution similarly to Richards et al. (2011). The “off”-state describes the period of time a blazar spends in quiescence, while the “on”-state the period of time a blazar spends flaring. Then the probability density function of the blazar emitting a certain flux-density will be given by,

$$P(S|f_t, S_{\text{off}}, S_{\text{on}}, \sigma_{\text{off}}, \sigma_{\text{on}}) = \frac{1-f_t}{\sigma_{\text{off}} \sqrt{2\pi}} \exp \left[ -\frac{(S - S_{\text{off}})^2}{2\sigma_{\text{off}}^2} \right] + \frac{f_t}{\sigma_{\text{on}} \sqrt{2\pi}} \exp \left[ -\frac{(S - S_{\text{on}})^2}{2\sigma_{\text{on}}^2} \right], \quad (2)$$

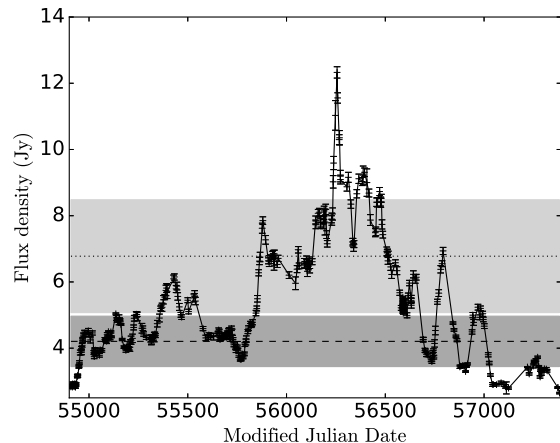


**Figure 2.** OVRO radio (15 GHz) light curve of BL Lac. The dashed line marks the mean flux-density of the “off”-state while the dotted line the mean flux-density of the “on”-state. The dark grey and light grey shaded areas are the 1-standard deviation of the “off”-state and “on”-state flux-densities respectively.

where  $f_t$  is the duty cycle,  $S_{\text{off}}$  is the mean flux-density of the “off”-state,  $\sigma_{\text{off}}$  is the standard deviation of the mean flux-density of the “off”-state,  $S_{\text{on}}$  is the mean flux-density of the “on”-state, and  $\sigma_{\text{on}}$  is the standard deviation of the mean flux-density of the “on”-state.

Marginalizing over all possible flux-densities  $S$  (limits of the integral from  $-\infty$  to  $\infty$ , see Venters & Pavlidou (2007); Richards et al. (2011) for a detailed derivation of the integral), the likelihood of observing  $f_t$ ,  $S_{\text{off}}$ ,  $S_{\text{on}}$ ,  $\sigma_{\text{off}}$ , and  $\sigma_{\text{on}}$  given a flux-density  $S_{\text{obs}}$  and error  $\sigma_{\text{obs}}$  is,

$$l_{\text{obs}} = \frac{1-f_t}{\sqrt{2\pi}(\sigma_{\text{off}}^2 + \sigma_{\text{obs}}^2)} \exp \left[ -\frac{(S_{\text{off}} - S_{\text{obs}})^2}{2(\sigma_{\text{off}}^2 + \sigma_{\text{obs}}^2)} \right] + \frac{f_t}{\sqrt{2\pi}(\sigma_{\text{on}}^2 + \sigma_{\text{obs}}^2)} \exp \left[ -\frac{(S_{\text{on}} - S_{\text{obs}})^2}{2(\sigma_{\text{on}}^2 + \sigma_{\text{obs}}^2)} \right]. \quad (3)$$

The first term of Eq. 3 describes the “off”-state, while the second the “on”-state. For a number of observations  $N$  ( $j = 1, 2, 3 \dots N$ ), the likelihood function is,

$$\mathcal{L} = \prod_{j=1}^N l_{\text{obs},j} \Rightarrow \log \mathcal{L} = \sum_{j=1}^N \log l_{\text{obs},j}. \quad (4)$$

We use the Simplex algorithm (also known as Nelder-Mead, Nelder & Mead 1965) implemented in the `scipy.optimize.minimize` python package to minimize the negative log-likelihood, and thus to maximize the likelihood. After several trials with different methods and minimizing routines implemented in various programming environments, the Simplex algorithm was proven to be the most consistent and stable, given the task at hand.

Given the complexity of the likelihood function, in order to avoid numerical instabilities and possible sensitivity to initial conditions, we perform the minimization  $10^3$  times, each time with random initial conditions, and choose as the best-fit parameter estimates those that gave the minimum function value. Figure 1 shows the maximum likelihood fit of our method to the 15 GHz flux-density distribution of BL Lacertae while Fig. 2 shows the OVRO light curve. The

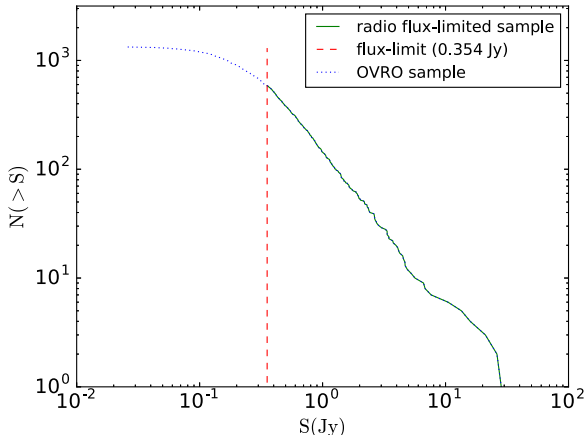


**Figure 3.** Source count distribution for the OVRO sources. The red dashed line marks the flux limit at 0.354 Jy.

horizontal lines mark the mean flux-densities of the “off”- and “on”-states and the grey shaded areas their 1-standard deviation.

To derive the error on our estimated parameter values, we use the Fisher information matrix. The information matrix gives a measure of the amount of information every parameter carries on the curvature of the likelihood at the best-fit values. From the information matrix, we calculate the variance-covariance matrix. The error on each parameter estimate is the square root of the corresponding diagonal element of the variance-covariance matrix. It is possible that the matrix is not positive definite. Since the likelihood is multi-parametric, this would suggest that two or more parameters are anti-correlated. In such a case, we estimate the error of that parameter using a slice of the likelihood surface parallel to the axis of the parameter of interest, with the values of the other parameters set at their best-fit values (i.e., a slice passing through the maximum likelihood point). Using that slice, we determine the values of the parameters that reduce the likelihood by factor  $e^{-1/2}$  (in a Gaussian slice, this would be the  $\pm 1\sigma$  points). These two values set the  $1\sigma$  uncertainty on that parameter.

The method described above can provide robust results as long as the number of observations is sufficiently large. In the application of our method (see section 3) the number of observations per source is 421 on average with a standard deviation of 89 (minimum 217 and maximum 1108).

### 3 SAMPLE

We apply our method to data from the Owens Valley Radio Observatory’s (OVRO) 15 GHz blazar monitoring program<sup>1</sup> (Richards et al. 2011). OVRO has been monitoring a sample of >1800 blazars in support of the *Fermi* Gamma-ray Space Telescope (*Fermi*, Acero et al. 2015) with an approximate cadence of twice per week since 2007. The monitoring program began using the 1158 sources from the Candi-

<sup>1</sup> <http://www.astro.caltech.edu/ovroblazars/>

**Table 1.** Mean parameter values and probabilities for the Wilcoxon and K-S test that the  $S$  and  $m$  parameters estimated by the two models (single-Gaussian and bimodal) are consistent (drawn from the same distribution).

Parameter	Single (mean)	Bimodal (mean)	Wilcoxon (%)	K-S (%)
$S$	1.11	1.11	90.0	99.5
$m$	0.18	0.20	0.28	1.26

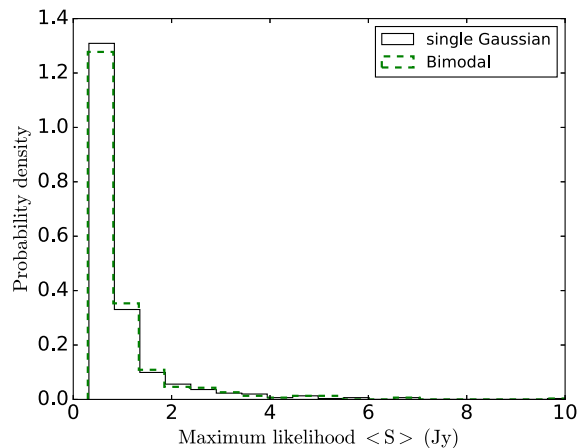


**Figure 4.** Distribution of the maximum likelihood  $\langle S \rangle$  for the single Gaussian and bimodal models.

date Gamma-ray Blazar Survey (CGRaBS) complete sample (Healey et al. 2008). Since then, however, to facilitate monitoring of additional sources detected by *Fermi*, the sample has increased by approximately 1/2 of its original size. In order to maintain the statistical integrity on the sample under investigation while taking advantage of the additional  $\gamma$ -ray sources that were added later, we construct a new statistically complete sample (a flux-density-limited one), as follows: we use the maximum likelihood mean flux-density from Richards et al. (2014) to plot the source count distribution for all OVRO monitored sources (Fig. 3). The flux limit is set at 0.354 Jy which is where the distribution shape starts to deviate from a power law. The final sample consists of 584 sources; 435 FSRQs, 81 BL Lacs, and 68 other sources (which we dubbed U-R), 17 of which are classified as radio galaxies and 51 as possible blazar or unidentified. We follow the classification of Richards et al. (2011, 2014) (and references therein) i.e. objects with broad emission lines in optical are classified as FSRQs whereas objects with weak or even no emission lines are classified as BL Lacs. We have included data from 05/01/2008 to 14/02/2016.

### 4 SINGLE GAUSSIAN VERSUS BIMODAL

Using the method described in section 2 we fit the flux-density distribution of every source in the flux-limited subsample defined above, in order to extract their variability properties. It is not necessary that the flux-density distribution of a source is described well by a “off”-“on” model.

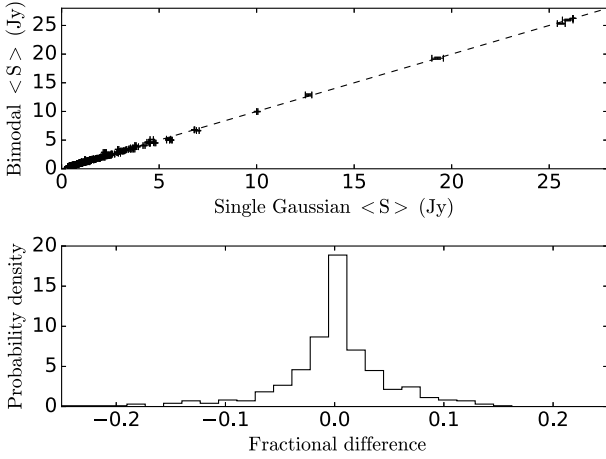


**Figure 5.** Upper panel: Bimodal MLE  $\langle S \rangle$  versus single Gaussian MLE  $\langle S \rangle$ . The dashed line corresponds to  $y = x$ . Lower panel: Distribution of the fractional difference between the bimodal  $\langle S \rangle$  and single Gaussian  $\langle S \rangle$ .

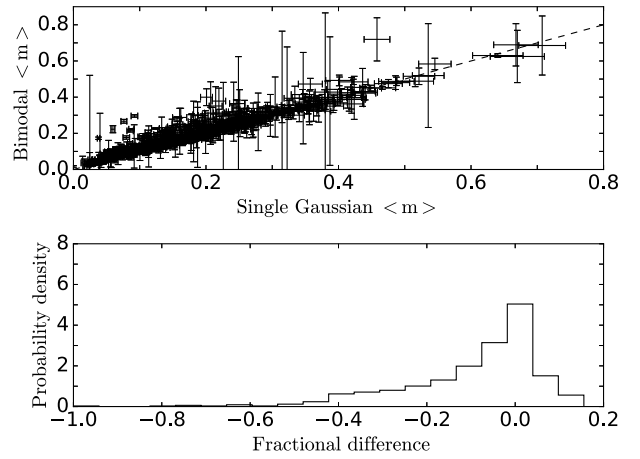


**Figure 7.** Upper panel: Bimodal MLE  $\langle m \rangle$  versus single Gaussian MLE  $\langle m \rangle$ . The dashed line corresponds to  $y = x$ . Lower panel: Distribution of the fractional difference between the bimodal MLE  $\langle m \rangle$  and single Gaussian MLE  $\langle m \rangle$ .

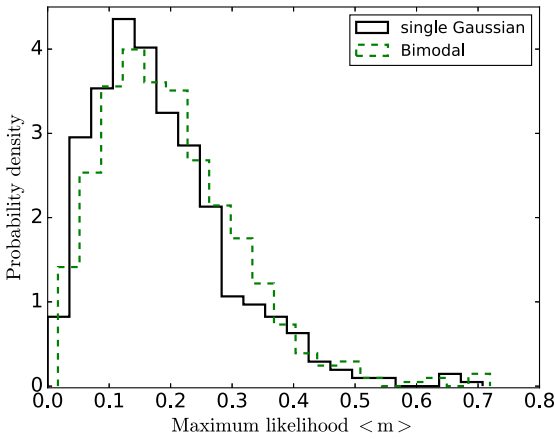


**Figure 6.** Distribution of the intrinsic modulation index for the single Gaussian and bimodal models.

It is very well possible that a source resides in either state for the entire duration of the monitoring period, which is roughly 8 years. In this case, the maximum likelihood best-fit model is degenerate. Models with duty cycle  $f_t = 1$ ,  $f_t = 0$ , or two identical states with  $f_t = 0.5$  are mathematically possible and describe the same single Gaussian distribution. For this reason, in this section we compare the results of our model and the single Gaussian model as in Richards et al. (2011) (fit to the 8-year dataset) in order to understand which model best describes the data, and identify all sources with such degeneracy. For the purposes of our analysis we use the Kolmogorov-Smirnov test (K-S test) and the Wilcoxon rank-sum test (Wilcoxon test). The K-S test gives the probability of two samples being drawn from the same distribution, while the Wilcoxon test gives the same probability but with the alternative hypothesis that the values of one sample are systematically larger than those of the

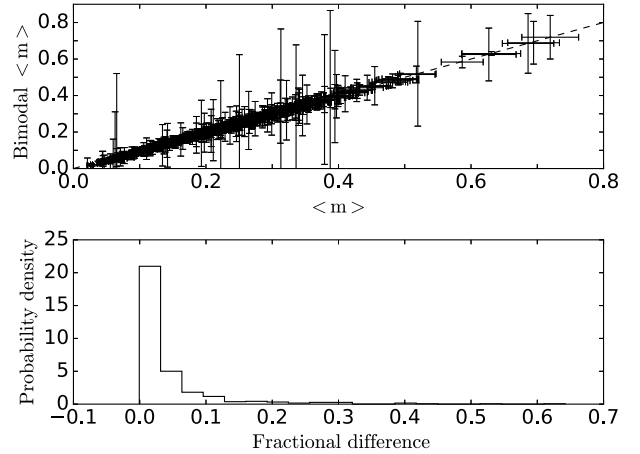


**Figure 8.** Upper panel: Bimodal likelihood  $\langle m \rangle$  versus sample  $\langle m \rangle$ . The dashed line corresponds to  $y = x$ . Lower panel: Distribution of the fractional difference between the bimodal MLE  $\langle m \rangle$  and sample  $\langle m \rangle$ .

other. For any probability higher than 5% we accept that neither test can reject the null hypothesis that the two samples are drawn from the same distribution. Only 52 sources (8.9%) can be well-described by a single-Gaussian model. For the purposes of the population studies (see section 5) we have excluded these sources from our analysis. The excluded sources also account for cases where the source has no significant variability, since the flux-density distribution of such a source would be consistent with a single narrow Gaussian distribution.

We next proceed to a comparison between the overall mean flux-density and modulation index (in contrast to the mean and modulation index of the individual variability states) of the bimodal model with the corresponding qualities of the single-Gaussian model, in order to evalu-

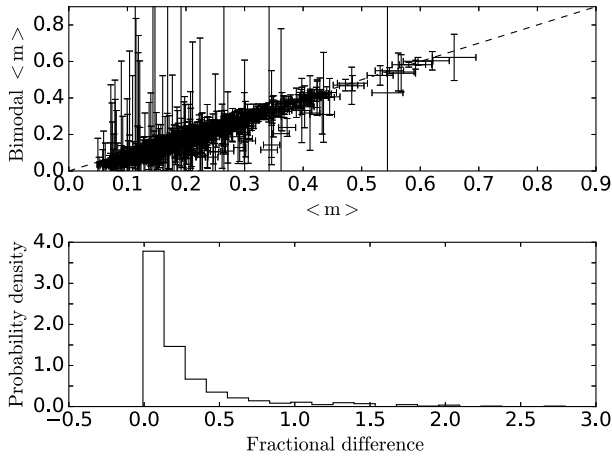


**Figure 9.** Upper panel: Bimodal MLE  $\langle m \rangle$  versus sample  $\langle m \rangle$  for the sources below the flux-density limit. The dashed line corresponds to  $y = x$ . Lower panel: Distribution of the fractional difference between the bimodal MLE  $\langle m \rangle$  and sample  $\langle m \rangle$  for the sources below the flux-density limit.

ate any systematic effects on these quantities due to the single-Gaussian assumption.

From the definition of the mean and variance, the mean flux-density of the bimodal distribution is equal to,

$$\langle S \rangle = (1 - f_t)S_{\text{off}} + f_t S_{\text{on}}, \quad (5)$$

and the variance is

$$\text{Var} = [(1 - f_t)(\sigma_{\text{off}}^2 + S_{\text{off}}^2) + f_t(\sigma_{\text{on}}^2 + S_{\text{on}}^2)] - \langle S \rangle^2. \quad (6)$$

Using Eq. 5 and 6 the overall modulation index is equal to  $\langle m \rangle = \sqrt{\text{Var}/\langle S \rangle}$ . We calculate the overall mean flux-density and intrinsic modulation index for each of our sources, and compare it with the corresponding values from a single Gaussian model from Richards et al. (2011). In order to estimate uncertainties on  $\langle S \rangle$  and  $\langle m \rangle$  we use the uncertainties estimated by the likelihood analysis for  $f_t$ ,  $S_{\text{on}}$ ,  $S_{\text{off}}$ ,  $\sigma_{\text{on}}$ , and  $\sigma_{\text{off}}$ , and standard error propagation.

For the mean flux-density the mean of the two samples is the same with both tests, while both K-S and Wilcoxon tests allow for the hypothesis that the samples are drawn from the same distribution (Table 1). Figure 4 shows the distribution of the overall  $\langle S \rangle$  for the single Gaussian (solid black line) and bimodal (dashed green line) models and Fig. 5 shows the comparison of the two models for individual sources (upper panel) and the distribution of the fractional difference  $(\langle S_{\text{Gaussian}} \rangle - \langle S_{\text{Bimodal}} \rangle) / \langle S_{\text{Bimodal}} \rangle$ , between models (lower panel). It is clear that the mean is very robust against the single-Gaussian assumption. The distribution of fractional differences is symmetric about zero, indicating that there is no bias in the mean introduced by the single-Gaussian assumption.

For the modulation index, Fig. 6 shows the distribution of the overall  $\langle m \rangle$  for both models and Fig. 7 shows the comparison of the two models for individual sources (upper panel) and the distribution of their fractional difference (lower panel). Both K-S and Wilcoxon test indicate disagreement between the two estimates, although not at extremely high significance (Table 1). The scatter between

models is larger than with the  $\langle S \rangle$  (Fig. 7). However, for most sources the values are consistent within uncertainties, and the fractional difference (lower panel of Fig. 7) is generally less than 20% with the exception of very few sources. For this reason, we do not expect the single-Gaussian assumption to have had a strong impact on the statistical comparison between populations in Richards et al. (2011) and Richards et al. (2014). It is nevertheless worth noting that the single-Gaussian assumption introduces a negative bias in the modulation index: the distribution of fractional difference between models is not symmetric about zero (mean  $\approx -0.09$ , median  $\approx -0.04$ ) with the single-Gaussian model tending to underestimate the modulation index and the overall variability of the sources.

The discrepancy originates from the fact that, for a source well-described by a bimodal distribution (e.g. Fig. 1), a single Gaussian model would favor the dominant peak (in that case the “off”-state) and attempt to accommodate the alternate state in the tail of the distribution. That is why although the  $\langle S \rangle$  derived by the two models are consistent, the  $\langle m \rangle$  are not.

On the other hand, if we compare the overall  $\langle m \rangle$  from the bimodal model (maximum-likelihood estimate, MLE) with a standard sample  $\langle m \rangle$  (ratio between sample standard deviation and sample mean, Fig. 8) we find that they are in good agreement within uncertainties. The Wilcoxon test yields a 45% and the K-S test a 87% probability of consistency respectively. In order to arrive to such result, two conditions need to be met. First, the model we have assumed (bimodal) has to be a good description of the underlying distribution of the sources, and second the observational errors have to be relatively small compared to the intrinsic variability of the sources. The latter is expected for the sources in our sample, because of the two filters we have used: a relatively high flux-density limit (which ensures that fractional observational uncertainties are low), and the rejection of sources well-described by a single-Gaussian (which ensures that the remaining sources are significantly variable). To test whether this is indeed the case we perform the same analysis, but for the fainter sources observed by OVRO that were not bright enough to be in our flux-density-limited subsample. For the fainter sources ( $\langle S \rangle \leq 0.354 \text{ Jy}$ , the flux-density limit) the observational errors are relatively larger and will contribute more to the overall variance. We find that the fractional difference increases (Fig. 9), with both tests (Wilcoxon, K-S) rejecting the null hypothesis that the two estimates of  $\langle m \rangle$  are drawn from the same distribution, as expected. Thus, for the brightest and most variable sources, the ability of the maximum likelihood approach to take errors into account does not provide a significant improvement on the overall estimate of  $\langle m \rangle$  over the simple direct standard deviation-over-mean estimate from the data. However, even for these sources the model introduced in this work has the advantages that: (a) it allows us to separate quiescent and flaring states; and (b) it provides information on the variability of each state, flaring ratio and duty cycle on a source-by-source basis.

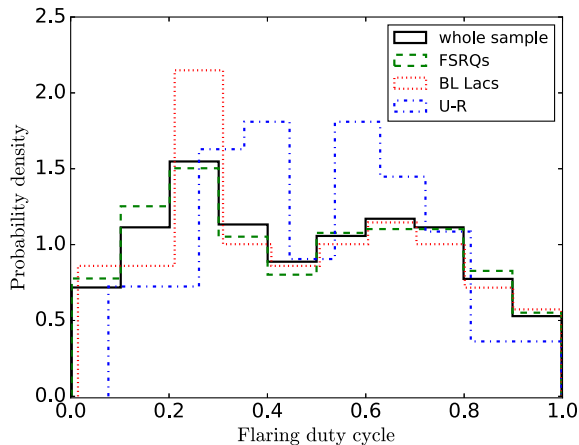


**Figure 10.** Distribution of the fraction of time spent on the on-state (duty cycle) for the different populations (BL Lacs, FSRQs, U-Rs).

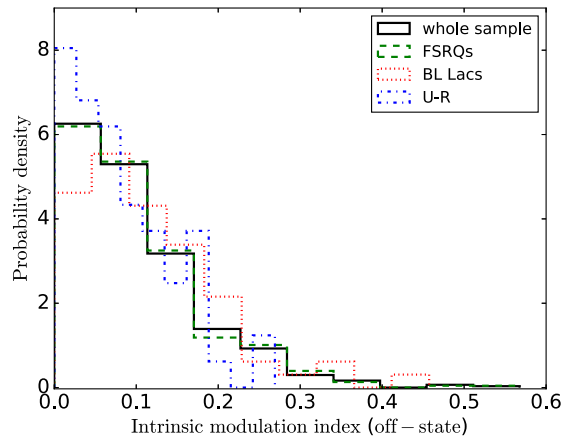


**Figure 12.** Distribution of the intrinsic modulation index for the off-state for the different populations (BL Lacs, FSRQs, U-Rs).

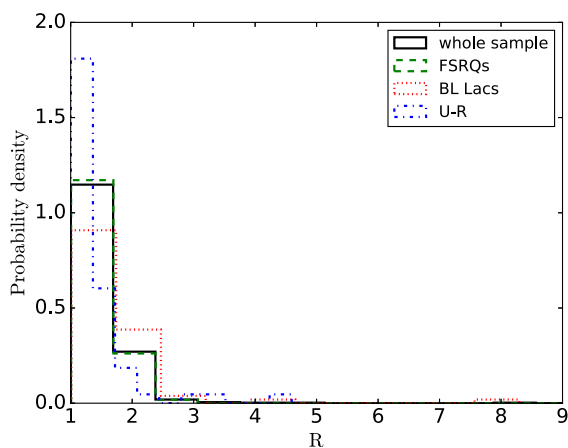


**Figure 11.** Distribution of the flaring ratio  $R$  for the different classes (BL Lacs, FSRQs, U-Rs).

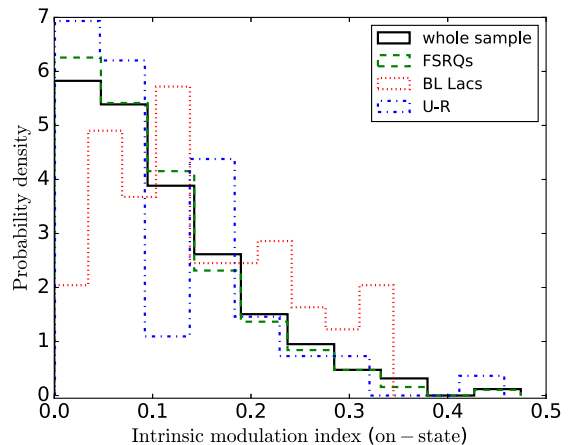


**Figure 13.** Distribution of the intrinsic modulation index for the on-state for the different populations (BL Lacs, FSRQs, U-Rs).

**Table 2.** Mean values for the duty cycle, flaring ratio and “off”- and “on”-state modulation indices for the entire sample

Parameter	$f_t$	$R$	$m_{\text{off}}$	$m_{\text{on}}$
Mean	0.47	1.56	0.10	0.10
Standard deviation	0.26	1.55	0.08	0.08

## 5 VARIABILITY PROPERTIES

### 5.1 Overall variability properties of the sample

The distribution of the flaring duty cycle  $f_t$ , the flaring ratio  $R$ , the intrinsic modulation index in the “off”-state,  $m_{\text{off}}$  and the intrinsic modulation index in the “on”-state,  $m_{\text{on}}$  for the entire sample, are shown in Figs. 10, 11, 12, and 13 respectively with the black solid line. Table 2 shows the sample mean and standard deviation for these quantities.

It has been shown in Richards et al. (2011) that intrinsic

**Table 3.** MLE exponential distributions for  $R$ ,  $m_{\text{on}}$ ,  $m_{\text{off}}$ , for the entire flux-density limited sample.

Quantity	Mean	error on mean
$R$	1.485	$\pm 0.006$
$m_{\text{off}}$	0.080	$\pm 0.004$
$m_{\text{on}}$	0.089	$\pm 0.004$

modulation index follows a mono-parametric exponential distribution. This appears to be true for the individual “on”- and “off”- state modulation indices as well as the flaring ratio, while the duty cycle appears to be consistent with a uniform distribution for the flux-limited subsample. Parameterizing such quantities could prove a useful tool in modeling blazars at the population level.

For the duty cycle, we test with the use of the K-S and Wilcoxon tests whether it is consistent with a uniform dis-

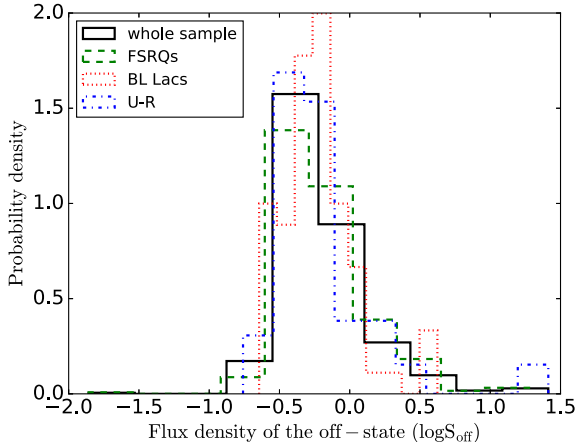


**Figure 14.** Distribution of the off-state flux-densities for the different populations (BL Lacs, FSRQs, U-Rs).

tribution in the  $[0,1]$  interval. Both tests cannot reject the null hypothesis that the duty cycle and a uniform distribution in the  $[0,1]$  range, are drawn from the same distribution (14% and 19% probability of consistency respectively). For this test, we have not excluded any sources based on their consistency with a single-Gaussian model.

For the flaring ratio and modulation indices, the mean of the exponential distribution ( $K_0$ , where  $K$  is the parameter to be fitted) given a set of observations ( $K_{\text{obs},i}$ ) with Gaussian uncertainty  $\sigma_{\text{obs},i}$ , can be calculated using,

$$l_i = \frac{1}{2K_0} \exp \left[ -\frac{K_{\text{obs},i}}{K_0} \left( 1 - \frac{\sigma_{\text{obs},i}^2}{2K_0 K_{\text{obs},i}} \right) \right] \times \left\{ 1 + \text{erf} \left[ \frac{K_{\text{obs},i}}{\sigma_{\text{obs},i} \sqrt{2}} \left( 1 - \frac{\sigma_{\text{obs},i}^2}{K_0 K_{\text{obs},i}} \right) \right] \right\}, \quad (7)$$

from Richards et al. (2011), where  $l_i$  is the likelihood and erf is the error function. The error on the quantities to be fitted is calculated through integration of the normalized likelihood. For the modulation indices we exclude all values of  $m < 0.06$  and re-normalize the likelihood accordingly (see Eq. 30 and the corresponding discussion in Richards et al. 2011).

Table 3 shows parameters of the best-fit distributions for each of the aforementioned quantities which can be used as inputs to population models for blazars that require some treatment of source variability and/or activity state, such as the derivation of luminosity functions from single-epoch surveys. From the fits we have excluded sources J1433–1548, J1823+7938, J1808+4542, J1852+4019 for being outliers (either of  $R$  or  $m$ ), preventing the maximum likelihood method to achieve a good fit. In subsequent sections we focus on the comparison of variability properties between blazar subclasses.

## 5.2 FSRQs versus BL Lacs

Figure 10 shows the distribution of the fraction of time spent on the “on” state (the blazar flaring duty cycle) for the whole sample (black solid line), BL Lacs (red dotted line),

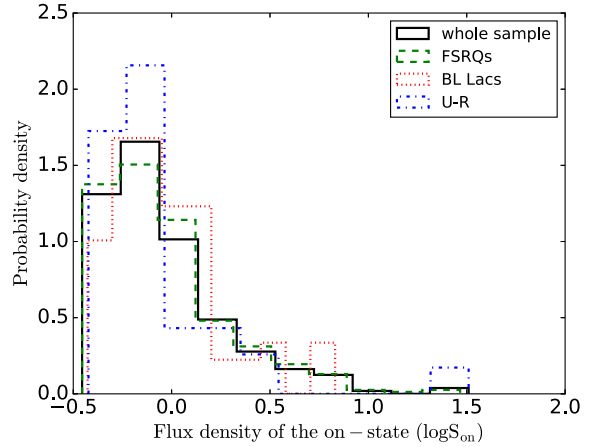


**Figure 15.** Distribution of the on-state flux-densities for the different populations (BL Lacs, FSRQs, U-Rs).

**Table 4.** Mean parameters and Wilcoxon and K-S test probability values that the two population are consistent.

Parameter	BL Lacs (mean)	FSRQs (mean)	Wilcoxon (%)	K-S (%)
$f_t$	0.46	0.47	92.3	86.1
$R$	1.71	1.55	0.3	0.8
$m_{\text{off}}$	0.11	0.10	32.8	64.6
$m_{\text{on}}$	0.14	0.10	$10^{-3}$	0.2

FSRQs (green dashed line), and U-Rs (blue dashed-dotted line). The distribution is similar to a uniform one with no apparent difference between BL Lacs and FSRQs. This is also confirmed by the K-S test and the Wilcoxon test.

We next explore the flaring ratio of the flux-density of the “off” and “on” states which is unaffected by redshift effects. This way we are not limited by the redshift completeness of our sample.

Figure 11 shows the ratio of the “on”-to-“off”-state ( $R$ ) for the different populations. The BL Lacs appear to have larger  $R$  (on average) than the FSRQs (Table 4). Both tests reject the null hypothesis that the samples are drawn from the same distribution with the values of one (BL Lacs) being systematically larger than the other. This would suggest that while flaring the BL Lacs reach, on average, higher flux-densities on the on-state relatively to their off-states than the FSRQs.

Although the ratio  $R$  is different for the BL Lacs and FSRQs, the individual flux-densities of the “off” (Fig. 14) and “on” states (Fig. 15) appear to be similar with the K-S (45% for the “off” and 46% for the “on” state) and Wilcoxon (83% for the off and 32% for the on-state) tests unable to reject the null hypothesis, suggesting that the BL Lacs exhibit relatively larger outbursts than the FSRQs.

We also explore the characteristic variability of the populations using the intrinsic modulation index defined as  $m = \sigma/S$  (Richards et al. 2011). Figures 12 and 13 show the distribution of  $m$  for the “off” and “on” states respectively.

**Table 5.** Mean parameters and Wilcoxon and K-S test probability values that the two populations are consistent.

Parameter	Blazars (mean)	U-Rs (mean)	Wilcoxon (%)	K-S (%)
$f_t$	0.47	0.50	32.9	13.3
$R$	1.57	1.44	0.08	0.01
$m_{\text{off}}$	0.10	0.08	9.0	30.8
$m_{\text{on}}$	0.11	0.10	46.7	33.1

**Table 6.** Mean parameters and Wilcoxon and K-S test probability values that the two populations are consistent.

Parameter	BL Lacs (mean)	U-Rs (mean)	Wilcoxon (%)	K-S (%)
$f_t$	0.46	0.50	34.4	33.9
$R$	1.71	1.44	0.007	0.009
$m_{\text{off}}$	0.11	0.08	0.3	0.4
$m_{\text{on}}$	0.14	0.10	5.9	27.0

For the “off”-state the two tests cannot reject the null hypothesis that the two samples are drawn from the same distribution. However, for the “on”-state the mean for the BL Lacs is significantly larger than the FSRQs both tests rejecting the hypothesis that the two samples are drawn from the same distribution. The fact that the mean “on”-state modulation index value is larger for the BL Lacs suggests that while flaring their flux-density distribution is on average wider. On the other hand, for the FSRQs, there is no difference of the intrinsic modulation index between the two states. We conclude that the BL Lacs are relatively more variable during outbursts than the FSRQs. All the mean parameter and probability values are summarized in Table 4.

### 5.3 Blazars versus Unidentified

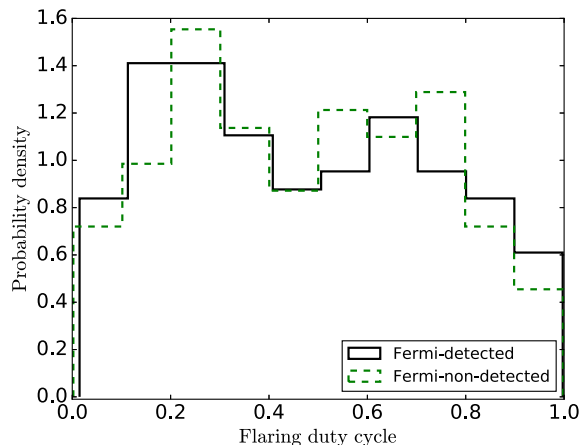
Comparing the blazar sample (FSRQs + BL Lacs) against the U-R sources we find very interesting similarities. The duty cycle is similar, with neither test rejecting the null hypothesis that the samples are drawn from the same distribution (Table 5). The mean flaring ratio  $R$  is mildly (but significantly) larger for the blazars than for the U-Rs, in both states the blazars have larger mean modulation index, yet both tests are unable to reject the null hypothesis that the two samples are drawn from the same distribution (Table 5).

We also compare individual classes (i.e., FSRQs, BL Lacs) versus U-Rs. Comparing the FSRQs none of the above results changes in any significant manner, which is to be expected since the FSRQs dominate the blazar sample (75% of the sample). For the BL Lacs the results are somewhat different. The duty cycle as well as the “off”-state modulation index are similar, with both tests not being able to reject the null hypothesis that the two samples are drawn from the same distribution. However, both tests reject the null hypothesis for the flaring ratio  $R$  and for the “on”-state modulation index (Table 6).

If the unidentified and blazar candidate sources in the

**Table 7.** Mean parameters and Wilcoxon and K-S test probability values that the two populations are consistent.

Parameter	<i>Fermi</i> (mean)	non- <i>Fermi</i> (mean)	Wilcoxon (%)	K-S (%)
$f_t$	0.47	0.48	65.4	52.8
$R$	1.60	1.51	$10^{-10}$	$10^{-8}$
$m_{\text{off}}$	0.11	0.09	0.009	0.26
$m_{\text{on}}$	0.13	0.09	$10^{-7}$	0.001


**Figure 16.** Distribution of the fraction of time spent on the on-state (duty cycle) for the *Fermi*-detected and non-detected sources.

U-R sample were unidentified BL Lacs due to the absence of spectral lines, we would expect the opposite results, i.e., the BL Lac sample to be more consistent with the U-R sample in the variability characteristics. Instead the FSRQs appear to be consistent with the U-Rs suggesting that the majority of the sources in the U-R sample are either unidentified FSRQs or radio galaxies with jets pointed close to our line of sight, yet not close enough to be considered a blazar (often referred to as misaligned blazars). The latter would suggest that the FSRQs and the radio galaxies share similar variability characteristics. All the mean parameter and probability values are summarized in Table 5.

### 5.4 *Fermi*-detected versus *Fermi* non-detected blazars

There are 267 sources in our flux-density-limited sample (50%) that have been associated with *Fermi* detected sources. Out of the 267 sources, 186 are FSRQs, 62 are BL Lacs, and 19 are U-Rs. Figure 16 shows the distribution of the duty cycle. The solid black line is for the *Fermi*-detected and the dashed green for the *Fermi*-non-detected sources. The distributions are very similar in shape with the Wilcoxon and K-S test suggesting the two samples being drawn from the same distribution (Table 7). The high probability of consistency, as well as the almost identical mean values suggest that there is no difference in the time the two samples spent in either state.

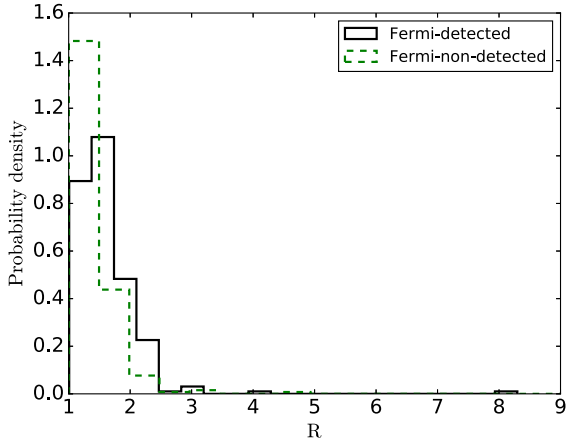


**Figure 17.** Distribution of the flaring ratio  $R$  for the for the *Fermi*-detected and non-detected sources.

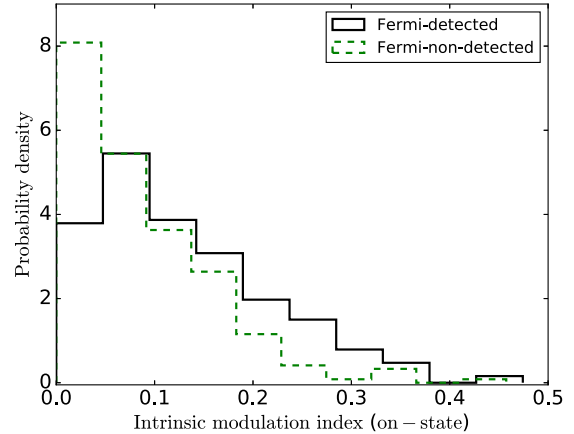


**Figure 19.** Distribution of the intrinsic modulation index for the on-state for the *Fermi*-detected and non-detected sources.

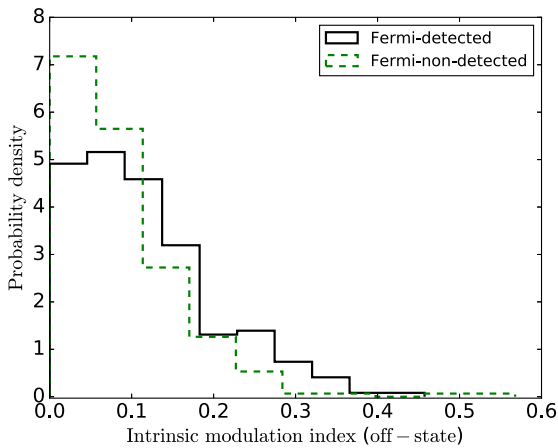


**Figure 18.** Distribution of the intrinsic modulation index for the off-state for the *Fermi*-detected and non-detected sources.

However, their flaring ratio  $R$  (Fig. 17) is rather different. Both tests rejected the null hypothesis of consistency between populations with high confidence (i.e., small probability value). The mean values combined with the results of the Wilcoxon test suggest that the *Fermi*-detected sources have systematically higher ratios, which translates to them having larger differences in flux-density between states, i.e., more powerful outbursts.

Examining the intrinsic modulation index in the different states (Fig. 18, 19), we find that in both the “off” and the “on” state, both tests rejected the null hypothesis. In both states the *Fermi*-detected sources have larger mean values which means that on average they are more variable than the *Fermi*-non-detected sources, contrary to the *Fermi*-detected. This could partially be attributed to the fact that the majority of the BL Lacs (which are more variable in the “on” state, see section 5.2) are in the *Fermi*-detected subsam-

ple, however, the fact that the *Fermi*-detected are systematically more variable than the *Fermi*-non-detected in both states, is in support of the *Fermi*-detected being intrinsically more variable than the *Fermi*-not-detected sources (see also Richards et al. (2014)). All the mean parameter and probability values are summarized in Table 7.

### 5.5 Low versus High redshift sources

Richards et al. (2011) and Richards et al. (2014) point out that FSRQs show a negative correlation between radio variability as quantified by their intrinsic modulation index and redshift ( $z$ ). They find that sources with  $z < 1$  are more variable in radio than sources with  $z > 1$  suggesting that the radio variability of FSRQs evolves with cosmic time. The trend first appeared in the two year dataset (Richards et al. 2011), and persisted in the four year dataset (Richards et al. 2014). We use the redshift values from Richards et al. (2014) to separate our sources into two subsamples according to their redshift. All the FSRQs in our sample have a known redshift. Separating our samples in low ( $z < 1$ ) and high ( $z > 1$ ) redshift sources we have 149 and 252 sources respectively.

For the duty cycle and the intrinsic modulation index in the “on”-state, both tests agree that the two subsamples are drawn from the same distributions. For the flaring ratio and the “off”-state modulation index the tests reject the null hypothesis. If instead of  $z = 1$  we separate our samples according to the mean ( $z \approx 1.22$ ) or median ( $z \approx 1.32$ ) value the results of both test vary for all parameters. Sensitivity to redshift separation makes the individual components of the analysis ( $f_t$ ,  $R$ ,  $m_{\text{off}}$ ,  $m_{\text{on}}$ ) unreliable indicators for cosmic evolution. However, if we compare the overall modulation index ( $\langle m \rangle$ ) we find that regardless of redshift separation the two samples are inconsistent. Separating the samples at  $z = 1$  and  $z = \langle z \rangle_{\text{median}}$  the probability values of both tests are  $\leq 10^{-3}$ . If we separate the samples at  $z = \langle z \rangle_{\text{mean}}$  the Wilcoxon test yields a 2%, whereas the K-S test yields a 6% probability of consistency which is marginally acceptable. Since the mean  $\langle m \rangle$  values for the two samples are dif-

ferent ( $\langle m \rangle_{\text{mean}} = 0.185$  for the low and  $\langle m \rangle_{\text{mean}} = 0.177$  for the high redshift sources) we conclude that the two samples are not drawn from the same distribution. On the other hand, if we correct for the cosmological time dilation ( $\Delta t_{\text{obs}} = (1+z)\Delta t_{\text{rest-frame}}$ ) and repeat the analysis, but this time using equal redshift-corrected observing lengths for all sources, we find no apparent trend of cosmic evolution. For all the parameters both tests cannot reject the null hypothesis that the two samples are drawn from the same distribution. However, we have not taken into account relativistic compression of variability timescales, which should be larger for higher- $z$  sources (because of flux-density selection effects) and thus affect results in the opposite direction to cosmological time dilation. Given the large span of Doppler factors in blazar jets (Hovatta et al. 2009; Liodakis et al. 2017) even the redshift-corrected observing lengths will be significantly different from the “true” jet rest-frame observing lengths for each source. Until a large enough number of Doppler factor estimates is available that will allow us to confidently correct for the relativistic effects on a source-by-source basis, we are unable to draw firm conclusions on the cosmic evolution of FSRQ variability properties.

A similar effect as the one discussed here and in Richards et al. (2011, 2014) is true for interstellar scintillation at 5 GHz (Lovell et al. 2008; Koay et al. 2012). The authors found that interstellar scintillation is suppressed a higher redshift and that high redshift sources have steeper spectra (in the 5-9 GHz range). That the interstellar scintillation of high redshift sources is suppressed indicates either a larger apparent angular size, beyond the expected cosmological expansion, or a smaller compact fraction in the high redshift blazars. However, since the OVRO dataset is single frequency we cannot test if a similar effect is present in our sample.

## 6 SUMMARY

We have presented a novel five-dimensional maximum likelihood formalism in order to characterize the variability properties of blazars and blazar-like sources as a series of two states: an “off” state describing the low activity periods of a source, and an “on” state that describes periods of outbursts. We used our method to fit the 15 GHz flux-density distribution of blazars as seen by OVRO (Richards et al. 2011), and extract their variability properties (Table 8).

For our statistical analysis of the population properties of the OVRO blazars, as well as for the comparison of the behaviors of blazar subclasses, we define a statistically complete subset of all OVRO monitored sources: a flux-density limited subsample, based on average fluxes from Richards et al. (2014). We have tested whether the model assumed in this work is a good description of the underlying flux-density distribution of the OVRO-monitored blazars. If this is the case, then for bright sources (where observational uncertainties do not widen appreciably the observed flux density distribution compared to the intrinsic one) we would expect the value of  $m$  obtained from the sample mean and sample standard deviation for each light curve to agree well with our likelihood-derived intrinsic  $\langle m \rangle$ . We have verified that the two are, in fact, in excellent agreement.

Having established that our model is a good description

of the underlying distribution, we compared the variability characteristics of different subsamples. Our results can be summarized as follows:

- BL Lacs are more variable than the FSRQs. This is consistent with the finding of Richards et al. (2011, 2014) that BL Lacs have a higher overall  $\langle m \rangle$ . However, we have now established that BL Lacs also exhibit stronger outbursts (have a higher flaring ratio), and that their increase in  $\langle m \rangle$  is dominated by the “on”-state (it is  $m_{\text{on}}$  that is significantly higher, while  $m_{\text{off}}$  is similar in BL Lacs and FSRQs). Interestingly, Liodakis & Pavlidou (2015); Liodakis et al. (2017) find that the Doppler factors of FSRQs are on average, significantly higher than those of BL Lacs, so this discrepancy must have its origin in rest-frame properties, rather than differences in boosting between the two classes.

- Sources classified as blazars (BL Lacs and FSRQs) have systematically larger flaring ratios (i.e., stronger outbursts) than the U-Rs with otherwise similar variability characteristics. The variability characteristics of U-Rs are similar to FSRQs. Since the majority of U-Rs are blazar candidates, it would suggest either that they are unclassified FSRQs most likely due to lack of multi-wavelength observations, or that they are unclassified radio galaxies, which in turn would suggest that FSRQs and radio galaxies share similar rest-frame variability characteristics.

- *Fermi*-detected sources are intrinsically more variable than the *Fermi*-non-detected sources. This result agrees with the overall findings of Richards et al. (2011, 2014), however the bimodal model offers an opportunity to trace the origin of this result in the details of the behavior of blazars in the flux density domain. Indeed, *Fermi*-detected sources have higher flaring ratios and higher modulation indices in both states, with the most significant difference being in the flaring ratio. This results indicates that the mechanisms responsible for the amplitude of radio variations and the  $\gamma$ -ray loudness of a source may share a physical link.

- The overall intrinsic modulation index ( $\langle m \rangle$ ) is consistently (regardless of redshift separation of subsamples) supporting the negative correlation between radio variability and redshift in FSRQs reported in Richards et al. (2011, 2014). Once we accounted for the cosmological time dilation we found no evidence for such negative correlation. However, since we are not yet able to take into account the relativistic effects compressing blazar timescales, we are not able to come to firm conclusions regarding a possible cosmic evolution of variability properties of FSRQs.

We caution the reader that for an analysis such as the one presented here, there is a dependence of the derived variability parameters to the length of the monitoring program. Short (in time) monitoring programs may not be able to sample the entire flux-density distribution of a blazar. However, given enough time, estimates will converge to their “true” values. For our well sampled sources, we find that by splitting the monitoring period in half (4 years) the difference in the derived variability estimates from the two periods is  $< 50\%$  in the majority of cases.

The overall radio modulation index as calculated by Richards et al. (2011) is one of the properties used to select samples for monitoring of other blazar properties (such as their optopolarimetric behavior e.g., King et al. 2014; Pavlidou et al. 2014). Given that we find the bimodal flux

distribution to be a much better description than the single Gaussian used by Richards et al. (2011) we would advice using the overall  $\langle m \rangle$  values from this work for sample characterization.

The tools presented in this work were used to explore the variability properties of a 15 GHz selected flux-density-limited sample. They are, however, not restricted to any particular frequency since the formalism is based on statistics alone and is independent of any emission mechanism or other physical arguments. Thus, are suitable for all wavelengths and sources that can be well described by a bimodal Gaussian distribution. However, one should keep in mind that using a large number of observations for the fitting (in our case 421 on average) is critical to ensure robust results for the estimated parameters and their errors.

## ACKNOWLEDGMENTS

The authors would like to thank the referee Hayley Bignall and Vassilis Karamanavis for constructive comments and suggestions that helped improve this work. I.L. thanks the Caltech Astronomy Department for their hospitality during the completion of this work. This research was supported by the European Commission Seventh Framework Program (FP7) through grants PCIG10-GA-2011-304001 “JetPop” and PIRSES-GA-2012-31578 “EuroCal”. T.H. was supported in part by the Academy of Finland project number 267324. This research has made use of data from the OVRO 40-m monitoring program (Richards et al. 2011) which is supported in part by NASA grants NNX08AW31G, NNX11A043G, and NNX14AQ89G and NSF grants AST-0808050 and AST-1109911.

## REFERENCES

- Acero F., et al., 2015, *ApJS*, **218**, 23  
Aller M. F., Aller H. D., Hughes P. A., Latimer G. E., 1999, *ApJ*, **512**, 601  
Angelakis E., et al., 2016, *MNRAS*, **463**, 3365  
Blandford R. D., Königl A., 1979, *ApJ*, **232**, 34  
Blinov D., et al., 2015, *MNRAS*, **453**, 1669  
Carrasco L., Dultzin-Hacyan D., Cruz-Gonzalez I., 1985, *Nature*, **314**, 146  
Dent W. A., 1965, *Science*, **148**, 1458  
Fuhrmann L., et al., 2014, *MNRAS*, **441**, 1899  
Healey S. E., et al., 2008, *ApJS*, **175**, 97  
Hovatta T., Niappola E., Tornikoski M., Valtaoja E., Aller M. F., Aller H. D., 2008, *A&A*, **485**, 51  
Hovatta T., Valtaoja E., Tornikoski M., Lähteenmäki A., 2009, *A&A*, **494**, 527  
Hovatta T., et al., 2016, *A&A*, **596**, A78  
King O. G., et al., 2013, *MNRAS*, **436**, L114  
King O. G., et al., 2014, *MNRAS*, **442**, 1706  
Koay J. Y., et al., 2012, *ApJ*, **756**, 29  
Komatsu E., et al., 2009, *ApJS*, **180**, 330  
Lähteenmäki A., Valtaoja E., 1999, *ApJ*, **521**, 493  
Lähteenmäki A., Valtaoja E., Wiik K., 1999, *ApJ*, **511**, 112  
Liodakis I., Pavlidou V., 2015, *MNRAS*, **451**, 2434  
Liodakis I., et al., 2017, preprint, ([arXiv:1701.01452](https://arxiv.org/abs/1701.01452))  
Lister M. L., 2001, *ApJ*, **561**, 676  
Lister M. L., et al., 2009, *AJ*, **137**, 3718  
Lister M. L., et al., 2013, *AJ*, **146**, 120  
Lovell J. E. J., et al., 2008, *ApJ*, **689**, 108

- Marscher A. P., et al., 2008, *Nature*, **452**, 966  
Marscher A. P., et al., 2010, *ApJ*, **710**, L126  
Max-Moerbeck W., et al., 2014, *MNRAS*, **445**, 428  
Mouschovias T. C., Tassis K., 2010, *MNRAS*, **409**, 801  
Nelder J. A., Mead R., 1965, *The Computer Journal*, **7**, 308  
Pavlidou V., et al., 2014, *MNRAS*, **442**, 1693  
Readhead A. C. S., 1980, *Phys. Scr.*, **21**, 662  
Readhead A. C. S., Cohen M. H., Pearson T. J., Wilkinson P. N., 1978, *Nature*, **276**, 768  
Richards J. L., et al., 2011, *ApJS*, **194**, 29  
Richards J. L., Hovatta T., Max-Moerbeck W., Pavlidou V., Pearson T. J., Readhead A. C. S., 2014, *MNRAS*, **438**, 3058  
Scheuer P. A. G., Readhead A. C. S., 1979, *Nature*, **277**, 182  
Valtaoja E., et al., 1985, *Nature*, **314**, 148  
Valtaoja E., et al., 1988, *A&A*, **203**, 1  
Valtaoja E., Lähteenmäki A., Teräsanta H., Lainela M., 1999, *ApJS*, **120**, 95  
Venters T. M., Pavlidou V., 2007, *ApJ*, **666**, 128

**Table 8.** Variability parameters for the OVRO monitored sources. Columns: (1) OVRO name; (2) duty cycle ( $f_t$ ); (3)  $1\sigma$  error on  $f_t$  from the information matrix; (4) upper  $1\sigma$  error on  $f_t$  from the likelihood slice; (5) lower  $1\sigma$  error on  $f_t$  from the likelihood slice; (6) off-state flux-density ( $S_{\text{off}}$ ); (7)  $1\sigma$  error on  $S_{\text{off}}$  from the information matrix; (8) upper  $1\sigma$  error on  $S_{\text{off}}$  from the likelihood slice; (9) lower  $1\sigma$  error on  $S_{\text{off}}$  from the likelihood slice; (10) standard deviation of the off-state flux-density ( $\sigma_{\text{off}}$ ); (11)  $1\sigma$  error on  $\sigma_{\text{off}}$  from the information matrix; (12) upper  $1\sigma$  error on  $\sigma_{\text{off}}$  from the likelihood slice; (13) lower  $1\sigma$  error on  $\sigma_{\text{off}}$  from the likelihood slice; (14) on-state flux-density ( $S_{\text{on}}$ ); (15)  $1\sigma$  error on  $S_{\text{on}}$  from the information matrix; (16) upper  $1\sigma$  error on  $S_{\text{on}}$  from the likelihood slice; (17) lower  $1\sigma$  error on  $S_{\text{on}}$  from the likelihood slice; (18) standard deviation of the on-state flux-density ( $\sigma_{\text{on}}$ ); (19)  $1\sigma$  error on  $\sigma_{\text{on}}$  from the information matrix; (20) upper  $1\sigma$  error on  $\sigma_{\text{on}}$  from the likelihood slice; (21) lower  $1\sigma$  error on  $\sigma_{\text{on}}$  from the likelihood slice. The parameter values for  $S_{\text{off}}$ ,  $\sigma_{\text{off}}$ ,  $S_{\text{on}}$  and  $\sigma_{\text{on}}$  are in Jansky. For uncertainty values in columns (3), (7), (11), (15), and (19) equal to zero, the information matrix failed to provide an error estimate. In this case, use upper and lower 1-sigma uncertainties from the likelihood slice. The full-version of the table is available online.

Name (1)	$f_t$ (2)	$\sigma_{f_t}$ (3)	upper- $\sigma_{f_t}$ (4)	lower- $\sigma_{f_t}$ (5)	$S_{\text{off}}$ (6)	$\sigma_{S_{\text{off}}}$ (7)	upper- $\sigma_{S_{\text{off}}}$ (8)	lower- $\sigma_{S_{\text{off}}}$ (9)	$\sigma_{\text{off}}$ (10)	$\sigma_{\sigma_{\text{off}}}$ (11)	upper- $\sigma_{\sigma_{\text{off}}}$ (12)	lower- $\sigma_{\sigma_{\text{off}}}$ (13)	$S_{\text{on}}$ (14)	$\sigma_{S_{\text{on}}}$ (15)	upper- $\sigma_{S_{\text{on}}}$ (16)	lower- $\sigma_{S_{\text{on}}}$ (17)	$\sigma_{\text{on}}$ (18)	$\sigma_{\sigma_{\text{on}}}$ (19)	upper- $\sigma_{\sigma_{\text{on}}}$ (20)	lower- $\sigma_{\sigma_{\text{on}}}$ (21)
J0001-1551	0.168	0.0373	+ 0.0369	- 0.0369	0.201	0.0018	+ 0.002	- 0.002	0.0	0.0048	+ 0.0037	- 0.0	0.222	0.0	+ 0.0044	- 0.0044	0.044	0.0	+ 0.0022	- 0.0022
J0001+1914	0.839	0.0208	+ 0.0252	- 0.0252	0.229	0.0017	+ 0.0023	- 0.0023	0.027	0.0014	+ 0.0016	- 0.0013	0.311	0.0	+ 0.0031	- 0.0031	0.009	0.0	+ 0.0023	- 0.0021
J0003+2129	0.978	0.012	+ 0.0196	- 0.0196	0.077	0.0006	+ 0.0008	- 0.0008	0.008	0.0005	+ 0.0006	- 0.0005	0.083	0.0	+ 0.0132	- 0.0124	0.033	0.0	+ 0.0115	- 0.0072
J0004-1148	0.205	0.0237	+ 0.0224	- 0.0216	0.366	0.0061	+ 0.0059	- 0.0059	0.04	0.0046	+ 0.0045	- 0.004	0.631	0.0	+ 0.0069	- 0.0069	0.113	0.0	+ 0.0055	- 0.0052
J0004+2019	0.59	0.0303	+ 0.0277	- 0.0283	0.289	0.0016	+ 0.0014	- 0.0014	0.015	0.0015	+ 0.0014	- 0.0013	0.374	0.0	+ 0.0049	- 0.0049	0.049	0.0	+ 0.0034	- 0.0032
J0004+4615	0.068	0.0121	+ 0.0129	- 0.0116	0.049	0.0021	+ 0.0025	- 0.0025	0.0	0.0044	+ 0.0038	- 0.0	0.207	0.018	+ 0.0041	- 0.0041	0.041	0.0134	+ 0.0017	- 0.0017
J0005+0524	0.997	0.0026	+ 0.01	- 0.01	0.107	0.0006	+ 0.0011	- 0.0011	0.007	0.0005	+ 0.0006	- 0.0006	0.172	0.0	+ 0.0103	- 0.0103	0.0	0.0	+ 0.0124	- 0.0
J0005-1648	0.526	0.0801	+ 0.0421	- 0.0421	0.131	0.0037	+ 0.0026	- 0.0026	0.014	0.0024	+ 0.0014	- 0.0013	0.159	0.0	+ 0.0016	- 0.0016	0.008	0.0	+ 0.0013	- 0.0012
J0005+3820	0.839	0.0181	+ 0.0176	- 0.0185	0.509	0.003	+ 0.0031	- 0.0031	0.053	0.0024	+ 0.0024	- 0.0023	0.698	0.0	+ 0.0049	- 0.0049	0.029	0.0	+ 0.0049	- 0.0042
J0006-0623	0.795	0.023	+ 0.0223	- 0.0239	2.243	0.0089	+ 0.0112	- 0.0112	0.141	0.0068	+ 0.0075	- 0.0071	3.413	0.0	+ 0.0819	- 0.0785	0.572	0.0	+ 0.0595	- 0.0526

# Reconciling inverse-Compton Doppler factors with variability Doppler factors in blazar jets

I. Liodakis<sup>1,2\*</sup>, A. Zezas<sup>1,2</sup>, E. Angelakis<sup>3</sup>, T. Hovatta<sup>4,5,6</sup>, and V. Pavlidou<sup>1,2</sup>

<sup>1</sup> Department of Physics and ITCP \*\*, University of Crete, 71003, Heraklion, Greece

<sup>2</sup> Foundation for Research and Technology - Hellas, IESL, Voutes, 7110 Heraklion, Greece

<sup>3</sup> Max-Planck-Institut für Radioastronomie, Auf dem Hügel 69, 53121 Bonn, Germany

<sup>4</sup> Aalto University Metsähovi Radio Observatory, Metsähovintie 114, 02540 Kylmälä, Finland

<sup>5</sup> Aalto University Department of Radio Science and Engineering, P.O. BOX 13000, FI-00076 AALTO, Finland

<sup>6</sup> Tuorla Observatory, Department of Physics and Astronomy, University of Turku, Finland

April 14, 2017

## ABSTRACT

**Context.** Blazar population models have shown that the inverse-Compton and variability Doppler factor estimates yield consistent results at the population level for flat spectrum radio quasars (FSRQs). The two methods, however, are inconsistent when compared on a source-by-source basis.

**Aims.** In this work, we attempt to understand the source of the discrepancy by tracing the potential sources of systematic and statistical error for the inverse-Compton Doppler factors. By eliminating these sources of error, we provide stronger constraints on the value of the Doppler factor in blazar jets.

**Methods.** We re-estimate the inverse-Compton Doppler factor for 11 sources that meet certain criteria for their synchrotron peak frequency and the availability of Doppler factor estimates in the literature. We compare these estimates with the average of two different estimates of the variability Doppler factor obtained using various datasets and methodologies to identify any discrepancies and, in each case, trace their sources in the methodology or assumptions adopted.

**Results.** We identify three significant sources of error for the inverse-Compton Doppler factors: a) contamination of the X-ray flux by non-synchrotron self-Compton emission; b) radio observations at frequencies other than the synchrotron turnover frequency; c) non-simultaneity between radio and X-ray observations. We discuss key aspects in the correct application of the inverse-Compton method in light of these potential errors. We are able to constrain the Doppler factor of 3C273, 3C345, 3C454.3, PKS1510-089, and PKS1633+382 effectively, since all available estimates from both methods converge to the same values for these five sources.

**Key words.** Relativistic processes - galaxies: active - galaxies: jets

## 1. Introduction

Blazars, and in particular flat spectrum radio quasars (FSRQs) and BL Lac objects, are active galactic nuclei (AGN) with jets closely aligned to our line of sight (Readhead et al. 1978; Blandford & Königl 1979; Scheuer & Readhead 1979; Readhead 1980). They constitute one of most interesting classes of AGN owing to the relativistic effects dominating their broadband emission, thereby complicating our understanding of their intrinsic properties. Revealing the properties of blazars and their jets in their rest frame would allow us to study important astrophysical processes in supermassive black hole jets, including emission mechanisms, and jet production, collimation, propagation, and energetics.

A major difficulty in the study of blazar jets in their rest frame is the limitation on obtaining reliable estimates of the Doppler factor in blazar jets, i.e., of the amount of relativistic boosting. Doppler factors are notoriously hard to estimate and the lack of confident estimates is known to hinder the identification of potentially revealing empirical correlations between rest-

frame blazar properties (e.g., Hovatta et al. 2010; Lister et al. 2011; Blinov et al. 2016a,b, and Angelakis et al. 2016).

Several methods have been proposed for the estimation of Doppler factors. Very often different methods rely on different assumptions regarding the physical properties of the jet, and in many cases these methods produce different results. The methods commonly used include the inverse-Compton method (Ghisellini et al. 1993, hereafter G93), which assumes that synchrotron self-Compton (SSC) is the dominant emission mechanism at X-ray frequencies, and methods relying on the assumption of equipartition between radiating particles and magnetic field (Readhead 1994). These latter methods include the equipartition Doppler factor (Readhead 1994; Gujosa & Daly 1996) and the variability Doppler factor methodologies (Valtaoja et al. 1999; Lähteenmäki & Valtaoja 1999; Hovatta et al. 2009; Liodakis et al. 2017). The different assumptions used by these methods make a direct comparison unfeasible. The situation is further complicated if the Doppler factor does not remain constant in time. Local acceleration, jet precession, and bends in the jet could in principle yield different results for the same source depending on the time of the observations.

Liodakis & Pavlidou (2015b) have been able to evaluate these methods in a statistical fashion via population models they optimized in Liodakis & Pavlidou (2015a). These models

\* liodakis@physics.uoc.gr

\*\* Institute for Theoretical and Computational Physics, formerly Institute for Plasma Physics

consist of distributions for the Lorentz factor and the intrinsic monochromatic luminosity for different blazar classes optimized to reproduce the observed apparent velocity and redshift distributions of the MOJAVE (Monitoring of Jets in Active galactic nuclei with VLBA Experiment; Lister & Homan 2005)<sup>1</sup> sample. Using these population models, the Doppler factor distributions of the FSRQs and BL Lac objects have been produced through Monte Carlo simulations assuming the continuous jet case.

Liodakis & Pavlidou (2015b) have compared these model distributions with the distributions of Doppler factors estimated through each of the methods above available in the literature, accounting for sample size and flux limit. These authors have found that both the inverse-Compton ( $\delta_{IC}$ ) and the variability ( $\delta_{var}$ ) Doppler factor methods can adequately describe the FSRQs population. For the inverse-Compton (IC) Doppler factors, an error analysis at the population level has shown that their errors are normally distributed and that each estimate has a  $\sim 63\%$  error on average. A Kolmogorov-Smirnov test (K-S test) gave a  $\sim 95\%$  probability of consistency between the observed and simulated (with errors) distributions. In addition, not only is the statistical error of the IC Doppler factors quite high, but there are also many potential sources of systematic error in the estimates as a result of the assumptions involved in the method. Individual estimates for the variability Doppler factors (Hovatta et al. 2009; hereafter H09) were found to have on average a  $\sim 30\%$  statistical error, making them more accurate, however the dominant source of error in this case is systematic and due to the finite cadence of observations. Sources most likely to be affected by this type of systematic uncertainty can be identified by comparing the cadence of observations to the fastest flare detected. In the remaining sources, the dominant source of error is the 30% statistical error that is due to the uncertainty in estimating the rise time and amplitude of a flare.

Recently, a different approach allowed for a more accurate estimation of  $\delta_{var}$ . By modeling the multiwavelength radio light curves from the F-GAMMA program<sup>2</sup> (Fuhrmann et al. 2007; Angelakis et al. 2010) and an upgraded version of the algorithms introduced in Angelakis et al. (2015), it was possible to estimate the  $\delta_{var}$  for 58 sources with an on-average 16% error (Liodakis et al. 2017; hereafter L17). This approach can, in addition, mitigate the effects of limited cadence and provide error estimates on a source-by-source basis.

Since both methods (IC and variability Doppler factors) can adequately describe the FSRQ population, a comparison on a blazar-by-blazar basis between the two should, in principle, allow us to control the (various) systematics that affect each method and effectively constrain the Doppler factor value in blazar jets for which both estimates are available. However, such a comparison of the two methods yields inconsistent results even when accounting for the large statistical errors of IC Doppler factors.

In this work, we attempt to trace the sources of these discrepancies and reconcile Doppler factor estimates produced by these two approaches. In the case of variability Doppler factors, the availability of two independent estimates facilitates systematics control and the bracketing of possible values. In the case of IC Doppler factors, we investigate possible sources of error and produce updated estimates by reducing, as far as possible, these sources of uncertainty.

This paper is organized as follows: In section 2 we provide a brief description of the inverse-Compton and variability methods

for Doppler factor estimation. In section 3 we analyze the potential sources of error in estimating the  $\delta_{IC}$ . In section 4 we discuss the selection criteria for the sources for which we compare the different Doppler factor estimates and describe our methodology for producing new estimates of  $\delta_{IC}$ . In section 5 we discuss our results and their implications of obtaining improved Doppler factor estimates of relativistic blazar jets, and in section 6 we summarize our findings.

Throughout this work we have adopted  $H_0 = 71 \text{ km s}^{-1} \text{ Mpc}^{-1}$ ,  $\Omega_m = 0.27$  and  $\Omega_\Lambda = 1 - \Omega_m$  (Komatsu et al. 2009).

## 2. Methods for Doppler factor estimation

A lower limit on the Doppler factor can be derived by acknowledging that the SSC flux density cannot exceed the observed flux density at high frequencies. The SSC emission is produced by the IC upscattering of synchrotron photons by the same relativistic electrons that produced these photons. The inverse-Compton Doppler factor  $\delta_{IC}$  (Ghisellini et al. 1993) is derived on the assumption that *all* of the observed flux density at X-ray frequencies is, in fact, due to the SSC process.

Assuming a homogeneous magnetic field, and that the energy distribution of the electrons follows a power law, the Doppler factor would be

$$\delta_{IC} = f(\alpha) F_m \left[ \frac{\ln(\nu_b/\nu_m)}{F_\chi \theta_d^{6+4\alpha} \nu_\chi^\alpha \nu_m^{5+3\alpha}} \right]^{1/(4+2\alpha)} (1+z), \quad (1)$$

where  $F_m$  is the synchrotron flux density of the core at frequency  $\nu_m$  and  $F_\chi$  is the X-ray flux density, both in Jy;  $\theta_d$  is the angular size of the core in milliarcsec,  $\nu_\chi$  is the X-ray observations energy in keV,  $\nu_m$  is the radio observations frequency in GHz; and  $\nu_b$  is the synchrotron high-energy cutoff, which is assumed to be  $10^{14}$  Hz. The function  $f(\alpha)$  is given by  $f(\alpha) \approx 0.08\alpha + 0.14$ , where  $\alpha$  is the optically thin spectral index (Ghisellini 1987) assumed to be  $\alpha = 0.75$ . Equation 1 is for the discrete jet case. For the continuous case the  $\delta_{IC}$  is transformed as

$$\delta_{cont} = \delta_{disc}^{(4+2\alpha)/(3+2\alpha)}. \quad (2)$$

A detailed description of the method can be found in Ghisellini et al. (1993) and Gujosa & Daly (1996).

The variability Doppler factor ( $\delta_{var}$ ) uses the evolution of a flare in the time domain to calculate the brightness temperature of the emission region. Either by fitting exponential curves (H09) or multiwavelength modeling (L17), one can calculate the observed variability brightness temperature. Assuming that during a flare the intrinsic brightness temperature is equal to the equipartition brightness temperature (Readhead 1994), the Doppler factor is proportional to the cube root of the ratio of the variability and equipartition brightness temperatures (Eq. 3), i.e.,

$$\delta_{var} \propto \left( \frac{T_{b,var}}{T_{eq}} \right)^{1/3}. \quad (3)$$

For a detailed description of both approaches see Valtaoja et al. (1999); Lähteenmäki et al. (1999); Lähteenmäki & Valtaoja (1999); Hovatta et al. (2009); Angelakis et al. (2015), and L17.

## 3. Sources of error for the inverse-Compton Doppler factors

Owing to the physics and the assumptions involved in the method, there are three main sources of error in inverse-

<sup>1</sup> <http://www.physics.purdue.edu/MOJAVE/>

<sup>2</sup> <http://www3.mpiifr-bonn.mpg.de/div/vlbi/fgamma/fgamma.html>

Compton Doppler factor estimates: the presence of external X-ray emission (not due to SSC), radio observations performed at a frequency that is different than the spectrum turnover frequency, and the lack of simultaneity between X-ray and radio observations.

### 3.1. External X-ray flux

As pointed out above and discussed by Britzen et al. (2007), the  $\delta_{IC}$  method can produce a reliable estimate only if all of the measured X-ray emission is caused by inverse-Compton scattering of synchrotron photons. Potential sources of the non-SSC X-ray flux could be the hot corona of the accretion disk, external Compton scattering of the broad-line region photon field, or synchrotron radiation of intermediate or high-peaked synchrotron sources. For this reason, as shown in Lioudakis & Pavlidou (2015b), the method fails to adequately describe the BL Lac population, for which the synchrotron peak reaches keV energies contaminating the X-ray flux. In addition, orphan X-ray flares (without a radio counterpart) might also indicate external origin of the X-ray flux. Sources with a prominent big blue bump also have to be treated with caution because of the output of the bump that possibly, but not necessarily, extends to the X-ray regime. Any one of these effects, or their combination, could lead to underestimating  $\delta_{IC}$  and introducing systematic errors. Thus in the application of the method, careful sample selection is of paramount importance.

### 3.2. Observed versus turnover radio frequency

In G93 the authors use the observed flux density and frequency for the estimation of the  $\delta_{IC}$ . It is argued in Lähteenmäki et al. (1999) that this is an approximation in the application and that the method requires the turnover frequency (i.e., the frequency at which the synchrotron spectrum changes from optically thick to optically thin) and flux density to be used instead. The counter-argument for this criticism is that at any given frequency, the VLBI observations show self-absorbed regions. Investigation of this effect is not trivial. Measurements at the turnover frequency are only available for a handful of sources. In addition, although the turnover is usually located in high frequencies ( $>43$  GHz), this is not always the case (Rabaça & Zensus 1994; Fromm 2015) and is different for every blazar. The location of the turnover frequency has also been shown to change, moving either to higher or lower frequencies during outbursts (Feng et al. 2006; Fromm 2015). Recent results from the F-GAMMA survey show that the turnover frequency can range from  $<2.6$  to  $>86$  GHz in a single source (Angelakis et al. in prep., also Angelakis et al. 2012). In order to estimate the impact of this approximation on Doppler factor estimation, data at multiple radio frequencies are necessary. Such data are available for a few sources we study in this work, and they indicate that this effect can play a crucial role in the correct application of the method.

### 3.3. Simultaneity of observations

The radio and X-ray observations should be contemporaneous since the SSC model requires the relativistic electrons producing the radio flux to up-scatter the synchrotron photons they themselves create to higher energies that produce the X-ray flux. Owing to the variable nature of blazars, a significant time difference between radio and X-ray observations can result in different initial emission conditions and thus can lead to either underesti-

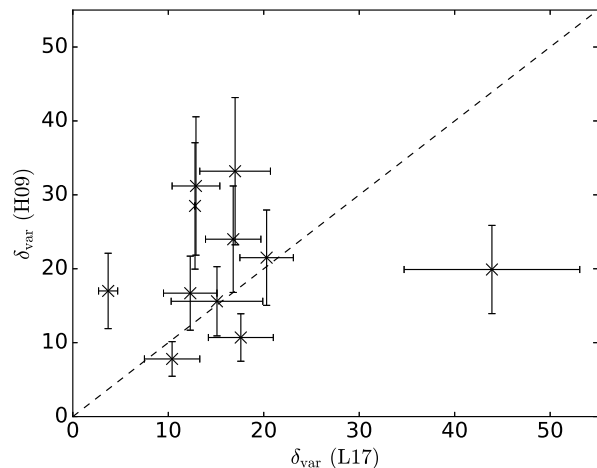


**Fig. 1.** Comparison between the  $\delta_{var}$  from H09 with the  $\delta_{var}$  from L17. The dashed line represents equality of the estimates. The error bars on the vertical axis are the on-average 30% from Lioudakis & Pavlidou (2015b).

mation or overestimation of the “true” Doppler factor. Past estimates of the inverse-Compton Doppler factor have not systematically pursued the use of simultaneous X-ray and radio observations, making the lack of simultaneity an obvious candidate for a source of error in the estimates. Since this effect can affect estimates in either direction, it will contribute to the statistical error budget. The G93 sample was found to be dominated by statistical error (63% on average on each estimate). How much of that 63% error can the lack of simultaneity between X-ray and radio observations account for is still to be determined, and the new  $\delta_{IC}$  estimates produced in this work using contemporaneous radio and X-ray measurements are a major step in this direction.

## 4. Sample and data

The sources of error discussed above, which were all entered through violations of basic assumptions underlying the inverse-Compton Doppler factor estimation method, are expected to dominate over observational errors in the quantities entered in Eq. 1. We adopted the following approach to form a quantitative understanding of the uncertainties in  $\delta_{IC}$  and resolve the discrepancy with variability Doppler factors:

- We selected a sample of sources to study for which two different  $\delta_{var}$  estimates, with various methodologies, are available (from both L17 and H09) so that we could control whether the  $\delta_{var}$ , for which we are comparing  $\delta_{IC}$  estimates against, are likely to be considerably plagued by systematics. Figure 1 shows the comparison between the  $\delta_{var}$  estimates. Differences between the variability estimates do not necessarily suggest problems with the  $\delta_{var}$ . Differences could arise from the different time span of observations between the datasets used especially if the Doppler factor varies with time. Exceptional outbursts or fast flares may occur in one dataset but (equivalent events) not in the other, leading to one producing a larger value for the  $\delta_{var}$ . Discrepancies between the variability estimates are discussed in more detail in L17.
- We focused on FSRQs (low-synchrotron-peaked sources) to minimize contamination of the X-ray flux by non-SSC

sources by at least eliminating the possibility of synchrotron emission at X-ray frequencies.

- We sought contemporaneous X-ray and radio data in the literature and used them to recalculate  $\delta_{IC}$ , thus eliminating the error induced by the lack of simultaneity between X-ray and radio observations.
- We re-examined any residual discrepancy between recalculated  $\delta_{IC}$  and  $\delta_{var}$ , and we evaluated this discrepancy on a source-by-source basis.

We began our source selection from the F-GAMMA sample, for which new estimates of  $\delta_{var}$  have been obtained by L17<sup>3</sup>. F-GAMMA is a multiwavelength monitoring program of the most interesting  $\gamma$ -loud sources with high radio power detected by the Large Area Telescope (LAT) on board the Fermi Gamma-ray Space Telescope (Acero et al. 2015).

We limited ourselves to a subsample of F-GAMMA sources that (a) are low-synchrotron-peaked FSRQs (Giommi et al. 2012), (b) have a previous estimation of both the  $\delta_{IC}$  and  $\delta_{var}$  (H09) available, (c) have available quasi-simultaneous (less than a week apart) VLBI and X-ray observations in the literature. There are 11 sources that meet these criteria. These sources are PKS0420-014, PKS0528+134, PKS1156+295, PKS1510-089, PKS1633+382, PKS1730-130, 3C273, 3C279, 3C345, 3C454.3, and CTA102.

The X-ray observations for PKS0528+134 were performed by the XMM-Newton observatory (Jansen et al. 2001), while the radio observations were performed as part of the Boston University group (BU group)<sup>4</sup> monthly monitoring program (Palma et al. 2011). The X-ray observations for 3C273 were performed by the ROSAT X-ray observatory, whereas the radio observations by the Very Long Baseline Interferometry (VLBI) were performed in a multifrequency campaign (Mantovani et al. 2000). The X-ray observations for PKS1510-089 and PKS1633+382 were conducted by the Rossi X-Ray Timing Explorer (RXTE) and the radio observations were conducted by the VLBA (Marscher et al. (2010), and Jorstad et al. (2011), respectively).

The X-ray flux for the remaining sources was taken from Chang (2010) (Swift X-ray telescope), while we used either Lister et al. (2013) or the data available online as part of the monitoring program by the BU group for the radio observations. For the data from the monitoring program by the BU group, we used standard DIFMAP procedures and the clean model available for each source for the phase and amplitude calibration. We then proceeded to fit Gaussian components to the calibrated maps. For our calculations, we use only the flux density of the core.

Determining the state of each source at the time of the observations is not trivial. A source might appear quiescent in one frequency (e.g., radio) while undergoing outbursts in another (e.g., optical). Unfortunately, the multiwavelength information necessary to characterize the state of a source is not always available. Regarding the sources for which we have that information, PKS0528+134 is in quiescent, PKS1510-089 is in outburst in multiple wavebands, and PKS1633+382 appears to be in quiescent in radio and X-rays while in outburst in  $\gamma$ -rays.

We converted all the broadband fluxes available in the literature to monochromatic flux densities at 1 keV required for Eq. 1, using the best-fit power-law spectrum for each source,

<sup>3</sup> Our selection of F-GAMMA sources also results in a sample of high-interest blazars, which, for example, are  $\gamma$ -ray loud (Acero et al. 2015) and are regularly monitored in optical polarization (King et al. 2014; Pavlidou et al. 2014).

<sup>4</sup> <http://www.bu.edu/blazars>

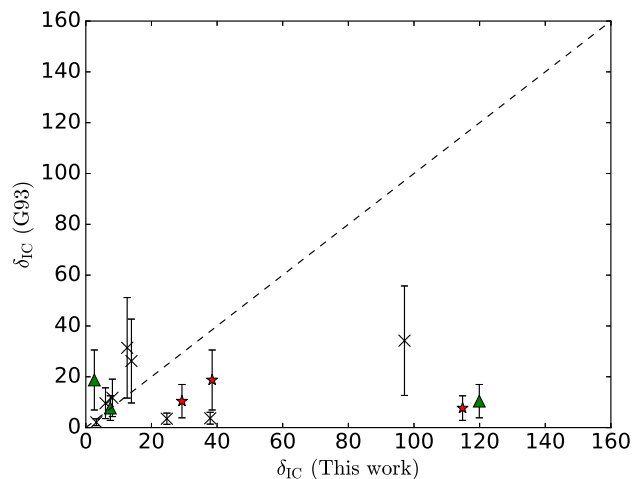


**Fig. 2.** Comparison between the  $\delta_{IC}$  from this work with the  $\delta_{IC}$  from G93. The red  $\star$  indicates the 15 GHz, whereas the green triangles indicate the 43 GHz values for the three sources with two  $\delta_{IC}$  estimates. The dashed line represents the equality of the estimates. The error bars on the vertical axis show the on-average 63% from Liodakis & Pavlidou (2015b).

and assuming the Galactic line-of-sight atomic hydrogen column density ( $N_H$ ) calculated from the survey of Dickey & Lockman (1990) via the Colden CIAO tool. In the cases for which we lacked spectral information, the X-ray photon index was taken from Williamson et al. (2014). All our Doppler factor estimates were calculated for the continuous jet case. The reason for this is that in Liodakis & Pavlidou (2015b) we found that the continuous jet case provided better agreement with blazar data on a population level.

All the values required for the estimation of the  $\delta_{IC}$  are summarized in Table 1. For the synchrotron high-energy cutoff and the optically thin spectral index we assumed  $\nu_b = 10^{14}$  Hz and  $\alpha = 0.75$ , respectively, to match the values used in G93. We verified that the method is not significantly affected by the choice of these two values. Any  $\nu_b$  in the range of  $10^{11} - 10^{17}$  Hz results in at most a  $\sim 10\%$  fractional difference from the estimated value (Table 2), while any  $\alpha$  in the range of 0.55 – 0.95 results in at most a  $\sim 20\%$  fractional difference.

## 5. Results

Using the values from Table 1 and Eq. 1 we re-estimated  $\delta_{IC}$  for the 11 sources in our sample. Radio observations at both 15 and 43 GHz were available for sources 3C345, 3C454.3, and PKS1730-130.

Figures 2 and 3 show the comparison between the  $\delta_{IC}$  derived in this work with various estimates in the literature. For the variability Doppler factors (Fig. 3) we plot the mean  $\pm 0.5\times$  (difference between H09, L17), since it quantifies our systematic uncertainty in the  $\delta_{var}$  estimate. In figure 3 for the sources with estimates for two radio frequencies, we only plot the estimate closest to the variability estimates. The various Doppler factor estimates are summarized in Table 2.

We see a wide range of results for the sources where there are estimates in two frequencies. This can be attributed to the fact that, at least for one of the estimates in each case, we used radio observations at a frequency other than the turnover frequency of the synchrotron spectrum. It is interesting to note that there is no systematic trend, i.e., a higher Doppler factor estimate at higher

**Table 1. Data.** Column: (1) Source name, (2) Redshift (3) Radio frequency, (4) X-ray flux density at 1 keV ( $F_{1keV}$ ), (5) radio flux density ( $F_R$ ), and (6) angular size ( $\theta_d$ ) of the core used in the estimation of the Doppler factor for each source.

Source	Redshift	Radio frequency (GHz)	$F_{1keV}$ ( $\mu$ Jy)	$F_R$ (Jy)	$\theta_d$ (mas)
PKS0420-014	0.915	15	0.61	4.26	0.306
PKS0528+134	2.070	43	0.06	0.84	0.048
PKS1156+295	0.729	43	0.29	1.49	0.1
PKS1510-089	0.360	15	1.44	3.80	0.2
PKS1633+382	1.814	43	0.30	1.60	0.07
PKS1730-130	0.902	15	0.20	2.54	0.144
PKS1730-130	0.902	43	0.20	0.9	0.126
3C273	0.158	43	$4.50 \times 10^{-7}$	2.57	0.42
3C279	0.536	15	1.18	13.3	0.18
3C345	0.593	15	$7.40 \times 10^{-3}$	5.09	0.165
3C345	0.593	43	$7.40 \times 10^{-3}$	3.55	0.221
3C454.3	0.859	15	3.18	22.20	0.45
3C454.3	0.859	43	3.18	20.30	0.09
CTA102	1.037	43	0.39	2.40	0.2

(Mantovani et al. 2000; Jansen et al. 2001; Marscher et al. 2010; Jorstad et al. 2011; Palma et al. 2011; Chang 2010; Lister et al. 2013)

**Table 2. Doppler factor estimates.** Column: (1) Source name, (2) Frequency, (3)  $\delta_{IC}$  derived in this work, (4)  $\delta_{IC}$  from G93, (5)  $\delta_{var}$  from H09, (6)  $\delta_{var}$  from L17, (7) average value of the  $\delta_{var}$  estimates, and (8) the spread of the  $\delta_{var}$  estimates. The errors in column 4 and 5 are the 63% and 30% errors, respectively, from Liodakis & Pavlidou (2015b), the errors in column 6 are the source-by-source estimates from L17, and the errors in column 7 are derived through standard error propagation.

Source	Frequency (GHz)	$\delta_{IC}$ (This work)	$\delta_{IC}$ (G93)	$\delta_{var}$ (H09)	$\delta_{var}$ (L17)	$\langle \delta_{var} \rangle$	$\sigma_{\langle \delta_{var} \rangle}$
PKS0420-014	15	12.6	$31.4 \pm 19.8$	$19.9 \pm 5.9$	$43.9 \pm 9.2$	$31.9 \pm 5.5$	12.0
PKS0528+134	43	37.9	$3.7 \pm 2.3$	$31.2 \pm 9.3$	$12.9 \pm 2.5$	$22.0 \pm 4.8$	9.2
PKS1156+295	43	6.0	$9.6 \pm 6.0$	$28.5 \pm 8.5$	$12.8 \pm 0.04$	$20.6 \pm 4.3$	7.9
PKS1510-089	15	13.9	$26.2 \pm 16.5$	$16.7 \pm 5.0$	$12.3 \pm 2.8$	$14.5 \pm 2.9$	2.2
PKS1633+382	43	24.7	$3.5 \pm 2.2$	$21.5 \pm 6.4$	$20.3 \pm 2.8$	$20.9 \pm 3.5$	0.6
PKS1730-130	15	38.5	$18.7 \pm 11.8$	$10.7 \pm 3.2$	$17.6 \pm 3.4$	$14.1 \pm 2.3$	3.5
PKS1730-130	43	2.6	$18.7 \pm 11.8$	$10.7 \pm 3.2$	$17.6 \pm 3.4$	$14.1 \pm 2.3$	3.5
3C273	43	8.1	$11.7 \pm 7.4$	$17.0 \pm 5.1$	$3.7 \pm 1.0$	$10.3 \pm 2.6$	6.7
3C279	15	97.1	$34.2 \pm 21.5$	$24.0 \pm 7.2$	$16.8 \pm 2.9$	$20.4 \pm 3.9$	3.6
3C345	15	114.8	$7.6 \pm 4.8$	$7.8 \pm 2.34$	$10.4 \pm 2.9$	$9.1 \pm 1.9$	1.3
3C345	43	7.5	$7.6 \pm 4.8$	$7.8 \pm 2.34$	$10.4 \pm 2.9$	$9.1 \pm 1.9$	1.3
3C454.3	15	29.3	$10.4 \pm 6.5$	$33.2 \pm 9.9$	$17.0 \pm 3.7$	$25.1 \pm 5.3$	8.1
3C454.3	43	119.9	$10.4 \pm 6.5$	$33.2 \pm 9.9$	$17.0 \pm 3.7$	$25.1 \pm 5.3$	8.1
CTA102	43	3.2	$2.1 \pm 1.3$	$15.6 \pm 4.6$	$15.1 \pm 4.8$	$15.3 \pm 3.3$	0.25

frequencies or vice versa. This result emphasizes the importance of treating each source separately and performing the radio observations at the turnover frequency. It is clear that one of the two estimates is more reliable for 3C345 ( $\delta_{IC} = 7.4$  obtained at 43 GHz), since it is consistent with  $\langle \delta_{var} \rangle$  and the alternative estimate is unrealistically high (114.8). In addition, the turnover varies between  $15 \leq$  and  $\leq 86$  GHz (Angelakis et al. in prep.), which is consistent with our results suggesting that the 43 GHz  $\delta_{IC}$  is an accurate estimate of the Doppler factor. A similar case is for 3C454.3. Although we cannot constrain the turnover for 3C454.3, it is obvious that one estimate (at 43 GHz) is unrealistically high (119.9), while the second (at 15 GHz) is consistent with  $\langle \delta_{var} \rangle$ . The unrealistically high value at 43 GHz could also be attributed to the relatively large decrease in angular size compared to the size of the core at 15 GHz. If this is indeed the size of the core at 43 GHz, it would suggest a significant decrease in the size of the jet between the two regions probed by these frequencies. This apparent decrease in size could be the result of small scale jet variation (e.g., a bent jet or precession), although

we are not able to excluded data-related artefacts. For this reason, our results for the 3C454.3 at 43 GHz should be treated with caution.

Given the typical span of reported estimates for blazar Doppler factors in the literature ( $\sim 0-45$ ) it is possible to have an offset from the “true” Doppler factor of an order of magnitude and still be within familiar limits. This might as well be the case for PKS1730-130 for which one estimate is 2.6 and the other 38.5. In addition neither estimate is in agreement with  $\langle \delta_{var} \rangle$  or any of the individual  $\delta_{var}$  estimates that lie in between those estimates. It is possible that the turnover is between 15 and 43 GHz so that one frequency overestimates while the other underestimates the Doppler factor. Results from F-GAMMA find that the turnover is changing, while residing  $< 86$  GHz, which does not provide any constraints on its position, and hence we cannot draw any firm conclusions.

Using these estimates we can roughly estimate (for this sample) the impact of not using the turnover frequency for IC Doppler factors. Taking the ratio of the two estimates

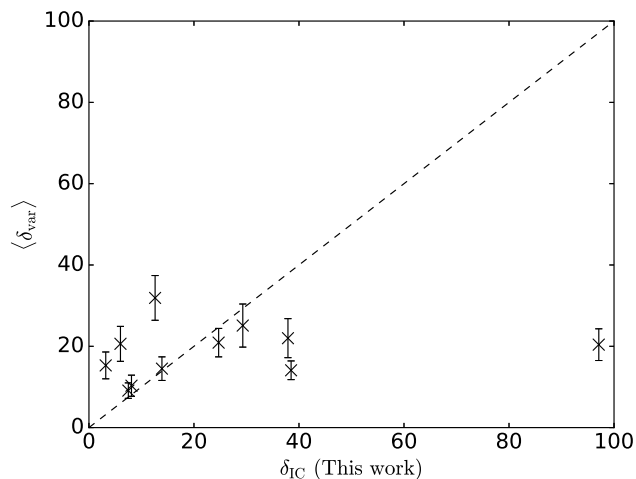


**Fig. 3.** Comparison between the  $\delta_{IC}$  from this work with the mean of the two estimates in the literature ( $\langle\delta_{var}\rangle$ , H09, L17). The dashed line represents equality of the estimates and the errors in the vertical axis represent the spread between the two methods. For the sources with estimates for two frequencies, we plot the estimate closest to  $\langle\delta_{var}\rangle$ .

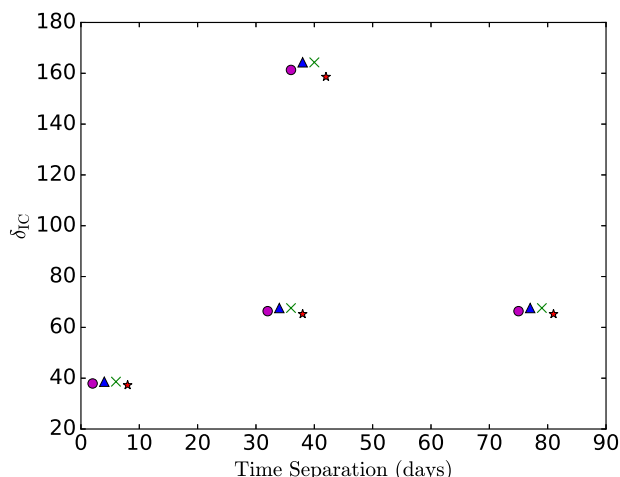


**Fig. 4.** Various estimates for PKS0528+134 against the time separation of X-ray and radio observations. Same symbols denote same X-ray but different radio observations.

( $\delta_{IC,high}/\delta_{IC,low}$ ), we find that the difference between estimates can be as high as a factor of  $\sim 15$ .

We can distinguish two cases: a) all estimates of the two methods, i.e., this work, average of H09, and L17, are in agreement; and b) the estimates derived in this work do not agree with the  $\langle\delta_{var}\rangle$  estimate.

- **a) All estimates of the two methods (this work and  $\langle\delta_{var}\rangle$ ) are in agreement.** There are five sources in this category: PKS1510-089, PKS1633+382, 3C273, 3C345, and 3C454.3. Given the different assumptions and approaches involved in the two estimates, it is highly unlikely that some unknown common bias would lead to the same result. Especially for 3C273 and 3C345, even the original  $\delta_{IC}$  estimate from G93 is in agreement with the  $\langle\delta_{var}\rangle$  estimate. Thus we can conclude that since all methods converge to the same result for these five sources, the Doppler factor of the jet in the radio region

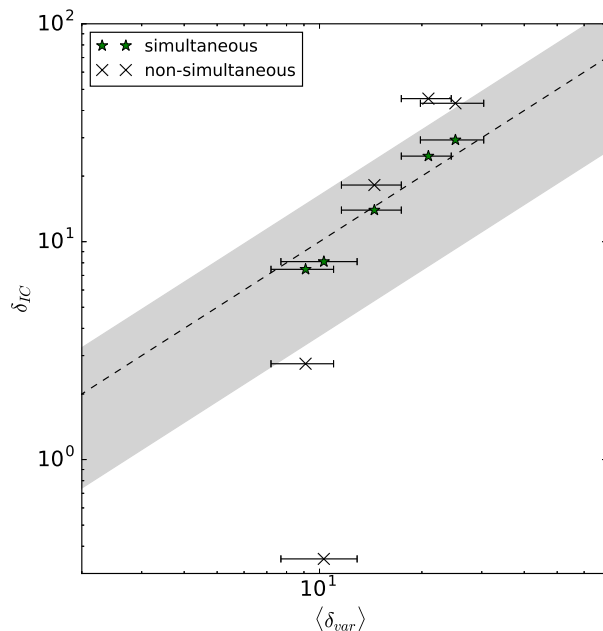


**Fig. 5.** Comparison of the  $\langle\delta_{var}\rangle$  against simultaneous and non-simultaneous estimates using the X-ray flux density from this work and from G93, respectively. The green  $\star$  indicates for simultaneous estimates and the black  $\times$  indicates non-simultaneous estimates. The dashed line represents the equality of the estimates and the gray shaded area the 63% on-average error from Liodakis & Pavlidou (2015b).

can be effectively constrained to the value reported in Table 2.

- **b) The estimates derived in this work do not agree with the  $\langle\delta_{var}\rangle$  estimate.** The sources in this category are PKS0420-014, PKS0528+135, PKS1156+295, PKS1730-130, 3C279, and CTA102. The source 3C279 has an unrealistically high value, which is most likely due to the turnover effect. This is also confirmed by the fact that the G93 estimate is consistent within errors with  $\langle\delta_{var}\rangle$  as well as with H09 and L17 estimates individually. As discussed above, the turnover frequency is prone to change over time. For this reason, it is possible that at the time of observations (when the G93 estimate was derived) the turnover frequency was close to 5 GHz (which is the observing frequency used in G93), while the turnover frequency at the time of the observations used in this work was far from 15 GHz.

For PKS1156+295, the  $\delta_{IC}$  and  $\langle\delta_{var}\rangle$  estimates do not converge and  $\delta_{IC}$  is not within  $1\sigma$  from any individual  $\delta_{var}$  estimate ( $3\sigma$  away from the H09 estimate). It is interesting that although the H09 estimate is relatively high (28.5) the re-estimated value (6.0) is more consistent with the G93 estimate (9.6) and the L17 (12.8) is relatively close, however the error estimate given in L17 is too small to account for the difference. The fact that the two  $\delta_{IC}$  estimates are consistent with each other reduces the likelihood of any turnover systematic effects since G93 and this work use different frequencies, while contamination of the X-ray flux from the big blue bump is unlikely (Abdo et al. 2010). The error estimate in L17 is derived through an iterative process where the best-fit model is altered both in flare rise time and flare amplitude, and by setting a limit to the maximum standard deviation of the residuals of the fitted light curve, these authors have acquired a range of acceptable models. The existence of a sharp

flare in the light curve of PKS1156+295 sets a relatively rigid limit to the range of flare rise times, which results in a small error estimate (0.3% percentage error) that is not necessarily accurate because in this case other, usually subdominant and ignored sources of error, may become more important<sup>5</sup>. If instead we use the 16% on average (for that sample) quoted in L17, the error estimate for this source becomes  $\sigma_{\delta_{var}} = 2.0$  which would bring both  $\delta_{IC}$  estimates within  $3\sigma$ . It is then possible that the uncertainty of the  $\delta_{var}$  in L17 is underestimated and the true value of the Doppler factor for this source lies between 6.0 and 12.8.

Similarly, for CTA102, the re-estimated  $\delta_{IC}$  is not consistent with the  $\langle\delta_{var}\rangle$  estimate and is instead consistent with the estimate from G93. Here there is also no prominent big blue bump (Fromm 2015) and we can rule out any problems with the individual  $\delta_{var}$  estimates since they are in very good agreement with each other. This case would indicate either significant external Compton flux or an additional unidentified source of error beyond those discussed in this work.

There are estimates derived in this work that agree with one of the  $\delta_{var}$  estimates. These sources are PKS0420-014 and PKS0528+135. All the estimates in agreement with H09 are above the pileups seen in the distribution of Doppler factors in the H09 sample (see Lioudakis & Pavlidou 2015b) and should not, in principle, be affected by the cadence of observations, which is the dominant source of systematics in the  $\delta_{var}$  method.

Possible interpretations of the discrepancies between the estimates in H09 and L17 (for example variability of  $\delta$ ) are discussed in L17. Unless an unknown cause has led to the false estimation of the  $\delta_{IC}$  derived in this work, agreement with an estimate from one approach and not the other should, in principle, weigh in favor of that  $\delta_{var}$  estimate being a better representation of the Doppler factor.

Another potential source of error is the imperfect simultaneity of the radio and X-ray observations. The observations used in this work are taken to be less than a week apart. This limit was set empirically given the typical X-ray and radio variability of LSP sources. To test whether this assumption would cause any shift in our estimates, we used PKS0528+134 for which there exist multiple quasi-contemporaneous observations. Keeping the date of the radio observation constant and letting that of the X-rays vary, we re-estimated the  $\delta_{IC}$  for four different time intervals.

Figure 4 shows various  $\delta_{IC}$  estimates versus time separation between observations for PKS0528+134. Even with observations obtained one week apart, the results are within the typical span of Doppler factor estimates (see H09 and L17). When, however, the separation of the observations is more than a month apart, the values for the Doppler factor become unrealistically high. Keeping in mind that this limit could be different for every source, it is possible that for some of our sources the radio and X-ray observations are not “simultaneous enough”. A more variable source in X-rays might have a smaller time tolerance between observations. This might constitute a problem especially in cases where observations are performed during outbursts (a very common observational bias), in which case the variability in either bands could increase.

We finally test whether lack of simultaneity between X-ray and radio observations is responsible for most of the statistical error in  $\delta_{IC}$  once all other sources of systematic error have been

accounted for. We used the sources for which the estimates derived in this work are in agreement with the  $\langle\delta_{var}\rangle$  estimates. We then tampered with our estimates, violating the simultaneity criterion. We use the same radio data, i.e., flux density, frequency, and angular diameter, but instead of the X-ray flux densities from Table 1, we used the corresponding values quoted in G93.

Figure 5 shows the comparison between  $\langle\delta_{var}\rangle$  and the simultaneous and non-simultaneous estimates using various X-ray flux densities. The gray band around the dashed line represents the 63% on-average uncertainty associated with  $\delta_{IC}$  from G93 (Lioudakis & Pavlidou 2015b). It is clear that the simultaneous estimates (green  $\star$ ) fare much better than the non-simultaneous estimates (black  $\times$ ). We can also roughly estimate the contribution of the lack of simultaneity to the statistical error by examining the fractional difference between the  $\delta_{IC}$  from this work with the  $\delta_{IC}$  from G93. We find that the percentage error is between  $\sim 3\%$  to  $\sim 540\%$  with an average of  $\sim 100\%$  using all of the estimates; for sources with multiple estimates we use the one closest to a  $\langle\delta_{var}\rangle$  estimate. If we only use the estimates that are consistent with either  $\langle\delta_{var}\rangle$  or at least one of the individual  $\delta_{var}$  estimates, we find the percentage error to be between  $\sim 3\%$  and  $\sim 97\%$  with an average of  $\sim 68\%$ , which is consistent with the on-average population estimate (63%) from Lioudakis & Pavlidou (2015b). We conclude that lack of simultaneity between X-ray and radio observations is the dominant contributor to the overall statistical error budget.

## 6. Summary

Population models have shown that the inverse-Compton and variability Doppler factor methods can describe FSRQs as a population, even though they are inconsistent on a source-by-source basis. In this work, we attempted to resolve this discrepancy by identifying and examining potential sources of systematic and statistical error involved in the inverse-Compton Doppler factor method, and by eliminating them, we provide a much more accurate estimate of the “true” Doppler factor of blazar jets to serve as a gateway to their, yet to be explored, rest frame.

To that end, we re-estimated the  $\delta_{IC}$  for 11 sources and compared them with the average of two independent estimates of  $\delta_{var}$  following various approaches. Our findings can be summarized as follows:

1. Careful sample selection is crucial for the correct application of the method, as application of the method to sources where the X-ray flux is contaminated by non-SSC sources can cause systematic shifts in the estimates of  $\delta_{IC}$ . Such sources are high synchrotron-peaked blazars; sources with a significant external Compton X-ray flux; or sources with a prominent big blue bump, although this is not always prohibitive. An example is PKS1510-089, where there is a visible big blue bump (D’Ammando et al. 2009), but it does not extend to high energies and thus has no contribution to the X-ray flux. Evidence of this is the fact that all the available estimates for the Doppler factor for PKS1510-089 converge to the same result.
2. Radio observations at the synchrotron turnover frequency are an important aspect of the IC method. Since the turnover frequency is likely to change over time or during events to ensure robust results, it is a condition that should not be violated. Departure from the turnover frequency could result in a Doppler factor error as high as a factor of  $\sim 15$ .
3. Errors due to the lack of simultaneity between X-ray and radio observations constitute the dominant fraction of the

<sup>5</sup> See, e.g., Cyburt et al. (2001) and Mouschovias & Tassis (2010) for a discussion of error underestimation due to usually subdominant error sources

statistical error in IC Doppler factors. Although the exact amount that can be accounted for varies from source to source, this value is on average  $\sim 68\%$ , which is consistent with the average estimate from Liodakis & Pavlidou (2015b). The time delay limit of seven days set in this work works reasonably well for most sources, although its applicability depends on the source and time of observations (e.g., observations during outbursts). Thus variability in both bands (X-ray and radio) should be taken into account when choosing the maximum reliable time separation between radio and X-ray observations.

4. By resolving the discrepancies between all methods, we were able to effectively constrain the Doppler factor for five sources (about 45% of our sample), namely: 3C273, 3C345, 3C454.3, PKS1510-089, and PKS1633+382, where the re-estimated  $\delta_{IC}$  and the  $\langle \delta_{var} \rangle$  converge to the same result. This not only gives us confidence in our analysis, but it also provides a strong case supporting that this is indeed the value of the “true” Doppler factor of each jet.

Throughout this work we have assumed that the Doppler factor does not vary significantly with time. This is not necessarily true. We have already discussed that the differences between the two  $\delta_{var}$  estimates (H09, L17) can arise from the different time span of observations of the two datasets (see Section 4). This can also be true for the  $\delta_{IC}$  estimates. Jet precession, bent jets, or local acceleration or deceleration of jet components (Lister et al. 2009b; Homan et al. 2009, 2015) might contribute to the overall uncertainty of estimating the “true” Doppler factor. For these reasons, the comparison of the various Doppler factor methods should be in principle performed using contemporaneous datasets although this is not always feasible given the availability of data. It is possible that such phenomena are responsible for the unidentified source of error for CTA102 as well as the remaining sources that did not converge.

We were able to constrain 5 out of the 11 sources in our sample using the only available archival data for which systematics effects, such as the choice of observing frequency with respect to the turnover, could not be fully accounted for. New contemporaneous radio and X-ray observations following the guidelines described in this work will in principle constrain the Doppler factor of blazar jets with higher efficiency for a larger number of sources or alternatively reveal new aspects of blazar emissions mechanisms and jet processes.

*Acknowledgements.* The authors would like to thank Bia Boccardi, Nicola Marchili, and the anonymous referee for comments and suggestions that helped improve this work. This research was supported by the “Aristeia” action of the “Operational Program Education and Lifelong Learning” and is co-funded by the European Social Fund (ESF) and Greek National Resources, and by the European Commission Seventh Framework Program (FP7) through grants PCIG10-GA-2011-304001 “JetPop” and PIRSES-GA-2012-31578 “EuroCal”. AZ acknowledges funding from the European Research Council under the European Union’s Seventh Framework Programme (FP/2007-2013)/ERC Grant Agreement n. 617001. T. Hovatta was supported by the Academy of Finland project number 267324. This research has made use of data from the MOJAVE database that is maintained by the MOJAVE team (Lister et al. 2009a). This study makes use of 43 GHz VLBA data from the VLBA-BU Blazar Monitoring Program (VLBA-BU-BLAZAR; <http://www.bu.edu/blazars/VLBAproject.html>), funded by NASA through the Fermi Guest Investigator Program. The VLBA is an instrument of the National Radio Astronomy Observatory. The National Radio Astronomy Observatory is a facility of the National Science Foundation operated by Associated Universities, Inc.

## References

Abdo, A. A., Ackermann, M., Agudo, I., et al. 2010, *ApJ*, 716, 30

- Ajero, F., Ackermann, M., Ajello, M., et al. 2015, *ApJS*, 218, 23
- Angelakis, E., Fuhrmann, L., Marchili, N., et al. 2015, *A&A*, 575, A55
- Angelakis, E., Fuhrmann, L., Nestoras, I., et al. 2012, *Journal of Physics Conference Series*, 372, 012007
- Angelakis, E., Fuhrmann, L., Nestoras, I., et al. 2010, *ArXiv e-prints*
- Angelakis, E., Hovatta, T., Blinov, D., et al. 2016, *MNRAS*
- Blandford, R. D. & Königl, A. 1979, *ApJ*, 232, 34
- Blinov, D., Pavlidou, V., Papadakis, I., et al. 2016a, *MNRAS*, 462, 1775
- Blinov, D., Pavlidou, V., Papadakis, I. E., et al. 2016b, *MNRAS*, 457, 2252
- Britzen, S., Brinkmann, W., Campbell, R. M., et al. 2007, *A&A*, 476, 759
- Chang, C.-S. 2010, PhD thesis, Max-Planck-Institut für Radioastronomie, [cschang@mpifr-bonn.mpg.de](mailto:cschang@mpifr-bonn.mpg.de)
- Cybur, R. H., Fields, B. D., & Olive, K. A. 2001, *New A*, 6, 215
- D’Ammando, F., Pucella, G., Raiteri, C. M., et al. 2009, *A&A*, 508, 181
- Dickey, J. M. & Lockman, F. J. 1990, *ARA&A*, 28, 215
- Feng, S.-W., Shen, Z.-Q., Cai, H.-B., et al. 2006, *A&A*, 456, 97
- Fromm, C. 2015, *Spectral Evolution in Blazars: The Case of CTA 102* (Springer Theses)
- Fuhrmann, L., Zensus, J. A., Krichbaum, T. P., Angelakis, E., & Readhead, A. C. S. 2007, in *American Institute of Physics Conference Series*, Vol. 921, The First GLAST Symposium, ed. S. Ritz, P. Michelson, & C. A. Meegan, 249–251
- Ghisellini, G. 1987, *MNRAS*, 224, 1
- Ghisellini, G., Padovani, P., Celotti, A., & Maraschi, L. 1993, *ApJ*, 407, 65
- Giommi, P., Polenta, G., Lähteenmäki, A., et al. 2012, *A&A*, 541, A160
- Gujosa, A. & Daly, R. A. 1996, *ApJ*, 461, 600
- Homan, D. C., Kadler, M., Kellermann, K. I., et al. 2009, *ApJ*, 706, 1253
- Homan, D. C., Lister, M. L., Kovalev, Y. Y., et al. 2015, *ApJ*, 798, 134
- Hovatta, T., Tammi, J., Tornikoski, M., et al. 2010, in *Astronomical Society of the Pacific Conference Series*, Vol. 427, Accretion and Ejection in AGN: a Global View, ed. L. Maraschi, G. Ghisellini, R. Della Ceca, & F. Tavecchio, 34
- Hovatta, T., Valtaoja, E., Tornikoski, M., & Lähteenmäki, A. 2009, *A&A*, 494, 527
- Jansen, F., Lumb, D., Altieri, B., et al. 2001, *A&A*, 365, L1
- Jorstad, S. G., Marscher, A. P., Agudo, I., et al. 2011, *Journal of Astrophysics and Astronomy*, 32, 239
- King, O. G., Blinov, D., Ramaprakash, A. N., Myserlis, I., et al. 2014, *MNRAS*, 432, 87
- Komatsu, E., Dunkley, J., Nolte, M. R., et al. 2009, *ApJS*, 180, 330
- Lähteenmäki, A. & Valtaoja, E. 1999, *ApJ*, 521, 493
- Lähteenmäki, A., Valtaoja, E., & Wiik, K. 1999, *ApJ*, 511, 112
- Liodakis, I., Marchili, N., Angelakis, E., et al. 2017, *MNRAS*, 466, 4625
- Liodakis, I. & Pavlidou, V. 2015a, *MNRAS*, 451, 2434
- Liodakis, I. & Pavlidou, V. 2015b, *MNRAS*, 454, 1767
- Lister, M. L., Aller, H. D., Aller, M. F., et al. 2009a, *AJ*, 137, 3718
- Lister, M. L., Aller, M., Aller, H., et al. 2011, *ApJ*, 742, 27
- Lister, M. L., Aller, M. F., Aller, H. D., et al. 2013, *AJ*, 146, 120
- Lister, M. L., Cohen, M. H., Homan, D. C., et al. 2009b, *AJ*, 138, 1874
- Lister, M. L. & Homan, D. C. 2005, *AJ*, 130, 1389
- Mantovani, F., Junor, W., McHardy, I. M., & Valerio, C. 2000, *A&A*, 354, 497
- Marscher, A. P., Jorstad, S. G., Larionov, V. M., et al. 2010, *ApJ*, 710, L126
- Mouschovias, T. C. & Tassis, K. 2010, *MNRAS*, 409, 801
- Palma, N. I., Böttcher, M., de la Calle, I., et al. 2011, *ApJ*, 735, 60
- Pavlidou, V., Angelakis, E., Myserlis, I., et al. 2014, *MNRAS*, 442, 1693
- Rabaça, C. R. & Zensus, J. A. 1994, in *Compact Extragalactic Radio Sources*, ed. J. A. Zensus & K. I. Kellermann, 163
- Readhead, A. C. S. 1980, *Phys. Scr.*, 21, 662
- Readhead, A. C. S. 1994, *ApJ*, 426, 51
- Readhead, A. C. S., Cohen, M. H., Pearson, T. J., & Wilkinson, P. N. 1978, *Nature*, 276, 768
- Scheuer, P. A. G. & Readhead, A. C. S. 1979, *Nature*, 277, 182
- Valtaoja, E., Lähteenmäki, A., Teräsranta, H., & Lainela, M. 1999, *ApJS*, 120, 95
- Williamson, K. E., Jorstad, S. G., Marscher, A. P., et al. 2014, *ApJ*, 789, 135

# Scale invariant jets: from blazars to microquasars

I. Liodakis<sup>1,2\*</sup>, V. Pavlidou<sup>1,2</sup>, I. Papadakis<sup>1,2</sup>, E. Palaiologou<sup>1,2</sup>,  
E. Angelakis<sup>3</sup>, N. Marchili<sup>4</sup>, J. A. Zensus<sup>3</sup>, L. Fuhrmann<sup>5</sup>, V. Karamanavis<sup>3</sup>,  
I. Myserlis<sup>3</sup>, I. Nestoras<sup>3</sup>, A. C. S. Readhead<sup>6</sup>

<sup>1</sup>Department of Physics and ITCP, University of Crete, 71003, Heraklion, Greece

<sup>2</sup>Foundation for Research and Technology - Hellas, IESL, Voutes, 7110 Heraklion, Greece

<sup>3</sup>Max-Planck-Institut für Radioastronomie, Auf dem Hügel 69, 53121 Bonn, Germany

<sup>4</sup>IAPS-INAF, Via Fosso del Cavaliere 100, 00133, Roma, Italy

<sup>5</sup>ZESS - Center for Sensorsystems, University of Siegen, Paul-Bonatz-Str. 9-11, 57076  
Siegen, Germany

<sup>6</sup>Cahill Center for Astronomy and Astrophysics, California Institute of Technology, 1200 E  
California Blvd, Pasadena, CA 91125

May 22, 2017

Black holes, anywhere in the stellar-mass to supermassive range, are often associated with relativistic jets. Models suggest that jet production may be a universal process common in all black hole systems regardless of their mass. Although in many cases observations support such hypotheses for microquasars and Seyfert galaxies, little is known on whether boosted blazar jets also comply with such universal scaling laws. We use uniquely rich multiwavelength radio light curves from the F-GAMMA program to probe blazar jets in their emission rest frame with unprecedented accuracy. We identify for the first time a strong correlation between the blazar intrinsic broad-band radio luminosity and

black hole mass, which extends over  $\sim 9$  orders of magnitude down to microquasars scales. Our results reveal the presence of a universal scaling law that bridges the observing and emission rest frames in beamed sources and allows us to effectively constrain jet models. They consequently provide an independent method for estimating the Doppler factor, and for predicting expected radio luminosities of boosted jets operating in systems of intermediate or tens-of-solar mass black holes, immediately applicable to cases as those recently observed by LIGO.

Blazars constitute unique laboratories for the study of extreme astrophysics, from relativistic magnetohydrodynamics and shocks, to particle acceleration, ultra-high energy cosmic rays and

neutrino production. Understanding the highly collimated plasma outflows of blazar jets has proven extremely difficult due to the relativistic effects dominating their emission from radio to  $\gamma$ -rays [5]. These relativistic effects are quantified by the Doppler factor  $\delta = [\gamma(1 - \beta \cos \theta)]^{-1}$ , where  $\gamma$  is the Lorentz factor ( $\gamma = (\sqrt{1 - \beta^2})^{-1}$ ),  $\beta$  is the velocity of the jet in units of speed of light, and  $\theta$  is the angle between their jet axis and the observer’s line of sight.

Even a small spread in the values of  $\gamma$  and  $\theta$  among blazars results in a large spread in observed properties, severely complicating the search for empirical correlations that can confirm or constrain jet models. If  $\delta$  could be confidently estimated, however, these relativistic effects could be corrected for and blazar jets could be studied in their emission rest frame. Several methods have been proposed for estimating blazar Doppler factors, but they frequently yield discrepant results [38]. Multi-frequency F-GAMMA radio data have recently enabled the calculation of the highest-ever accuracy variability Doppler factors for 58 well-studied blazars [36]. In this work, we use these estimates to establish a scaling between the black hole mass ( $M_{\text{BH}}$ ) and intrinsic (rest-frame) broad-band radio luminosity in blazars. This is the first such scaling ever identified in relativistically boosted jets.

Correlations between  $M_{\text{BH}}$  and monochromatic radio flux density, or the monochromatic radio flux density and the X-ray flux density or even all the above combined, have long been established [39]. The latter suggests the existence of a plane, termed “fundamental plane of black hole activity”, which extends from X-ray binaries to active galaxies. These results support the hypothesis of scale invariance, which implies that the jet formation processes are independent

of the black hole mass of the system. Such a hypothesis has been predicted by theoretical models [27].

The above mentioned method [39] as well as similar attempts to establish a relation connecting BH-powered jets of different  $M_{\text{BH}}$  [45, 13, 33, 49, 55] have either explicitly avoided blazars focusing on low-luminosity active galactic nuclei (LLAGNs) or have included a handful of blazars. They have either ignored the relativistic effects or specifically chosen their sample to include only low-beamed sources. In cases where there was some treatment of the relativistic effects [13, 33, 49], the common practice was to use a single value of  $\delta$  (when in reality Doppler factors are estimated to range between 1 and 45 based on individual source studies [34, 29, 14, 36] and between 1 and 60 based on a population studies [37]).

However, studies focused on blazars fully and accurately accounting for their relativistic effects cannot be circumvented, if the aim is to study the physics of jets in particular: it is only in such highly beamed sources where the jet emission is boosted enough so that we can be confident it dominates the observed spectrum. For this reason, the extension of such scalings to blazars would have a strong impact on unification models of radio-loud active galactic nuclei and our knowledge of BH-powered jets, increasing many-fold our ability to constrain jet models.

There have been attempts to create similar scaling relations in blazars either using luminosity-luminosity correlations [47, 15] or different jet quantities with the properties of the central engine [65, 28, 7]. However, the relativistic effects hamper any attempt to establish a strong correlation between the rest-frame emission of the jet and the BH mass in beamed sources.

Nevertheless, as we find in this work, when we accurately correct for the relativist effects, we can show that a strong relation exists between the  $M_{\text{BH}}$  and the intrinsic broad-band (Br-B) radio luminosity (the total radio output of the supermassive BH in the emission rest frame,  $\mathcal{L}_{\text{int}}^{\text{Br-B}}$ ) in blazars.

To resolve the relativistic effects, we used the most accurate Doppler factor estimates in the literature to date [36], to account for the relativistic effects and measure the rest-frame broad-band radio luminosity in blazars. We used data from the multi-frequency F-GAMMA monitoring program [22] and the maximum likelihood analysis described in [53] to construct the mean radio spectral energy distribution (SED) for each source. The use of broad-band radio luminosity is very important in highly beamed sources viewed at small angles. For in such sources, synchrotron self-absorption results in different regions of the jet probed by different frequencies in a way that differs between different sources. Using broad-band radio luminosities allows us to overcome this difficulty, it is novel in this work, and it is only made possible by the availability of F-GAMMA data. After accounting for errors in measurements and source variability, we calculated  $\mathcal{L}_{\text{int}}^{\text{Br-B}}$  from 2.64 to 142.33 GHz assuming either a continuous jet ( $\mathcal{L}_{\text{int,c}}^{\text{Br-B}}$ ) or a discrete jet ( $\mathcal{L}_{\text{int,d}}^{\text{Br-B}}$ , see Methods). Additionally we calculated the  $M_{\text{BH}}$  in our sample and complemented it with literature values (see section Methods). We opted to use only mass estimates from spectral lines (as opposed to, e.g. SED fitting [24]) specifically to eliminate as much as possible any effect (such as luminosity-luminosity correlations) that could induce fake correlations.

The number of sources with available esti-

mates for both Doppler factor and  $M_{\text{BH}}$  in our sample is 26 (20 FSRQs, 4 BL Lacs, and 2 radio galaxies). In order to extend our sample towards lower black hole masses, we also included three  $\gamma$ -ray loud Narrow Line Seyfert 1 galaxies (NLS1s) [4] for which there was a Doppler factor computed with the same method as in [36]. In total our sample consists of 29 sources with  $M_{\text{BH}}$  spanning from  $\sim 10^{6.5} - 10^{9.5} M_{\odot}$ .

Assuming that the jet is composed of a series of plasma blobs (discrete jet) we tested for a correlation between the  $\mathcal{L}_{\text{int,d}}^{\text{Br-B}}$  and  $M_{\text{BH}}$ . We used the partial correlation test [3] in order to obtain the Kendall correlation coefficient ( $\tau$ ) and its significance taking into account the effects of redshift. The partial correlation test yielded a correlation coefficient of  $\tau = 0.35$  with  $2 \times 10^{-3}$  probability of uncorrelated samples, indicating a strong correlation. If we assume the jet is a continuous stream of plasma (continuous jet,  $\mathcal{L}_{\text{int,c}}^{\text{Br-B}}$ ), the correlation becomes significantly stronger ( $\tau = 0.51$  with  $5 \times 10^{-6}$  probability of no correlation). The correlation is stronger in this case, which is to be expected since the continuous jet is, most likely, the most accurate representation of the jet structure, as has been repeatedly supported by interferometric radio observations (VLBI, e.g. [72]). For this reason, for the remaining of this work we focus on the continuous jet case. Examining different subsamples there was no case where the p-value was  $> 10^{-3}$  supporting the robustness of the correlation (see section Methods). Having established that a significant correlation exists, we performed a fit between the  $\mathcal{L}_{\text{int,c}}^{\text{Br-B}}$  and the  $M_{\text{BH}}$ . The linear model is in form of  $\log \mathcal{L}_{\text{int,c}}^{\text{Br-B}} = A \times \log\left(\frac{M}{10^8 M_{\odot}}\right) + B$ . For the fit we used the BCES bisector method described in [2] which takes into account uncertainties in both x and y-axis as well as any intrinsic scatter.

The best-fit line between the  $\mathcal{L}_{\text{int,c}}^{\text{Br-B}}$  and the  $M_{\text{BH}}$  would then be,

$$\log\left(\frac{\mathcal{L}_{\text{int,c}}^{\text{Br-B}}}{\text{Watt}}\right) = (1.12 \pm 0.13) \times \log\left(\frac{M}{10^8 M_{\odot}}\right) + (35.5 \pm 0.1). \quad (1)$$

The  $\log \mathcal{L}_{\text{int,c}}^{\text{Br-B}}$  versus  $\log M$  plot is shown in Fig. 1 together with the best-fit line.

If jets are indeed scale invariant, then stellar mass BH systems (i.e. microquasars with  $M_{\text{BH}} \approx 10 M_{\odot}$ ) will have intrinsic broad-band radio luminosities of  $\sim 10^{27.6}$  Watt according to the best-fit relation derived above. To test this prediction, we collected archival data from the literature for five well studied microquasars with available contemporaneous multi-wavelength radio observations. Given the uncertainty in the measurements of different parameters for the microquasars (viewing angle, jet velocity, distance,  $M_{\text{BH}}$ ), with each source having multiple estimates in the literature, we used a Monte-Carlo approach to calculate the mean and spread of the  $\mathcal{L}_{\text{int,c}}^{\text{Br-B}}$  and  $M_{\text{BH}}$  for each source (see section Methods).

Figure 1 shows the position of the microquasars with respect to the best-fit line from the supermassive  $M_{\text{BH}}$  sample. The values represent the mean and the errorbars the spread given the different estimates for each source. All microquasars are consistent with the best-fit  $\mathcal{L}_{\text{int,c}}^{\text{Br-B}} - M_{\text{BH}}$  relation for blazars, within the  $3\sigma$  confidence area of the fit, straddling the best-fit line. In fact, four out of the five sources are within  $1\sigma$ . While both fit and measurement uncertainties are quite significant at this mass range, our results suggest that the scaling derived from the supermassive BH sample is in fact a universal scaling extending over at least  $\sim 9$  orders of magnitude both in  $\mathcal{L}_{\text{int,c}}^{\text{Br-B}}$  and  $M_{\text{BH}}$ .

A non-linear relation between the flux of the jet (and hence the luminosity) and the  $M_{\text{BH}}$  ( $S_{\nu} \propto M^{1.42}$ ) was predicted by [27] for flat spectrum sources ( $s = 0$ ). Our best-fit slope is about  $2.3\sigma$  from the theoretical prediction. However, [27] pointed that if the jets are powered by spin extraction from the black hole [6], then the jet variables will not only depend on  $M_{\text{BH}}$  and the accretion rate but on the spin as well. Within the framework of the Blandford-Znajek mechanism [6], the power of the jet should be proportional to  $M_{\text{BH}}$ :  $P \propto \dot{m} f(a) M_{\text{BH}}$  ([60, 11] and references therein) where  $\dot{m}$  the accretion rate in Eddington units and  $f(a)$  is the spin function ( $f(a) = a/[1 + \sqrt{1 - a^2}]$ ,  $a$  being the dimensionless spin parameter). A linear scaling such as the one we find is then expected provided that the product  $\dot{m} f(a)$  does not depend on  $M_{\text{BH}}$ . The intrinsic scatter around the best-fit relation found in blazars (by a factor of 0.56dex on average, see section Methods) may be due to either  $\dot{m}$  or  $f(a)$  random variations around the blazar mean  $\dot{m} f(a)$  product.

Our best-fit slope is consistent with the results of similar studies on LLAGNs and microquasars using the monochromatic radio flux density versus BH mass ( $1.14 \pm 0.16$  [45] and  $1.23 \pm 0.20$  [39]) however with smaller scatter. The larger scatter found in LLAGNs could be the result of mild beaming that has not been accounted for (see [39, 26]) or other effects related to the use of single-frequency measurements. Beaming effects can also be responsible for the slightly steeper slope, since sources where beaming is important (blazar-like sources) will have systematically higher luminosities compared to the parent population. Thus the slope will be swiftened to steeper values. The fact that our results are consistent with those derived for mildly-beamed and unbeamed sources: (a) provides further support

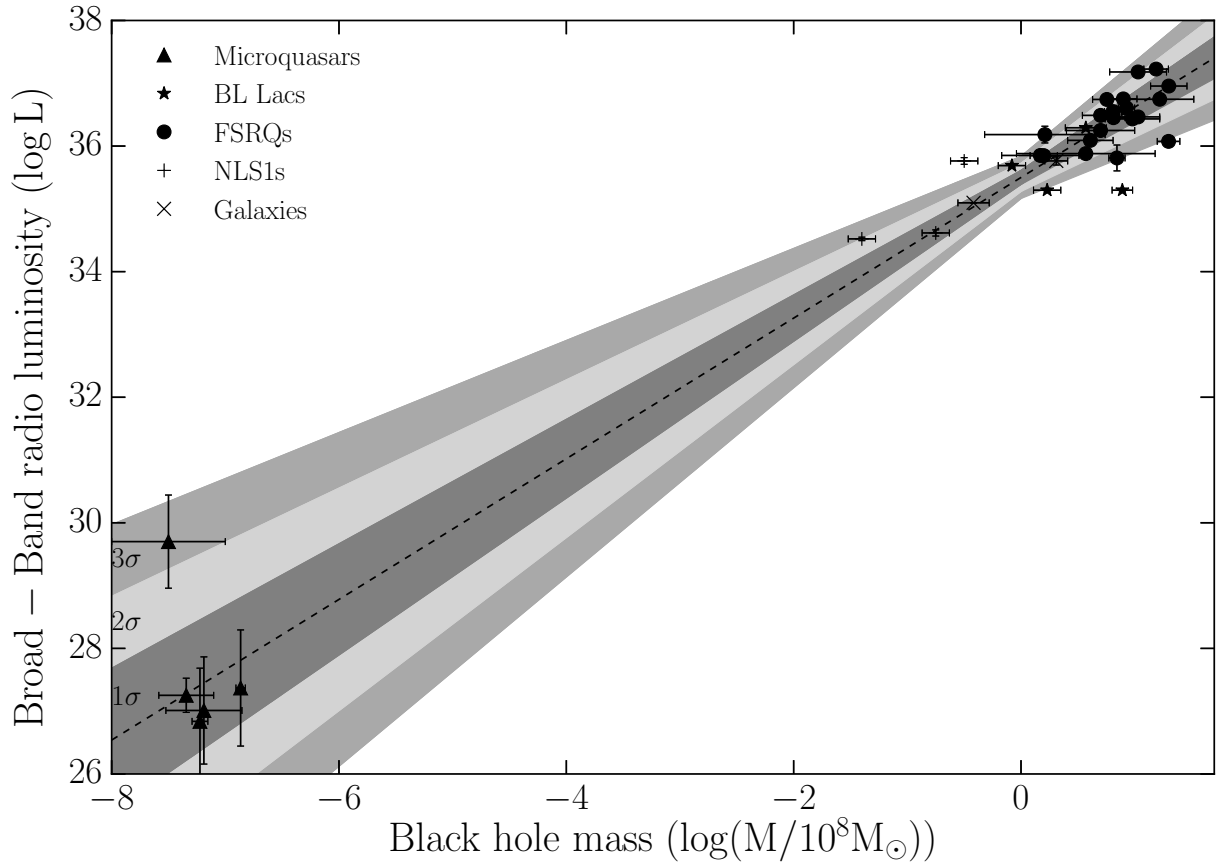


Figure 1: Intrinsic broad-band radio luminosity ( $\mathcal{L}_{\text{int,c}}^{\text{Br-B}}$ ) versus  $M_{\text{BH}}$ . Luminosity is in Watts, and  $M_{\text{BH}}$  in  $10^8 M_{\odot}$ . The dashed line represents the best-fit model using only sources with a supermassive BH. The grey shaded areas are the  $1\sigma$ ,  $2\sigma$ , and  $3\sigma$  confidence regions respectively, taking into account the error on both slope and intercept. For the microquasars every point represents the mean and the errorbar the spread given the different estimates for each source.

that we are correctly correcting for the relativistic effects; and (b) provides supportive evidence for the universality of the derived scaling.

The scaling derived in this work constitutes an important breakthrough in blazar physics. First, it comprises clear evidence of scale-invariant BH jets and of a connection between the proper-

ties of supermassive black holes and the large scale jets they cause in beamed sources. Second, it provides a solid prediction on the  $\mathcal{L}_{\text{int,c}}^{\text{Br-B}}$  of intermediate mass black holes if such exist, and if they form jets. Third, it provides an independent method of estimating the Doppler factor, which will undoubtedly prove an impor-

tant contribution in constraining SED fitting and the different jet emission models in beamed sources. Fourth, the universality of the scaling suggests that blazars share the same physical conditions and accretion regime as microquasars in the hard-state (where they form jets). Finally, our findings point towards the Blandford-Znajek mechanism as the dominant mechanism for jet production in black hole powered jets, and set strong constraints on other potential jet models since they have to reproduce such linear relation.

### Author Contribution

I. L. Performed the analysis and wrote the text. V.P., A. C. S. R., and I. P. contributed with tests for the correlation. I. P. contributed with the interpretation of the results. E. P. contributed with the formalism for the error propagation. E. A., L. F., N. M., V. K., I. M., H. U., and J. A. Z. contributed with the observations and data reduction within the framework of the F-GAMMA program.

### Acknowledgements

This research was supported by the “Aristeia” Action of the “Operational Program Education and Lifelong Learning” and is co-funded by the European Social Fund (ESF) and Greek National Resources, and by the European Commission Seventh Framework Program (FP7) through grants PCIG10-GA-2011-304001 “JetPop” and PIRSES-GA-2012-31578 “EuroCal”. Our study is based on observations carried out with the 100 m telescope of the MPIfR (Max-Planck-Institut für Radioastronomie) and the IRAM 30 m telescope. IRAM is supported by INSU/CNRS (France), MPG (Germany) and IGN (Spain). I. N., I.M. and V.K. were supported for this re-

search through a stipend from the International Max Planck Research School (IMPRS) for Astronomy and Astrophysics at the Universities of Bonn and Cologne.

## References

- [1] F. Acero, M. Ackermann, M. Ajello, A. Albert, W. B. Atwood, M. Axelsson, L. Baldini, J. Ballet, G. Barbiellini, D. Bastieri, A. Belfiore, R. Bellazzini, E. Bissaldi, R. D. Blandford, E. D. Bloom, J. R. Bogart, R. Bonino, E. Bottacini, J. Bregeon, R. J. Britto, P. Bruel, R. Buehler, T. H. Burnett, S. Buson, G. A. Caliandro, R. A. Cameron, R. Caputo, M. Caragiulo, P. A. Caraveo, J. M. Casandjian, E. Cavazzuti, E. Charles, R. C. G. Chaves, A. Chekhtman, C. C. Cheung, J. Chiang, G. Chiaro, S. Ciprini, R. Claus, J. Cohen-Tanugi, L. R. Cominsky, J. Conrad, S. Cutini, F. D’Ammando, A. de Angelis, M. DeKlotz, F. de Palma, R. Desiante, S. W. Digel, L. Di Venere, P. S. Drell, R. Dubois, D. Dumora, C. Favuzzi, S. J. Fegan, E. C. Ferrara, J. Finke, A. Franckowiak, Y. Fukazawa, S. Funk, P. Fusco, F. Gargano, D. Gasparrini, B. Giebels, N. Giglietto, P. Giommi, F. Giordano, M. Giroletti, T. Glanzman, G. Godfrey, I. A. Grenier, M.-H. Grondin, J. E. Grove, L. Guillemot, S. Guiriec, D. Hadasch, A. K. Harding, E. Hays, J. W. Hewitt, A. B. Hill, D. Horan, G. Iafate, T. Jogler, G. Jóhannesson, R. P. Johnson, A. S. Johnson, T. J. Johnson, W. N. Johnson, T. Kamae, J. Kataoka, J. Katsuta, M. Kuss, G. La Mura, D. Landriu, S. Larsson, L. Latronico, M. Lemoine-Goumard, J. Li, L. Li, F. Longo, F. Loparco, B. Lott, M. N.

- Lovellette, P. Lubrano, G. M. Madejski, F. Massaro, M. Mayer, M. N. Mazziotta, J. E. McEnery, P. F. Michelson, N. Mirabal, T. Mizuno, A. A. Moiseev, M. Mongelli, M. E. Monzani, A. Morselli, I. V. Moskalenko, S. Murgia, E. Nuss, M. Ohno, T. Ohsugi, N. Omodei, M. Orienti, E. Orlando, J. F. Ormes, D. Paneque, J. H. Panetta, J. S. Perkins, M. Pesce-Rollins, F. Piron, G. Pivato, T. A. Porter, J. L. Racusin, R. Rando, M. Razzano, S. Razaque, A. Reimer, O. Reimer, T. Reposeur, L. S. Rochester, R. W. Romani, D. Salvetti, M. Sánchez-Conde, P. M. Saz Parkinson, A. Schulz, E. J. Siskind, D. A. Smith, F. Spada, G. Spandre, P. Spinelli, T. E. Stephens, A. W. Strong, D. J. Suson, H. Takahashi, T. Takahashi, Y. Tanaka, J. G. Thayer, J. B. Thayer, D. J. Thompson, L. Tibaldo, O. Tibolla, D. F. Torres, E. Torresi, G. Tosti, E. Troja, B. Van Klavere, G. Vianello, B. L. Winer, K. S. Wood, M. Wood, S. Zimmer, and Fermi-LAT Collaboration. Fermi Large Area Telescope Third Source Catalog. *ApJS*, 218:23, June 2015.
- [2] M. G. Akritas and M. A. Bershady. Linear Regression for Astronomical Data with Measurement Errors and Intrinsic Scatter. *ApJ*, 470:706, October 1996.
- [3] M. G. Akritas and J. Siebert. A test for partial correlation with censored astronomical data. *MNRAS*, 278:919–924, February 1996.
- [4] E. Angelakis, L. Fuhrmann, N. Marchili, L. Foschini, I. Myserlis, V. Karamanavis, S. Komossa, D. Blinov, T. P. Krichbaum, A. Sievers, H. Ungerechts, and J. A. Zensus. Radio jet emission from GeV-emitting narrow-line Seyfert 1 galaxies. *A&A*, 575:A55, March 2015.
- [5] R. D. Blandford and A. Königl. Relativistic jets as compact radio sources. *ApJ*, 232:34–48, August 1979.
- [6] R. D. Blandford and R. L. Znajek. Electromagnetic extraction of energy from Kerr black holes. *MNRAS*, 179:433–456, May 1977.
- [7] G. C. Bower, J. Dexter, S. Markoff, M. A. Gurwell, R. Rao, and I. McHardy. A Black Hole Mass-Variability Timescale Correlation at Submillimeter Wavelengths. *ApJL*, 811:L6, September 2015.
- [8] M. G. Bowler. The mass of SS 433: a conflict resolved? *ArXiv e-prints*, June 2010.
- [9] A. M. Cherepashchuk, N. V. Borisov, M. K. Abubekkerov, D. K. Klochkov, and E. A. Antokhina. Parameters of V404 Cyg-A black-hole binary. *Astronomy Reports*, 48:1019–1028, December 2004.
- [10] A. M. Cherepashchuk, R. A. Sunyaev, S. V. Molkov, E. A. Antokhina, K. A. Postnov, and A. I. Bogomazov. INTEGRAL observations of SS433: system’s parameters and nutation of supercritical accretion disc. *MNRAS*, 436:2004–2013, December 2013.
- [11] R. A. Daly. Spin properties of supermassive black holes with powerful outflows. *MNRAS*, 458:L24–L28, May 2016.
- [12] G. Dubus, B. Cerutti, and G. Henri. The relativistic jet of Cygnus X-3 in gamma-rays. *MNRAS*, 404:L55–L59, May 2010.

- [13] H. Falcke, E. Körding, and S. Markoff. A scheme to unify low-power accreting black holes. Jet-dominated accretion flows and the radio/X-ray correlation. *A&A*, 414:895–903, February 2004.
- [14] J.-H. Fan, Y. Huang, T.-M. He, J. H. Yang, T. X. Hua, Y. Liu, and Y. X. Wang. Radio Variability and Relativistic Beaming Effect for Blazars. *PASJ*, 61:639–643, August 2009.
- [15] J. H. Fan, J. H. Yang, H. B. Xiao, C. Lin, D. Constantin, G. Y. Luo, Z. Y. Pei, J. M. Hao, and Y. W. Mao. Intrinsic Correlations for Flaring Blazars Detected by Fermi. *ApJL*, 835:L38, February 2017.
- [16] R. Fender and T. Belloni. GRS 1915+105 and the Disc-Jet Coupling in Accreting Black Hole Systems. *ARAA*, 42:317–364, September 2004.
- [17] R. P. Fender. Powerful jets from black hole X-ray binaries in low/hard X-ray states. *MNRAS*, 322:31–42, March 2001.
- [18] R. P. Fender. Uses and limitations of relativistic jet proper motions: lessons from Galactic microquasars. *MNRAS*, 340:1353–1358, April 2003.
- [19] R. P. Fender, T. M. Belloni, and E. Gallo. Towards a unified model for black hole X-ray binary jets. *MNRAS*, 355:1105–1118, December 2004.
- [20] R. P. Fender, S. J. B. Burnell, and E. B. Waltman. The radio-jet X-ray binaries. *Visitas in Astronomy*, 41:3–13, 1997.
- [21] R. P. Fender, E. Gallo, and D. Russell. No evidence for black hole spin powering of jets in X-ray binaries. *MNRAS*, 406:1425–1434, August 2010.
- [22] L. Fuhrmann, E. Angelakis, J. A. Zensus, I. Nestoras, N. Marchili, V. Pavlidou, V. Karamanavis, H. Ungerechts, T. P. Krichbaum, S. Larsson, S. S. Lee, W. Max-Moerbeck, I. Myserlis, T. J. Pearson, A. C. S. Readhead, J. L. Richards, A. Sievers, and B. W. Sohn. The F-GAMMA programme: multi-frequency study of active galactic nuclei in the Fermi era. Programme description and the first 2.5 years of monitoring. *A&A*, 596:A45, November 2016.
- [23] E. Gallo, R. P. Fender, and R. I. Hynes. The radio spectrum of a quiescent stellar mass black hole. *MNRAS*, 356:1017–1021, January 2005.
- [24] G. Ghisellini and F. Tavecchio. Fermi/LAT broad emission line blazars. *MNRAS*, 448:1060–1077, April 2015.
- [25] D. C. Hannikainen, R. W. Hunstead, D. Campbell-Wilson, K. Wu, D. J. McKay, D. P. Smits, and R. J. Sault. Radio Emission from GRO J1655-40 during the 1994 Jet Ejection Episodes. *ApJ*, 540:521–534, September 2000.
- [26] S. Heinz and A. Merloni. Constraints on relativistic beaming from estimators of the unbeamed flux. *MNRAS*, 355:L1–L5, November 2004.
- [27] S. Heinz and R. A. Sunyaev. The non-linear dependence of flux on black hole mass and accretion rate in core-dominated jets. *MNRAS*, 343:L59–L64, August 2003.
- [28] T. Hovatta, J. Tammi, M. Tornikoski, E. Valtaoja, J. Torrealba, V. Chavushyan,

- T. G. Arshakian, and I. Cruz-Gonzales. Connection Between Jet Parameters and Black Hole Masses in Quasars. In L. Maraschi, G. Ghisellini, R. Della Ceca, and F. Tavecchio, editors, *Accretion and Ejection in AGN: a Global View*, volume 427 of *Astronomical Society of the Pacific Conference Series*, page 34, October 2010.
- [29] T. Hovatta, E. Valtaoja, M. Tornikoski, and A. Lähteenmäki. Doppler factors, Lorentz factors and viewing angles for quasars, BL Lacertae objects and radio galaxies. *A&A*, 494:527–537, February 2009.
- [30] T. Isobe, E. D. Feigelson, M. G. Akritas, and G. J. Babu. Linear regression in astronomy. *ApJ*, 364:104–113, November 1990.
- [31] J. Khargharia, C. S. Froning, and E. L. Robinson. Near-infrared Spectroscopy of Low-mass X-ray Binaries: Accretion Disk Contamination and Compact Object Mass Determination in V404 Cyg and Cen X-4. *ApJ*, 716:1105–1117, June 2010.
- [32] K. I. I. Koljonen, D. C. Hannikainen, M. L. McCollough, G. G. Pooley, and S. A. Trushkin. The hardness-intensity diagram of Cygnus X-3: revisiting the radio/X-ray states. *MNRAS*, 406:307–319, July 2010.
- [33] E. Körding, H. Falcke, and S. Corbel. Refining the fundamental plane of accreting black holes. *A&A*, 456:439–450, September 2006.
- [34] A. Lähteenmäki and E. Valtaoja. Total Flux Density Variations in Extragalactic Radio Sources. III. Doppler Boosting Factors, Lorentz Factors, and Viewing Angles for Active Galactic Nuclei. *ApJ*, 521:493–501, August 1999.
- [35] Z. Ling, S. N. Zhang, and S. Tang. Determining the Distance of Cyg X-3 with its X-Ray Dust Scattering Halo. *ApJ*, 695:1111–1120, April 2009.
- [36] I. Liodakis, N. Marchili, E. Angelakis, L. Fuhrmann, I. Nestoras, I. Myserlis, V. Karamanavis, T. P. Krichbaum, A. Sievers, H. Ungerechts, and J. A. Zensus. F-GAMMA: Variability Doppler factors of blazars from multiwavelength monitoring. *ArXiv e-prints*, January 2017.
- [37] I. Liodakis and V. Pavlidou. Population statistics of beamed sources - I. A new model for blazars. *MNRAS*, 451:2434–2446, August 2015.
- [38] I. Liodakis, A. Zezas, E. Angelakis, T. Hovatta, and V. Pavlidou. Reconciling inverse-Compton Doppler factors with variability Doppler factors in blazar jets. *A&A*, April 2017.
- [39] A. Merloni, S. Heinz, and T. di Matteo. A Fundamental Plane of black hole activity. *MNRAS*, 345:1057–1076, November 2003.
- [40] J. C. A. Miller-Jones, P. G. Jonker, V. Dhawan, W. Brisken, M. P. Rupen, G. Nelemans, and E. Gallo. The First Accurate Parallax Distance to a Black Hole. *ApJL*, 706:L230–L234, December 2009.
- [41] J. C. A. Miller-Jones, D. G. McCormick, R. P. Fender, R. E. Spencer, T. W. B. Muxlow, and G. G. Pooley. Multiple relativistic outbursts of GRS1915+105: radio emission and internal shocks. *MNRAS*, 363:867–881, November 2005.
- [42] I. F. Mirabel, R. Mignani, I. Rodrigues, J. A. Combi, L. F. Rodríguez, and

- F. Guglielmetti. The runaway black hole GRO J1655-40. *A&A*, 395:595–599, November 2002.
- [43] I. F. Mirabel and L. F. Rodríguez. A superluminal source in the Galaxy. *Nature*, 371:46–48, September 1994.
- [44] S. E. Motta, T. M. Belloni, L. Stella, T. Muñoz-Darias, and R. Fender. Precise mass and spin measurements for a stellar-mass black hole through X-ray timing: the case of GRO J1655-40. *MNRAS*, 437:2554–2565, January 2014.
- [45] N. M. Nagar, H. Falcke, A. S. Wilson, and J. S. Ulvestad. Radio sources in low-luminosity active galactic nuclei. III. “AGNs” in a distance-limited sample of “LLAGNs”. *A&A*, 392:53–82, September 2002.
- [46] R. Narayan and J. E. McClintock. Inclination Effects and Beaming in Black Hole X-Ray Binaries. *ApJ*, 623:1017–1025, April 2005.
- [47] R. S. Nemmen, M. Georganopoulos, S. Guiriec, E. T. Meyer, N. Gehrels, and R. M. Sambruna. A Universal Scaling for the Energetics of Relativistic Jets from Black Hole Systems. *Science*, 338:1445, December 2012.
- [48] A. A. Panferov. Revision of distance to SS433. *ArXiv e-prints*, January 2010.
- [49] R. M. Plotkin, S. Markoff, B. C. Kelly, E. Körding, and S. F. Anderson. Using the Fundamental Plane of black hole activity to distinguish X-ray processes from weakly accreting black holes. *MNRAS*, 419:267–286, January 2012.
- [50] B. Punsly. Models of the compact jet in GRS 1915+105. *MNRAS*, 418:2736–2743, December 2011.
- [51] B. Punsly and J. Rodriguez. A Temporal Analysis Indicates a Mildly Relativistic Compact Jet in GRS 1915+105. *ApJ*, 823:54, May 2016.
- [52] M. J. Reid, J. E. McClintock, J. F. Steiner, D. Steeghs, R. A. Remillard, V. Dhawan, and R. Narayan. A Parallax Distance to the Microquasar GRS 1915+105 and a Revised Estimate of its Black Hole Mass. *ApJ*, 796:2, November 2014.
- [53] J. L. Richards, W. Max-Moerbeck, V. Pavlidou, O. G. King, T. J. Pearson, A. C. S. Readhead, R. Reeves, M. C. Shepherd, M. A. Stevenson, L. C. Weintraub, L. Fuhrmann, E. Angelakis, J. A. Zensus, S. E. Healey, R. W. Romani, M. S. Shaw, K. Grainge, M. Birkinshaw, K. Lancaster, D. M. Worrall, G. B. Taylor, G. Cotter, and R. Bustos. Blazars in the Fermi Era: The OVRO 40 m Telescope Monitoring Program. *ApJS*, 194:29, June 2011.
- [54] L. F. Rodríguez, E. Gerard, I. F. Mirabel, Y. Gomez, and A. Velazquez. Radio Monitoring of GRS 1915+105. *ApJS*, 101:173, November 1995.
- [55] P. Saikia, E. Körding, and H. Falcke. The Fundamental Plane of black hole activity in the optical band. *MNRAS*, 450:2317–2326, July 2015.
- [56] F. Seward, J. Grindlay, E. Seaquist, and W. Gilmore. Diffuse X-ray emission from the jets of SS 433. *Nature*, 287:806–808, October 1980.

- [57] M. S. Shaw, R. W. Romani, G. Cotter, S. E. Healey, P. F. Michelson, A. C. S. Readhead, J. L. Richards, W. Max-Moerbeck, O. G. King, and W. J. Potter. Spectroscopy of Broad-line Blazars from 1LAC. *ApJ*, 748:49, March 2012.
- [58] T. Siebert, R. Diehl, J. Greiner, M. G. H. Krause, A. M. Beloborodov, M. C. Bel, F. Guglielmetti, J. Rodriguez, A. W. Strong, and X. Zhang. Positron annihilation signatures associated with the outburst of the microquasar V404 Cygni. *Nature*, 531:341–343, March 2016.
- [59] Z. Stuchlík and M. Kološ. Models of quasi-periodic oscillations related to mass and spin of the GRO J1655-40 black hole. *A&A*, 586:A130, February 2016.
- [60] A. Tchekhovskoy, R. Narayan, and J. C. McKinney. Black Hole Spin and The Radio Loud/Quiet Dichotomy of Active Galactic Nuclei. *ApJ*, 711:50–63, March 2010.
- [61] J. Torrealba, V. Chavushyan, I. Cruz-González, T. G. Arshakian, E. Bertone, and D. Rosa-González. Optical Spectroscopic Atlas of the MOJAVE/2cm AGN Sample. *RMxAA*, 48:9–40, April 2012.
- [62] S. A. Trushkin. Radio emission of galactic X-ray binaries with relativistic jets. *Astronomical and Astrophysical Transactions*, 19:525–535, 2000.
- [63] S. A. Trushkin, N. N. Bursov, and N. A. Nizhelskij. The multifrequency monitoring of microquasars. SS433. *Bulletin of the Special Astrophysics Observatory*, 56:57–90, 2003.
- [64] O. Vilhu and D. C. Hannikainen. Modeling the X-ray light curves of Cygnus X-3. Possible role of the jet. *A&A*, 550:A48, February 2013.
- [65] J.-M. Wang, B. Luo, and L. C. Ho. The Connection between Jets, Accretion Disks, and Black Hole Mass in Blazars. *ApJL*, 615:L9–L12, November 2004.
- [66] F.-G. Xie, Q.-X. Yang, and R. Ma. Jet-dominated quiescent states in black hole X-ray binaries: the case of V404 Cyg. *MNRAS*, 442:L110–L114, July 2014.
- [67] M. Zamaninasab, E. Clausen-Brown, T. Savolainen, and A. Tchekhovskoy. Dynamically important magnetic fields near accreting supermassive black holes. *Nature*, 510:126–128, June 2014.
- [68] A. A. Zdziarski. The jet kinetic power, distance and inclination of GRS 1915+105. *MNRAS*, 444:1113–1118, October 2014.
- [69] A. A. Zdziarski, J. Mikołajewska, and K. Belczyński. Cyg X-3: a low-mass black hole or a neutron star. *MNRAS*, 429:L104–L108, February 2013.
- [70] A. A. Zdziarski, A. Segreto, and G. G. Pooley. The radio/X-ray correlation in Cyg X-3 and the nature of its hard spectral state. *MNRAS*, 456:775–789, February 2016.
- [71] A. A. Zdziarski, M. Sikora, G. Dubus, F. Yuan, B. Cerutti, and A. Ogorzałek. The gamma-ray emitting region of the jet in Cyg X-3. *MNRAS*, 421:2956–2968, April 2012.
- [72] J. A. Zensus. Parsec-Scale Jets in Extragalactic Radio Sources. *ARAA*, 35:607–636, 1997.

## Methods

### Data & Analysis

#### Intrinsic broad-band radio luminosity

We calculated the intrinsic broad-band radio luminosity ( $\mathcal{L}_{\text{int}}^{\text{Br-B}}$ ) of our sources using data from the F-GAMMA program <sup>1</sup>. The F-GAMMA program [22] monitored a total of about 100 blazars detected by the *Fermi* Gamma-ray space telescope [1] for eight years with roughly monthly cadence at ten frequencies from 2.64 to 142.33 GHz. For each frequency we use the maximum likelihood approach described in [53] to calculate the maximum likelihood mean flux-density taking into account errors in measurements, uneven sampling and source variability. From that we construct the “mean” spectrum which we convert to the intrinsic luminosity using the Doppler factor estimates from [36]. In [36], a novel approach is used to model and track the evolution of the flares through multiple frequencies. That method has provided the most accurate estimates to date with an on average 16% error. We use only estimates with quality indicator “confident” or “very confident” to ensure robust results. The level of confidence is defined by the number of available frequencies and flares used in the estimation of the Doppler factor (see [36]).

We convert the maximum likelihood mean flux density for each frequency to the intrinsic luminosity using the following equation:

$$S_\nu = \frac{L_\nu \delta^p}{4\pi d_L^2} (1+z)^{1+s}, \quad (2)$$

where  $S_\nu$  is the flux-density at a given frequency,  $L_\nu$  the intrinsic luminosity at that frequency,  $\delta$  is the Doppler factor,  $d_L$  the luminosity distance,  $z$

the redshift,  $s$  the spectral index which we have defined as  $S \propto \nu^s$ , and  $p$  is equal to  $p = 2 - s$  for the continuous, and  $p = 3 - s$  for the discrete jet case.

By integrating over frequency we calculate the intrinsic broad-band radio luminosity ( $\mathcal{L}_{\text{int}}^{\text{Br-B}}$ ) for each source. The errorbars in the y-axis of Fig. 1 are estimated through formal error propagation taking into account errors in the Doppler factor [36], flux-density, spectral index, and redshift. For the error in the Doppler factor estimates for the three NLS1s we assumed the 16% average error from [36]. Since our redshift estimates are all spectroscopic we have assumed a common error of  $\delta z = 0.01$ .

Previous studies have opted to use the monochromatic radio luminosity of the jet [45, 39]. We can estimate the mean radio luminosity at a fixed frequency and account for the blazar variability using maximum likelihood. However, observer’s frame frequencies are significantly different in the emission rest-frame due to the large redshift span ( $z = [0, 2]$ ) of our sample. Since different rest-frame frequencies probe different emission regimes (optically thick or optically thin) in different blazars as well as different regions, the use of single frequency measurements should affect the scatter of the correlation (see also discussion in [13]). Figure 2 shows the intrinsic monochromatic luminosity at 4.8 GHz versus  $M_{\text{BH}}$  for our sample. There is a strong correlation ( $\tau = 0.44$ , p-value  $2 \times 10^{-4}$  and a slope of  $A = 0.83 \pm 0.17$  and  $B = 24.8 \pm 0.15$ ). Although we find consistent results between monochromatic and broad-band luminosities, the above effects induce a larger scatter around the best-fit line in the former case. We therefore conclude that using the broad-band luminosity provides stronger constrains for the  $\mathcal{L}_{\text{int}}-M_{\text{BH}}$  relation.

<sup>1</sup><http://www.mpifr-bonn.mpg.de/div/vlbi/fgamma>

## BH mass estimation

In order to estimate the  $M_{\text{BH}}$  of our sample we used data from [61] and the scaling relations from [57] using the line luminosities of the MgII and Hb spectral lines. The scalings were calibrated using the virial mass estimation method. We complemented our sample with values from the literature with estimates using the same method for consistency ([57, 67], and references therein). We avoided using methods that involve assumptions on the radio flux density, beaming, SED fitting etc., that could potentially create artificial correlations. The errors in the x-axis of Fig. 1 are the result of error propagation or for the literature values provided by the authors. When that was not possible, we assumed as error the average uncertainty of the available estimates using the same spectral line. All the estimates for the  $\mathcal{L}_{\text{int}}^{\text{Br-B}}$  and  $M_{\text{BH}}$  used in this work are summarized in Table 1.

## Correlation and best-fit model

To test whether there is a correlation between  $\mathcal{L}_{\text{int}}^{\text{Br-B}}$  and the  $M_{\text{BH}}$  we performed a partial correlation analysis [3]. Our partial correlation analysis uses the Kendrall test and yields the probability of no correlation between two variables taking into account the effect of a third. We found that even after removing any redshift effects the correlation coefficient  $\tau = 0.35$  (-1 for negative correlation, 0 for no correlation, 1 for positive correlation) with  $2 \times 10^{-3}$  probability of uncorrelated samples (discrete jet) and  $\tau = 0.51$  with  $5 \times 10^{-6}$  probability of uncorrelated samples (continuous jet). Focusing on the continuous jet case, we examined whether the correlation holds for sub-sets of our sample. For FSRQs alone we find  $\tau = 0.44$  with p-value  $6 \times 10^{-4}$ . Including the

BL Lacs the test yielded  $\tau=0.43$  with p-value  $7 \times 10^{-4}$ , and including the radio galaxies  $\tau=0.45$  with probability  $2 \times 10^{-4}$ . In all cases there is a significant correlation indicating that this is a real trend and not an artifact of the large range of  $M_{\text{BH}}$ .

The fit was performed using the BCES bisector methods described in [2] which takes into account errors in both axis and any intrinsic variability. The slope (A) and intercept (B) of the best-fit for our sample is  $1.12 \pm 0.13$ ,  $B = 35.5 \pm 0.1$ . If we take only intrinsic scatter into account using the bisector method in [30], the slope and intercept become  $A = 1.05 \pm 0.01$  and  $B = 35.55$  consistent with the [2] method. In fact, even with any of the methods described in [2] and [30] the results remain consistent within the uncertainties.

There is some scatter around the best-fit scaling which, if intrinsic, has been accounted for during the fit. To test whether this scatter is induced by the errors in the measurements or it is intrinsic to the sources, we compare the average distance of each measurement from the best-fit scaling to the average distance due to the uncertainty. Using the best-fit scaling, for each measurement of the  $M_{\text{BH}}$  we estimated the predicted intrinsic radio broad-band luminosity and subtracted it from the observed one to determine the distance in the y-axis. We perform the reverse for the x-axis. We calculate the vertical distance for each observation using  $z = \sqrt{x^2 + y^2}$  and the scatter is estimated using  $\text{scatter} = \sqrt{(\sum_{i=1}^N z_i^2)/N}$ . For the expected distance due to error we use the average error on the y- and x-axis and calculate the vertical distance and scatter in the same manner. We found that the scatter of our sample is  $\text{Sc} = 0.56$  whereas the scatter due to error is  $\text{Sc}_{\text{error}} = 0.19$  suggesting that the scatter

Table 1: Blazar sample. (1) F-GAMMA identification name, (2) alternative source name, (3) class (Q is for FSRQs, B for BL Lacs, G for radio galaxies, N for Narrow line Seyferts), (4) redshift, (5) logarithm of the intrinsic brad-band radio luminosity, (6) uncertainty of the luminosity (7) logarithm of the BH mass in solar masses, (8) uncertainty of the BH mass.

Name	ALT-Name	Class	z	$\log \mathcal{L}_{\text{int,c}}^{\text{Br-B}}$	$\sigma_{\log \mathcal{L}}$	$M_{\text{BH}}$	$\sigma_M$
J0102+5824	0059+5808	Q	0.644	35.88	0.05	8.57	0.61
J0136+4751	0133+476	Q	0.859	36.45	0.03	8.81	0.10
J0237+2848	0234+285	Q	1.206	36.75	0.02	9.22	0.30
J0324+3410	1H0323+342	N	0.063	34.61	0.05	7.25	0.12
J0418+3801	3C111	G	0.049	35.76	0.02	8.31	0.10
J0423-0120	0420-014	Q	0.916	35.81	0.21	8.84	0.07
J0433+0521	3C120	G	0.033	35.10	0.02	7.58	0.14
J0530+1331	PKS0528+134	Q	2.070	37.18	0.05	9.03	0.25
J0654+4514	S40650+453	Q	0.928	35.85	0.04	8.17	0.34
J0948+0022	PMN J0948+0022	N	0.583	35.76	0.05	7.5	0.12
J1130-1449	1127-145	Q	1.184	36.07	0.07	9.30	0.10
J1159+2914	PKS1156+295	Q	0.725	36.09	0.06	8.61	0.20
J1221+2813	QSOB1219+285	B	0.102	35.30	0.02	8.89	0.09
J1229+0203	3C273	Q	0.158	36.74	0.02	8.76	0.13
J1256-0547	3C279	Q	0.536	36.75	0.03	8.90	0.12
J1310+3220	OP+313	B	0.997	36.29	0.02	8.57	0.18
J1504+1029	PKS1502+106	Q	1.839	36.43	0.07	8.98	0.24
J1505+0326	PKS1502+036	N	0.408	34.52	0.03	6.6	0.12
J1512-0905	PKS1510-089	Q	0.360	35.85	0.06	8.20	0.12
J1635+3808	4C+38.41	Q	1.814	36.96	0.06	9.30	0.16
J1642+3948	3C345	Q	0.593	36.46	0.02	9.03	0.19
J1800+7828	S51803+78	B	0.680	35.69	0.03	7.92	0.12
J1848+3219	TXS1846+322	Q	0.798	36.18	0.13	8.21	0.53
J1849+6705	S41849+670	Q	0.657	36.55	0.02	8.81	0.07
J2202+4216	BL Lac	B	0.069	35.30	0.03	8.23	0.12
J2229-0832	2227-088	Q	1.560	36.49	0.05	8.70	0.16
J2232+1143	CTA102	Q	1.037	36.61	0.04	8.93	0.07
J2253+1608	3C454.3	Q	0.859	37.23	0.06	9.19	0.11
J2327+0940	PKS2325+093	Q	1.841	36.25	0.04	8.70	0.30

around the best-fit scaling is intrinsic. As discussed above, the intrinsic scatter could be due to random variations of either  $\dot{m}$  or  $f(a)$  around a mean value. An additional source of scatter could be variation of the broad-band luminosity. Our estimates of the  $\mathcal{L}^{\text{Br-B}}$  are limited by the time span of the observations. Although the 8 year dataset of the F-GAMMA program is sufficiently long, it is still possible that exceptional events can occur outside the monitoring period (so that the mean luminosity is actually higher) or alternately a source was unusually active (so that the mean luminosity is actually lower). Cases such as the ones described above are both unlikely and should have a relatively small contribution to the overall scatter.

Correcting for the relativistic effects is essential in order to identify the correct scaling. We investigated the  $\mathcal{L}^{\text{Br-B}} - M_{\text{BH}}$  relation correcting only for redshift. A correlation is detected, however, the sources appear to occupy unrelated regions of the  $\mathcal{L}^{\text{Br-B}} - M_{\text{BH}}$  plot (similar to the uncorrected sample of [47]) and the scaling from the supermassive BHs under-predicts the broad-band radio luminosity of microquasars by roughly ten orders of magnitude (Fig. 3). Accounting for beaming not only brings all classes with supermassive BHs onto one single line, but it also accurately predicts the position of their stellar mass BH counterparts.

## Microquasars

Our sample of microquasars was selected on the availability of contemporaneous multi-wavelength radio observations during their hard-state where there is the presence of a radio jet. Calculating  $\mathcal{L}_{\text{int,c}}^{\text{Br-B}}$  for microquasars is not trivial, the main obstacle being the lack of robust estimates for key parameters (e.g., distance, Doppler

factor), as well as the lack of contemporaneous multi-wavelength radio observations. In most cases the range of available frequencies was confined in the lower frequency range ( $< 43$  GHz). The observed flux density at higher frequencies was the result of extrapolation.

To estimate the relativistic boosting and revert to the rest-frame, we gathered for each source all available estimates in the literature for the velocity of the jet, distance, and viewing angle. For each source we created a parameter space set by the extrema of the aforementioned quantities. We then uniformly drew a random value for each of these parameters and calculated  $\mathcal{L}_{\text{int,c}}^{\text{Br-B}}$ . We repeated this process  $10^4$  times and calculated the mean and spread (minimum, maximum) of  $\mathcal{L}_{\text{int,c}}^{\text{Br-B}}$  for each source. The y-values for the microquasars in Fig. 1 are the mean, and the y-axis errorbars the spread for each of the sources that resulted from the random sampling.

We follow a similar procedure for the  $M_{\text{BH}}$ , by gathering all the available estimates in the literature and calculating the mean and spread. The x-values for the microquasars in Fig. 1 are the mean, and the x-axis errorbars the spread for each of the sources.

The microquasars, parameter ranges, and the references to them are the following:

For SS433 we used radio data from [63], and parameter values from [56, 17, 63, 8, 48, 10] and references therein.

For GRS1915+10 we used radio data from [54], and parameter values from [43, 17, 18, 16, 41, 50, 52, 68, 51] and references therein.

For Cyg-X3 we used radio data from [32], and parameter values from [20, 35, 12, 64, 71, 69, 70] and references therein.

For GROJ1655-40 we used radio data from [25], and parameter values from [25, 62, 42, 18, 19, 46, 21, 44, 59] and references therein.

Table 2: Range of estimates for the different parameters of the microquasars.

	Distance (kpc)	Lorentz factor	Viewing angle (degrees)	$M_{\text{BH}}$ solar masses
SS433	3-5.5	1.02-1.05	73-85	2.7-7.9
GRS1915+10	8.6-13.7	1.01-5.03	60-71	12.4-15
Cyg-X3	7.2-12	1.05-2.40	20-80	1-10
GROJ1655-40	3-3.5	1.04-4.12	70-85	5.10-7.02
V404Cyg	2.25-2.53	1.2-10.0	46-73	3-14

For V404Cyg we used radio data from [23], and parameter values from [9, 26, 40, 31, 66, 58] and references therein. Since the only available estimate for the jet Lorentz factor [26] was a lower limit ( $\Gamma > 5$ , higher than the alternate estimate) given the typical range of Lorentz factors in these sources we assumed an upper limit of 10. Assuming a smaller value (e.g.,  $\Gamma = 7$ ) would result in a difference of maximum values lower than a factor two.

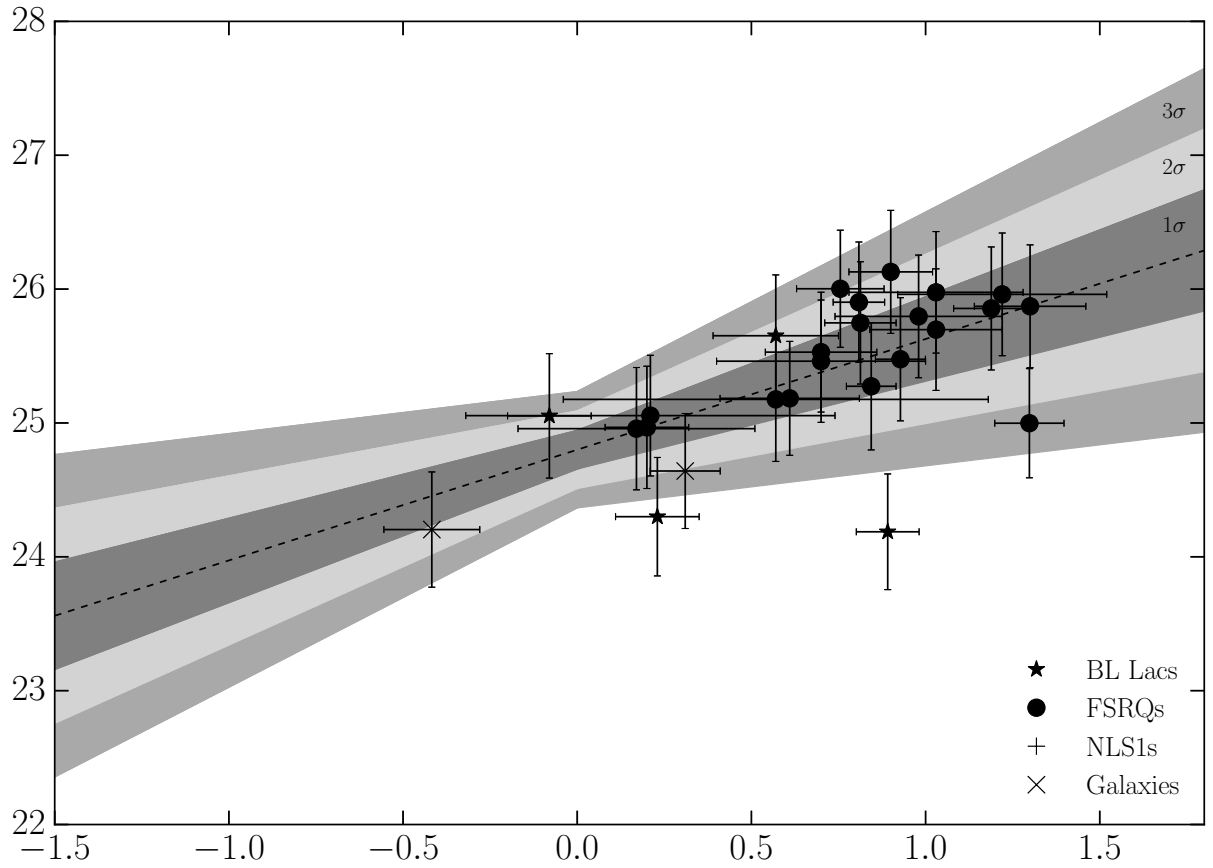


Figure 2: Intrinsic monochromatic radio luminosity (4.8 GHz) versus  $M_{\text{BH}}$ . The dashed line indicates the best-fit model. Symbols and grey areas as in Fig. 1.

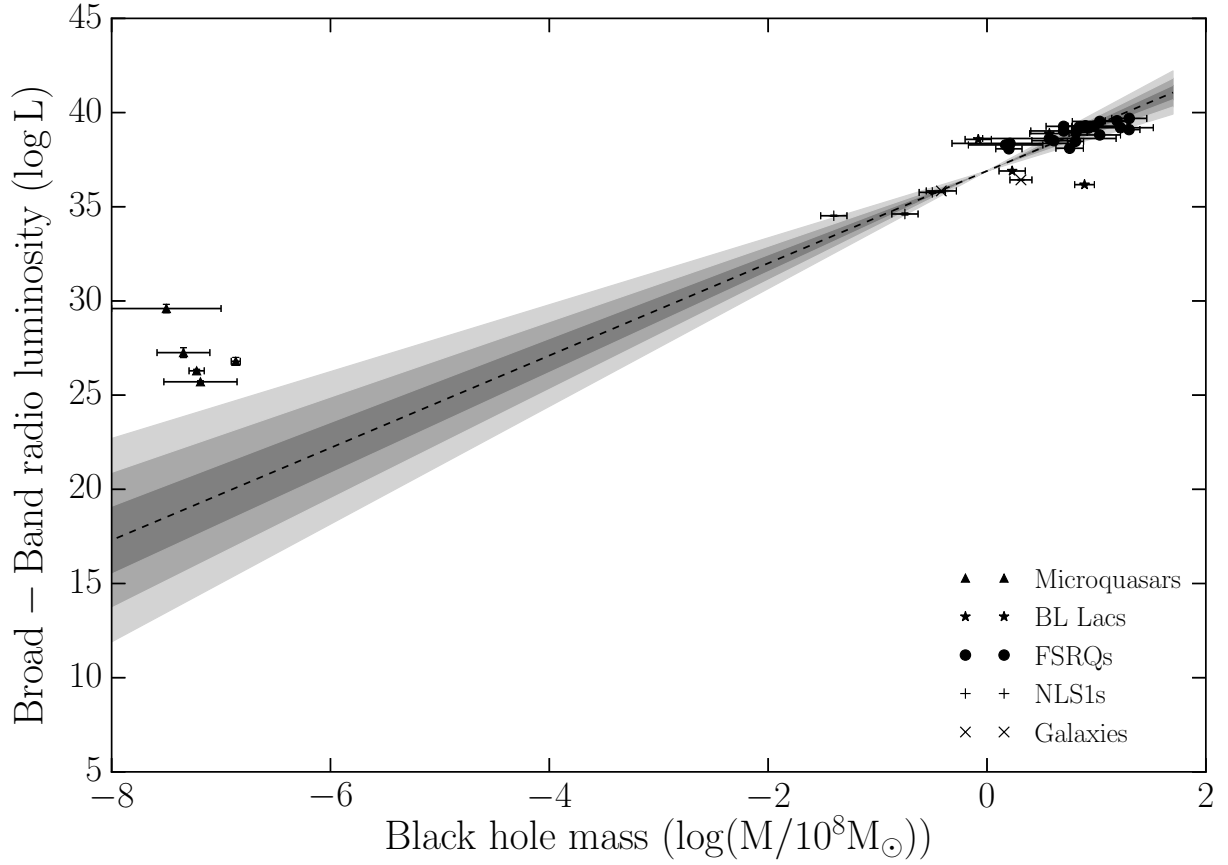


Figure 3: Observer-frame broad-band radio luminosity versus  $M_{\text{BH}}$ . The dashed line indicates the best-fit model. Symbols and grey areas as in Fig. 1.